

A SEARCH FOR SUPERSYMMETRY IN EVENTS WITH A Z BOSON,
JETS, AND MISSING TRANSVERSE ENERGY IN $p - p$ COLLISIONS
WITH $\sqrt{s}=13$ TEV WITH THE ATLAS DETECTOR

TOVA RAY HOLMES



Physics Department
University of California, Berkeley

August 2016 – version 1.0

Tova Ray Holmes: *A Search for Supersymmetry in Events with a Z Boson, Jets, and Missing Transverse Energy in $p - p$ Collisions with $\sqrt{s}=13$ TeV with the ATLAS Detector*, © August 2016

ABSTRACT

A search for new phenomena in final states containing a Z boson decaying to electrons or muons, jets, and large missing transverse momentum is presented. This search uses proton–proton collision data collected during 2015 and 2016 at a center of mass energy $\sqrt{s} = 13$ TeV by the ATLAS detector at the Large Hadron Collider, which correspond to an integrated luminosity of 3.3 fb^{-1} . The search targets the pair production of supersymmetric particles, squarks or gluinos, which decay via jets and a Z boson to the lightest Supersymmetric particle, which does not interact with the ATLAS detector. Results are interpreted in simplified models of gluino-pair (squark-pair) production, and provide sensitivity to gluinos (squarks) with masses as large as 1.3 (1.0) TeV.

PUBLICATIONS

Some results and ideas presented have previously appeared in the following publications:

[this_paper]

ACKNOWLEDGEMENTS

Put your acknowledgements here.

CONTENTS

I	INTRODUCTION	1
1	INTRODUCTION	3
II	THEORY AND MOTIVATION	7
2	THEORY AND MOTIVATION	9
2.1	The Standard Model	9
2.1.1	Matter	10
2.1.2	Forces	11
2.1.3	Phenomenology of Proton-Proton Collisions	19
2.1.4	Problems in the Standard Model	20
2.2	Supersymmetry	22
2.2.1	The Minimal Supersymmetric Standard Model	23
2.2.2	Solutions to Standard Model Problems	24
2.2.3	Simplified Models of Supersymmetry	25
2.3	Monte Carlo Generation	29
III	THE EXPERIMENT	33
3	THE LARGE HADRON COLLIDER	35
3.1	The Injector Complex	36
3.2	Operation of the Large Hadron Collider	37
3.3	Luminosity	39
3.4	Pile-up in proton-proton Collisions	40
4	THE ATLAS DETECTOR	43
4.1	Coordinate System Used in the ATLAS Detector	43
4.2	The Inner Detector	44
4.2.1	The Pixel Detector	44
4.2.2	The Silicon Microstrip Tracker	46
4.2.3	The Transition Radiation Tracker	46
4.3	The Calorimeters	47
4.4	The Muon Spectrometer	48
4.5	The Magnet System	51
4.6	The Trigger System and Data Acquisition	52
5	OBJECT RECONSTRUCTION IN THE ATLAS DETECTOR	57
5.1	Electrons	57
5.2	Photons	60
5.3	Muons	62
5.4	Jets	64
5.5	Overlap Removal	67
5.6	Missing Transverse Momentum	69
6	APPLICATION OF A NEURAL NETWORK TO PIXEL CLUSTERING	73
6.1	Clustering in the Pixel Detector	73
6.1.1	Charge Interpolation Method	74

6.1.2	Improving Measurement with Neural Networks	74
6.2	Impact of the Neural Network	75
6.2.1	The Neural Network in 13 TeV Data	76
IV	SEARCHING FOR SUPERSYMMETRY	81
7	BACKGROUND PROCESSES	83
7.1	Data and Monte Carlo Samples	85
8	OBJECT IDENTIFICATION AND SELECTION	87
8.1	Electrons	87
8.2	Muons	88
8.3	Jets	88
8.4	Photons	89
9	EVENT SELECTION	91
9.1	Trigger Strategy	92
9.2	Signal Efficiency and Contamination	94
10	BACKGROUND ESTIMATION	97
10.1	Flavor Symmetric Processes	97
10.1.1	Flavor Symmetry Method	97
10.1.2	Sideband Fit Method	99
10.2	Z/γ^* + jets Background	101
10.2.1	Photon and Z Event Selection	103
10.2.2	Smearing of Photon Events	104
10.2.3	p_T Reweighting of Photon Events	106
10.2.4	Determining H_T and $m_{\ell\ell}$	107
10.2.5	Subtraction of $V\gamma$ Events	109
10.2.6	Validation in Data	111
10.3	Fake and Non-Prompt Leptons	113
10.4	Diboson and Rare Top Processes	114
11	SYSTEMATIC UNCERTAINTIES	121
11.1	Uncertainties on Data-Driven Backgrounds	121
11.1.1	Uncertainties on the Flavor Symmetry Method	121
11.1.2	Uncertainties on the γ + jets Method	125
11.1.3	Uncertainties on the Fakes Background	128
11.2	Theoretical and Experimental Uncertainties	129
11.3	Impact of Uncertainties on the Signal Region	130
12	RESULTS	135
13	INTERPRETATIONS	141
V	CONCLUSIONS	145
14	CONCLUSIONS AND OUTLOOK	147
	BIBLIOGRAPHY	149

LIST OF FIGURES

Figure 1	The Standard Model of particle physics, containing all known bosons and fermions, with the addition of the hypothetical graviton. [7]	10
Figure 2	Gluon self coupling Feynman diagrams involving 3- and 4-gluon interactions.	14
Figure 3	Quark couplings to the different types of gauge bosons. The $q_{u,d}$ labels represent any up- or down-type quarks.	14
Figure 4	The running of the strong coupling constant, α_s . [13]	15
Figure 5	Trilinear gauge couplings in the Standard Model (SM).	16
Figure 6	Weak couplings to leptons in the SM.	17
Figure 7	Higgs couplings to the weak gauge bosons in the SM.	19
Figure 8	Higgs couplings to fermions in the SM.	19
Figure 9	2008 MSTW Parton Distribution Functions (PDFs) for various particle types given as a function of x and Q^2 , the square of the parton-parton momentum transfer. [14]	20
Figure 10	Galactic rotation curve showing that the discrepancy between the observed luminous matter and the total mass in the system can be described as a non-luminous halo of matter. [16]	21
Figure 11	Two example vertices allowed by the Minimal Supersymmetric Standard Model (MSSM).	24
Figure 12	Running of the strong, weak, and electromagnetic coupling constants for the SM (left) and MSSM (right). [19]	25
Figure 13	Feynman diagram of the decay considered in the simplified models used in the analysis presented in Part iv.	26
Figure 14	Results of an 8 TeV search performed by the ATLAS collaboration in a signal region targeting events like those in ???. The SM backgrounds are shown with their full uncertainties based on data-driven background estimations, and two signals are superimposed on the distribution. The observed datapoints are higher than the expected background, with a total excess of 3.0σ . The events in the signal region are displayed as a function of $m_{\ell\ell}$, the invariant mass of the event's leading leptons [1].	27

Figure 15	Results of an 8 TeV search performed by the Compact Muon Solenoid (CMS) collaboration in a signal region including a broad range of $m_{\ell\ell}$. A 2.4σ local excess is seen in the low $m_{\ell\ell}$ region, and no excess of events is seen in the region with $m_{\ell\ell}$ consistent with an on-shell Z boson. The data is fit based on a data driven estimate of the flavor symmetric background (FS) and the Drell-Yan background (DY), with an additional component for the signal [21].	28
Figure 16	Preliminary results from a 13 TeV search targeting the same signal region as Figure 14 , performed on 3.2 fb^{-1} of 2015 data. Flavor symmetric and $Z/\gamma^* +$ jets backgrounds are taken from data-driven methods, while the other backgrounds are taken from Monte Carlo simulation (MC). They are compared to the data, which shows a 2.2σ excess of events. Distributions from two signal points are superimposed [2].	29
Figure 17	13 TeV production cross-sections for sparticles, as a function of sparticle mass [23].	30
Figure 18	Number of secondary vertices in a module in the first layer of the pixel detector in data (top) and MC (bottom). There are more events in the data than the MC [33].	32
Figure 19	The Large Hadron Collider (LHC) main collider ring and pre-accelerator Super Proton Synchrotron (SPS) overlaid on a map of Switzerland and France, with the four main LHC experiments identified.	35
Figure 20	The pre-accelerators of the LHC	36
Figure 21	Bunch structure in the Proton Synchrotron (PS), SPS , and LHC	37
Figure 22	Cross-section of a cryodipole magnet in the LHC . . .	38
Figure 23	Beam spot in the ATLAS detector for one run in 2015. Distributions show only the highest p_T vertex per event. Left is the $x - y$ distribution of vertices, while the right plot shows the $x - z$ distribution. . .	38
Figure 24	Cross-sections for many SM processes at the Tevatron and LHC [40].	39
Figure 25	Instantaneous luminosity of one fill of 7 TeV data in 2011.	40
Figure 26	ATLAS luminosity for Run 1 and Run 2, as of September 2016.	41
Figure 27	Average number of interactions per crossing shown for 2015 and 2016 separately, as well as the sum of the two years.	41
Figure 28	Diagram of the ATLAS detector, with subsystems and magnets identified.	43

Figure 29	Diagram of the ATLAS Inner Detector, containing the Pixel, SCT, and TRT subsystems.	45
Figure 30	Diagram of one-quarter of the ATLAS Inner Detector in the $R - z$ plane, with lines drawn to indicate various η locations.	46
Figure 31	The calorimeter system of the ATLAS detector.	47
Figure 32	Layout of the LAr calorimeter module at central η [36].	48
Figure 33	An x - y view of the Muon Spectrometer (MS). In it, the three barrel layers are visible, as well as the overlapping, differently sized chambers. The outer layer of the MS is about 20m in diameter.	49
Figure 34	An r - z view of the MS . The three layers of the barrel and endcap MS are visible, and all muons at $ \eta < 2.7$ should traverse three detectors, assuming they propagate in an approximately straight line from the interaction point.	50
Figure 35	The magnet system of the ATLAS detector. The inner cylinder shows the solenoid which gives a uniform magnetic field in the Inner Detector (ID). Outside of that are the barrel and endcap toroids, which provide a non-uniform magnetic field for the MS	51
Figure 36	Plots of the magnetic field within the ATLAS detector. Top is the field (broken into its R and z components) as a function of z for several different values of R . Bottom is the field integral through the Monitored Drift Tubes (MDTs) as a function of $ \eta $ for two different ϕ values.	53
Figure 37	Level One (L1) trigger rates for for a run in July 2016 as a function of luminosity block, an approximately 60-second long period of data-taking. The total rate is lower than the combined stack because of overlapping triggers.	54
Figure 38	High Level Trigger (HLT) trigger rates for for a run in July 2016 as a function of luminosity block, an approximately 60-second long period of data-taking. The total rate is lower than the combined stack because of overlapping triggers.	55
Figure 39	Trigger efficiencies as a function of E_T for data and MC . Efficiencies are given for offline selected loose electrons.	55
Figure 40	Identification efficiencies from MC samples for Loose, Medium, and Tight working points. Left is the efficiency for identification of true electrons taken from $Z \rightarrow ee$ MC , and right is the efficiency for mis-identification of jets as electrons taken from dijet MC [43].	58

Figure 41	Combined electron reconstruction and identification efficiencies measured as a function of η for data (using the tag-and-probe method on $Z \rightarrow ee$ events) and $Z \rightarrow ee$ MC. Distributions include all electrons with $E_T > 15$ GeV. [43]	59
Figure 42	Comparison of Tight identification efficiency measurements from data and $Z \rightarrow \ell\ell\gamma$ MC for unconverted (left) and converted (right) photons, with an inclusive η selection. The bottom of each figure shows the ratio of data and MC efficiencies. [46]	61
Figure 43	Muon reconstruction efficiency for the Medium and (for small $ \eta $) Loose working points measured with $Z \rightarrow \mu\mu$ events in data using the tag-and-probe method and in MC as a function of η . The ratio between the two is shown at the bottom. [48]	63
Figure 44	Muon reconstruction efficiency for the High- p_T working point measured with $Z \rightarrow \mu\mu$ events in data using the tag-and-probe method and in MC as a function of η . The ratio between the two is shown at the bottom. [48]	64
Figure 45	Distribution of event p_T density, ρ , taken from MC dijets for different numbers of primary vertices. [50]	66
Figure 46	Energy response as a function of energy and η for Electromagnetic (EM) jets in dijet MC. [50]	66
Figure 47	Dijet MC distributions of the number of pile-up jets passing the Jet Vertex Tagger (JVT) and Jet Vertex Fraction (JVF) cuts (left) and the efficiency for jets from the primary vertex (right) as a function of number of primary vertices in the event [51].	67
Figure 48	Distribution of MV2c20 output for b -jets, c -jets, and light-flavor jets in $t\bar{t}$ MC [52].	68
Figure 49	Distributions of the resolution of the x and y components of Track Soft Term (TST) E_T^{miss} in $Z \rightarrow \mu\mu$ events in data and MC [54].	69
Figure 50	Distributions of the jet term (top left), muon term (top right), and TST (bottom) E_T^{miss} in $Z \rightarrow \mu\mu$ events in data and MC. In the jet term distribution, the feature at zero is due to events with no jets, and the spike at 20 GeV corresponds to the minimum jet p_T considered for the analysis [54].	71
Figure 51	A few possible types of clusters in the Pixel Detector. (a) shows a single particle passing through a layer of the detector, (b) shows two particles passing through the detector, creating a single merged cluster, and (b) shows a single particle emitting a δ -ray as it passes through the detector [55].	73

Figure 52	One example of a two-particle cluster and its truth information compared with the output of the Neural Networks (NNs). The boxes represent pixels, with a color scale indicating Time Over Threshold (ToT). At top, the $p(N = i)$ values give the output of the Number NN , the probabilities that the cluster contains 1, 2, and 3 particles. Given the highest probability is for $N = 2$, the other NNs predict the position and errors of the two particles (in white). The black arrows and squares represent the truth information from the cluster, and the black dot and dotted line show the position measurement for the un-split cluster [55].	76
Figure 53	x resolutions for clusters with 3 (top) and 4 (bottom) pixels in the x direction in 7 TeV data for Connected Component Analysis (CCA) (using only charge interpolation to determine position) and NN clustering taken from MC [55].	77
Figure 54	Performance of the pixel neural network used to identify clusters created by multiple charged particles, as a function of constant coherent scaling of the charge in each pixel in the cluster. The top figure shows the rate at which the neural network wrongly identifies clusters with one generated particle as clusters with multiple particles. The bottom figure shows the rate at which the neural network correctly identifies clusters generated by multiple particles as such.	79
Figure 55	Fraction of cluster classes as a function of the distance between tracks for IBL (top) and 2nd pixel layer (bottom).	80
Figure 56	An example Feynman diagram of $t\bar{t}$ production and decay.	83
Figure 57	An example Feynman diagram of the production and decay of a WZ event.	84
Figure 58	An example Feynman diagram of the production and decay of a $Z/\gamma^* + \text{jets}$ event.	84
Figure 59	Schematic diagrams of the control, validation and signal regions for the on-shell Z (top) and edge (bottom) searches. For the on-shell Z search the various regions are shown in the $m_{\ell\ell} - E_T^{\text{miss}}$ plane, whereas in the case of the edge search the signal and validation regions are depicted in the $H_T - E_T^{\text{miss}}$ plane.	92

Figure 60	Signal region acceptance (left) and efficiency (right) in SRZ for the simplified model with gluino pair production with $\tilde{\chi}_2^0$ decays to $\tilde{\chi}_1^0$ and an on-shell Z boson with 1GeV neutralino LSP. Acceptance is calculated by applying the signal-region kinematic requirements to truth objects in MC, which do not suffer from identification inefficiencies or measurement resolutions.	94
Figure 61	Expected signal contamination in CRT (left) and CR-FS (right) for the signal model with gluino pair production, where the gluinos decay to quarks and a neutralino, with the neutralino subsequently decaying to a Z boson and a 1GeV neutralino LSP.	95
Figure 62	Expected signal contamination in VRS (left) and VRT (right) for the signal model with gluino pair production, where the gluinos decay to quarks and a neutralino, with the neutralino subsequently decaying to a Z boson and a 1GeV neutralino LSP.	95
Figure 63	Comparison of data and MC in a selection like SRZ, without the E_T^{miss} cut.	101
Figure 64	MC comparison of boson p_T in a selection of photon and $Z \rightarrow \ell\ell$ events with $H_T > 600$ GeV.	103
Figure 65	$E_{T,\parallel}^{\text{miss}}$ distributions in MC for $Z+\text{jets}$ ee (left) and $\mu\mu$ (right) channels compared to $\gamma + \text{jets}$ in an inclusive region with $H_T > 600$ GeV.	105
Figure 66	$E_{T,\parallel}^{\text{miss}}$ distributions in MC for $Z+\text{jets}$ ee (left) and $\mu\mu$ (right) channels compared to $\gamma + \text{jets}$ in an inclusive region with $H_T > 600$ GeV after the smearing procedure has been performed. These distributions have also been p_T reweighted, as described in Section 10.2.3.	106
Figure 67	Photon reweighting factors for the ee (left) and $\mu\mu$ (right) channels derived from data and MC.	107
Figure 68	E_T^{miss} distribution comparing MC distributions of photon and Z events before any smearing is applied (top), with only p_T reweighting applied (bottom left), and after p_T reweighting and smearing have both been applied (bottom right) in the ee channel of 2016 data.	108
Figure 69	E_T^{miss} distribution comparing MC distributions of photon and Z events before any smearing is applied (top), with only p_T reweighting applied (bottom left), and after p_T reweighting and smearing have both been applied (bottom right) in the $\mu\mu$ channel of 2016 data.	109

Figure 70	$Z/\gamma^* + \text{jets}$ MC $m_{\ell\ell}$ distribution compared to the prediction from $\gamma + \text{jets}$ method performed on MC (left) and the prediction from $\gamma + \text{jets}$ method performed on data (right).	110
Figure 71	Comparison of data and MC in CR- γ without any H_T cut, including the contributions from various $V\gamma$ processes.	110
Figure 72	Total $\gamma + \text{jets}$ data prediction in SRZ (excluding the E_T^{miss} cut) and the prediction after the $V\gamma$ subtraction.	111
Figure 73	E_T^{miss} distribution in VRZ ee (left) and $\mu\mu$ (right) with total data yield compared to the sum of the prediction from the $\gamma + \text{jets}$ method, the prediction from the flavor symmetry method, the prediction from the fake background estimation (included under “other”), and the remaining backgrounds taken from MC.	112
Figure 74	$\Delta\phi(\text{jet}, p_T^{\text{miss}})$ distribution in for the leading jet (left) and the subleading jet (right). The comparison is performed in VRZ with the cut on $\Delta\phi(\text{jet}_{12}, p_T^{\text{miss}})$ removed. The total data yield is compared to the sum of the prediction from the $\gamma + \text{jets}$ method, the prediction from the flavor symmetry method, the prediction from the fake background estimation (included under “other”), and the remaining backgrounds taken from MC.	112
Figure 75	Sub-leading lepton p_T for ee (left) and $\mu\mu$ (right) events in the tight-tight region used to measure the real-lepton efficiency for 2016.	114
Figure 76	Sub-leading lepton p_T for $e\mu$ (left) and $\mu\mu$ (right) events in the tight-tight region used to measure the fake-lepton efficiency for 2016.	115
Figure 77	Same sign validation regions in the ee (top left), $\mu\mu$ (top right), $e\mu$ (bottom left) and μe (bottom right) channels combining 2015+2016 data. Uncertainty bands include both statistical and systematic uncertainties.	115
Figure 78	Distribtuions of data and MC in VR-WZ. Reconstructed transverse mass of the W (top) and mass of the Z (bottom).	117
Figure 79	Distribtuions of data and MC in VR-WZ. p_T of the W (top) and Z (bottom).	118
Figure 80	Distribtuions in VR-WZ. On the top, mass of the Z bosons in the event, and on the bottom, p_T of the Z bosons.	119

Figure 81	<code>MC</code> closure plots of VRS (top) and SRZ (bottom). The number of events from <code>MC</code> (black points) is compared to the number of events predicted from the flavor symmetry method (yellow histogram). The comparison is performed before the expanded $m_{\ell\ell}$ window is used to predict the on-Z bin, but because the shape is taken from the same <code>MC</code> , the result is identical.	122
Figure 82	Measurements of k , the ratio of electron to muon events, in bins of p_T and η . On the top is the measurements indexed by the leading lepton, while the measurements indexed by the subleading lepton are on the bottom. These efficiencies are for the 2016 dataset.	123
Figure 83	α , the trigger efficiency ratio, calculated as a function of E_T^{miss} from three different sources: data (blue), the usual skimmed $t\bar{t}$ <code>MC</code> (red), and an unskimmed $t\bar{t}$ <code>MC</code> (green).	125
Figure 84	Plots of the fraction of on-Z events with a VR-FS-like selection as a function of H_T . The top figure shows 2015 data and <code>MC</code> while the bottom figure shows the same for 2016.	126
Figure 85	E_T^{miss} distributions for $\gamma + \text{jets}$ predictions using different reweighting variables, as well as distributions with the nominal reweighting but with smearing functions taken from data and from <code>MC</code> in a ≥ 2 -jet region.	127
Figure 86	<code>MC</code> closure of the $\gamma + \text{jets}$ method as a function of E_T^{miss} comparing the <code>MC</code> prediction of the Z background with the $\gamma + \text{jets}$ method performed on $\gamma + \text{jets}$ <code>MC</code> . The uncertainty band includes both statistical and reweighting uncertainties.	128
Figure 87	Distributions of $m_T(\ell, E_T^{\text{miss}})$, the transverse mass of the lepton and the E_T^{miss} in a Validation Region (<code>VR</code>) designed to target $W\gamma$ processes. Top is the distribution with a E_T^{miss} cut at 100 GeV, and bottom is the same distribution with a E_T^{miss} cut of 200 GeV. .	133
Figure 88	Comparison of background predictions and data yields in four validation regions, as well as the signal region. Definitions of all regions can be found in Table 7 , with both rare top and fake backgrounds grouped together under the “other” label. The uncertainty band includes all statistical and systematic uncertainties. Below is a panel of the one-sided statistical significances of the deviations between the predicted and observed quantities for each region.	135

Figure 93	Expected and observed exclusion contours derived from the results in SRZ for the \tilde{g} - $\tilde{\chi}_1^0$ on-shell grid. The dashed blue line indicates the expected limits at 95% CL and the yellow band shows the 1σ variation of the expected limit as a consequence of the uncertainties in the background prediction and the experimental uncertainties in the signal ($\pm 1\sigma_{\text{exp}}$). The observed limits are shown by the solid red line, with the dotted red lines indicating the variation resulting from changing the signal cross section within its uncertainty ($\pm 1\sigma_{\text{theory}}^{\text{SUSY}}$)	143
Figure 94	Expected 95% Confidence Level (CL) exclusion contours (dashed) and 5σ discovery contours (solid) for $L_{\text{int}} = 300^{-1}$ (black) and 3000^{-1} (red) for gluino pair-production, with 1σ bands representing the uncertainty on the production cross-section. Superimposed is the observed 8 TeV exclusion for similar models. [94]	148

LIST OF TABLES

Table 1	Supermultiplets of the MSSM . Sfermions, on the first five rows, are all spin-0. Higgsinos and gauginos are all spin-1/2. Three sets of each fermion's supermultiplet exist, one for each generation. [17]	22
Table 2	Simulated background event samples used in this analysis with the corresponding matrix element and parton shower generators, cross-section order in α_s used to normalise the event yield, underlying-event tune and PDF set.	86
Table 3	Summary of the electron selection criteria. The signal selection requirements are applied on top of the baseline selection.	87
Table 4	Summary of the muon selection criteria. The signal selection requirements are applied on top of the baseline selection.	88
Table 5	Summary of the jet and b -jet selection criteria. The signal selection requirements are applied on top of the baseline requirements.	89
Table 6	Summary of the photon selection criteria.	90
Table 7	Overview of all signal, control and validation regions used in the on-shell Z search. More details are given in the text. The flavour combination of the dilepton pair is denoted as either “SF” for same-flavour or “DF” for different flavour. All regions require at least two leptons, unless otherwise indicated. In the case of CR γ , VR-WZ, VR-ZZ, and VR-3L the number of leptons, rather than a specific flavour configuration, is indicated. The main requirements that distinguish the control and validation regions from the signal region are indicated in bold. Most of the kinematic quantities used to define these regions are discussed in the text. The quantity $m_T(\ell_3, E_T^{\text{miss}})$ indicates the transverse mass formed by the E_T^{miss} and the lepton which is not assigned to either of the Z -decay leptons.	93
Table 8	Lepton trigger requirements used for the analysis in different regions of lepton- p_T phase space.	94

Table 9	Yields in signal and validation regions for the flavor symmetric background. Errors include statistical uncertainty, uncertainty from MC closure, uncertainty from the k and α factors, uncertainty due to deriving triggers efficiencies from a DAOD, and uncertainty on the MC shape used to correct for the $m_{\ell\ell}$ expansion.	99
Table 10	Background fit results from the sideband fit method. The $t\bar{t}$ MC's normalization is taken as a free parameter in the fit to data in CRT, then that normalization factor is applied in SRZ. The results are shown here both divided between the ee and $\mu\mu$ channels and summed together. All other backgrounds are taken from MC in CRT, while in SRZ, the $Z/\gamma^* + \text{jets}$ contribution is taken from the $\gamma + \text{jets}$ method. The uncertainties quoted include both statistical and systematic components.	100
Table 11	Summary of the $t\bar{t}$ normalization factors calculated by the sideband fit to CRT and VRT for the 2015+2016 data.	101
Table 12	Comparison of Flavor Symmetric (FS) background predictions from the nominal method, the flavor symmetry method, and the cross-check, the sideband fit method. Uncertainties include statistical and systematic uncertainties in both cases.	102
Table 13	List of triggers used to collect photon events in 2015 and 2016 data-taking.	104
Table 14	Control regions used to measure efficiencies of real and fake leptons. The flavour combination of the dilepton pair is denoted as either "SF" for same-flavour or "DF" for different flavour. The charge combination of the leading lepton pairs are given as "SS" for same-sign or "OS" for opposite-sign.	114
Table 15	Yields in validation regions. In VRS, data-driven background estimates are used for $Z/\gamma^* + \text{jets}$, fakes, and FS processes. All other backgrounds are taken from MC, including all backgrounds in the multi-lepton VRS. Uncertainties include statistical and systematic components.	116

Table 16	Uncertainties in the on-Z signal and validation regions. Nominal predictions are given with statistical uncertainty (including uncertainty from subtracted backgrounds), MC Closure uncertainty, uncertainty on the prediction from varying k and α by their statistical uncertainties, comparing the efficiencies from AODs to that of DAODs, and on the $m_{\ell\ell}$ widening, which includes MC statistics and a data/MC comparison in a loosened region.	121
Table 17	Uncertainty breakdown for the $\gamma + \text{jets}$ method in SRZ. Uncertainties considered are the impact of MC uncertainty on $V\gamma$ backgrounds, MC closure, uncertainty on $m_{\ell\ell}$ shape (also determined via MC closure), reweighting uncertainties, smearing uncertainties, and statistical uncertainty on the $\gamma + \text{jets}$ events used in the method.	129
Table 18	Systematic uncertainties on the fake-lepton background for on-Z regions for 2015+2016 yields. The nominal yield includes statistical uncertainty from the baseline selection in a given region. The following rows indicate the results of varying the real and fake lepton efficiencies up and down by by their statistical uncertainty. Real cont. gives an uncertainty on the the contamination of real leptons in the fake lepton efficiency. b -jet and no b -jet indicate the impact of requiring or vetoing b -tagged jets in the regions used to measure the fake efficiency.	129
Table 19	Fractional uncertainties of dibosons in signal and validation regions from Sherpa scale variations. . .	131
Table 20	Comparison of yields in on-Z and off-Z regions in Sherpa and Powheg diboson MC at 14.7 fb^{-1} . . .	131
Table 21	Overview of the dominant sources of systematic uncertainty on the total background estimate in the signal regions. The values shown are relative to the total background estimate, shown in %.	132
Table 22	Number of events expected and observed in the ee , $\mu\mu$, and combined channels. Expected predictions include all systematic and statistical uncertainties discussed in Chapter 11 . Also shown is the discovery p -value for zero signal strength ($p(s = 0)$) [88], Gaussian significance, 95% CL observed and expected upper limits on the number of signal events (S^{95}), and the corresponding observed upper limit on the visible cross section ($\langle e\sigma \rangle_{\text{obs}}^{95}$).	136

LISTINGS

ACRONYMS

- IBL Insertable B-Layer
MS Muon Spectrometer
ID Inner Detector
SCT Silicon Microstrip Tracker
TRT Transition Radiation Tracker
NN Neural Network
CCA Connected Component Analysis
ToT Time Over Threshold
MDT Monitored Drift Tube
CSC Cathode-Strip Chamber
RPC Resistive Plate Chamber
TGC Thin Gap Chamber
L₁ Level One
HLT High Level Trigger
L₁Calo L₁ Calorimeter Trigger
L₁Topo L₁ Topological Trigger
CTP Central Trigger Processor
TTC Trigger Timing and Control
ROB Read Out Board
RoI Region of Interest
LHC Large Hadron Collider
LEP Large Electron-Positron
SPS Super Proton Synchrotron
CMS Compact Muon Solenoid
ALICE A Large Ion Collider Experiment
LHCb Large Hadron Collider beauty
RF Radiofrequency

PSB	Proton Synchrotron Booster
PS	Proton Synchrotron
OR	Overlap Removal
EM	Electromagnetic
LCW	Local Cluster Weighting
JES	Jet Energy Scale
JER	Jet Energy Resolution
JVT	Jet Vertex Tagger
JVF	Jet Vertex Fraction
CST	Calorimeter Soft Term
TST	Track Soft Term
MC	Monte Carlo simulation
SM	Standard Model
BSM	Beyond the Standard Model
SUSY	Supersymmetry
QCD	Quantum Chromodynamics
PDF	Parton Distribution Function
DM	Dark Matter
LO	Leading Order
NLO	Next to Leading Order
NLO+NLL	Next-to-Leading-Logarithmic Accuracy
SUSY	Supersymmetry
MSSM	Minimal Supersymmetric Standard Model
LSP	Lightest Supersymmetric Particle
AOD	Analysis Object Data
dAOD	derived AOD
SR	Signal Region
VR	Validation Region
CR	Control Region
FS	Flavor Symmetric

CL Confidence Level

HL-LHC High Luminosity Large Hadron Collider

¹

Part I

²

INTRODUCTION

³

4

5 INTRODUCTION

6 In 2010, the LHC began colliding protons in its 27 km ring, taking its place
7 as the most powerful in a long line of accelerators aimed at uncovering the
8 fundamental rules that govern particle physics. Its primary goal was to
9 complete the Standard Model of particle physics by discovering the Higgs
10 boson, the last remaining particle that physicists felt sure must exist. With
11 its presence, the Standard Model would be consistent, explaining every ob-
12 served interaction of known particles, with a complete mathematic frame-
13 work to describe each feature. However, even with a Higgs boson, the
14 Standard Model contained hints that it might be incomplete, suspicious
15 features that suggested that at a higher energy, there might be something
16 more.

17 In 2012, the ATLAS and CMS Experiments discovered the Higgs boson,
18 leaving the LHC physics community without a single primary goal, but
19 rather a host of theories to explore, each extending the Standard Model
20 in a different way. Each theory attempts to solve one of the mysteries left
21 by the Standard Model, providing an explanation for Dark Matter, sug-
22 gesting a mechanism that could explain Gravity's weakness, or explain-
23 ing the Higgs boson's mass. For decades, the most popular of these has
24 been Supersymmetry, which proposes a fermionic symmetry and requires
25 a menagerie of new Supersymmetric particles, none of which has yet been
26 observed.

27 Supersymmetry simultaneously solves more of the Standard Model's
28 problems than any other, making it appealing to theorists and experimen-
29 talists alike. But in order to do this, Supersymmetric particles must appear
30 with masses of approximately 1 TeV, precisely the range of energies the
31 LHC is capable of exploring. In 2015, after a three-year shutdown, the LHC
32 nearly doubled the energy of its collisions, opening up new territory to
33 be explored by analyzers, and providing data that could either discover or
34 exclude many Supersymmetric models.

35 The analysis presented in this thesis searches for Supersymmetry, seek-
36 ing to identify events in which Supersymmetric particles are produced in
37 proton-proton collisions, then decay via a Z boson to a chargeless Super-
38 symmetric particle which escapes ATLAS without detection. A similar AT-
39 LAS search, performed with data from the lower-energy collisions 2012,
40 observed a 3σ excess of events over the expected Standard Model back-
41 ground [1].

42 The excess generated a great deal of interest in this channel, and re-
43 investigating it became a top priority when the upgraded LHC turned back
44 on in 2015. A preliminary search, performed using the 2015 data only, was
45 released at the end of that year. Again an excess was observed, this time
46 with a significance of 2.2σ [2].

47 This thesis describes a search for Supersymmetry performed in this
48 channel using data taken by the ATLAS detector in 2015 and 2016, includ-
49 ing an explanation of the theory and motivation behind the search, and a
50 description of the LHC and the ATLAS detector. The remaining chapters
51 are laid out as follows:

52 CHAPTER 2 outlines the Standard Model of Particle Physics and the
53 benefits of extending it to include Supersymmetry, then continues on to
54 introduce the specific models used in the search presented in later chapters.
55 It also provides an overview of the process of generating MC for use in the
56 ATLAS experiment.

57 CHAPTER 3 describes the LHC and its operation, including the magnet
58 system, the preaccelerator complex, and some of the phenomenology of
59 collisions at 13 TeV.

60 CHAPTER 4 contains descriptions of the many pieces of the ATLAS de-
61 tector, and how they serve to detect particles coming from LHC collisions.
62 ATLAS’s magnet and trigger systems are also discussed.

63 CHAPTER 5 details the process of reconstruction, the procedure by which
64 the electric signals in the ATLAS detector are interpreted as particles to be
65 used for analysis.

66 CHAPTER 6 presents a neural network designed to improve tracking in
67 the ATLAS Pixel Detector, and describes the benefits of its implementation.

68 CHAPTER 7 lists the main backgrounds for the Supersymmetry search
69 described in this thesis, and provides general ideas of how they can be
70 reduced.

71 CHAPTER 8 outlines how objects are identified and selected for this anal-
72 ysis, referencing many of the working points defined in Chapter 5.

73 CHAPTER 9 explains the analysis’s search strategy, defining signal, con-
74 trol, and validation regions, and briefly describing how each contributes
75 to the search.

76 CHAPTER 10 describes, for each of the backgrounds described in Chap-
77 ter 7, how estimates of the Standard Model contributions to the signal
78 region are performed.

79 CHAPTER 11 builds off of Chapter 11, and continues to detail how the
80 uncertainties on each estimate are assessed.

81 CHAPTER 12 shows the results of the analysis, comparing expectations
82 based on background estimates to the observed data.

⁸³ CHAPTER 13 provides interpretations of the results, and explains the
⁸⁴ statistical procedure used to define exclusions on Supersymmetric models.

⁸⁵ CHAPTER 14 concludes with a summary of the results, and an outlook
⁸⁶ for future searches.

87

Part II

88

THEORY AND MOTIVATION

89

This section describes the theoretical foundation for the analysis presented in [Part iv](#). It includes an overview of the Standard Model, including its phenomenology in a pp collider. The theory of Supersymmetry is explained, and the motivation for extending the Standard Model to include it is presented. In addition, this section includes an explanation of Monte Carlo generators and details about the specific form of Supersymmetry searched for in this analysis.

90

91

92

93

94

95

96

97

98 THEORY AND MOTIVATION

99 The Standard Model ([SM](#)) of particle physics represents all particles and
100 interactions currently understood by the particle physics community. It is
101 formulated using the principles of Quantum Field Theory, with the con-
102 straints of several symmetries and physical requirements to determine the
103 rules for allowed interactions [3]. Developed in the 1960s and 70s [4–6], it
104 has been immensely successful at predicting the existence of particles be-
105 fore their discovery, and has held up to many high-precision tests. Despite
106 this success, it has several shortcomings which point to its incompleteness.
107 Though the [SM](#) is likely correct at the energies thus far probed, it may be
108 missing key components that become more important at higher energies.
109 Models supplementing the [SM](#) with additional particles and interactions
110 are referred to as Beyond the Standard Model ([BSM](#)) theories.

111 One possible extension of the [SM](#) is Supersymmetry ([SUSY](#)), a theory
112 which postulates an additional symmetry between bosons and fermions
113 to the [SM](#), creating a spectrum of [SUSY](#) particles (sparticles) which interact
114 with the particles of the [SM](#). This theory motivates the search performed
115 in [Part iv](#), and its theoretical appeals are discussed in this section, along
116 with specific simplified models considered in the search.

117 2.1 THE STANDARD MODEL

118 The [SM](#) of particle physics describes the interactions of all of the particles
119 currently known to exist, and consists of both matter particles and force
120 carriers. This model has been unprecedentedly successful in predicting
121 new particles and phenomena, including the prediction of the Higgs par-
122 ticle almost 50 years before its discovery in 2012, which completed the [SM](#).
123 This section describes the components of the [SM](#) and how they interact,
124 focusing on the environment of the [LHC](#).

125 The particles of the [SM](#) are divided into two categories: fermions and
126 bosons. The fermions comprise all the matter described by the [SM](#), and are
127 spin- $\frac{1}{2}$ particles. The bosons, integer-spin particles, are the force carriers.
128 They provide a mechanism to explain three of the four forces known to
129 particle physics, with gravity still lacking a quantum formulation. The
130 Higgs boson, the only spin-0 particle in the [SM](#), provides a mechanism for
131 giving mass to the other particles. The full [SM](#), with the addition of the
132 hypothetical graviton, is presented in [Figure 1](#).

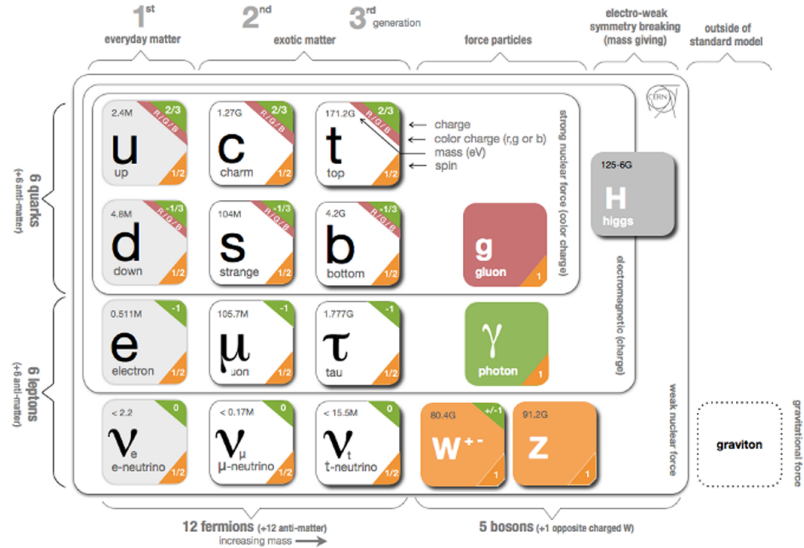


Figure 1: The Standard Model of particle physics, containing all known bosons and fermions, with the addition of the hypothetical graviton. [7]

133 2.1.1 *Matter*

134 The matter described by the SM is made up of fermions, spin- $\frac{1}{2}$ particles
 135 which can be broken into two groups, quarks and leptons. The leptons all
 136 interact weakly, while the quarks additionally interact strongly.

137 2.1.1.1 *Leptons*

138 Leptons, as seen in the bottom left of Figure 1, come in three generations,
 139 each labeled by a flavor: electron, muon, and tau. In the case of the massive
 140 leptons, these flavors are mass eigenstates, and the generations are placed
 141 in an order based on increasing mass. Each massive lepton is negatively
 142 electromagnetically charged and has a positively charged anti-particle.

143 The three neutrinos come in the same flavors as the massive leptons,
 144 but these flavor eigenstates do not correspond exactly to mass eigenstates.
 145 As a consequence, neutrinos oscillate between flavors as they propagate
 146 through space. These oscillations are the only evidence of neutrino mass,
 147 which is bound from below by the mass splittings determined from the
 148 oscillation and bound from above by cosmological limits on the universe's
 149 mass density [8]. Though it is still uncertain if the masses of the neutrinos
 150 follow the same hierarchy as the massive leptons, that expected ordering
 151 is slightly preferred over the inverted hierarchy [9].

152 Unlike the massive leptons, the neutrinos are uncharged, and it is not
 153 yet known whether each neutrino has a separate anti-particle, or if it is its
 154 own antiparticle. Because they are not electromagnetically charged, they
 155 can only interact weakly, making them extremely difficult to detect. In the
 156 ATLAS detector, neutrinos pass through all layers undetected, and their
 157 presence can only be inferred from the non-conservation of momentum

that results in the observed particles. As a consequence of their ability to evade detection, neutrinos are the least understood particles of the SM.

The SM conserves lepton number, L , which is defined as the number of leptons minus the number of anti-leptons in a state, and can also be defined for each lepton flavor. Though there are anomalies that appear in second order SM interactions which could provide very small violations of this conservation, it holds to great precision in experiment. $\mu \rightarrow e\gamma$ branching ratios, for example, have been constrained to 10^{-13} [10]. As a consequence of this conservation, the lightest massive lepton, the electron, is stable.

2.1.1.2 Quarks

Quarks, as seen in the top left of Figure 1, are also electromagnetically charged particles that interact weakly, but are differentiated from the leptons by their strong interactions. They are also organized in three generations ordered by mass, and come in pairs of *up*-type and *down*-type quarks, named after the lightest generation. Though the up quark is lighter than the down, that rule is reversed in the subsequent two generations. Up-type quarks are electromagnetically charged $+\frac{2}{3}$, while the down-type quarks are charged $-\frac{1}{3}$. Quarks are also charged under the strong interaction, whose three charges are often characterized by colors: red, green, and blue. Each quark has an anti-particle with the opposite charges.

These fractional charges and individual colors are never seen in nature because of the requirement (discussed further in Section 2.1.2.2) that stable particle states be color-neutral. To accomplish this, quarks can create two-particle bound states called *mesons* consisting of one quark and one anti-quark with the same color charge or three-particle bound states of quarks or anti-quarks with the three different color charges, which are called *baryons*. The lightest color neutral state containing only quarks, the proton (uud), is stable. Extremely unstable bound states consisting of higher numbers of quarks can also exist, such as the pentaquark discovered in 2015 at the LHC. [11] Collectively, these multi-quark bound states are called *hadrons*.

Like leptons, the number of quarks in a state is conserved, up to very small anomalies. However, because quarks cannot exist in an isolated state, that conservation is described in terms of baryon number (B) defined similarly to lepton number. Mesons, because they have one quark and one anti-quark, have $B = 0$.

2.1.2 Forces

The fermions in the previous section interact via the electromagnetic, weak, and strong forces. In a perturbative quantum field theory, interactions via these forces are represented by mediating bosons. These force carriers interact only with particles charged with their force's quantum numbers. The photon, for example, interacts only with electromagnetically charged

201 particles. Gluons, mediators of the strong force, interact only with color
 202 charged particles, quarks and gluons. All fermions are weakly charged
 203 and interact with the weak force's mediators, the W and Z bosons.

204 The formulation for each of these forces is developed by requiring that
 205 the **SM** lagrangian be locally gauge invariant. [12] This can be accom-
 206 plished by adding gauge fields to the lagrangian, whose behavior under
 207 gauge transformations cancels out the gauge dependence of the free la-
 208 grangian. However, adding a mass term for these fields reintroduces gauge
 209 dependence, so this mechanism only creates forces mediated by massless
 210 gauge bosons. The addition of the Higgs field provides mass terms for the
 211 weak gauge bosons (as well as other particles) without interfering with the
 212 gauge invariance.

213 The total gauged symmetry group for the **SM** is $SU_C(3) \times SU_L(2) \times$
 214 $U_Y(1)$, where C stands for color, the charge of the strong force, L stands
 215 for left, because the weak force is left-handed, and Y is the hypercharge
 216 quantum number, the charge of the unified electroweak force.

217 2.1.2.1 *The Electromagnetic Force*

218 Electromagnetism provides the simplest example of a requirement of local
 219 gauge invariance generating a lagrangian description of a force. Electro-
 220 magnetism has one massless mediator, the photon, which interacts with
 221 all electromagnetically charged particles. What follows is a brief descrip-
 222 tion of how enforcing this invariance generates a lagrangian of the same
 223 form as the classical electromagnetic lagrangian, which can be easily incor-
 224 porated into the **SM**.

225 The particles in [Section 2.1.1](#) are fermions, and so the lagrangian de-
 226 scribing their free propagation are Dirac lagrangians and all follow the
 227 form

$$\mathcal{L} = i\bar{\psi}\gamma^\mu\partial_\mu\psi - m\bar{\psi}\psi. \quad (1)$$

228 Requiring that the free lagrangians for these particles be invariant under
 229 a $U(1)$ local gauge transformation, $e^{iq\lambda(x)}$, can be accomplished by adding
 230 a term to the lagrangian which cancels the derivative term arising from
 231 λ 's dependence on x :

$$\mathcal{L} = i\bar{\psi}\gamma^\mu\partial_\mu\psi - m\bar{\psi}\psi - (q\bar{\psi}\gamma^\mu\psi)A_\mu \quad (2)$$

232 where A_μ is a “gauge field” that transforms according to

$$A_\mu \rightarrow A_\mu + \partial_\mu\lambda. \quad (3)$$

233 This vector field must also come with a free term,

$$\mathcal{L} = -\frac{1}{16\pi}F^{\mu\nu}F_{\mu\nu} + \frac{1}{8\pi}m_A^2A^\nu A_\nu. \quad (4)$$

234 The mass term for this field would not itself be invariant under the
 235 transformation, but the field can simply be made massless to avoid this
 236 problem. The final lagrangian, then, is

$$\mathcal{L} = i\bar{\psi}\gamma^\mu\partial_\mu\psi - m\bar{\psi}\psi - \frac{1}{16\pi}F^{\mu\nu}F_{\mu\nu} - (q\bar{\psi}\gamma^\mu\psi)A_\mu \quad (5)$$

237 which is precisely the original lagrangian with the addition of terms
 238 replicating the form of the Maxwell lagrangian. In a quantized interpre-
 239 tation, it describes a field that interacts with particles with non-zero elec-
 240 tromagnetic charge q via interactions with a massless spin-1 boson, the
 241 photon.

242 For the purpose of succinct notation, this lagrangian is often rewritten
 243 in terms of the “covariant derivative”

$$D_\mu = \partial_\mu + iq\lambda A_\mu \quad (6)$$

244 which immediately cancels the gauge dependent term created by the
 245 transformation. This mechanism is mathematically simple in the $U(1)$ case,
 246 but can be replicated for more complicated gauge transformations with
 247 perturbative approximations.

248 2.1.2.2 *The Strong Force*

249 The strong force is generated by a similar process of requiring local gauge
 250 invariance, but in this case, for a $SU(3)$ transformation. The interactions of
 251 the strong force are described by the theory of quantum chromodynamics,
 252 which is given by the lagrangian

$$\mathcal{L}_{strong} = -\frac{1}{4}G_{\mu\nu}^\alpha G^{\alpha\mu\nu} - \frac{1}{2}\bar{Q}_m D^\nu Q_m \quad (7)$$

253 where the α index runs from 1 to 8 and represents the different genera-
 254 tors of $SU(3)$, and m indexes the three quark generations. $G_{\mu\nu}^\alpha$ is the field
 255 strength tensor and is defined as

$$G_{\mu\nu}^\alpha = \partial_\mu G_\nu^\alpha - \partial_\nu G_\mu^\alpha + g_3 f_{\beta\gamma}^\alpha G_\mu^\beta G_\nu^\gamma \quad (8)$$

256 where g_3 is a function of the energy scale of the interaction μ , and is
 257 related to the strong coupling constant by

$$\alpha_s(\mu) = g_s(\mu)^2 / 4\pi. \quad (9)$$

258 This first term of the lagrangian gives the gluon self-coupling interac-
 259 tions, with terms involving 2, 3, and 4 gluon field terms. The 2-field por-
 260 tion is simply the field strength tensor, but the other terms give couplings
 261 that can be described by the feynman diagrams in [Figure 2](#).

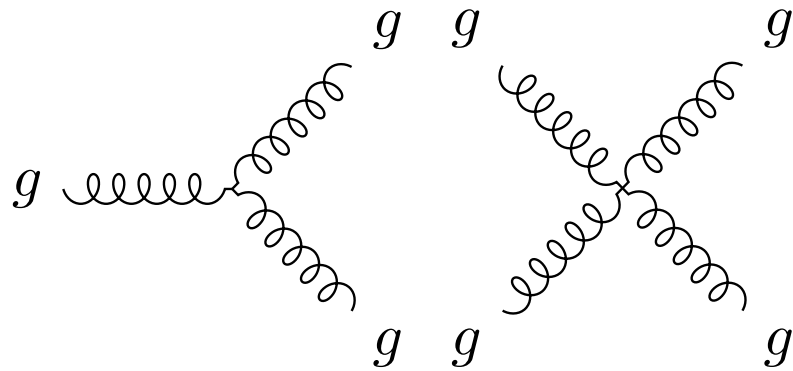


Figure 2: Gluon self coupling Feynman diagrams involving 3- and 4-gluon interactions.

262 In the second term, $\not{D}Q_m$ is the covariant derivative acting on the quark
 263 field. The quarks are in fact charged under all three forces, strong, electro-
 264 magnetic, and weak, so the covariant derivative includes terms to make
 265 each of the force's lagrangians gauge invariant. Thus this term introduces
 266 quark-boson interactions of four types, seen in [Figure 3](#). The quarks' cou-
 267 pling to the gluon is the strongest, with the other couplings happening at
 268 lower rates. The couplings to the W and Z bosons are described in [Sec-](#)
 269 [tion 2.1.2.3](#).

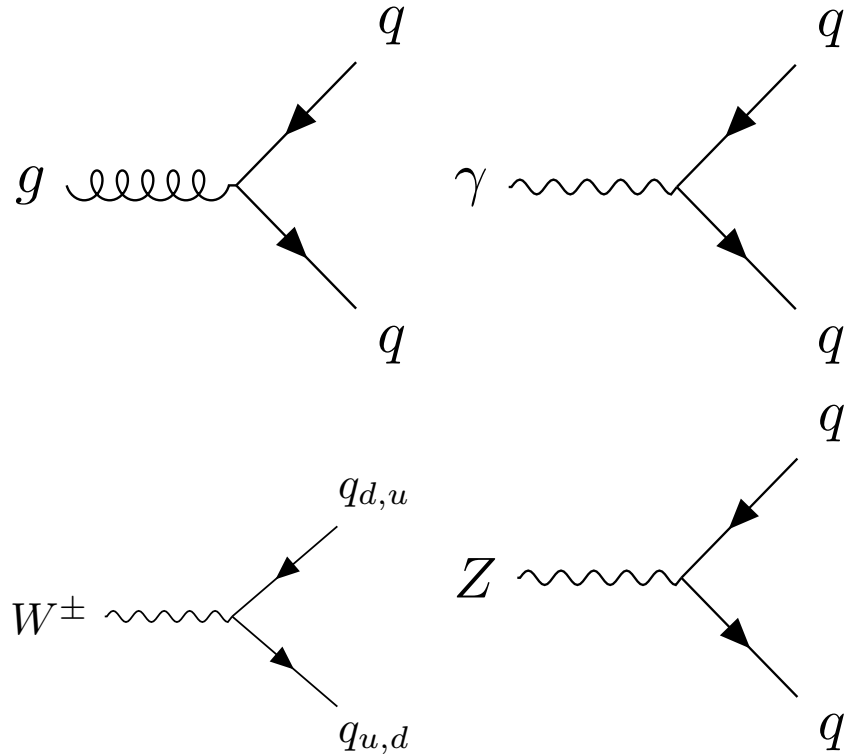


Figure 3: Quark couplings to the different types of gauge bosons. The $q_{u,d}$ labels represent any up- or down-type quarks.

The canceling required to make the lagrangian gauge invariant is only satisfied to a first order expansion of the transformation, guaranteeing its validity only for infinitesimally small perturbations from the ground state. However, the strong coupling constant, α , depends on the energy scale of the interaction, decreasing at higher energy scales and asymptotically increasing at low energies. Figure 4 shows this effect translated to distance scales, demonstrating that QCD is weak and can be considered perturbatively at small distance scales, but at large distance scales this approximation breaks down, and the colorless hadrons introduce in Section 2.1.1.2 must be used to describe interactions instead.

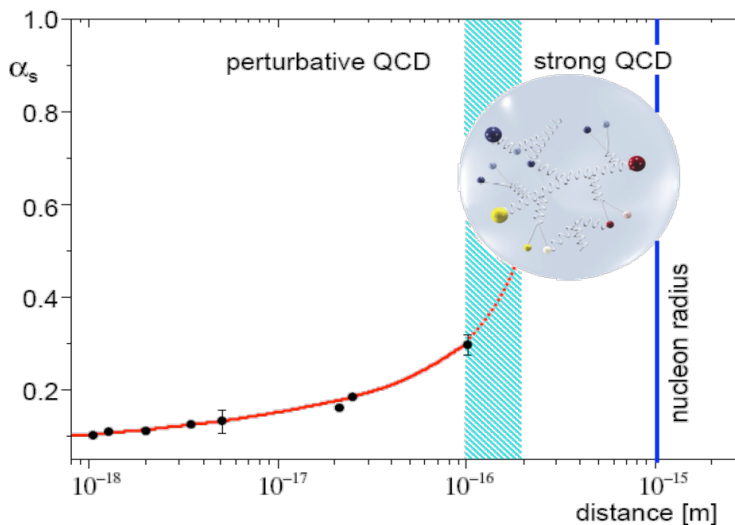


Figure 4: The running of the strong coupling constant, α_s . [13]

The boundary between these regimes is referred to as Λ_{QCD} and differentiates energies at which quarks can be considered free particles and the energies at which they must instead be described by their colorless bound states. The LHC is capable of producing individual quarks, but they instantaneously hadronize, producing showers of particles referred to as *jets*.

2.1.2.3 The Electroweak Force

A similar process, using an $SU(2)$ gauge transformation, can produce a lagrangian that would suffice to describe the W and Z bosons of the SM, if only they were massless. However, they are not, so an alternate mechanism must be used to add masses to the lagrangian.

Before a mechanism for their masses was understood, and before they were discovered, the large masses of the W and Z bosons were proposed in order to unify the electromagnetic and weak forces into the electroweak force. The large masses were crucial to explain the discrepancy in the strength of the two forces.

296 This unified theory resulted in a triplet, W , with coupling g_W , and a
 297 singlet field B , with coupling $g'/2$. However, this electroweak symmetry is
 298 broken, and mixing between these states occurs. Rewritten in their mass
 299 basis, the more familiar electroweak force carriers are produced: W^\pm , two
 300 states with identical coupling resulting from the first two states of the W
 301 triplet, then Z^0 and the photon field A resulting from the mixing of the
 302 last W state and B .

303 The electroweak lagrangian is much more complicated than the strong
 304 lagrangian, and can be divided into several terms:

$$\mathcal{L}_{electroweak} = \mathcal{L}_{gauge} + \mathcal{L}_{fermions} + \mathcal{L}_{Higgs} + \mathcal{L}_{Yukawa}. \quad (10)$$

305 The first term can be written as follows

$$\mathcal{L}_{gauge} = -\frac{1}{4}W^{a\mu\nu}W_{\mu\nu}^a - \frac{1}{4}B^{\mu\nu}B_{\mu\nu} \quad (11)$$

306 where the a indices are numbered 1 through 3 and indicate the genera-
 307 tors of $SU(2)$ which are written

$$W_{\mu\nu}^a = \partial_\mu W_\nu^a - \partial_\nu W_\mu^a + g_2 \epsilon_{abc} W_\mu^b W_\nu^c \quad (12)$$

308 The gauge portion of the lagrangian then generates interaction terms
 309 of between the gauge fields, which when rewritten in terms of the mass-
 310 eigenstate basis, generates interactions between three gauge bosons, like
 311 the ones in [Figure 5](#), as well as interactions between four gauge bosons.

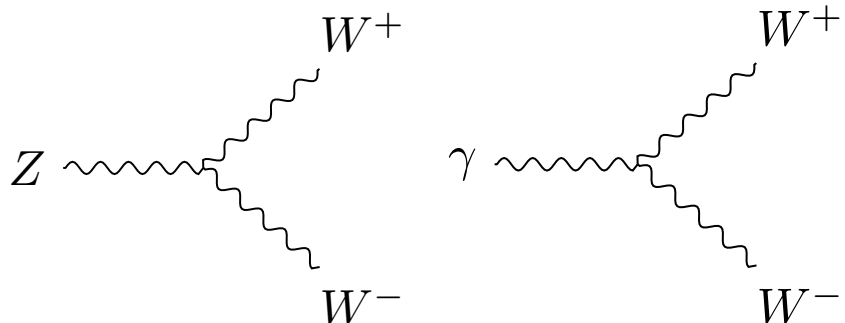


Figure 5: Trilinear gauge couplings in the [SM](#).

312 The fermion portion of the lagrangian is written as

$$\begin{aligned} \mathcal{L}_{fermion} = & -\frac{1}{2}\bar{L}_m \not{D} L_m - \frac{1}{2}\bar{Q}_m \not{D} Q_m \\ & -\frac{1}{2}\bar{U}_m \not{D} U_m - \frac{1}{2}\bar{D}_m \not{D} D_m \\ & -\frac{1}{2}\bar{E}_m \not{D} E_m \end{aligned} \quad (13)$$

where L is the left-handed lepton doublet, Q is the left-handed quark doublet, U is the right-handed singlet for up-type quarks, D is the same for down-type quarks, and E is the right-handed singlet for electrons, muons and taus. Each of these fields has an implicit index running from 1 to 3 to represent the three generations. The covariant derivative in each term includes terms including all the gauge fields the fermion is charged under. Unlike the other forces, the weak force treats left- and right-handed fermion fields differently; it only interacts with the left-handed fields, so only the first two terms' covariant derivatives include W terms. The first term in this lagrangian, for example, produces weak interactions depicted in Figure 6. The Z bosons, because they represent a mixing between the W and B fields, can interact with right-handed leptons and quarks, but do so at different rates than left-handed particles.

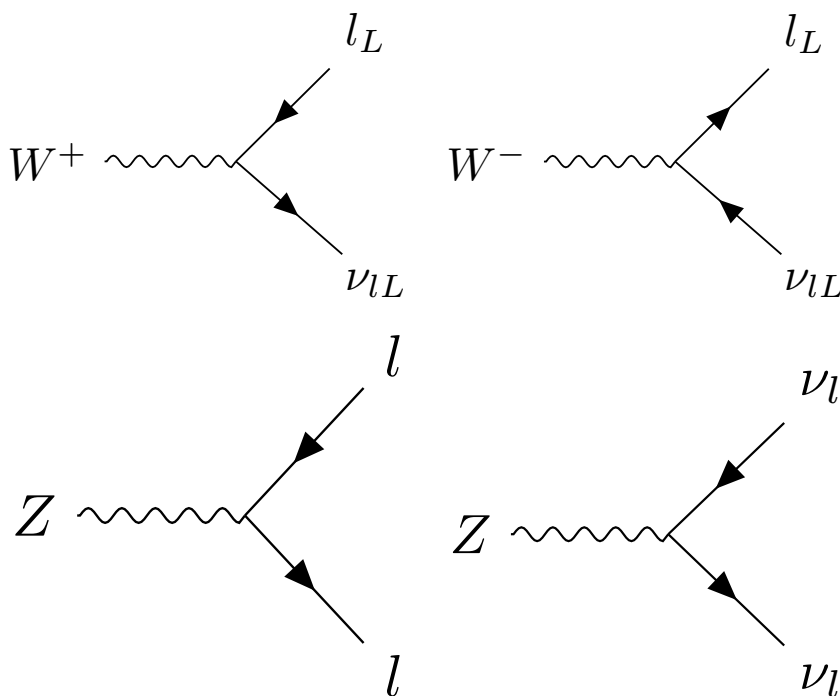


Figure 6: Weak couplings to leptons in the SM.

No right-handed term appears for the neutrino field, because only left-handed neutrinos and right-handed anti-neutrinos have been observed. However, because neutrinos have non-zero mass, their chirality can change with frame boosts, which complicates any claim that right-handed neutrinos do not exist. It is possible that neutrinos are their own antiparticle, making the right-handed anti-neutrino the solution to this problem. It's also possible that very massive right-handed neutrinos do exist, and simply haven't been discovered yet.

The remaining portions of the electroweak lagrangian are related to the Higgs field, which is the source of electroweak symmetry breaking.

336 2.1.2.4 *The Higgs Mechanism*

337 The Higgs mechanism presents an alternate way to generate a mass term
338 for the electroweak gauge bosons, through an unexpected route. It is a
339 scalar field, with a lagrangian

$$\mathcal{L}_{\text{Higgs}} = \frac{1}{2}(\partial_\mu \phi)^*(\partial^\mu \phi) + \frac{1}{2}\mu^2\phi^*\phi - \frac{1}{4}\lambda^4(\phi^*\phi)^2 \quad (14)$$

340 where ϕ is a complex scalar field, $\phi = \phi_1 + i\phi_2$. This looks very similar
341 to a standard scalar field lagrangian, but the signs on the mass and in-
342 teraction terms are reversed, implying an imaginary mass term. However,
343 this isn't a good interpretation of the lagrangian, because differs from all
344 previously considered lagrangians in one important way: its ground state
345 does not occur at $\phi = 0$. Because quantum field theory is perturbative, its
346 validity only holds when expanded around a ground state, which, when
347 calculated for this Higgs lagrangian, must satisfy

$$\phi_1^2 + \phi_2^2 = -\frac{\mu}{\lambda}. \quad (15)$$

348 The original lagrangian can then be rewritten in terms of a field $v + H(x)$
349 centered around the ground state with energy v called the vacuum expec-
350 tation value. This rewriting produces a lagrangian with a non-imaginary
351 mass. However, in an effect called "spontaneous symmetry breaking", the
352 original $SO(2)$ rotational symmetry of the lagrangian is lost, resulting only
353 in a $U(1)$ rotational symmetry; the lagrangian is invariant under a phase
354 transformation.

355 As in [Section 2.1.2.1](#), it is possible to make the lagrangian invariant un-
356 der a local $U(1)$ transformation, $\phi \rightarrow e^{i\theta(x)\phi}$ by adding a massless gauge
357 field A^μ and using the covariant derivative. Due to the many cross terms
358 from the non-zero ground state, terms for the mass of one of the scalar
359 bosons as well as the gauge field appear, leaving only one massless scalar
360 boson. This massless boson, it turns out, can be completely removed from
361 the theory via local $U(1)$ transformations, ultimately producing a theory
362 with one massive scalar (the Higgs) and a massive gauge field (W). The
363 Higgs interaction with the weak gauge bosons also creates couplings be-
364 tween the particles, which can be seen in [Figure 7](#).

365 The remaining piece of the lagrangian, $\mathcal{L}_{\text{Yukawa}}$ describes the Higgs field's
366 interactions with the fermions of the [SM](#), and can be written as

$$\mathcal{L}_{\text{Yukawa}} = -\Gamma_{mn}^e \bar{L}_m \phi E_n - \Gamma_{mn}^u \bar{Q}_m \phi U_n - \Gamma_{mn}^d \bar{Q}_m \phi D_n + h.c. \quad (16)$$

367 where *h.c.* is the hermitian conjugate term, and the Γ matrices are in-
368 dexed by generation, and, when diagonalized, are proportional to the
369 masses of the fermions. The Higgs field's vacuum expectation value pro-
370 duces terms that look like fermion mass terms. Additionally, terms that
371 couple the fermions to the Higgs field are produced, with each fermion's
372 coupling proportional to its mass. Feynman diagrams for lepton and quark
373 terms can be seen in [Figure 8](#).

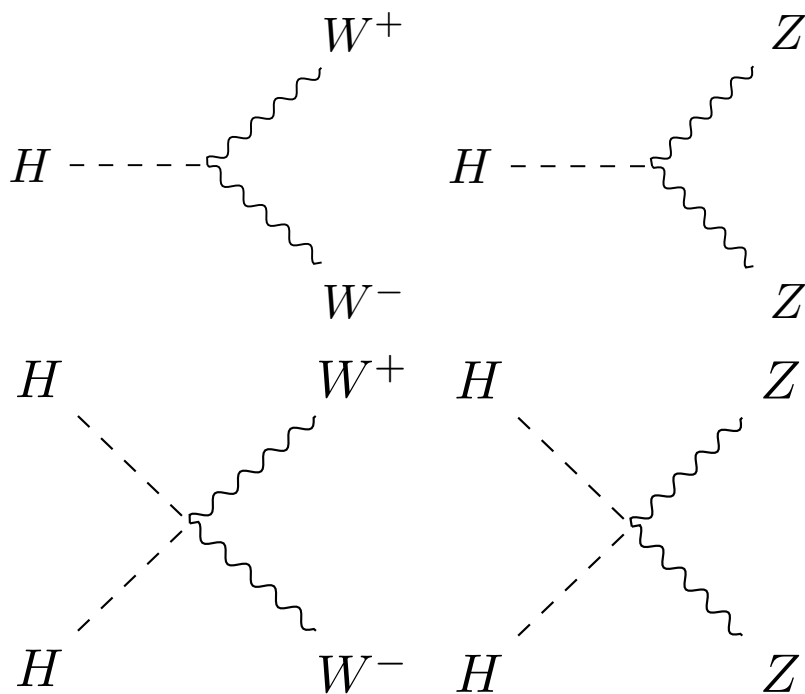


Figure 7: Higgs couplings to the weak gauge bosons in the SM.

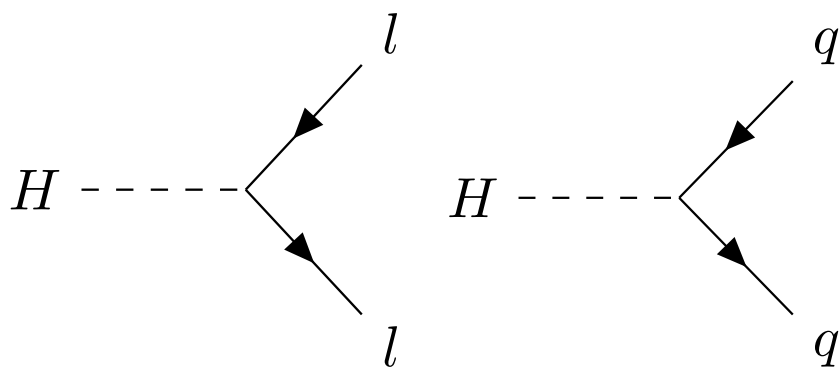


Figure 8: Higgs couplings to fermions in the SM.

³⁷⁴ 2.1.3 Phenomenology of Proton-Proton Collisions

³⁷⁵ As discussed in [Chapter 3](#), the [LHC](#) collides bunches of high-energy protons, and the interactions of these protons' constituent quarks produce the wide array of particles seen in the ATLAS detector. The [LHC](#) typically cites its energy in terms of \sqrt{S} , the center of mass energy of protons in the two colliding beams, which in Run 2 is 13 TeV. However, because the proton is not fundamental, this energy is divided among many particles that make up the proton.

³⁸² To first order, a proton consists of three quarks: two up quarks and one down quark. However, a real quantum mechanical system is much more chaotic, with other quarks popping into and out of existence and gluons

³⁸³

³⁸⁴

385 flying between them. These additional quarks are called *sea* quarks and
 386 can also carry fractions of the proton's energy.

387 The particles inside the proton can have a wide range of energies de-
 388 pending on the internal dynamics at the moment of the collision. These
 389 cannot be predicted exactly, but probabilistic models called Parton Dis-
 390 tribution Functions (PDFs) describe the likelihood of any given configura-
 391 tion. These models are determined using data from hard scattering experiments
 392 and give probabilistic estimates for how often a given type of particle ap-
 393 pears with a fraction x of the total proton energy, as seen in Figure 9.

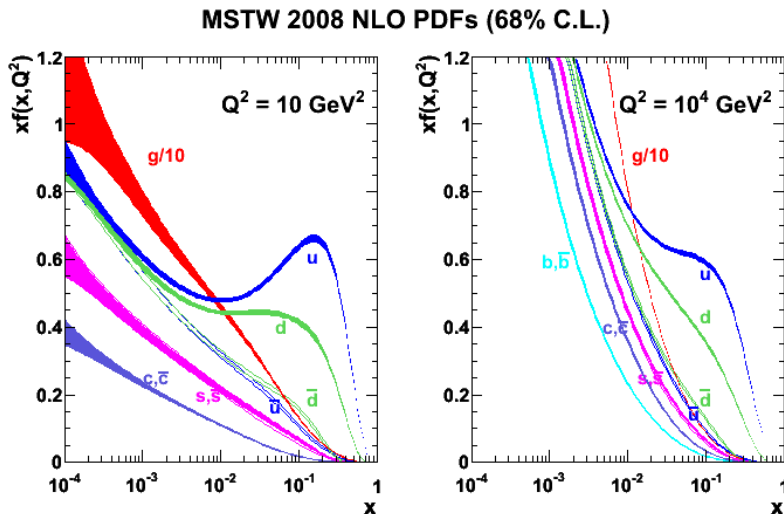


Figure 9: 2008 MSTW PDFs for various particle types given as a function of x and Q^2 , the square of the parton-parton momentum transfer. [14]

394 2.1.4 Problems in the Standard Model

395 Thought the SM is a self-consistent theory that describes to great accuracy
 396 all of the particles and forces it includes, it does have certain shortcomings.
 397 The most glaring is the omission of gravity. Though the force is well un-
 398 derstood at large scales via the theory of General Relativity, no satisfying
 399 quantum description of gravity has been accepted, much less proven. The
 400 Planck scale, the energy scale at which gravitational interactions become
 401 large enough that no sound theory can ignore gravity, is at about 10^{28} eV,
 402 16 orders of magnitude above the electroweak scale, so the exclusion of
 403 gravity from the SM is unlikely to directly affect LHC physics.

404 Another clear omission of the SM is Dark Matter (DM). This matter was
 405 first identified in 1933 through the observation of galactic rotation curves.
 406 [15] The speed of rotation indicated both that there was more mass in the
 407 system than could be accounted for by observations made directly of the
 408 galaxy, and that this additional matter was distributed in a halo, not a disk
 409 like the typical luminous matter. This effect can be seen in Figure 10. Since
 410 then, the gravitational impact of DM has been observed in colliding clus-
 411 ters and many more rotational curves, but the particles that form DM have

never been directly detected or seen at a particle accelerator. As a consequence, very few details are known about the nature of this matter, only its density throughout the universe and that it does not interact strongly or electromagnetically.

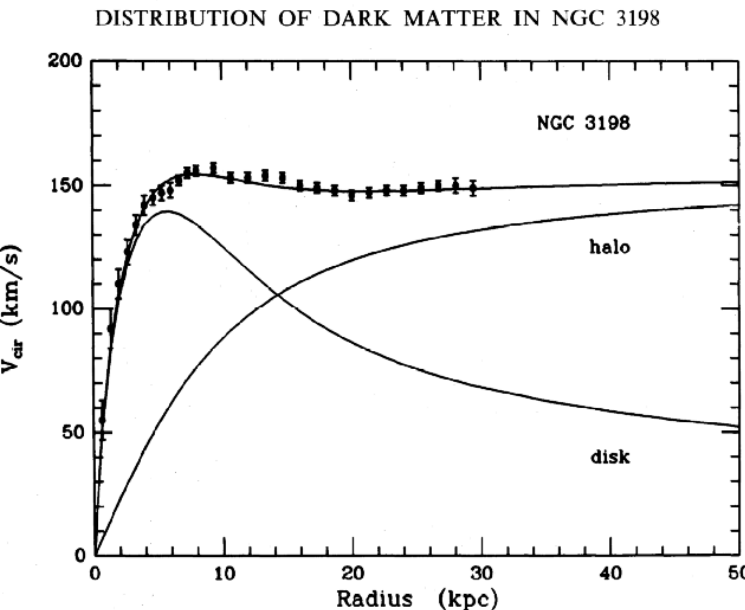


Figure 10: Galactic rotation curve showing that the discrepancy between the observed luminous matter and the total mass in the system can be described as a non-luminous halo of matter. [16]

Beyond the omissions of the SM, there are several aesthetic problems - ones that could have no solution, but seem to suggest that the current SM are missing some pieces that could unify it and provide more order. The first is the sheer number of parameters in the SM. There are 26 independent parameters determining the mass of the particles and all the couplings between them. Besides the rough grouping of fermions into generations, there seems to be no order to masses of particles, and no way to predict the masses or couplings. Each, it seems, is independently provided by nature.

In the past, large numbers of seemingly unrelated parameters have indicated that a theory has a more fundamental form at shorter distance scales. The large number of elements, it turned out, could be explained by different groupings of three particles, the proton, neutron and electron. Later, the menagerie of hadrons became so large that a similar reimagining of what was fundamental took place, and the theory of quarks gave an order to the many mesons and baryons. This pattern leaves physicists suspicious of any theory with too many particles and free parameters, suggesting that perhaps, at a higher energy, there is a simpler model that can unify many of the seemingly disparate elements of the SM.

In addition, some of these seemingly independent parameters have suspicious symmetry. The Higgs mass, for example, has been measured to be 125 GeV. This mass is the sum of the bare mass, the one that appears

Names		sparticles	particles	$SU(3)_C, SU(2)_L, U(1)_Y$
squarks, quarks	Q	$(\tilde{u}_L \tilde{d}_L)$	$(u_L d_L)$	$(3, 2, \frac{1}{6})$
	\tilde{u}	\tilde{u}_R^*	u_R^\dagger	$(\bar{3}, 1, -\frac{2}{3})$
	\tilde{d}	\tilde{d}_R^*	d_R^\dagger	$(\bar{3}, 1, \frac{1}{3})$
sleptons, leptons	L	$(\tilde{\nu} \tilde{e}_L)$	(νe_L)	$(1, 2, -\frac{1}{2})$
	\tilde{e}	\tilde{e}_R^*	e_R^\dagger	$(1, 1, 1)$
Higgs, higgsinos	H_u	$(\tilde{H}_u^+ \tilde{H}_u^0)$	$(H_u^+ H_u^0)$	$(1, 2, \frac{1}{2})$
	H_d	$(\tilde{H}_d^0 \tilde{H}_d^-)$	$(H_d^0 H_d^-)$	$(1, 2, -\frac{1}{2})$
gluino, gluon		\tilde{g}	g	$(8, 1, 0)$
winos, W bosons		$\tilde{W}^\pm \tilde{W}^0$	$W^\pm W^0$	$(1, 3, 0)$
bino, B boson		\tilde{B}^0	B^0	$(1, 1, 0)$

Table 1: Supermultiplets of the [MSSM](#). Sfermions, on the first five rows, are all spin-0. Higgsinos and gauginos are all spin-1/2. Three sets of each fermion's supermultiplet exist, one for each generation. [[17](#)]

437 in the lagrangian, and quantum corrections from interactions with other
 438 particles, which are proportional to the square of the particles' mass. Since
 439 new physics must exist at the Planck scale to account for gravity, these
 440 corrections could be up to 35 orders of magnitude larger than the Higgs
 441 mass. Though the bare mass could theoretically cancel out this massive
 442 correction, these parameters should be independent, and the odds that
 443 they would be precisely the same to 35 places are very, very small. This
 444 near-exact canceling is often called *fine-tuning*, an undesirable trait in a
 445 theory which suggests that some more fundamental symmetry has been
 446 missed. A *natural* solution, one free of this fine-tuning, is sought to resolve
 447 this [SM](#) problem.

448 2.2 SUPERSYMMETRY

449 Supersymmetry ([SUSY](#)) was proposed and developed in the 1970s to give
 450 solutions to many of these [SM](#) shortcomings. The theory works by intro-
 451 ducing a fermionic symmetry to the [SM](#), in addition to the usual spacetime
 452 symmetries of translations, rotations, and changes of Lorentz frame. The
 453 combination of the usual spacetime with this fermionic dimension is called
 454 a *superspace*. Rotations in this dimension result in a particle's spin chang-
 455 ing by 1/2, turning a spin-1/2 fermion into a spin-0 particle, for example.
 456 As a consequence, this symmetry requires the existence of many new parti-
 457 cles - a bosonic *sfermion* for each fermion of the [SM](#) and a fermionic *gaugino*
 458 for each of the gauge bosons. These superpartners of [SM](#) particles should
 459 have identical quantum numbers to the original particle, except for their
 460 spins. [Table 1](#) shows the [SM](#) particles and their superpartners.

If the theory is symmetric under these fermionic rotations, these particle-sparticle pairs can be described by a single *superfield*, which simultaneously describes the behavior of both **SM** and **SUSY** particles in the superspace. However, this completely symmetric behavior is untenable given basic observations of matter in the universe. For example, if there were a *selectron* (the superpartner of the electron, \tilde{e}), with identical mass to the electron, it would have been detected long ago. In fact, such a particle would fundamentally change atomic structure, with the bosonic selectrons capable of piling into the ground state of an atom, and removing all the interesting valence-shell interactions of electrons that determine molecular structure. Thus, if **SUSY** does exist, the symmetry must be broken, with much higher masses for the superpartners than the original **SM** particles.

2.2.1 The Minimal Supersymmetric Standard Model

The Minimal Supersymmetric Standard Model (**MSSM**) was designed to be the simplest supersymmetric extension of the **SM** that remains self consistent, and it results in the particles seen in Table 1[17]. The formulation of the **MSSM** begins by introducing a second Higgs doublet to account for the different masses of the sparticles. As with the **SM** Higgs, electroweak symmetry breaking results in the loss of degrees of freedom, and only five of the original eight states remain, the lightest of which, h^0 , can be interpreted as the **SM** Higgs already discovered. There are two remaining neutral states, A^0 and H^0 , as well as two charged Higgses, H^\pm .

The neutral Higgs states mix with the neutral gauge bosons, while the charged Higgs states mix with the charged gauge bosons, producing a series of states labeled only by their charge and the order of their masses. The neutral states, collectively called the neutralinos, are identified from lightest to heaviest, $\tilde{\chi}_1^0, \tilde{\chi}_2^0, \tilde{\chi}_3^0$, and $\tilde{\chi}_4^0$. The charged states, referred to as charginos, are similarly called $\tilde{\chi}_1^\pm$ and $\tilde{\chi}_2^\pm$.

The **MSSM** introduces many new interactions between **SM** particles and sparticles. Though these don't represent all possible interactions, a general rule is that any **SM** vertex can have two interacting particles replaced with their sparticle equivalents, and this vertex will be part of the **MSSM**. Figure 11 gives two examples of such vertices.

In addition to these interactions, there are several terms that appear in the **MSSM** lagrangian that violate the B and L conservation observed in the **SM**. In fact, these terms violate $B - L$, which, unlike B and L conservation individually, does not have even small violations in the **SM**. These superpotential terms appear as follows

$$W_{\Delta L=1} = \frac{1}{2} \lambda^{ijk} L_i L_j \bar{e}_k + \lambda'^{ijk} L_i Q_j \bar{d}_k + \mu'^i L_i H_u \quad (17)$$

$$W_{\Delta B=1} = \frac{1}{2} \lambda''^{ijk} \bar{u}_i \bar{d}_j \bar{d}_k. \quad (18)$$

Because there are very strong limits on non-conservation of $B - L$ from proton decay experiments, these terms present a challenge for the **MSSM**. It

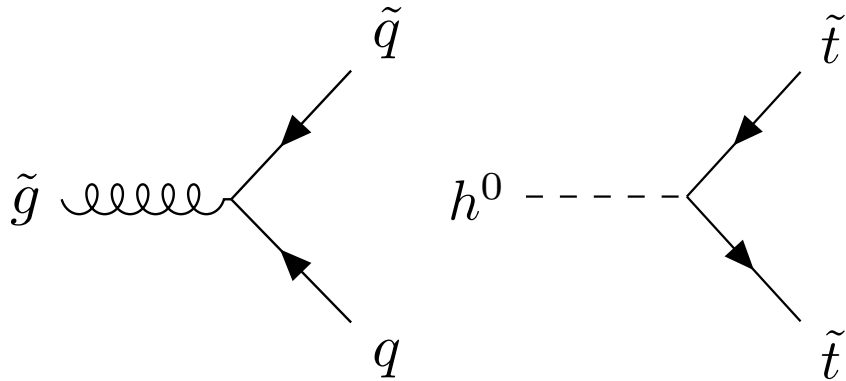


Figure 11: Two example vertices allowed by the [MSSM](#).

would be possible, of course, to simply tune the λ parameters to be small enough to fit within experimental constraints, but these terms can also be eliminated by introducing a new conserved quantity, R -parity. It is defined by

$$P_R = -1^{3(B-L)+2s} \quad (19)$$

where s is the spin of the particle. Requiring that all terms in the lagrangian have a multiplicative P_R of 1 excludes the terms in [Equation 18](#), removing the problem of proton decay. All [SM](#) particles are R -parity even, while the sparticles are R -parity odd, so the conservation of R -parity can translate into a conservation of number of particles and sparticles. As a consequence, massive sparticles typically decay through a chain of lighter sparticles, emitting [SM](#) particles along the way.

2.2.2 Solutions to Standard Model Problems

Perhaps the most compelling consequence of [SUSY](#) comes from R -parity, which, through the formation of a new quantum number unique to sparticles, requires the Lightest Supersymmetric Particle ([LSP](#)) to be stable. This stable particle, if it is neutrally charged, provides an excellent candidate [DM](#) particle. The lightest neutralino, for example, is a viable [DM](#) candidate because it does not interact electromagnetically or strongly, a constraint required due to measurements of the relic density of [DM](#) in the universe. An interaction cross-section higher than what's expected for weak interactions would have led the [DM](#) particle and its anti-particle to annihilate at lower densities, leaving a much smaller amount of [DM](#) in the universe than what is observed today [18].

Many believe that a complete [SM](#) would include a unification of the three forces, as electromagnetism and the weak force have already been unified. This requires that at some higher energy, the coupling constants of all three forces merge. However, in the [SM](#), the coupling constants come close to aligning, but don't perfectly cross. With the addition of [MSSM](#)

529 particles with masses at the TeV scale, the alignment is near perfect, as
 530 shown in [Figure 12](#). This may be a mathematical coincidence, but it's very
 531 compelling to those physicists who believe that "Grand Unified Theory"
 532 must exist.

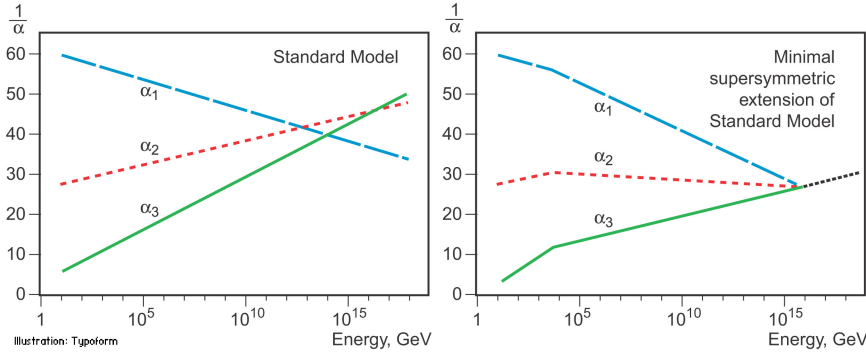


Figure 12: Running of the strong, weak, and electromagnetic coupling constants for the [SM](#) (left) and [MSSM](#) (right). [[19](#)]

533 [SUSY](#) also has the potential to solve the naturalness problem in the [SM](#).
 534 In the [SM](#), the massive amounts of fine tuning are required to cancel the
 535 quadratic corrections to the Higgs mass that result from loops involving,
 536 most importantly, the top quark. In the [MSSM](#), a similar loop involving
 537 the stop quark (the vertex for which is depicted in [Figure 11](#)) contributes
 538 to the Higgs mass with the opposite sign, making it possible to naturally
 539 cancel the corrections without fine tuning. However, the larger the mass
 540 difference between the top quark and stop quark, the larger the remaining
 541 correction when the two terms cancel. Consequentially, to preserve a rea-
 542 sonable degree of naturalness (and here the definition of "reasonable" is
 543 subject to some debate), the stop quark should appear at masses not too
 544 much larger than the top's, at approximately the TeV scale.

545 This naturalness mass limit, as well as the unification of couplings, make
 546 the argument for searching for [SUSY](#) at the [LHC](#) particularly compelling, as
 547 the [LHC](#) is the first collider capable of producing particles at the TeV scale.
 548 As new exclusions on [SUSY](#) are set, the remaining phase space becomes
 549 slightly less natural, but there is no shortage of unexcluded [SUSY](#) theories,
 550 which are continually proposed as new limits are created.

551 2.2.3 Simplified Models of Supersymmetry

552 There are many different theorized models of [SUSY](#), with different mecha-
 553 nisms for breaking the symmetry. Each of these theories typically contains
 554 on order hundreds of free parameters, with complex interactions that de-
 555 termine the mass hierarchy and interaction rates of the sparticles. From an
 556 experimental point of view, the details of these theories and the exact way
 557 the hierarchies are generated are often less relevant to a search than their
 558 outputs.

559 Simplified models, which are typically inspired by more complete theo-
 560 ries, are used to tune the observables of a model more directly. These mod-

els each consist of one production and decay diagram, with the masses of the particles free to be tuned directly. In a more complete theory, it is instead necessary to modify more fundamental parameters like the symmetry breaking scale. A change like this impacts the properties of all the sparticles, but the details of its impact are model dependent. The simplified models allow for relatively model independent interpretations that can also be reinterpreted in the context of a more complete SUSY theory.

In the analysis presented in Part iv, a simplified model is used which produces the decay depicted in Figure 13. This decay chain begins with the pair production of gluinos, which decay via a pair of quarks to the second lightest neutralino, which then decay via a Z boson to the lightest neutralino. In this simplified model, the lightest neutralino is the LSP, and is stable.

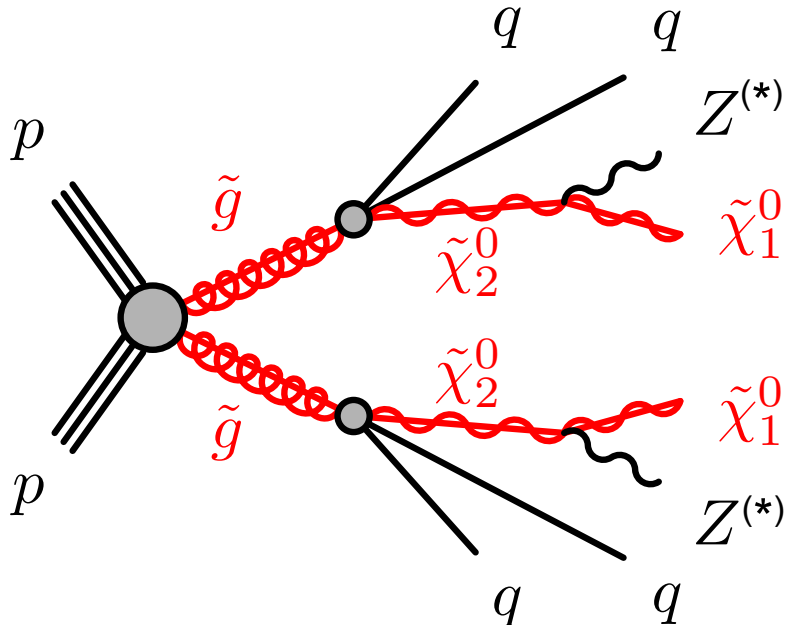


Figure 13: Feynman diagram of the decay considered in the simplified models used in the analysis presented in Part iv.

Using this simplified model, the masses of the particles can be tuned directly. This is very helpful for the generation of MC, discussed in Section 2.3, because a grid of different mass values of the important sparticles involved in the decay can be generated, allowing analyzers to make predictions of likely signals, and to exclude the simplified models as a function of the mass of the sparticles in the case that no discrepancies between predictions and observations are seen.

2.2.3.1 Context and Motivation

Processes similar to the one described by Figure 13 have been the target of previous LHC searches. Both CMS and ATLAS performed searches for SUSY in the two lepton channel with the 8 TeV data collected in 2012. The

585 ATLAS search saw a 3σ excess, shown in Figure 14 [1]. The CMS search
 586 saw no excess in a similarly motivated signal region, albeit with different
 587 kinematic cuts than ATLAS's, following up on a 7 TeV search that saw no
 588 excess [20, 21].

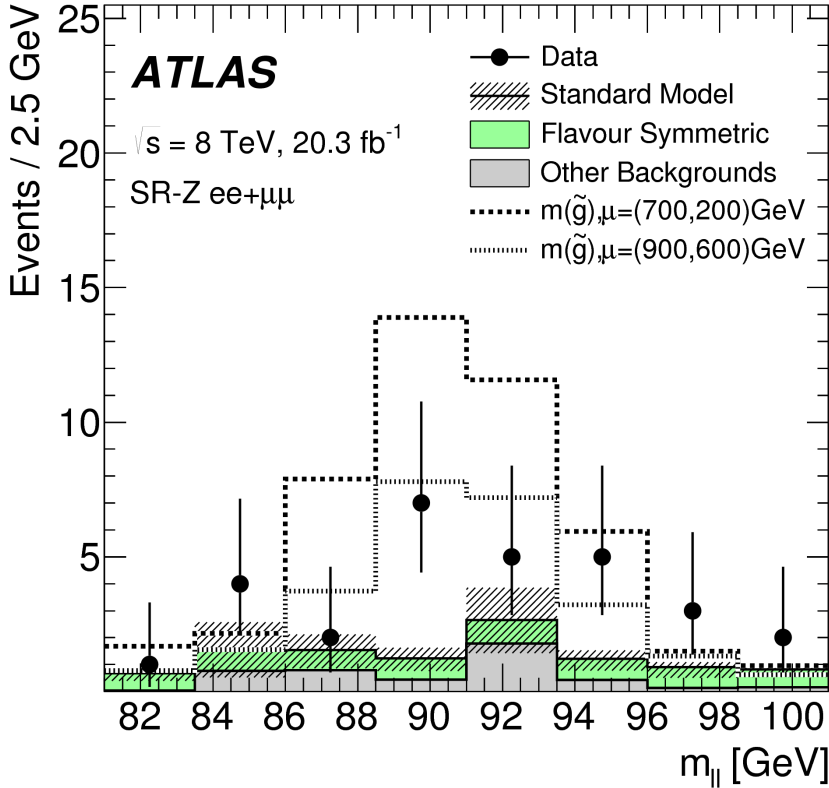


Figure 14: Results of an 8 TeV search performed by the ATLAS collaboration in a signal region targeting events like those in ???. The SM backgrounds are shown with their full uncertainties based on data-driven background estimations, and two signals are superimposed on the distribution. The observed datapoints are higher than the expected background, with a total excess of 3.0σ . The events in the signal region are displayed as a function of m_{ll} , the invariant mass of the event's leading leptons [1].

589 Both searches also identified events with two leptons that weren't con-
 590 sistent with an on-shell Z decay, and in this region, an excess with a local
 591 significance of 2.4σ was observed by CMS, shown in Figure 15. No excess
 592 was observed by the ATLAS collaboration in a signal region with identical
 593 kinematic cuts [1].

594 These two excesses generated significant interest in the two lepton chan-
 595 nel, and both CMS and ATLAS produced preliminary results in December
 596 2015 with the first 3.2 fb^{-1} of 13 TeV data. ATLAS again reported an excess
 597 on the Z mass peak [2], shown in Figure 16, while CMS saw no excesses
 598 [22].

599 Aside from the history of excesses, the channel is well-motivated from
 600 a theoretical perspective. The pair production of gluinos is the most com-
 601 mon production mode for most SUSY models which describe gluinos with

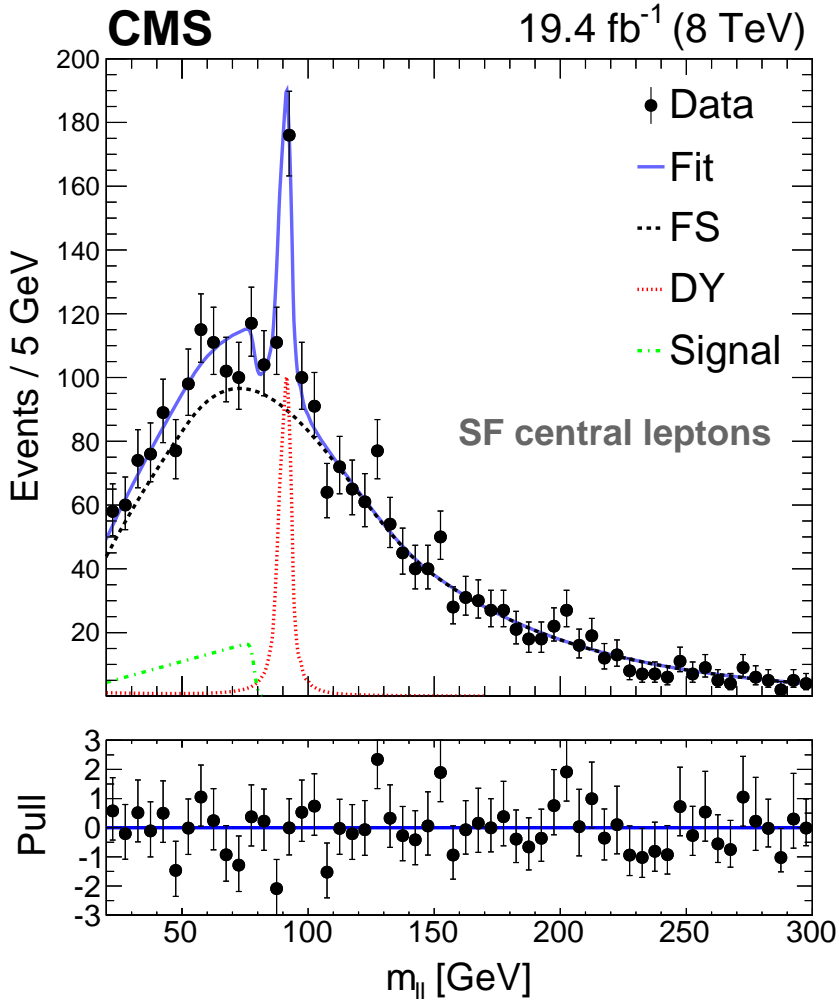


Figure 15: Results of an 8 TeV search performed by the CMS collaboration in a signal region including a broad range of $m_{\ell\ell}$. A 2.4σ local excess is seen in the low $m_{\ell\ell}$ region, and no excess of events is seen in the region with $m_{\ell\ell}$ consistent with an on-shell Z boson. The data is fit based on a data driven estimate of the flavor symmetric background (FS) and the Drell-Yan background (DY), with an additional component for the signal [21].

much smaller masses than squarks. Figure 17 shows the production cross-sections for sparticles at the LHC as a function of their mass. The specific decay considered in these simplified models does not have the largest branching ratio of all possible decays; even considering only changes to the SM decays involved, a $Z \rightarrow q\bar{q}$ decay is roughly seven times more likely than $Z \rightarrow \ell\bar{\ell}$. However, processes with higher branching ratios, like those producing an all-jet final state, often have much higher SM backgrounds, making them difficult to identify, even if they occur more frequently. This final state balances SM backgrounds and branching ratios, and when compared to other searches performed by the ATLAS collaboration, has competitive sensitivity to SUSY.

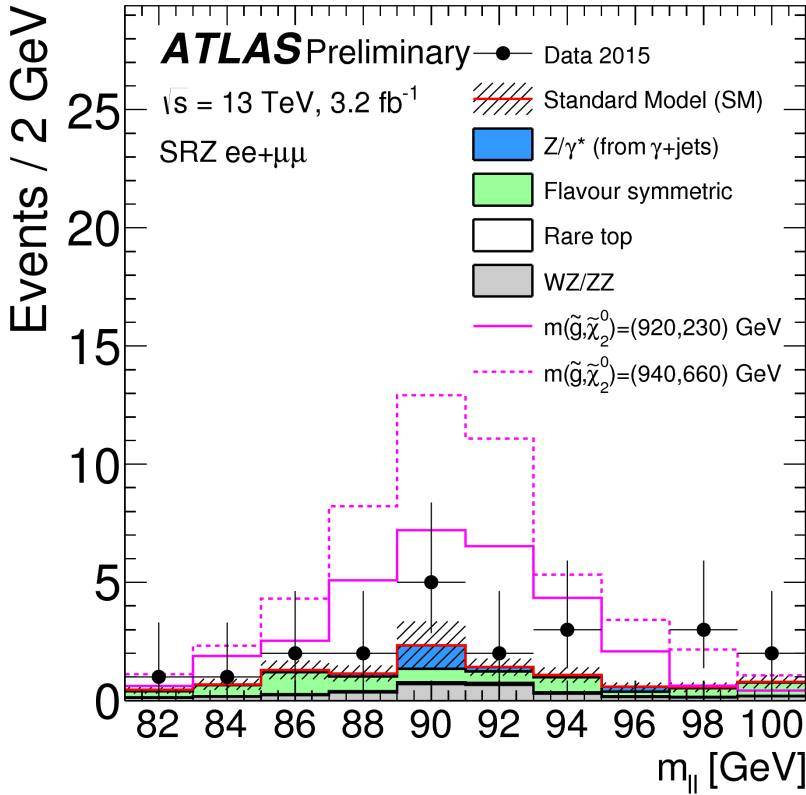


Figure 16: Preliminary results from a 13 TeV search targeting the same signal region as Figure 14, performed on 3.2 fb^{-1} of 2015 data. Flavor symmetric and $Z/\gamma^* + \text{jets}$ backgrounds are taken from data-driven methods, while the other backgrounds are taken from MC. They are compared to the data, which shows a 2.2σ excess of events. Distributions from two signal points are superimposed [2].

613 2.3 MONTE CARLO GENERATION

614 The complex events of the LHC are difficult to model, but modeling them
 615 is crucial to analyzers' understanding of SM backgrounds and potential
 616 signals. To simplify the modeling process, particle interactions are broken
 617 down into very small steps, each with associated probabilities of various
 618 outcomes. This modeling method is called Monte Carlo simulation (MC),
 619 and, at the LHC it is broken into several larger steps which are each han-
 620 dled by different software.

621 The first step, discussed in Section 2.1.3, is to determine the energies
 622 of the initial particles in a collision, which are provided by several differ-
 623 ent PDF sets. These distributions come from experimental measurements,
 624 though there is some variation between different sets. Three different sets
 625 are used in this analysis: NNPDF2.3LO [24] and NLO CT10 [25] for back-
 626 ground and signal processes, and MSTW 2008 [14] for pile-up events, dis-
 627 cussed more in Section 3.4.

628 With the initial states of the constituents of the protons described by
 629 these probabilistic models, the next step is to model the hard scattering

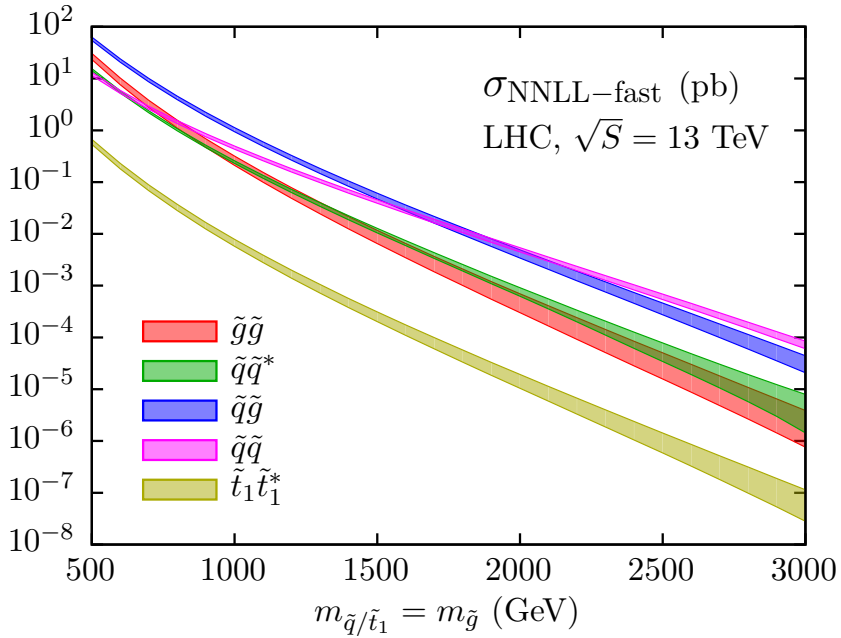


Figure 17: 13 TeV production cross-sections for sparticles, as a function of sparticle mass [23].

process resulting from the interaction of two of these particles. This is accomplished by a generator, which calculates the cross-sections of the Feynman diagrams of a given process. In particular, these generators typically produce *matrix elements*, which describe the probability to go from an initial to final state via a hard scattering, including the kinematics of the output. The generator uses these matrix elements to assign one of these hard scattering final states to each event. These hard scattering outputs are then passed to the next step, where parton showering, fragmentation, final and initial state radiation, and hadronization can occur.

The calculation of these diagrams can become very complicated when more and more loops are allowed. The simplest calculations, which include diagrams without any loops, are referred to as Leading Order (LO), while calculations including diagrams with one loop are called Next to Leading Order (NLO), and additional Ns can be added to describe more complex calculations. In addition, the total cross-section for a given process can be calculated at a higher order and used to scale the overall number of events generated for the process.

These calculations can also be tuned, varying parameters in the generation to create outputs that most closely match experimental data. In some cases, this can mean that a tune might include values for certain physical quantities that are different from their measured values because this configuration ultimately produces a result more similar to data.

Examples of generators include `MADGRAPH5_AMC@NLO` [26], `POWHEG Box` [27–29], and `SHERPA` [30]. Each has different strengths and is used to describe processes that best match those strengths. `POWHEG Box`, for example, cannot perform its own parton showering, and must be inter-

faced with another generator, typically PYTHIA [31], in order to describe any physics processes beyond the hard scattering, which can cause discontinuities in its predictions for large numbers of partons. However, it can calculate matrix elements at NLO, giving it an advantage in calculating some complex processes. SHERPAPERFORMS its own parton showering, but in most cases calculates its matrix elements at LO. The main advantage MADGRAPH5_AMC@NLO, which must also be interfaced with another generator perform parton showering, is its simple user interface. This makes it popular for producing SUSY signal samples, which must be done by each analysis team searching for a different SUSY process.

Once the final state particles of the hard interaction and showering have been calculated, the pile-up of the LHC (described in Section 3.4) must be accounted for. Events called *minimum bias* are generated to match the overall production of the LHC collisions, with no preselection. These events are overlaid on the original hard scatter to produce a more realistic representation of the many simultaneous interactions observed in the ATLAS detector.

This collection of particles must then be translated into signals in the detector. Their trajectories in the magnetic fields of the detector, their interactions in each layer, and the way these interactions deposit charge in each subdetector are modeled in software called GEANT4 [32]. In this software, every piece of the ATLAS detector is modeled, including the magnetic field and the many different materials. Particles then follow trajectories through the simulated detector and interact with the different materials based on several preprogrammed options for each material. For example a photon traveling through a material could continue along its trajectory, convert into a positron-electron pair, or deposit energy. As it crosses into a new material, a new set of options opens up for interactions. The particle is tracked until all of its energy is lost or it exits the geometry of the simulation.

The model of the detector used for this process is iteratively perfected by comparing data to MC. Figure 18 shows an example of a discrepancy between the simulation and observed data in the number of secondary vertices in a pixel module, which should correspond to the amount of material in the area. Observations of discrepancies like this can be used to correct the materials in the simulation.

Custom ATLAS code converts the energy deposited in active sensors into signals that resemble the expected detector response. These responses are typically very complicated with many parameters, and are frequently iterated on to best match the data. Electronic noise must also be added to correctly approximate the operating conditions of the detector. Additional alterations to this signal translation, including dead sensors and misalignments of the detector, can also be added at this stage.

Once the simulated particles have been converted into detector signals, the same reconstruction software used on data can be used on the MC, converting the detector signals back into particle interpretations. This reconstruction process is described in Chapter 5. The original information

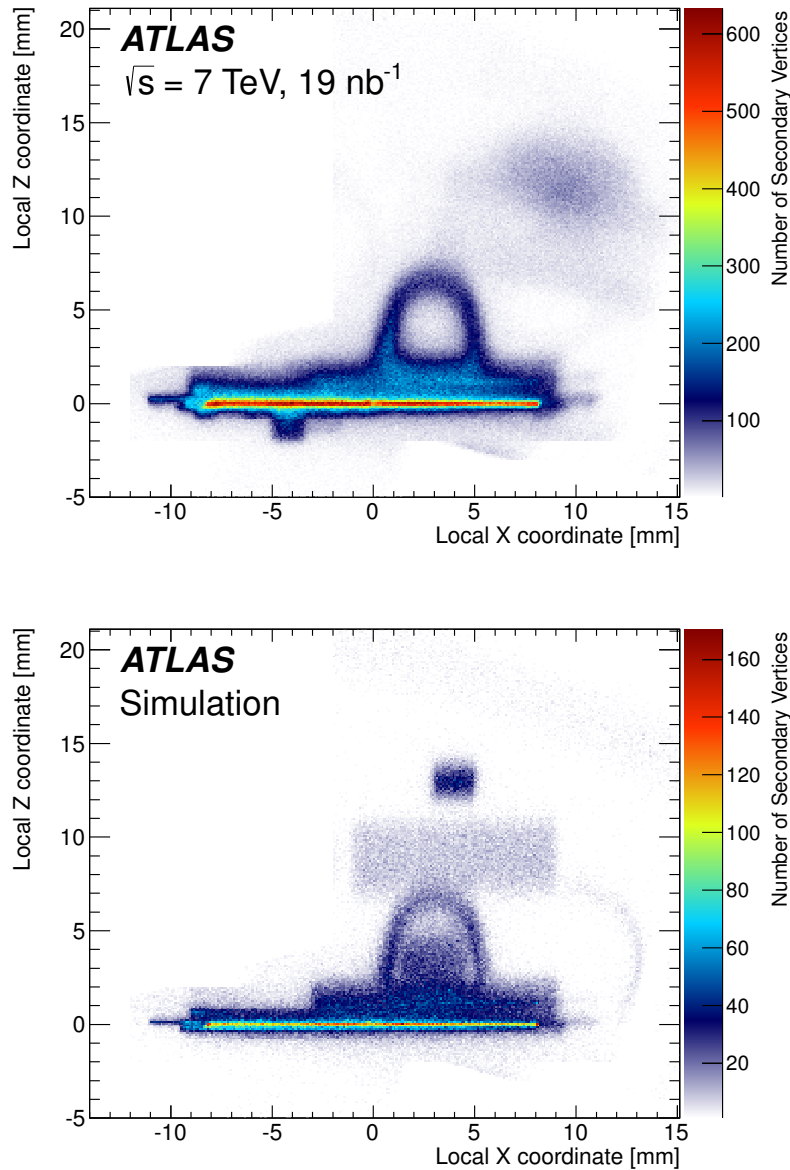


Figure 18: Number of secondary vertices in a module in the first layer of the pixel detector in data (top) and MC (bottom). There are more events in the data than the MC [33].

about the particles from the generator, referred to as *truth* information, is also kept, and can be compared to the reconstruction output to study its efficacy.

706

Part III

707

THE EXPERIMENT

708

This section describes the LHC and the ATLAS detector, which
709 collectively provide the physical environment and the data col-
710 lection for the analysis discussed in Part iv. Reconstruction of
711 events in the ATLAS detector is also explained, with an empha-
712 sis on the reconstruction of tracks in the innermost part of the
713 detector.

3

714 715 THE LARGE HADRON COLLIDER

716 The LHC is unique in the world, producing proton-proton collisions at en-
717 ergies an order of magnitude higher than any accelerator before [34]. It
718 provides unique environments at its collision points where massive, unsta-
719 ble particles can exist for an instant, then decay to the ordinary material of
720 the universe. It is the goal of the ATLAS experiment to identify these short-
721 lived particles, but the LHC's work of producing them is equally complex.

722 The LHC sits in a 26.7 km circular tunnel that straddles the French-Swiss
723 border outside of Geneva, originally built in 1989 for the Large Electron-
724 Positron (LEP) collider [35]. In the LHC, two beams of protons are accel-
725 erated to 6.5 TeV, then focused and collided at four points around the
726 ring, which can be seen in Figure 19. These points are each encased by
727 particle detectors, which can examine the outputs of the collisions, and
728 have different strengths and goals. The two multipurpose detectors are AT-
729 LAS and CMS, which have very complex detectors aimed and measuring
730 as many SM particles as possible and discovering new processes [36, 37].
731 Large Hadron Collider beauty (LHCb) examines processes related to the b
732 quark [38]. Meanwhile, A Large Ion Collider Experiment (ALICE) focuses
733 on special runs of the LHC which collide lead ions instead of protons, and
734 seeks to understand the high energy densities resulting from the collisions
735 of such massive, complex particles [39].

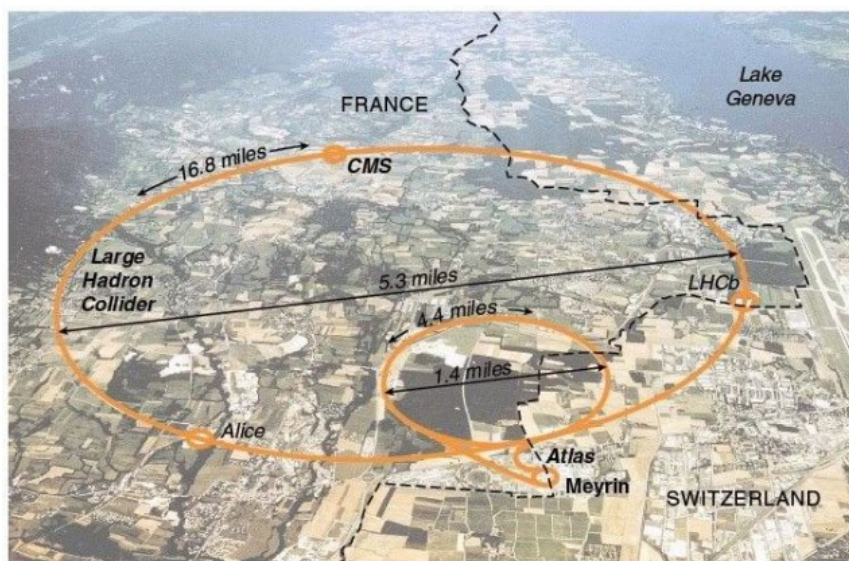


Figure 19: The LHC main collider ring and pre-accelerator SPS overlaid on a map of Switzerland and France, with the four main LHC experiments identified.

736 3.1 THE INJECTOR COMPLEX

737 The goal of the LHC is to provide high luminosity proton-proton collisions
 738 at 13 TeV. To achieve this, it must be capable of rapidly accelerating large
 739 numbers of protons and holding them at a constant energy, and organizing
 740 them into bunches which can be focused and collided at precise points
 741 and times. To do this, a complex system of pre-accelerators is required, as
 742 well as a precisely engineered system of magnets within the LHC. The full
 743 system of pre-accelerators is shown in Figure 20.

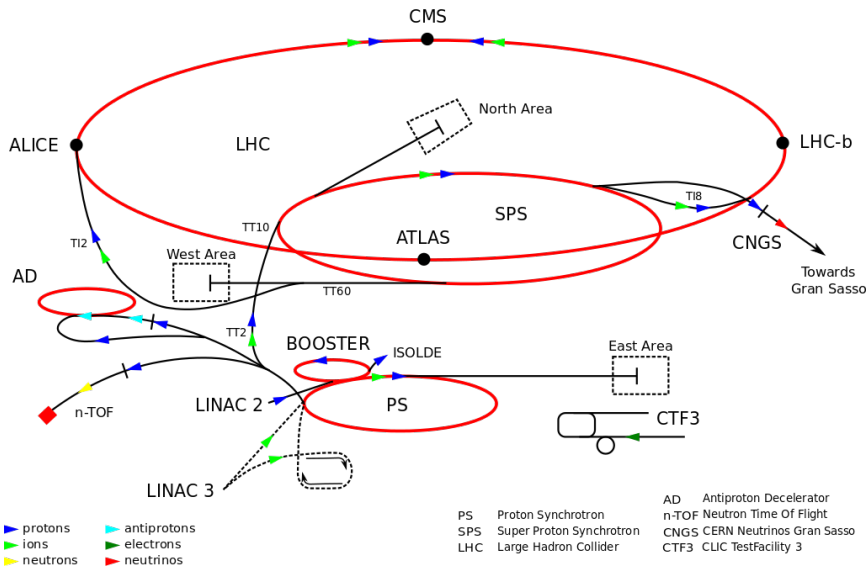


Figure 20: The pre-accelerators of the LHC.

744 The chain begins with when hydrogen gas is stripped of its electrons
 745 and injected in short pulses into Linac2, a linear accelerator which uses
 746 Radiofrequency (RF) cavities, which use alternating positive and negative
 747 electric fields to simultaneously push and pull particles forward through
 748 the accelerator. This RF behavoir keeps the bunches of protons resulting
 749 from the original pulses separated, beginning the formation of the bunch
 750 structure used for collisions. Quadropole magnets along the accelerator
 751 keep the beam focused. By the end of the accelerator, protons have reached
 752 50 MeV.

753 The proton beam is then injected into the Proton Synchrotron Booster
 754 (PSB), the first circular accelerator in the pre-accelerator chain. It increases
 755 its magnetic field as the protons increase in speed, ultimately accelerating
 756 them to 1.4 GeV.

757 At this point the proton beam moves on to the PS, a 600 m long circular
 758 accelerator that consists of 277 electromagnets that accelerate the protons
 759 up to 25 GeV, and 100 additional dipole magnets to bend the beam.

760 The last accelerator before injection into the LHC is the SPS, a 7 km long
 761 ring which, long before the LHC tunnel was built, was responsible for the
 762 discovery of the W and Z bosons. The SPS accelerates particles up to 450
 763 GeV before they are launched into the LHC.

Proton bunches are structured for ease of acceleration, with distinct features resulting from each of the pre-accelerators. The PS produces 72 bunches separated by 25 ns, which are injected into the SPS, as seen in Figure 21. However, as the magnetic field directing these protons out of the PS loop is turned on, there must be a gap in the bunch structure. Without this gap, called the injection kicker rise time, the changing magnetic field would direct particles out of the accelerator and produce high amounts of unsafe radiation around the PS. A similar gap in bunch structure is required for the injection from the SPS to the LHC. The injection process is repeated until the LHC is completely filled with around 2000 bunches, which takes about three minutes.

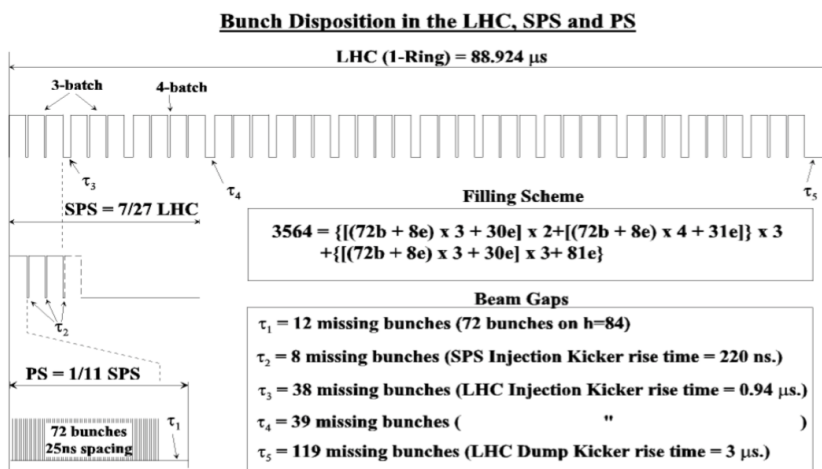


Figure 21: Bunch structure in the PS, SPS, and LHC.

3.2 OPERATION OF THE LARGE HADRON COLLIDER

The LHC consists of eight straight sections each connected by an arc. In each straight section, RF cavities accelerate protons, ultimately bringing them up to 6.5 GeV. Between these straight sections, 8.4 T dipole magnets bend the beams to maintain the approximately circular path. However, because the LHC is a proton-proton collider as opposed to a proton-antiproton collider, the two counter-rotating beams must be housed in separate rings and be accelerated separately. To achieve this, twin-bore superconducting magnets, one example of which can be seen in Figure 22, surround the two rings and accelerate them both. Quadropole magnets are used at the four collision points to focus the beams, which cross at an interaction point at the center of a detector. In total there are 1232 main dipole magnets over 5000 additional magnets, which are all superconducting and kept below their critical temperatures by liquid helium cooling.

When first injected into the LHC, the protons must be accelerated over many turns through the machine, with the magnetic field from the dipoles increasing with each pass to apply more force with which to bend the beam. Once the protons have reached a maximum energy, a process called

LHC DIPOLE : STANDARD CROSS-SECTION

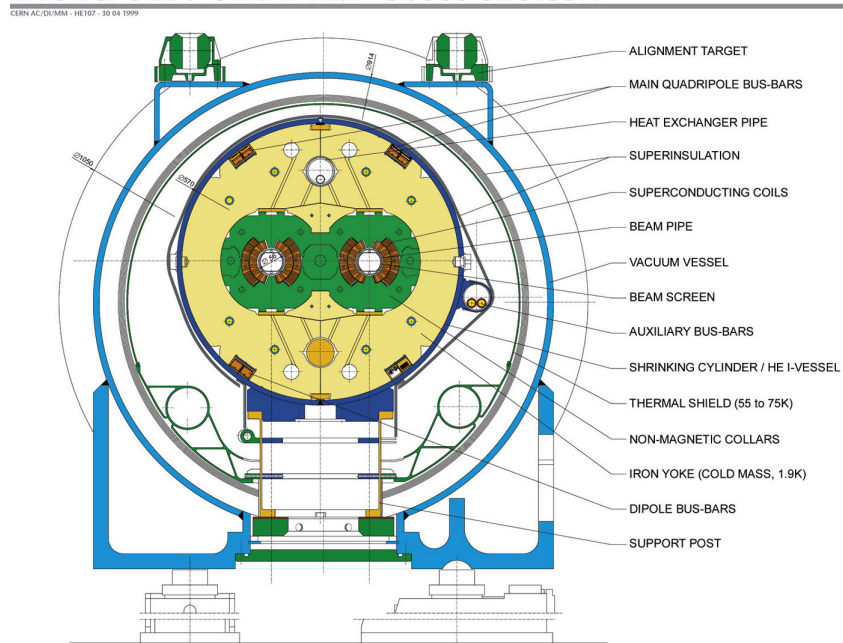


Figure 22: Cross-section of a cryodipole magnet in the LHC.

“squeezing” occurs, in which the total transverse area of the beam is reduced and bunches are elongated slightly. The shape produced by this process determines the “beam spot” for the ATLAS detector, the measurement of the area in which collisions occur within the detector. As shown in Figure 23, the collisions all occur very close together in the $x - y$ plane, but have a long spread in the z direction¹.

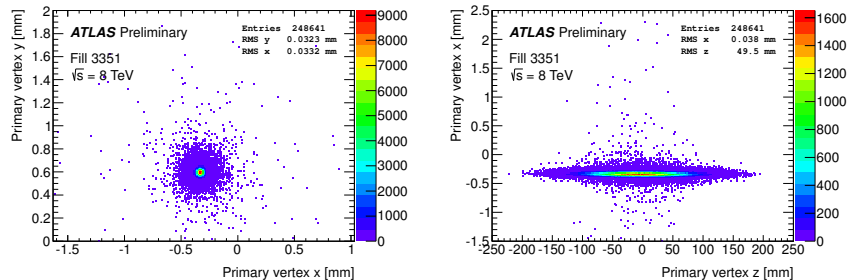


Figure 23: Beam spot in the ATLAS detector for one run in 2015. Distributions show only the highest p_T vertex per event. Left is the $x - y$ distribution of vertices, while the right plot shows the $x - z$ distribution.

Once the beams are at a stable energy and have been squeezed, the LHC indicates that it is physics-ready to the experiments around the ring, and, after some additional checks by each experiment, data-taking can begin. As collisions occur, the beam is depleted, and when it is sufficiently depleted to require a new fill, or if any instability occurs, the beam is dumped into a cavern filled with steel and concrete, which absorbs the energy.

¹ The coordinate system used here is discussed in Section 4.1.

806 3.3 LUMINOSITY

807 The goal of the collisions provided by the LHC is to produce SM and BSM
 808 particles, which can be observed by the detectors. How frequently a given
 809 process could occur was a crucial consideration in its design. The number
 810 of events of a given type is given by

$$N_{event} = L\sigma_{event} \quad (20)$$

811 where L is the luminosity delivered by the LHC and σ_{event} is the cross-
 812 section of the process in question. These cross-sections vary over many or-
 813 ders of magnitude for different processes, as shown in Figure 24, a plot of
 814 many different SM cross-sections. As a consequence, a very large amount
 815 of luminosity is required to produce the more rare events, and to have
 816 enough statistical power to differentiate them from other much more com-
 817 mon events.

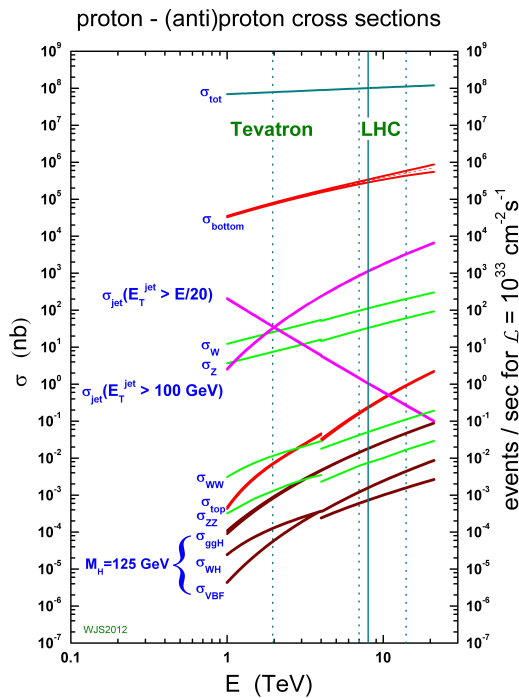


Figure 24: Cross-sections for many SM processes at the Tevatron and LHC [40].

818 The instantaneous luminosity at the LHC is given by

$$L = \frac{N_b^2 n_b f_{rev} \gamma_r}{4\pi \epsilon_n \beta_*} F \quad (21)$$

819 where N_b is the number of protons per bunch ($\sim 10^{11}$), n_b is the number
 820 of bunches in each beam ($\sim 10^3$), f_{rev} is the number of times per second
 821 that the beam travels around the ring, γ_r is the relativistic gamma factor,

ϵ_n is the normalized transverse beam emittance, and β^* is the β -function at the collision point, which describes the transverse displacement of particles in the beam. F gives the reduction factor due to the geometry of the beam crossings, and is given by

$$F = \left(1 + \left(\frac{\theta_c \sigma_z}{2\sigma^*}\right)^2\right)^{-1/2} \quad (22)$$

where θ_c is the crossing angle of the beams, σ_z is the RMS of the bunch length in the z direction, and σ^* is the same in the transverse direction.

As the proton beams circulate and collide, N_b decreases, producing a falling instantaneous luminosity, as seen in a Run 1 example in Figure 25. In Run 2, peak instantaneous luminosity was brought up to $10^{34} \text{ cm}^{-2}\text{s}^{-1}$. This high instantaneous luminosity and consistent running resulted in much faster data collection than in Run 1, which is depicted in Figure 26.

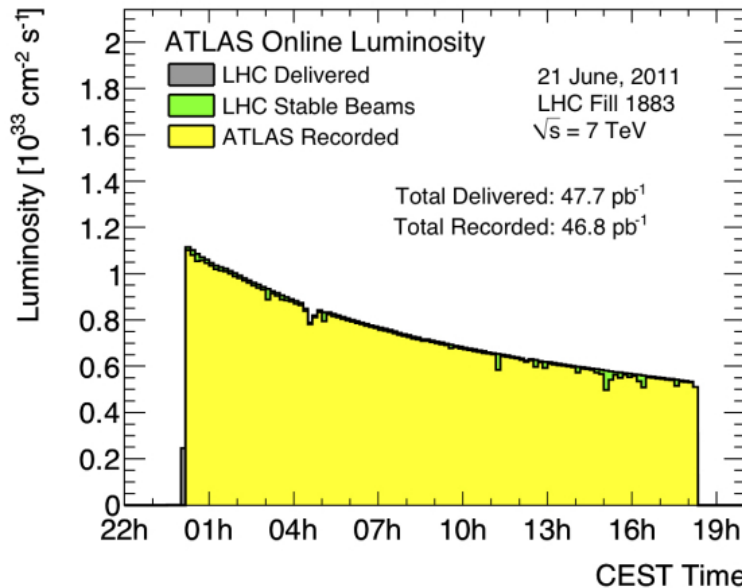


Figure 25: Instantaneous luminosity of one fill of 7 TeV data in 2011.

3.4 PILE-UP IN PROTON-PROTON COLLISIONS

One consequence of the high instantaneous luminosity is “pile-up”, or multiple simultaneously interactions. Because each bunch has on order 100 billion protons, it is very likely that multiple protons will collide in the same bunch crossing. In fact, the average number of simultaneous interactions in 13 TeV data, shown in Figure 27, is about twenty.

Pile-up can be a difficult challenge for the ATLAS collaboration because it typically results in additional jets in an event, and can increase SM backgrounds for analyses seeking to identify events with jets. It can also add to the overall hadronic energy of an event, and that energy can be misassigned to other objects. Fortunately, it is typically possible to resolve the

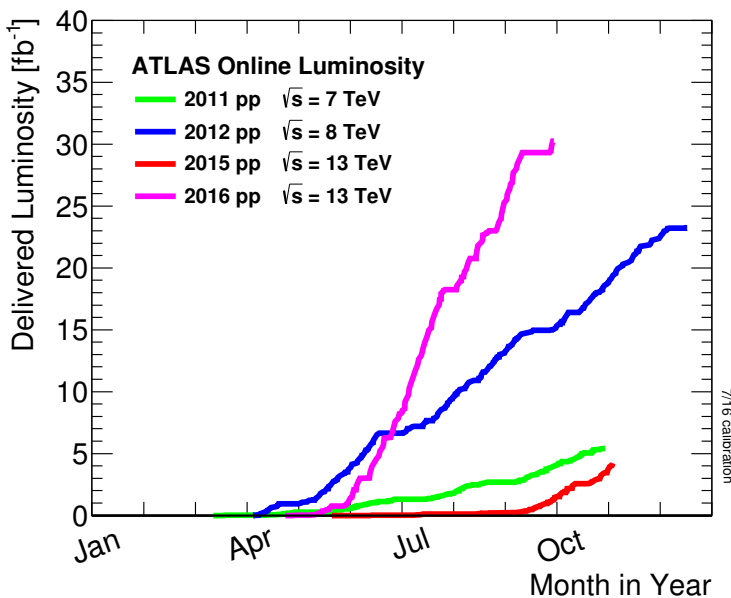


Figure 26: ATLAS luminosity for Run 1 and Run 2, as of September 2016.

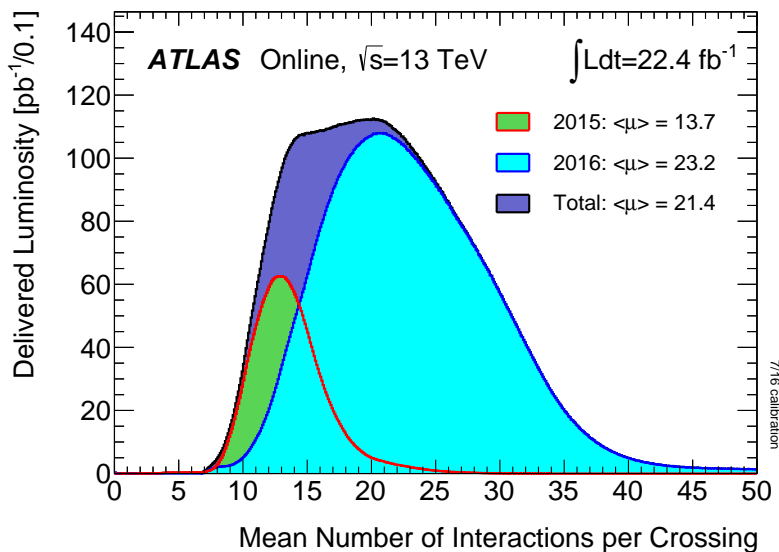


Figure 27: Average number of interactions per crossing shown for 2015 and 2016 separately, as well as the sum of the two years.

844 different vertices that each proton-proton collision makes, and so pile-up
 845 jets can be identified and rejected.

846

847 THE ATLAS DETECTOR

848 The ATLAS detector circumscribes the LHC’s beam pipe, enclosing the col-
 849 lision point with a series of particle detecting layers, aimed at making as
 850 many measurements of the particles leaving the collision point as possible.
 851 Its goal is to get a precise measurement of all the stable or semi-stable par-
 852 ticles flying from proton-proton collisions at its center, allowing analyzers
 853 to fully reconstruct the kinematics of the underlying processes.

854 The ATLAS detector is the largest detector of its kind, measuring 44
 855 m in length and 25 m in height, as seen in Figure 28. The size is mainly
 856 determined by the constraints of the MS, discussed in Section 4.4, which is
 857 the largest and outermost subsystem. The MS is submerged in a spatially
 858 varying magnetic field provided by three toroidal magnets, while the ID
 859 (Section 4.2) is encased by a superconducting solenoid, which provides a
 860 uniform 2 T field throughout its volume [36].

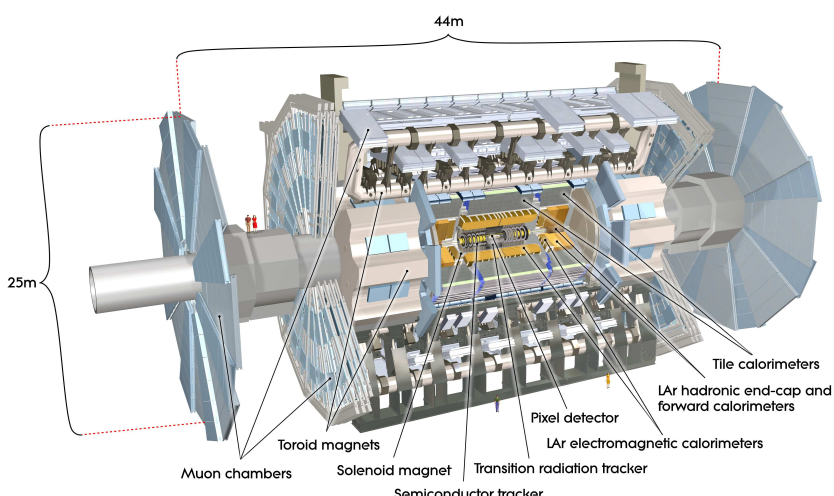


Figure 28: Diagram of the ATLAS detector, with subsystems and magnets identified.

861 4.1 COORDINATE SYSTEM USED IN THE ATLAS DETECTOR

862 The ATLAS detector is centered around the $p - p$ collision point, and is
 863 built radially out from the beam pipe, maintaining as much rotational
 864 symmetry around the beam pipe as possible. It is also symmetric in the
 865 forward-backward directions. A coordinate system using the collision point
 866 as the origin is used, with the beam line defining the z -axis. The positive
 867 x direction is defined as pointing to the center of the LHC ring, while the
 868 positive y direction points upwards. For ease of reference, the side of the

869 detector in the positive- z direction is referred to as the A side, and the
870 other side is referred to as the C side.

871 Because of the cylindrical design of the detector, angular coordinates are
872 often used. The azimuthal angle ϕ defines the angle around the beam pipe
873 and the polar angle θ defines the angle from the beam axis (z). However, a
874 transformation of the polar angle called pseudorapidity (η) is used more
875 often, and is defined as

$$\eta = -\ln[\tan \frac{\theta}{2}]. \quad (23)$$

876 η is used because the particle distribution from LHC collisions is roughly
877 uniform in this variable. Building on this definition, angular distance be-
878 tween objects is typically defined as

$$\Delta R = \sqrt{\Delta\eta^2 + \Delta\phi^2}. \quad (24)$$

879 Often variables are defined purely in the transverse plane, which is in-
880 dicated by a subscripted T , as in p_T , which gives an object's transverse
881 momentum.

882 4.2 THE INNER DETECTOR

883 The Inner Detector (**ID**) is responsible for the production of tracks, esti-
884 mates of the paths charged particles take as they travel through the detec-
885 tor. Collisions in the detector can produce about 1000 particles, so identi-
886 fying and differentiating all the tracks resulting from a collision is both a
887 hardware and a computational challenge.

888 The **ID** consists of three separate subdetectors, each of which has mul-
889 tiple layers capable of producing an electrical signal, called a *hit*, when a
890 charged particle travels through its active material. ATLAS tracking soft-
891 ware considers all these hits and forms tracks, with the goal of minimizing
892 fake tracks due to random noise and maximizing the efficiency of identi-
893 fying a real particle. Some details of this procedure are discussed in [Chapter 6](#). The full **ID** can be seen in [Figure 29](#), while a schematic in [Figure 30](#)
894 shows more detail on the placement of each layer.
895

896 4.2.1 *The Pixel Detector*

897 The pixel detector lies closest to the beam pipe of the LHC, and has four lay-
898 ers comprising 92 million pixels. There are three standard layers, referred
899 to as Layers 0-2 (L0, L1, L2), and an additional layer added for the 2015
900 data-taking, called the Insertable B-Layer (**IBL**).

901 4.2.1.1 *The Original Pixel Detector*

902 The Pixel Detector consists of high-precision silicon chip pixel modules,
903 with 1744 in total, and each module is made up of 16 sensors each with

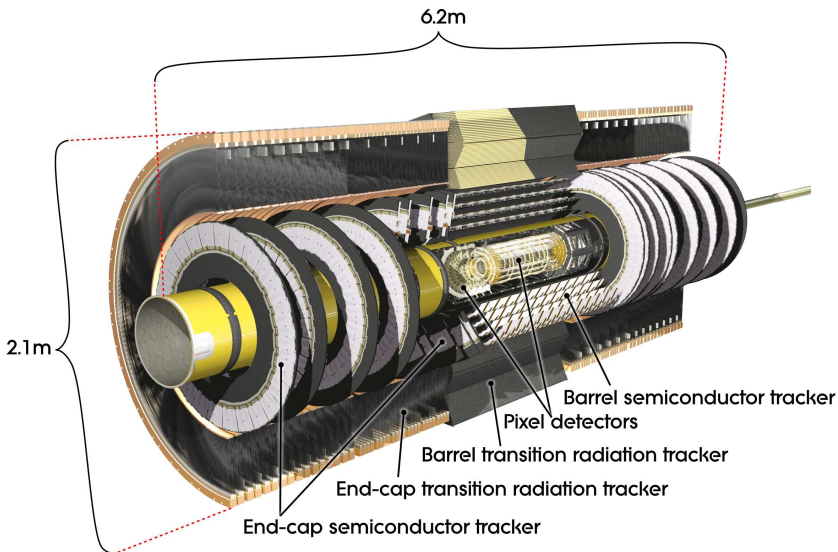


Figure 29: Diagram of the ATLAS Inner Detector, containing the Pixel, SCT, and TRT subsystems.

904 its own read-out system. Each sensor is identical, containing 47232 pixels,
 905 which are typically each $50 \times 400 \mu\text{m}^2$, though pixels at the edges of the
 906 sensors are slightly longer, at $50 \times 600 \mu\text{m}^2$.

907 As shown in Figure 30, the central η region (barrel) is covered by three
 908 concentric cylindrical layers of sensors, while the higher η region (end-cap)
 909 is covered by a series of three disks positioned in the $x - y$ plane. Together,
 910 they give complete coverage out to $|\eta| = 2.5$, and a particle coming from
 911 the collision point will typically produce hits in three layers.

912 The sensors are n-type silicon wafers with a voltage applied, and a pass-
 913 ing charged particle produces thousands of electron-hole pairs inside the
 914 material, which drift in the electric field towards the mounted read-out
 915 system. A hit occurs when the resulting current becomes large enough to
 916 pass a threshold designed to suppress noise. A larger total charge deposit
 917 will result in the signal remaining over the threshold for a longer period
 918 of time. The initial timing of the hit, and the Time Over Threshold (ToT)
 919 are both recorded. This measurement is spatially accurate in the barrel
 920 (endcap) to $10 \mu\text{m}$ in the $R - \phi$ direction and $115 \mu\text{m}$ in the $z (R)$ direction.

921 4.2.1.2 Addition of the IBL

922 In 2014, the IBL was added to the pixel detector. This layer sits on top
 923 of the beam pipe, inside barrel Lo, providing a measurement of particles
 924 only about 3 cm away from the interaction point. Its addition provides
 925 greater precision for all track measurements, but it is especially useful for
 926 the detection of B mesons, whose non-trivial lifetimes lead to secondary
 927 vertices in ATLAS events. The location of the IBL gives a measurement
 928 closer to these secondary vertices, and its increased pixel density increases
 929 the probability that these vertices can be resolved.

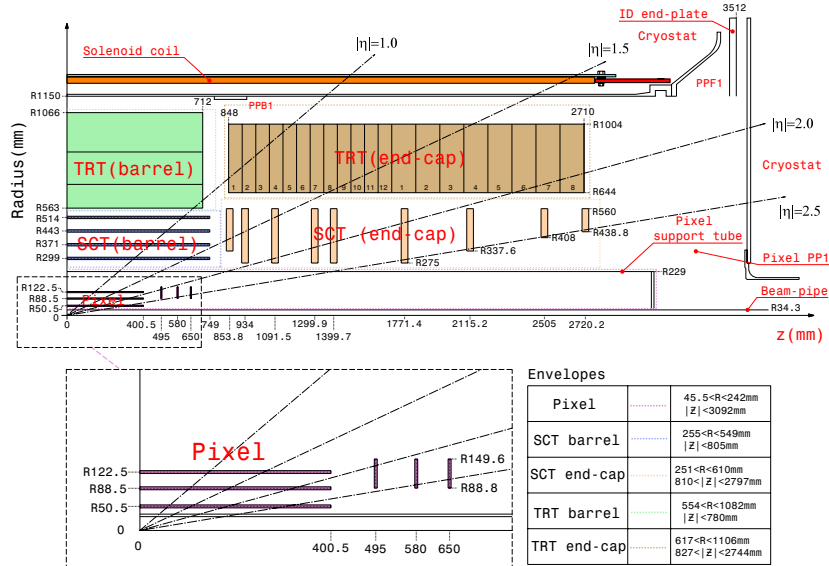


Figure 30: Diagram of one-quarter of the ATLAS Inner Detector in the $R - z$ plane, with lines drawn to indicate various η locations.

930 4.2.2 The Silicon Microstrip Tracker

931 The Silicon Microstrip Tracker (**SCT**) employs a similar technology to the
 932 Pixel Detector, with 15912 sensors and 6.3 million readout channels. Its
 933 difference from the Pixel Detector is in the readout, which is performed
 934 by a series of 12 cm long strips with a width of $80\text{ }\mu\text{m}$. These layers are
 935 paired, placed on top of one another at a small (40 mrad) angle to allow for
 936 position determination in both directions, giving 4 spatial measurements
 937 for each particle passing through the **SCT**. In the barrel, these strips run
 938 parallel to the beam pipe, while in the endcap, they are arranged radially.
 939 These strips have a resolution in the barrel (endcap) of $17\text{ }\mu\text{m}$ in the $R - \phi$
 940 direction and $580\text{ }\mu\text{m}$ in the z (R) direction.

941 4.2.3 The Transition Radiation Tracker

942 The Transition Radiation Tracker (**TRT**) uses 4 mm diameter gas-filled tubes,
 943 each with a high voltage wire suspended along the center of the tube. The
 944 tubes run the length of the barrel, with a separate wire in the positive and
 945 negative z direction. In the endcap, the tubes are arranged radially. In total,
 946 there are about 351,000 readout channels in the **TRT**. This detector makes
 947 measurements only in the $R - \phi$ direction, where the resolution of each
 948 measurement is $130\text{ }\mu\text{m}$, and coverage extends to $|\eta| = 2.0$. Each particle
 949 typically creates about 36 hits as it passes through the **TRT**.

950 Particles passing through the gas mixture of the **TRT** ionize the gas, pro-
 951 ducing electrons which drift towards the wire due to a potential difference
 952 applied between it and the tube. The **TRT** also responds to low-energy trans-
 953 sition radiation photons, which produce a much larger signal than charged

954 particles passing through the detector. Because of this strong difference in
 955 signals, hits from the [TRT](#) are used to help differentiate between electrons
 956 and photons in the detector.

957 4.3 THE CALORIMETERS

958 Unlike the tracking detectors, which aim to take measurements of a parti-
 959 cile with minimal alterations of its trajectory, the calorimeters measure the
 960 energy of objects by stopping them entirely. The calorimeters, which can be
 961 seen in [Figure 31](#), provide coverage out to $|\eta| < 4.9$. High granularity elec-
 962 tronagnetic measurements are made within $|\eta| < 2.5$ to complement the
 963 [ID](#)'s tracking capability. In this range, high p_T electrons and photons have
 964 nearly straight tracks, making momentum measurement through track cur-
 965 vature difficult, leaving the calorimeter as the primary energy measure-
 966 ment. The hadronic calorimeters, as well as the higher $|\eta|$ electromag-
 967 netic calorimeters, have a coarser granularity.

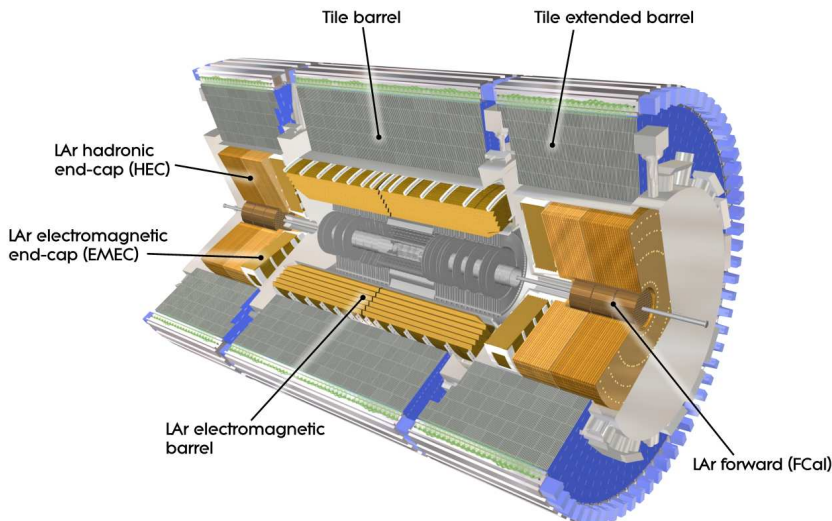


Figure 31: The calorimeter system of the ATLAS detector.

968 Besides measuring the energy of passing particles, another task of the
 969 calorimeter system is to limit punch-through to the [MS](#), described in [Sec-](#)
 970 [tion 4.4](#). All other particles must be fully stopped by the calorimeters to
 971 allow for clean signals from muons, and to measure the total energy of the
 972 particle. This requirement sets a minimum number of interaction lengths
 973 for each of the calorimeters.

974 **THE LAR ELECTROMAGNETIC CALORIMETER** uses liquid argon as its
 975 active detector medium alternating with layers of lead acting as the ab-
 976 sorber. The layers are shaped like accordions, which allows for complete
 977 coverage with multiple layers of active material, three in central η ($0 <$
 978 $|\eta| < 2.5$) and two at higher η ($2.5 < |\eta| < 3.2$). [Figure 32](#) shows the layout
 979 of a central η module, including this accordion-like layering. At $|\eta| < 1.8$,

980 an instrumented liquid argon presampler provides a measurement of en-
 981 ergy lost prior to reaching the calorimeters. The total energy resolution for
 982 this detector is about 10%.

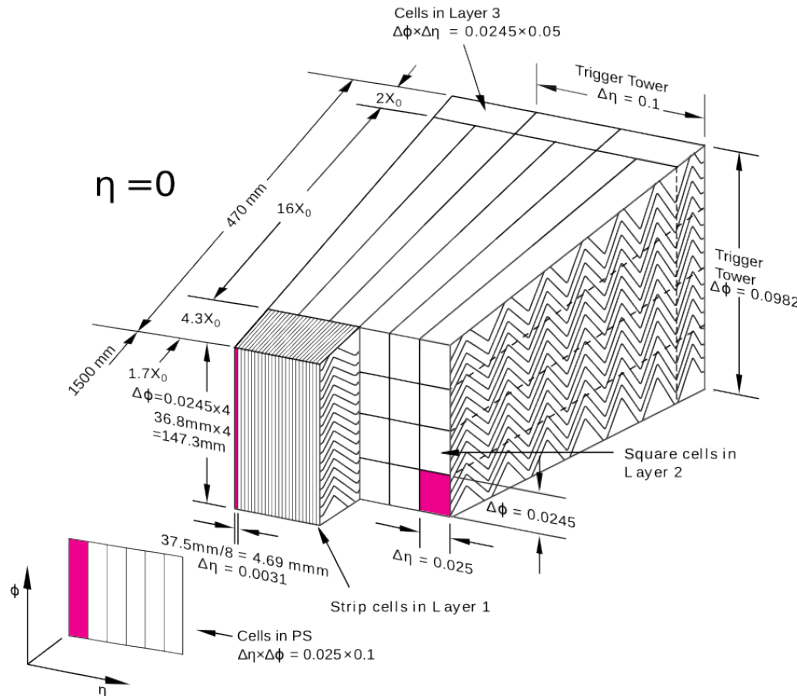


Figure 32: Layout of the LAr calorimeter module at central η [36].

983 **THE TILE CALORIMETER** is a hadronic calorimeter which surrounds
 984 the LAr Calorimeter. It uses layers of steel as its absorber with scintillating
 985 tiles as the active material between them, which are read out by photomul-
 986 tiplier tubes. The Tile Calorimeter covers $|\eta| < 1.7$ with a typical energy
 987 resolution of about 50%.

988 **THE LAR HADRONIC ENDCAP CALORIMETER** covers the hadronic calorime-
 989 try for higher η . It uses liquid argon active material and copper plate
 990 absorbers, resulting in an energy resolution of approximately 50%. This
 991 calorimeter covers $1.5 < |\eta| < 3.2$, overlapping with the hadronic calorime-
 992 ters in either direction of its η range.

993 **THE FCAL** or forward calorimeter provides electromagnetic and hadronic
 994 coverage at very high η ($3.1 < |\eta| < 4.9$). This calorimeter also uses liquid
 995 argon as its active material, and uses copper-tungsten as the absorber. Its
 996 energy resolution is about 100%.

997 4.4 THE MUON SPECTROMETER

998 The Muon Spectrometer ([MS](#)) measures charged particles that penetrate the
 999 calorimeter system. Because the calorimeters are designed to completely

absorb electrons, photons, and hadrons, the [MS](#) mainly detects muons, which pass through the calorimeter with very little loss of energy. The goal of the [MS](#) is to give a high-precision measurement of these muons, and also to be able to quickly identify events with muons for the sake of triggering, discussed in [Section 4.6](#). The layout of the [MS](#) can be seen in Figures 33 and 34. Muons can be measured for all $|\eta| < 2.7$, and they can be triggered on for $|\eta| < 2.4$. The entire system is about 24 m tall and 40 m long.

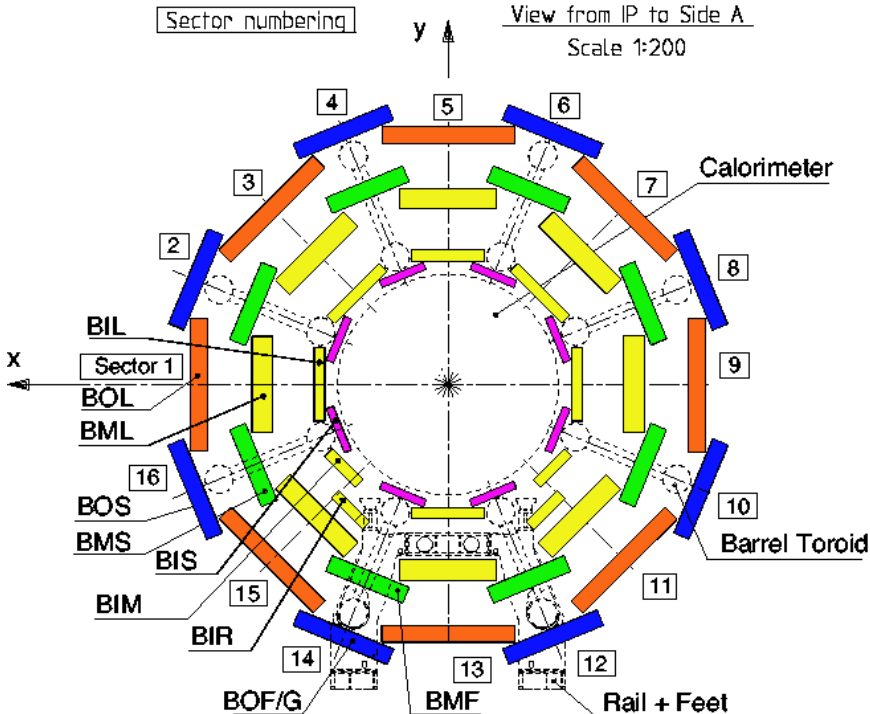


Figure 33: An x - y view of the [MS](#). In it, the three barrel layers are visible, as well as the overlapping, differently sized chambers. The outer layer of the [MS](#) is about 20m in diameter.

To achieve these goals, the [MS](#) has several subsystems. The system responsible for precision measurement is called the Monitored Drift Tubes ([MDTs](#)). This subdetector consists of chambers of three to eight layers of tubes, with three layers of chambers covering both the barrel and end-cap regions. In the barrel, these chambers are arranged in layers concentric cylinders with small overlaps between adjacent chambers. The chambers are oriented such that the drift tubes are parallel to the beam line. In the endcap, the chambers form disks with drift tubes approximately aligned in the R direction.

The tubes each contain an Ar/CO₂ gas mixture and a single high voltage wire which runs at its center along its length. Charged particles excite the gas as they pass through it, producing electrons which drift towards the high voltage wire. The resulting electric signal is read out, and the magnitude and timing of the signals are both used to differentiate particle traces from noise.

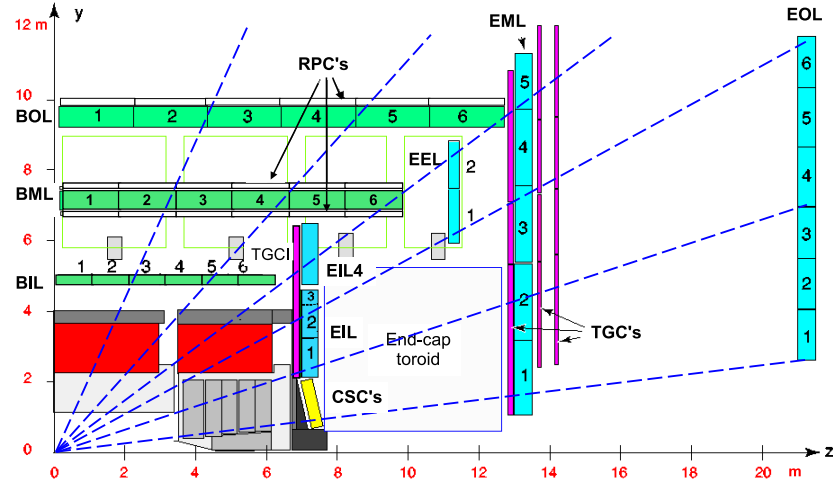


Figure 34: An r - z view of the MS. The three layers of the barrel and endcap MS are visible, and all muons at $|\eta| < 2.7$ should traverse three detectors, assuming they propagate in an approximately straight line from the interaction point.

Though very effective at giving a precise measurement, the MDTs have two shortcomings. The first is that the measurement is only precise in the direction perpendicular to the tubes; in the direction parallel to them, the resolution is not much better than the length of the drift tube, which are typically several meters long. The resolution in the perpendicular direction is about $35 \mu\text{m}$ with the combined measurement of all the tubes in a chamber. The second major shortcoming is that the MDTs are slow, with a maximum drift time of about 700 ns.

The slow drift time means that muons from sequential collisions can appear in the same event, and that the signals from the MDTs are received too late to be used for triggering. To solve the former problem, another detector called the Cathode-Strip Chambers (CSCs) is used in high-rate regions of the MS. This detector consists of multi-wire proportional chambers which have cathode strips on either side of the anode in orthogonal directions, providing a $40\ \mu\text{m}$ resolution in one direction and 5mm resolution in the other. Their drift times are much shorter than those of the MDTs, at about $40\ \text{ns}$. They are placed in the forward region of the detector ($2 < |\eta| < 2.7$) where the incident particle rates are highest.

To achieve responses fast enough to be used for triggering, Resistive Plate Chambers ([RPCs](#)) and Thin Gap Chambers ([TGCs](#)) are used. These chambers both take less than 25 ns to produce a signal. The [RPCs](#) are used in the barrel and are made up of two high-resistance plastic plates with a gas mixture under an electric field between them. Passing particles ionize this gas, and the resulting signal is read out via metallic strips mounted to the plastic plates. The [TGCs](#) used in the endcap are a form of multi-wire proportional chambers, like the [CSCs](#). Unlike the [CSCs](#), the cathode is placed extremely close to the wires, speeding up its operation.

1050 The massive **MS** is subject to deformations due to gravity and the mag-
 1051 netic field. To achieve a high precision alignment, these deformations are
 1052 constantly monitored in each **MDT** chamber with a set of four optical align-
 1053 ment rays, which give alignment information at the precision of $<30\ \mu\text{m}$.
 1054 In addition, a sag-adjustment system can use this information to re-align
 1055 any wires that droop under gravity's pull. Lastly, the **MS** can be aligned
 1056 using the tracks made from hits it measures, discussed more in [Section 5.3](#).

1057 **4.5 THE MAGNET SYSTEM**

1058 The ATLAS magnet system consists of four superconducting magnets: an
 1059 inner solenoid, a barrel toroid, and two endcap toroids. Collectively, they
 1060 are 22m in diameter and 26m long, and their basic layout can be seen in
 1061 [Figure 35](#).

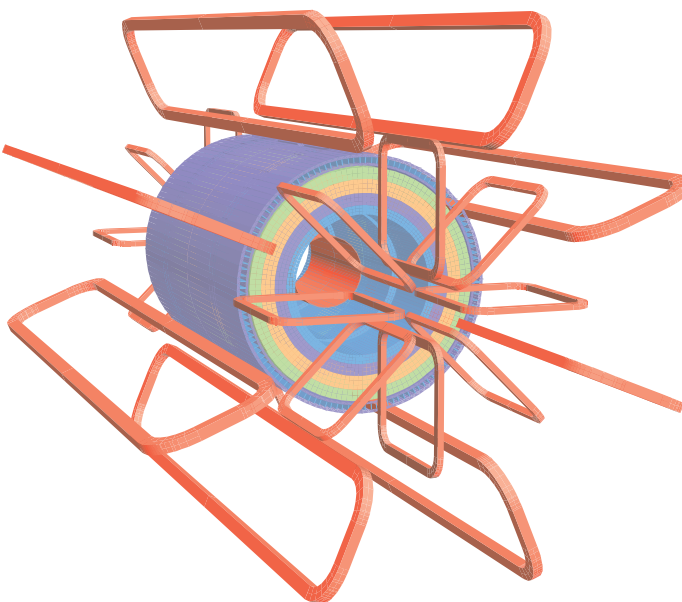


Figure 35: The magnet system of the ATLAS detector. The inner cylinder shows the solenoid which gives a uniform magnetic field in the **ID**. Outside of that are the barrel and endcap toroids, which provide a non-uniform magnetic field for the **MS**.

1062 The solenoid is inside the calorimeter volume and provides a uniform
 1063 2T magnetic field for particles traveling through the **ID**. This axial field
 1064 causes the trajectories of charged particles to bend in the $x - y$ plane, and
 1065 measurements of the curvature of these trajectories give the most accurate
 1066 p_{T} measurement for many particles according to the equation

$$p_{\text{T}} = qB\rho \quad (25)$$

1067 where q is the charge of the particle, B is the magnetic field in the z
 1068 direction, and ρ is the radius of curvature.

Because the solenoid is placed between the tracking system and the calorimeter, it is important that it interfere minimally with particles in order to allow the calorimeter to measure their full energies. The solenoid is placed inside the same vacuum chamber as the LAr calorimeter and is made of Al-stabilized NbTi superconductor with aluminum casing, giving it a total thickness of about 0.66 radiation lengths.

The barrel toroid is outside the calorimeters and provides the magnetic field for the barrel [MS](#), which varies from 0.2–2.5T. The endcap toroids have a magnetic field range of 0.2–3.5T. All three toroid magnets are made with Al-stabilized Nb/Ti/Cu superconducting coils supported by Al-alloy struts.

The magnets are cooled with liquid helium, and take up to a month to be brought down to operating temperatures. All magnets have cold masses surrounding them to absorb heat in the event of a quench.

The B -field resulting from this magnet system can be seen in [Figure 36](#). The plot on top demonstrates the relatively constant field rate within the barrel which drops steeply at $|z|=2$. The bottom plot shows the field integral in the [MDTs](#) as a function of $|\eta|$, demonstrating the good coverage out to $|\eta|<2.6$ excluding a transition region between the barrel and endcap, where the field changes rapidly, making precise p_T construction difficult.

4.6 THE TRIGGER SYSTEM AND DATA ACQUISITION

The [LHC](#) provides proton bunch crossings every 25 ns, and each of these events contains about one MB of data, corresponding to 40 TB/s, a completely unmanageable amount of data. In addition to this concern, many of ATLAS’s subdetectors like the pixel detector and [MDTs](#) take much longer than 25 ns to read out, making keeping up with the bunch crossing rate impossible. To reduce the total data read out and allow for selective reading out of the slower detectors, a triggering system is used.

The trigger system uses fast detectors to get a coarse picture of an event’s topology, which is then compared to a trigger menu, which lists the types of events that are interesting enough to keep. Overall, the trigger system reduces the 40 million events a second to about 1000 to be fully read out from the ATLAS detector.

This filtering of events is done in two steps: the [L₁](#) trigger is implemented in hardware and reduces the initial 40MHz to 100kHz, while the [HLT](#) is implemented in software, further reducing the rate to 1kHz [[41](#)]. The [L₁](#) trigger uses coarse granularity information from the fast read-out subdetectors: the calorimeters, the [RPCs](#) and [TGCs](#).

The coarse grained calorimeter information used for the [L₁](#) trigger decision is referred to as [L₁ Calorimeter Trigger \(\[L₁Calo\]\(#\)\)](#) and uses information from all calorimeter systems. [L₁Calo](#) is responsible for all triggers excluding muons, meaning it must be capable of identifying a large number of different objects and event topologies, including high- p_T objects, E_T^{miss} , and large amounts of hadronic energy. The trigger can also identify isolated

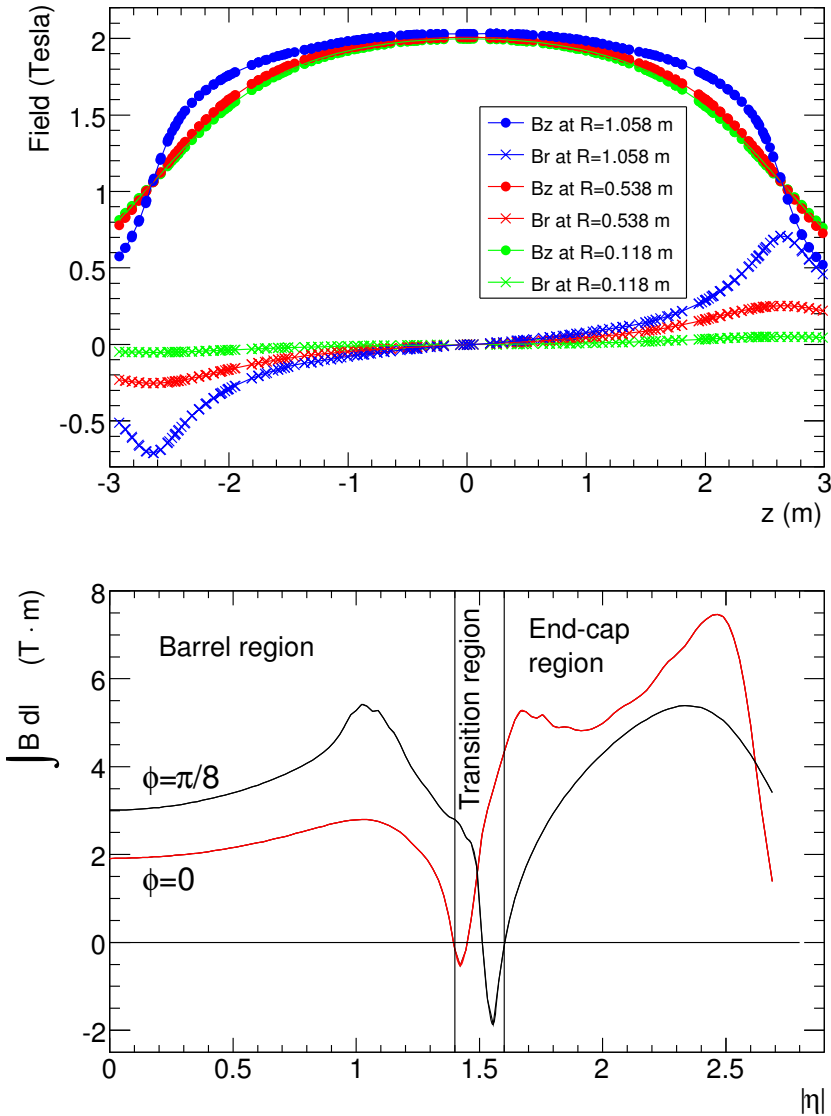


Figure 36: Plots of the magnetic field within the ATLAS detector. Top is the field (broken into its R and z components) as a function of z for several different values of R . Bottom is the field integral through the MDTs as a function of $|\eta|$ for two different ϕ values.

1113 objects, objects with very few calorimeter deposits from other objects near
 1114 them.

1115 For muon triggers, the trigger algorithm looks for patterns of hits from
 1116 the RPC and TGC that are consistent with high- p_T muons with origins at
 1117 the interaction point.

1118 An example of the L1 trigger rates for different types of events can be
 1119 seen in Figure 37 for one run in July 2016. The common features to all rates
 1120 are due to LHC luminosity changes, deadtimes due to detector inefficiency,
 1121 and adjustment of prescales to optimize trigger bandwidth.

1122 All of this information is analyzed by the Central Trigger Processor
 1123 (CTP), which uses a trigger menu identifying all types of events to be kept

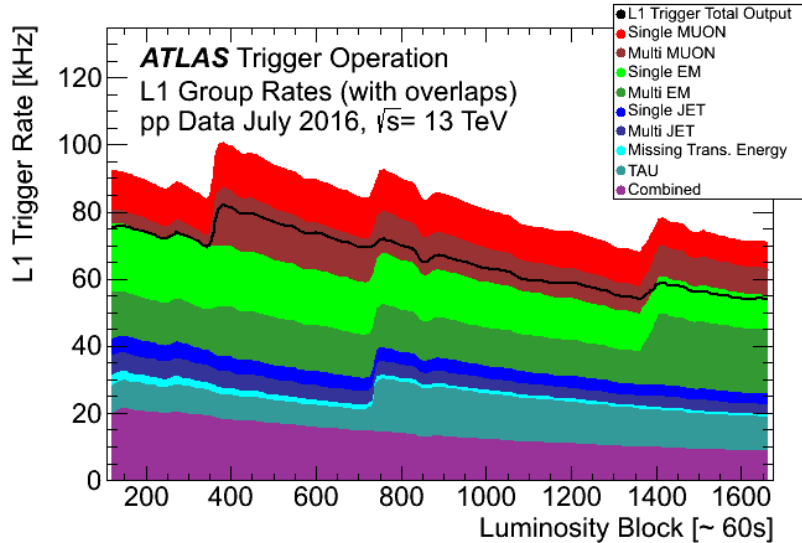


Figure 37: L_1 trigger rates for a run in July 2016 as a function of luminosity block, an approximately 60-second long period of data-taking. The total rate is lower than the combined stack because of overlapping triggers.

to return a trigger decision. The event must be processed in about 2.5 μs so that the remaining event information not yet read out is still available on the subdetectors when the trigger decision is made. This decision is passed to the Trigger Timing and Control (TTC), which communicates with all subdetectors. Upon receiving a L_1 trigger, the subdetectors read out all the information they've stored about the event and place it on their Read Out Boards (ROBs).

The HLT takes the data from particular Region of Interests (RoIs), areas containing interesting objects that caused the L_1 trigger, and analyzes this much more complete picture of the region to decide whether or not the event is still interesting enough to keep. This process has its own trigger menu with dedicated L_1 seeds for each item. HLT triggers typically have slightly higher thresholds than their corresponding L_1 triggers to ensure that events that would pass the HLT requirements are very likely to have passed the L_1 requirements. Figure 38 shows the HLT rates for the same run in July. In addition to the event types seen in Figure 37, the HLT can also identify events with b -jets, differentiate between electrons and photons, and identify events interesting for B-physics.

Events passing the HLT trigger are written to disk to be analyzed. An example of the total trigger efficiency for single electron triggers is shown in Figure 39. Trigger efficiencies can be taken directly from MC , and are measured in data via a method called tag-and-probe, the main principles of which are discussed in Section 10.3.

Events types that occur very frequently, such that it would require too much of the total trigger bandwidth to record all events passing a given threshold, are prescaled. Events passing these triggers are only recorded a

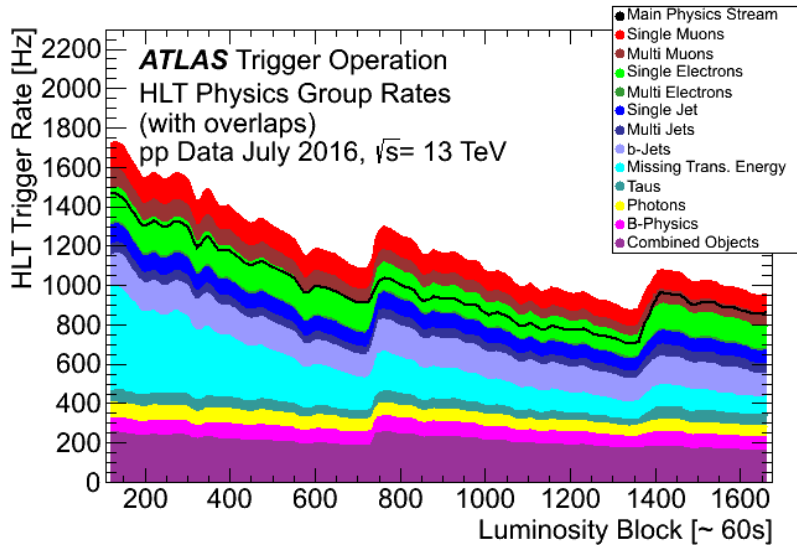


Figure 38: HLT trigger rates for a run in July 2016 as a function of luminosity block, an approximately 60-second long period of data-taking. The total rate is lower than the combined stack because of overlapping triggers.

fraction of the time, and these prescaling rates are used to adjust the final data to account for the limited rate. For example, the lowest unprescaled single electron trigger in 2016 data-taking required an electron with 60 GeV p_T . A trigger requiring electrons with only 10 GeV p_T also exists, but is prescaled by approximately a factor of ten.

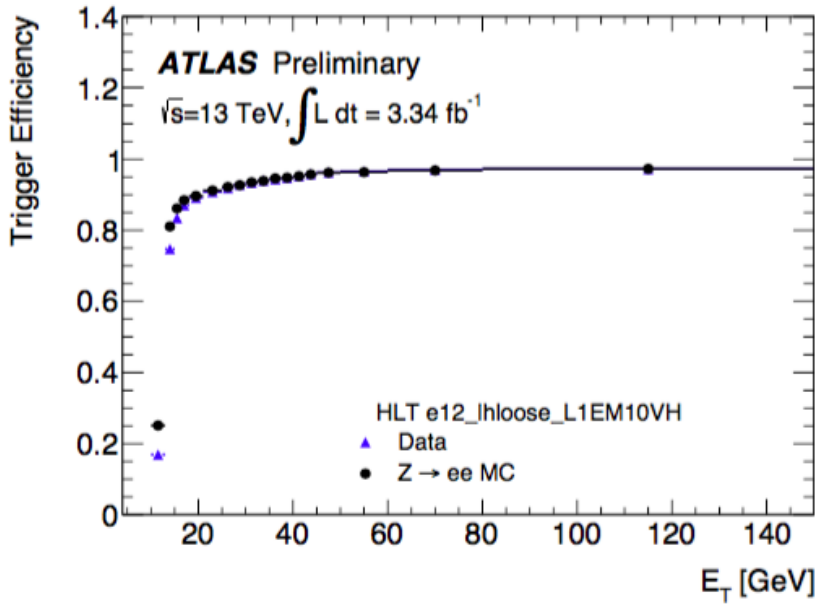


Figure 39: Trigger efficiencies as a function of E_T for data and MC. Efficiencies are given for offline selected loose electrons.

1155

1156 OBJECT RECONSTRUCTION IN THE ATLAS DETECTOR

1157 Object reconstruction is the computationally intensive process of interpreting
1158 the signals from the approximately 100 million read-out channels of
1159 the ATLAS detector into a collection of particles and jets, the objects with
1160 which physics analysis can be performed. This process is complicated, and
1161 requires dedicated working groups in the ATLAS experiment that optimise
1162 the understanding of each type of object. These groups must all col-
1163 laborate to provide a full picture of the events in the detector. For each
1164 object type, candidate objects are reconstructed, and then an identification
1165 step is performed, which chooses which candidates will be used at the
1166 analysis level, based on a series of quality requirements.

1167 5.1 ELECTRONS

1168 Electrons are reconstructed through a combination of [ID](#) and calorimeter
1169 measurements. They travel through the tracking system, leaving charge de-
1170 posits in each layer, then are absorbed by the electromagnetic calorimeter.
1171 These two measurements work in conjunction to deliver high resolution
1172 measurements of electron momentum from low- p_T , where track curvature
1173 gives the most reliable measure of the electron's energy, to high- p_T , where
1174 the tracks are almost perfectly straight, but the calorimeter can still pro-
1175 vide a reliable measurement.

1176 In the central region ($|\eta| < 2.47$) of the ATLAS detector, electron recon-
1177 struction begins with the identification of energy deposits in the electro-
1178 magnetic calorimeter. The calorimeter clusters are seeded by sliding longi-
1179 tudinal windows, which are measured in units of 0.025 in η and ϕ . 3×5
1180 unit windows are used, which require at least 2.5 GeV in the window to
1181 form a seed [42].

1182 These clusters are matched to [ID](#) tracks by extrapolating each track to the
1183 middle layer of the calorimeter and identifying nearby clusters. If there are
1184 multiple tracks associated with a given cluster, tracks with silicon hits are
1185 preferentially chosen, and then the track with the smallest ΔR to the center
1186 of the cluster is selected. If a matching track is found, it is used to deter-
1187 mine the likely direction of bremsstrahlung radiation in the calorimeter,
1188 and maximum distance to match a track to a cluster is expanded in the ϕ
1189 direction to account for this radiation. If no track is found, the cluster is
1190 rejected.

1191 The calorimeter clusters are then rebuilt in larger windows, 3×7 in the
1192 barrel and 5×5 in the end-caps. An estimate of the energy is made by sum-
1193 ming the measured calorimeter energy with estimates of the energy lost
1194 before the electron reached the calorimeter, energy outside of the cluster
1195 window, and energy not fully deposited in the calorimeter. These estimates

1196 are made with parametrized functions determined from a combination of
 1197 **MC** and measurements of energy loss determined with the presampler.

1198 The momentum of a central electron is determined through a combina-
 1199 tion of the calorimeter and track measurements of the electron, while its η
 1200 and ϕ are taken from the track at its vertex.

1201 In the forward region, where no tracking is available, electron energy is
 1202 determined more roughly. Calorimeter cells are formed into variable-sized
 1203 clusters in regions of significant energy deposition, and the center of the
 1204 cluster is used to determine angular coordinates of the electron. However,
 1205 because these electrons have worse resolution in both their position and
 1206 energy, they are often rejected by analyses that depend on well-measured
 1207 objects.

1208 These reconstructed electron candidates' quality are then assessed based
 1209 on an algorithm that uses multivariate analysis to assign a likelihood that
 1210 a candidate is a true electron based on input from just under twenty differ-
 1211 ent variables. These include track quality, hadronic leakage, cluster shape,
 1212 and transition radiation, incorporating information from as many subde-
 1213 tectors as possible in its determination of the candidate's quality. Each
 1214 variable is assigned a probability distribution function for true electrons
 1215 and background processes, and they are collectively used to provide a
 1216 *likelihood* value which can be cut on.

1217 Three levels of identification, **Loose**, **Medium**, and **Tight**, are defined with
 1218 different likelihood cuts, with electron candidates passing tighter identifi-
 1219 cation levels always a subset of looser electrons. [Figure 40](#) gives the effi-
 1220 ciencies at each of these working points both for true electrons and for
 1221 hadrons, which can be misidentified as electrons. Tighter working points
 1222 have worse efficiencies, but lower misidentification rates for hadrons as
 1223 well as photons.

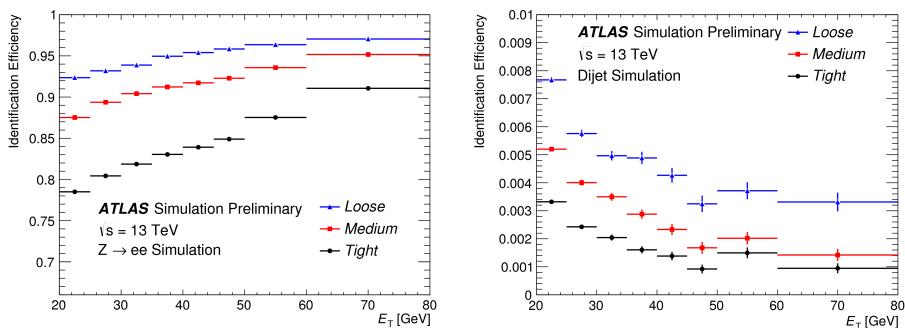


Figure 40: Identification efficiencies from **MC** samples for **Loose**, **Medium**, and **Tight** working points. Left is the efficiency for identification of true electrons taken from $Z \rightarrow ee$ **MC**, and right is the efficiency for misidentification of jets as electrons taken from dijet **MC** [43].

1224 **MC** efficiencies can be compared to efficiencies measured in data using
 1225 the tag-and-probe method, to obtain a *scale factor*, a correction factor ap-
 1226 plied to **MC** to better emulate the rates at which electrons are reconstructed
 1227 and identified in data. [Figure 41](#) shows a comparison of the combined re-

construction and identification efficiencies in data and MC, with the resulting scalefactors also displayed as the ratio.

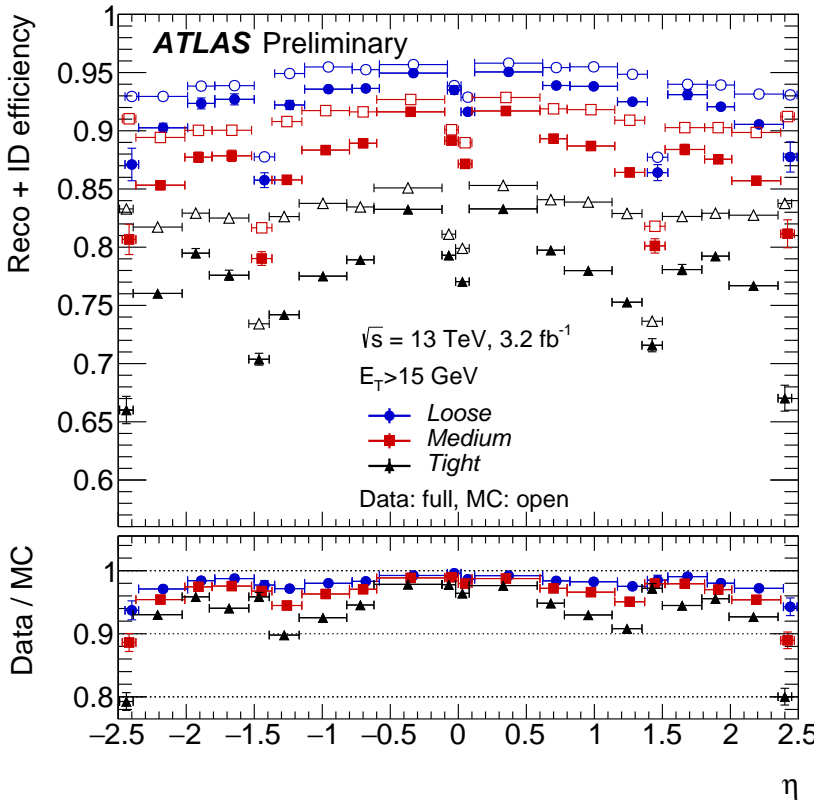


Figure 41: Combined electron reconstruction and identification efficiencies measured as a function of η for data (using the tag-and-probe method on $Z \rightarrow ee$ events) and $Z \rightarrow ee$ MC. Distributions include all electrons with $E_T > 15$ GeV. [43].

Electrons can also have *isolation* requirements, cuts on nearby calorimeter activity or tracks. Isolation variables are primarily used to reject non-prompt leptons, leptons which aren't produced by the initial hard scattering of the $p - p$ collision. These can be produced by heavy flavor hadron decays and converted photons, as well as misidentified hadrons. Cuts are made on the amount of nearby calorimetric energy and sum of the p_T of any nearby tracks relative to the electron's energy, forming a series of working points. Fixed cut working points, which specify the relative fraction to cut on, can be used, but efficiency targeted working points are more popular. These include Tight and Loose working points, which operate at 95 and 98% efficiency respectively, and working points that target higher efficiencies at higher electron p_T , Gradient and GradientLoose. These working points each have 99% efficiency for electrons with $p_T > 60$ GeV, but 90 and 95% efficiencies at 25 GeV.

1244 5.2 PHOTONS

1245 The reconstruction of photons is performed in parallel to electron recon-
 1246 struction. Seed clustering is performed, and tracks are matched to these
 1247 clusters, as in the case of the electron reconstruction described in [Sec-](#)
 1248 [tion 5.1](#).

1249 Photons can be converted to electron-positron pairs in the [ID](#), leaving
 1250 a pair of tracks, or they can pass through without conversion, leaving no
 1251 tracks behind. As a consequence, calorimeter clusters resulting from pho-
 1252 tons can have no tracks associated with them, two tracks, or one track, in
 1253 the case that one of the conversion tracks is not reconstructed. The recon-
 1254 struction software attempts to identify all these scenarios and differentiate
 1255 these clusters from electron and hadron deposits [44].

1256 Two-track clusters are required to consist of two oppositely charged
 1257 tracks that emerge from a conversion vertex running parallel to one an-
 1258 other. A likelihood that these tracks are from electrons is determined using
 1259 the high threshold hits in the [TRT](#), and quality requirements are made on
 1260 the tracks using this likelihood. For tracks with silicon hits, a loose like-
 1261 lihood requirement of 10% is made, while tracks without silicon hits are
 1262 required to have at least 80% likelihood. The tracks are then fit to deter-
 1263 mine the conversion vertex, and quality cuts are made, such as requiring
 1264 that conversion vertices within the silicon volume correspond to tracks
 1265 with silicon hits.

1266 Single track clusters occur most often from conversions in the outermost
 1267 layers of the [ID](#), and are more difficult to reconstruct. Tracks are typically
 1268 lost because an electron or positron resulting from the conversion has a p_T
 1269 too low to be reconstructed, or because the two tracks are so close together
 1270 that they're identified as a single track. The single track is required to have
 1271 at least a 95% electron likelihood from [TRT](#) hits, and must not have a hit in
 1272 the innermost layer of the pixel detector. The conversion vertex is defined
 1273 as the first hit of the single track.

1274 The tracks associated with these conversion vertices are extrapolated to
 1275 the calorimeter and matched to cluster, except in the case that there are two
 1276 tracks that differ substantially in their p_T measurements, in which case the
 1277 position of the conversion vertex is used for extrapolation to the calorime-
 1278 ter, assuming a straight-line trajectory. If multiple vertices are matched to
 1279 a single cluster, preference is given to vertices with double tracks, silicon
 1280 hits, and finally to tracks closest to the interaction point.

1281 Any cluster with neither a conversion vertex or a track associated with
 1282 it is identified as an unconverted photon. Clusters associated with both
 1283 electrons and photons are assigned to one or the other based on their
 1284 properties. Clusters are preferentially identified as photons in the case that
 1285 they are matched to a conversion vertex in which at least one track is
 1286 associated with both the vertex and the cluster, or if the associated tracks
 1287 have a p_T smaller than the cluster's p_T . E/p , the ratio of the cluster and
 1288 track energy measurements, can also be used to differentiate electrons and

1289 photons. Electron candidates are instead reconstructed as photons if they
 1290 have $E/p > 10$ or if the track matched to the electron has p_T below 2 GeV.

1291 Photon energy is determined in a 3×5 (3×7) window for unconverted
 1292 (converted) photons in the barrel, where the window is expanded to com-
 1293 pensate for the increased spread of energy from the conversion products.
 1294 In the endcap, the 5×5 window is used in all cases. Like the electrons,
 1295 the calibration of the photon's energy accounts for energy loss before the
 1296 calorimeter, as well as energy deposited outside the cell and beyond the
 1297 electromagnetic calorimeter.

1298 Photon identification is performed in the range $|\eta| < 2.37$ using a se-
 1299 ries of cuts on the shape of the shower in the electromagnetic calorime-
 1300 ter, as well as the amount of additional energy deposited in the hadronic
 1301 calorimeter. Photons in the the so called *crack* region of the calorime-
 1302 ter ($1.37 < |\eta| < 1.52$), where a discontinuity prevents accurate assess-
 1303 ment of photon energy, are rejected. The photon identification has only
 1304 one working point, called **Tight**, which has an identification efficiency
 1305 of 53–64% (47–61%) for unconverted (converted) photons with $E_T = 10$
 1306 GeV and 88–92% (96–98%) for photons with $E_T \geq 100$ GeV [45]. Effici-
 1307 cies as a function of p_T measured in the 2016 data and compared to **MC**
 1308 can be seen in Figure 42.

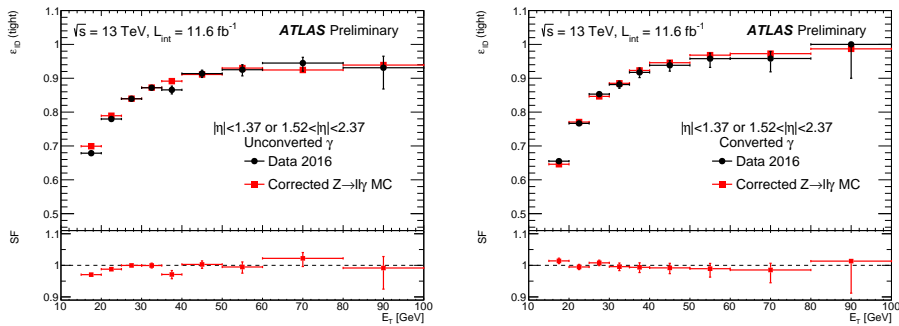


Figure 42: Comparison of Tight identification efficiency measurements from data and $Z \rightarrow \ell\ell\gamma$ MC for unconverted (left) and converted (right) photons, with an inclusive η selection. The bottom of each figure shows the ratio of data and MC efficiencies. [46].

1309 Photon isolation, like electron isolation, can be determined as the com-
 1310 bination of nearby calorimeter deposits and tracks. Fixed cuts on the iso-
 1311 lation as a fraction of photon energy is typically used. A working point
 1312 called **FixedCutTight** reconstructs the amount of calorimeter energy (ex-
 1313 cluding that of the photon) in a cone of $\Delta R = 0.4$ around the photon and
 1314 the amount of energy from the sum of track p_T in a cone of $\Delta R = 0.2$,
 1315 including only tracks associated with the primary vertex. Defined relative
 1316 to the photon's p_T , this working point includes photons with calorimetric
 1317 isolation less than $0.022 p_T + 2.45$ GeV and track isolation less than $0.05 p_T$
 1318 [47].

1319 5.3 MUONS

1320 Muon reconstruction is performed independently in the **ID** and the **MS**,
 1321 then the two measurements are combined when consistent tracks are found
 1322 in each system [48]. The **ID** reconstruction is performed using the tracking
 1323 mechanism over the $|\eta| < 2.5$ range. As with electrons, hits in the layers
 1324 of the **ID** are fit to tracks, a process described in more detail in [Chapter 6](#).

1325 The **MS** track reconstruction is performed in the $|\eta| < 2.7$ range and
 1326 begins with a search in each muon chamber for patterns of hits consistent
 1327 with a track, called *segments*. The **MDT** chamber hits are fit to a straight line,
 1328 and nearby **RPC** and **TGC** chambers provide the coordinate orthogonal to
 1329 the magnetic curvature for these hits. Segments are also built in the **CSC**,
 1330 where they are required to be loosely consistent with a track originating
 1331 from the interaction point.

1332 These segments are then fit together, starting from the middle layers
 1333 of the **MS**, with track quality requirements on the resulting combinations
 1334 based on the χ^2 of the fits. Tracks must have at least two segments, except
 1335 in the transition region between the barrel and endcap, where a single high
 1336 quality segment can qualify as a track. Segments are allowed to be shared
 1337 between multiple tracks in the initial reconstruction, but after the combi-
 1338 nation, tracks with shared segments and low quality fits are removed.

1339 These **MS** tracks are then combined with measurements from other parts
 1340 of the ATLAS detector. The best quality muons are combined muons,
 1341 which have **ID** and **MS** tracks associated to them, the hits of which are re-fit
 1342 to form a combined track. **MS** hits can be added or removed at this stage
 1343 based on their consistency with the new track. Other types of muons exist,
 1344 including extrapolated muons, which have only **MS** tracks that are con-
 1345 sistent with the interaction point, calorimeter-tagged muons, which com-
 1346 bine an **ID** track with a calorimeter deposit consistent with a muon, and
 1347 segment-tagged muons, which combine an **ID** track with a segment in the
 1348 **MS**. Muons with shared **ID** tracks are not allowed, with preference given
 1349 to combined muons, then calorimeter-tagged muons, and lastly segment-
 1350 tagged muons.

1351 There are four muon identification working points for muons: **Loose**,
 1352 **Medium**, **Tight**, and **High- p_T** . These working points all have different effi-
 1353 ciencies for the identification of muons, balanced against the mis-identification
 1354 of hadrons. One of the key variables for their discrimination is q/p signif-
 1355 icance, which quantifies the consistency between the **ID** and **MS** mea-
 1356 surements of momentum. The χ^2 of the combined fit is also an important
 1357 discriminator.

1358 The **Loose**, **Medium**, and **Tight** efficiencies are inclusive, with all **Tight**
 1359 muons passing the **Medium** requirements, and **Medium** muons passing the
 1360 **Loose** requirements. The **Loose** requirement includes all types of recon-
 1361 structed muons, but allows muons without **MS** tracks only in the $\eta < 0.1$
 1362 range where there is a gap in the **MS** coverage to accomodate cabling
 1363 for the calorimeter system. The **Medium** working point includes only com-
 1364 bined and extrapolated muons, and is the default for most ATLAS analy-

ses. Extrapolated muons are allowed only outside the **ID** tracking system ($|\eta| > 2.5$), a region often excluded by analyses because of the decreased efficiency and larger p_T resolution of these muons. For the combined muons, at least three hits in at least two **MDT** layers are required (except in the $\eta < 0.1$ region) and a q/p significance cut is made to reduce backgrounds. Even with the reduced requirements at low η , there is a drop in efficiency in this region, as shown in Figure 43. The Tight working point additionally cuts on χ^2 and makes further requirements on the consistency between **ID** and **MS** p_T measurements.

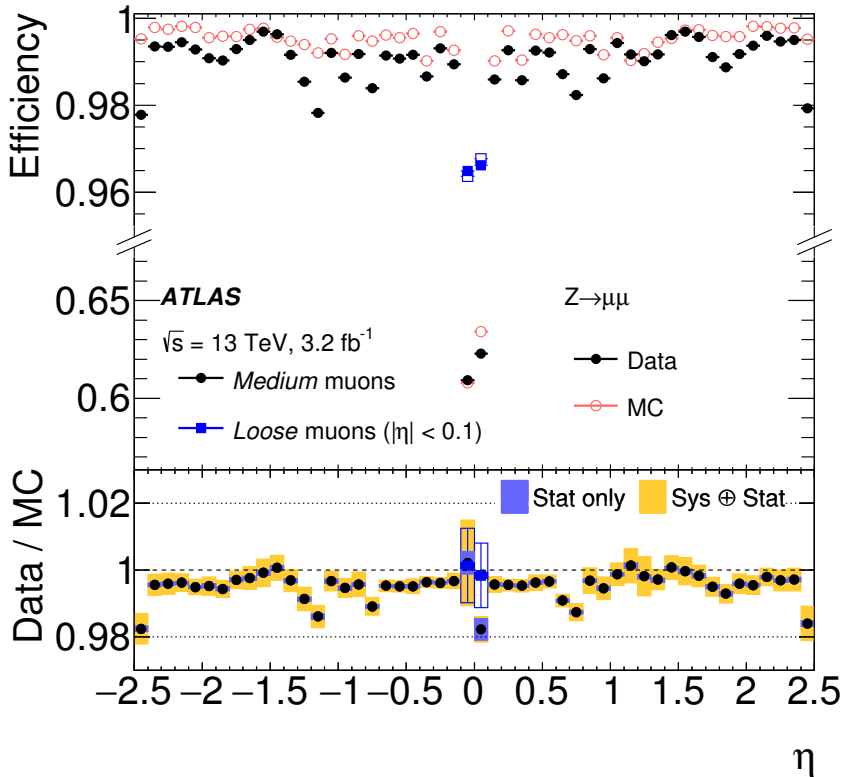


Figure 43: Muon reconstruction efficiency for the Medium and (for small $|\eta|$) Loose working points measured with $Z \rightarrow \mu\mu$ events in data using the tag-and-probe method and in MC as a function of η . The ratio between the two is shown at the bottom. [48]

The High- p_T working point is designed to minimize the resolution for high- p_T muons, at the cost of lower efficiencies. Muons passing the High- p_T requirements must have at least three **MDT** hits in three layers, which decreases efficiency but gives greatly improved p_T resolution. In addition, some regions of the **MS** with poor alignment are vetoed to cut down on mismeasurement. Compared to the default working point these muons have much lower efficiency: 78% (90%) for High- p_T muons compared to 96% (96%) for Medium in the p_T range of 4-20 GeV (20-100 GeV). The efficiency as a function of η for this working point can be seen in Figure 44, where the efficiency loss due to the of vetoing of some chambers is especially apparent. Mismodeling of the alignment and the specificity of the

momentum resolution cuts cause a large discrepancy between data and MC efficiencies, resulting in scale factors that differ from unity by as much as 10%.

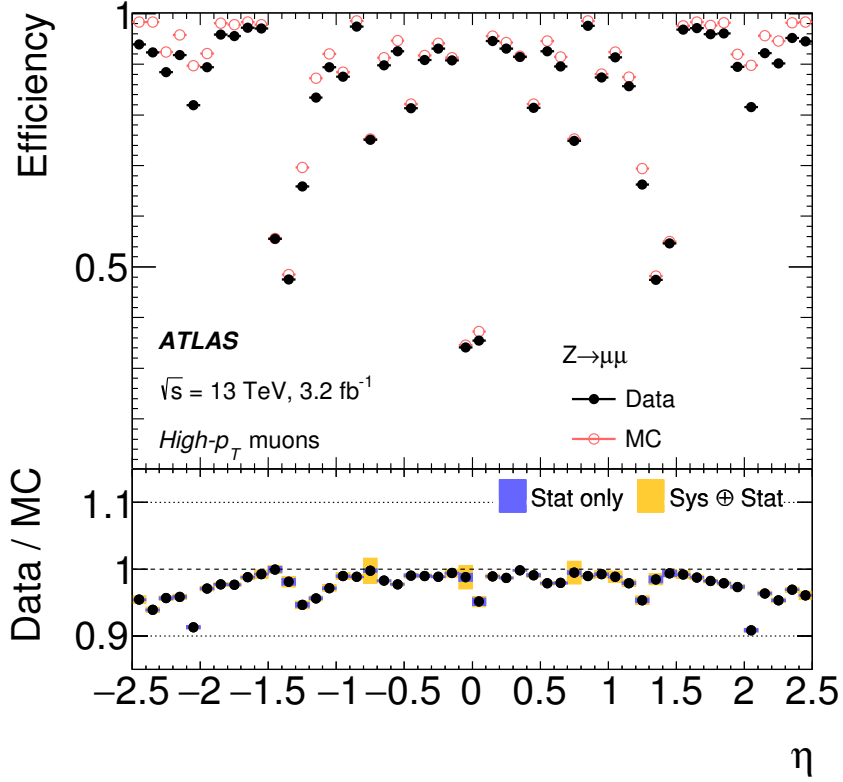


Figure 44: Muon reconstruction efficiency for the High- p_T working point measured with $Z \rightarrow \mu\mu$ events in data using the tag-and-probe method and in MC as a function of η . The ratio between the two is shown at the bottom. [48]

The most common isolation selection for muons is designed in the same way as the electron isolation, and also called GradientLoose. It is constructed such that muons with p_T of 25 GeV have an efficiency of 95%, and muons with p_T of 60 GeV have an efficiency of 99%.

5.4 JETS

Jets are the most complicated objects to reconstruct in the ATLAS detector because each jet is an assembly of many hadronic particles. In contrast to a lepton, whose reconstructed energy can easily be compared to its true energy from simulation, even a jet's true energy is ambiguous, and is dependent on the choice of the jet's definition. The standard jet reconstruction algorithm used in the ATLAS experiment is called anti- k_t [49].

This algorithm begins with clusters in the calorimeter defined by topologically connected cells with energy deposits significantly higher than the noise background. These clusters can be defined in multiple ways, but

1402 there are two collections used most commonly for analysis. One uses cluster
 1403 energies calibrated for electromagnetic showers ([EM](#)), and another uses clusters
 1404 calibrated to hadronic showers. The second uses a method called
 1405 Local Cluster Weighting ([LCW](#)), which first determines the extent to which
 1406 the cluster is electromagnetic or hadronic based on the energy density and
 1407 the shower depth, then applies a calibration accordingly for each cluster.

1408 To reconstruct jets, a set of clusters is chosen and the anti- k_t algorithm
 1409 is then applied, beginning with the highest energy cluster and grouping it
 1410 with nearby clusters according to the distance measure

$$d_{ij} = \min(k_{ti}^{-2}, k_{tj}^{-2}) \frac{\Delta_{ij}^2}{R^2} \quad (26)$$

1411 where R is the algorithm's radius parameter, typically set to 0.4, Δ gives
 1412 the angular separation of the two clusters, and k_t is the transverse mo-
 1413 mentum associated with the cluster. The jet is defined by clusters grouped
 1414 within the cone radius, then the axis of the jet is reassessed. This process
 1415 is iterated upon until a stable jet is produced. The inverse dependence on
 1416 the k_t of the cluster produces jets with energetic cores and softer edges,
 1417 which matches the expectation from a hadronic shower. In addition it is
 1418 infrared and collinear safe, with neither soft emission or collinear particles
 1419 altering the reconstruction of the jet.

1420 A series of calibrations are then applied to these jets. The first is to cor-
 1421 rect for additional hadronic energy due to pile-up. [Figure 45](#) demonstrates
 1422 the impact of pile-up on the energy density of an event, and this overall
 1423 change in energy density can affect the amount of stray energy associated
 1424 with reconstructed jets. To remove this dependence, a correction is taken
 1425 from [MC](#) and parametrized in terms p_T , η , and the number of primary ver-
 1426 tices in the event, as well as the average number of vertices, which makes
 1427 correction for out-of-time pile-up possible. Next, jets are corrected to have
 1428 their origin at the primary vertex instead of the center of the ATLAS de-
 1429 tector. After that, the jets are corrected based on η dependent Jet Energy
 1430 Scale ([JES](#)) factors derived from [MC](#). [Figure 46](#) shows the energy response,
 1431 the inverse of these factors, for [EM](#) jets. Lastly, an observed bias in the η
 1432 measurement of jets is accounted for.

1433 In addition to correcting for additional energy due to pile-up, it is neces-
 1434 sary to reject reconstructed jets that come from pile-up vertices. To accom-
 1435 plish this, a multivariate algorithm called [JVT](#) was created which builds
 1436 upon an older method, [JVF](#) [51]. The original method vetoed jets by sum-
 1437 ming the total p_T of associated tracks and assessing the fraction of that p_T
 1438 that came from tracks associated with the event's primary vertex. This frac-
 1439 tion decreases with higher pile-up, making the construction of an explicit
 1440 cut difficult in varying pile-up conditions. [JVT](#) improved on the method
 1441 by producing a pile-up corrected [JVF](#)-like variable and including it in the
 1442 inputs of the tagger with other variables measuring the fraction of jet en-
 1443 ergy that can be associated with the primary vertex. [Figure 47](#) shows the
 1444 efficiency and fake rate for the two methods, demonstrating [JVT](#)'s superior
 1445 stability across events with different numbers of pile-up vertices.

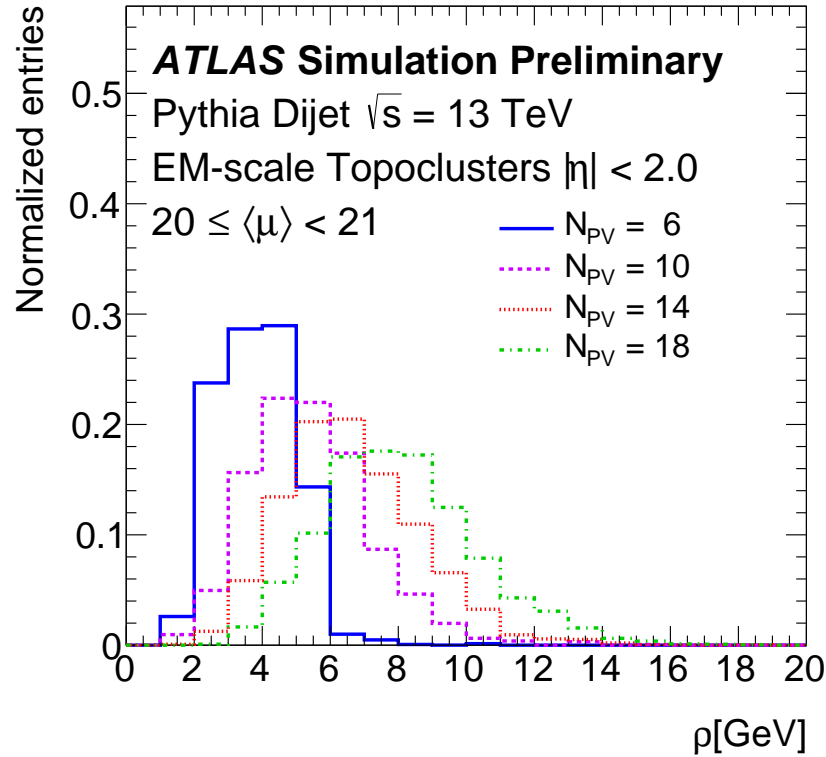


Figure 45: Distribution of event p_T density, ρ , taken from MC dijets for different numbers of primary vertices. [50]

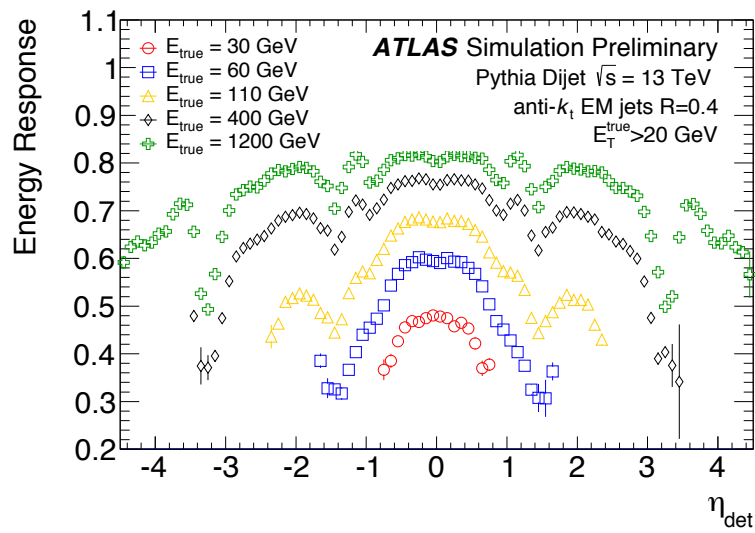


Figure 46: Energy response as a function of energy and η for EM jets in dijet MC. [50]

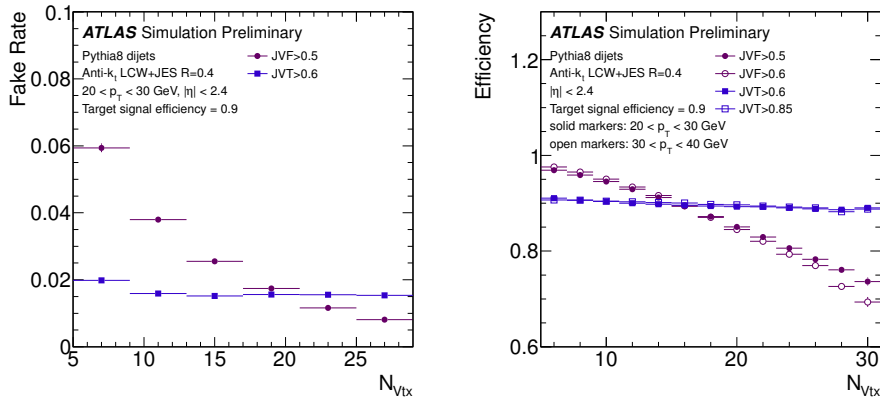


Figure 47: Dijet MC distributions of the number of pile-up jets passing the [JVT](#) and [JVF](#) cuts (left) and the efficiency for jets from the primary vertex (right) as a function of number of primary vertices in the event [51].

It is possible to differentiate jets resulting from b -hadron decays from other jets due to the non-negligible lifetimes of the hadrons. Many [BSM](#) processes preferentially produce b quarks, as does any process involving top quarks, so this identification can be useful for targeting specific decays in many analyses. Multivariate techniques are used to identify secondary vertices using the [ID](#) [52]. In ATLAS, separate algorithms are used to identify jets with tracks with significantly non-zero impact parameters, tracks that reconstruct a secondary vertex, and tracks that can be identified with a chain of vertices beginning with the primary vertex. This information is fed into a boosted decision tree called [MV2c20](#), which outputs a discriminant shown in [Figure 48](#). Using this discriminant, a working point is chosen such that b -jets can be identified with a 70% efficiency, with misidentification rates at around 12% for c -jets and 0.2% for light-flavor jets.

5.5 OVERLAP REMOVAL

Because most of these reconstruction methods are run independently, it is common for energy deposits and tracks to be shared between jets and particles of different types. To account for this, a process called Overlap Removal ([OR](#)) is used, which iteratively removes overlapping objects. The process is performed at the *baseline* level, a set of loose selections on objects which are later further refined to create the *signal* objects used in analysis. Each analysis defines these levels according to its needs; the specific requirements made for the analysis described in [Part iv](#) are outlined in [Chapter 8](#).

The first step in the [OR](#) process is to remove reconstructed jets that appear to be due to calorimetric deposits from an electron. To accomplish this, any baseline jet within $\Delta R = 0.2$ from a baseline electron is removed. A caveat is added due to the frequent production of leptons in the decay of heavy-flavor jets; if the jet is b -tagged, the electron will be removed instead. After these electrons and jets have been removed, a new search is

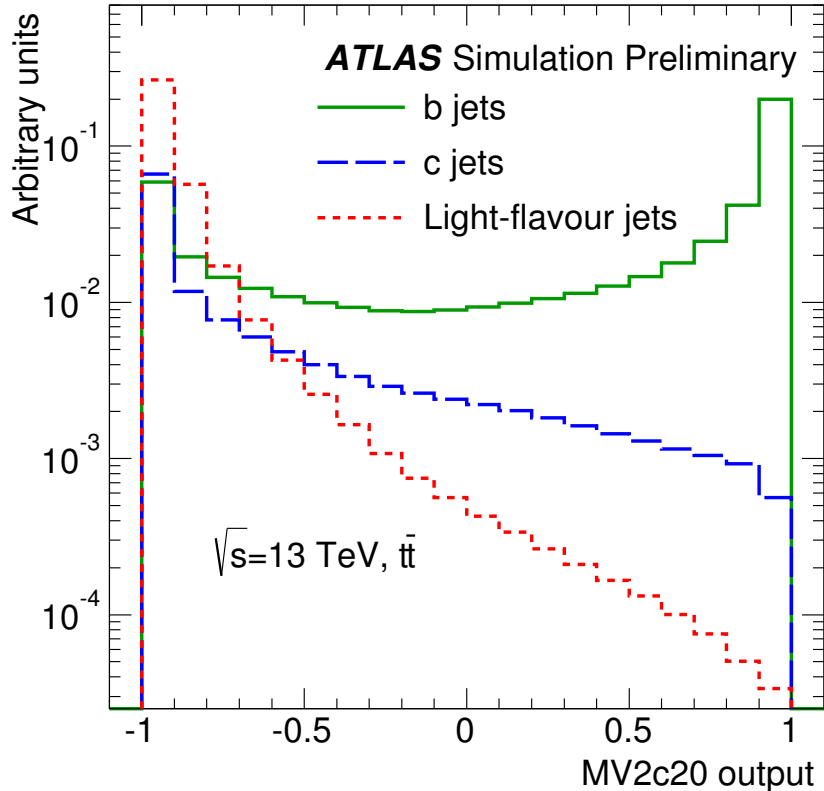


Figure 48: Distribution of MV2c20 output for b -jets, c -jets, and light-flavor jets in $t\bar{t}$ MC [52].

1475 done for jets and electrons within $\Delta R = 0.4$ of one another. In this iteration,
 1476 the electron is removed, again to reduce backgrounds from heavy-flavor
 1477 decays.

1478 Next, the muon-jet OR is applied, which is very similar to that of the
 1479 electron. Any jet within $\Delta R = 0.2$ of a muon is removed, unless the jet is
 1480 b -tagged, in which case the muon is removed due to the likelihood that it
 1481 resulted due to a heavy-flavor decay. The muon-jet OR then differs from the
 1482 electron's in that a p_T -based ΔR cut is used in the last step. Muons within
 1483 $\Delta R < \min(0.04 + (10 \text{ GeV})/p_T, 0.4)$ of a jet are removed, with the shrink-
 1484 ing cone for high- p_T muons designed to improve efficiency for energetic
 1485 muons that produce significant calorimeter deposits, while still rejecting
 1486 the heavy-flavor muons that are typically lower p_T .

1487 The next step is to remove electrons resulting from muon bremsstrahlung.
 1488 Any remaining electron within $\Delta R = 0.1$ of a muon is removed from the
 1489 event.

1490 Lastly, overlap between photons and both jets and electrons is consid-
 1491 ered. Baseline photons within $\Delta R = 0.4$ of an electron are removed, as are
 1492 jets within $\Delta R = 0.4$ of a remaining photon.

1493 5.6 MISSING TRANSVERSE MOMENTUM

1494 Missing transverse momentum ($\mathbf{p}_T^{\text{miss}}$, with magnitude E_T^{miss}), is the neg-
 1495 ative vector sum of p_T measured in an event. Because colliding parti-
 1496 cles have no initial transverse momentum, the true value of this quan-
 1497 tity should be zero unless a particle escapes the detector without being
 1498 measured, as neutrinos do. In practice, the reconstructed E_T^{miss} can also be
 1499 non-zero due to mismeasurement. E_T^{miss} reconstruction is perhaps the most
 1500 complex because it depends on all other object reconstructions performed
 1501 in the ATLAS detector.

1502 E_T^{miss} components are calculated independently for each type of base-
 1503 line object reconstructed, as well as for a soft term, which accounts for
 1504 low- p_T radiation [53]. This component comprises the energy observed by
 1505 the ATLAS detector but not associated with a baseline object, and can be
 1506 calculated based either based on calorimeter or track measurements. While
 1507 the Calorimeter Soft Term (CST) is very sensitive to pile-up, the Track Soft
 1508 Term (TST) is much more robust, as it can exclude tracks emanating from
 1509 pile-up vertices. Tracks associated with any reconstructed object are also
 1510 removed. Figure 49 shows the TST resolution's dependence on number of
 1511 primary vertices, which is considerably more stable than CST. Because of
 1512 this improved performance, using TST to reconstruct E_T^{miss} is now the stan-
 1513 dard for ATLAS analyses.

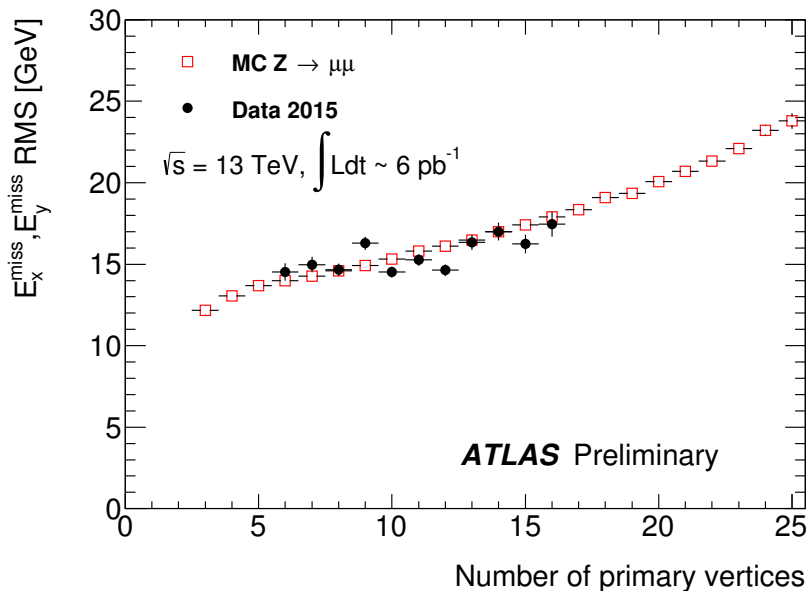


Figure 49: Distributions of the resolution of the x and y components of TST E_T^{miss} in $Z \rightarrow \mu\mu$ events in data and MC [54].

1514 Figure 50 shows the the E_T^{miss} resulting from muons, jets, and the soft
 1515 term in $Z \rightarrow \mu\mu$ events. These events very rarely have any true E_T^{miss} , so
 1516 these distributions primarily demonstrate how mismeasurement of vari-
 1517 ous objects contributes to the E_T^{miss} term. Though the soft term falls off
 1518 very quickly, rarely producing events with more than 50 GeV of E_T^{miss} , both

- 1519 the jet and muon distributions have longer tails, producing more events
1520 with higher E_T^{miss} .
1521 The jet and muon distributions both have significant high tails, while
1522 the soft term falls off much more quickly.

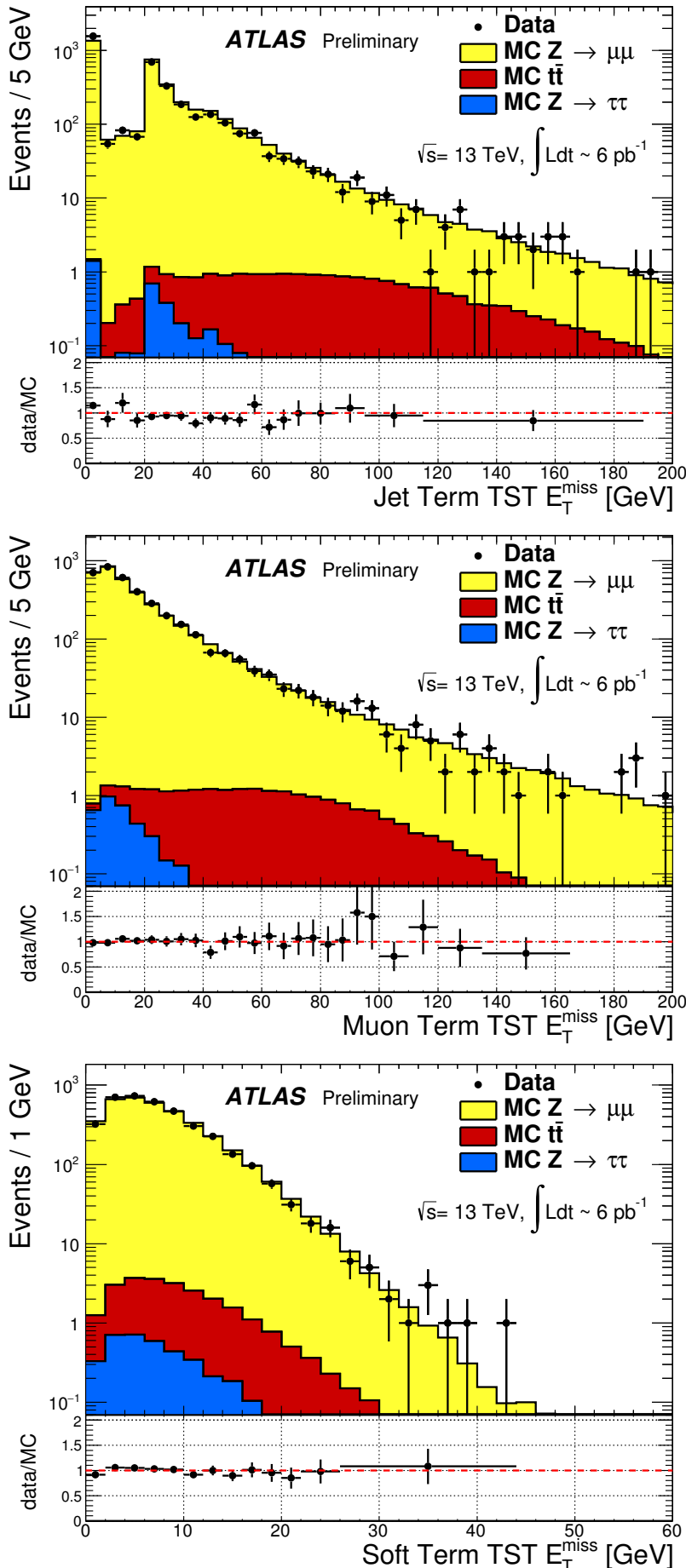


Figure 50: Distributions of the jet term (top left), muon term (top right), and TST (bottom) E_T^{miss} in $Z \rightarrow \mu\mu$ events in data and MC. In the jet term distribution, the feature at zero is due to events with no jets, and the spike at 20 GeV corresponds to the minimum jet p_T considered for the analysis [54].

1523

1524 APPLICATION OF A NEURAL NETWORK TO PIXEL 1525 CLUSTERING

1526 6.1 CLUSTERING IN THE PIXEL DETECTOR

1527 Creating tracks from individual hits in the Inner Detector is one of most
 1528 computationally challenging parts of the reconstruction of ATLAS events.
 1529 Each event typically contains thousands of hits in the pixel detector alone,
 1530 which must be combined into one coherent picture of which particles tra-
 1531 versed the detector, and how they moved and lost energy as they traveled.
 1532 A typical particle deposits charge in several pixels per layer, forming a se-
 1533 ries of clusters which can be connected together to form a track. This track
 1534 can in turn be used to measure the charge, momentum, and trajectory of
 1535 the particle.

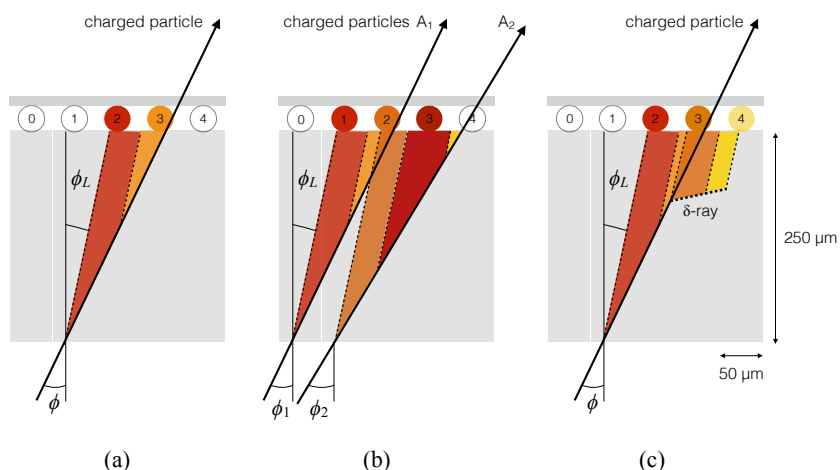


Figure 51: A few possible types of clusters in the Pixel Detector. (a) shows a single particle passing through a layer of the detector, (b) shows two particles passing through the detector, creating a single merged cluster, and (c) shows a single particle emitting a δ -ray as it passes through the detector [55].

1536 The process of going from clusters to track is relatively simple in an
 1537 isolated environment in which one particle travels cleanly through all the
 1538 layers, but can be complicated by multiple close-by tracks and by a single
 1539 particle's emission of low energy particles, called δ -rays. In these cases, it
 1540 can be hard to tell how many particles were involved in creating a clus-
 1541 ter, and where exactly each of those particles passed through the layer. A
 1542 few examples of particle interactions with the pixel sensor can be seen in
 1543 [Figure 51](#).

1544 Clusters are initially made by a process called Connected Component
 1545 Analysis ([CCA](#)). In this process, pixels in a given layer are grouped together
 1546 if they share any edge or corner. The position of the resulting cluster is
 1547 defined by local x and y coordinates, which describe its position and size
 1548 within the pixel module on which it appears. Determining the position
 1549 of the particle that formed that cluster is less straightforward, and has
 1550 recently been updated from a charge interpolation method to a method
 1551 using a [NN](#).

1552 6.1.1 Charge Interpolation Method

1553 A typical cluster contains a few pixel hits spanning in the x and y direc-
 1554 tions, each with its own measurement of charge deposition, or [ToT](#). In the
 1555 charge interpolation method, these individual hits are combined to make
 1556 one estimation of the position a single particle which passed through them,
 1557 using the following equation:

$$x_{cluster} = x_{center} + \Delta_x(\phi, N_{row}) \cdot \left[\Omega_x - \frac{1}{2} \right] \quad (27)$$

$$x_{cluster} = x_{center} + \Delta_x(\phi, N_{row}) \cdot \left[\Omega_x - \frac{1}{2} \right] \quad (28)$$

1558 where $\Omega_{x(y)}$ is defined by

$$\Omega_{x(y)} = \frac{q_{last\ row(col)}}{q_{first\ row(col)} + q_{last\ row(col)}} \quad (29)$$

1559 and q represents the [ToT](#) of a given pixel, and $\Delta_{x(y)}$ is a function derived
 1560 from either data or [MC](#) and produces an output related to the projected
 1561 length of the particles track on the pixel sensor and is measured as a func-
 1562 tion of ϕ , the incident angle of a particle on the sensor, and $N_{row(col)}$, the
 1563 number of pixels in the x and y direction.

1564 In a simple case, such as (a) of [Figure 51](#), this method works quite effec-
 1565 tively. However, in cases like (b), it has no ability distinguish two-particle
 1566 from one-particle clusters, and can only assign a cluster center between the
 1567 two particles' locations, despite that intermediate pixel having the lowest
 1568 [ToT](#). Furthermore, because this method can't differentiate two-particle clus-
 1569 ters, the tracking software can't use that information to preferentially al-
 1570 low multiple tracks to share two-particle clusters. Allowing tracks to share
 1571 clusters indiscriminately in dense track environments creates fake tracks
 1572 from the many possible cluster combinations, so this cannot be broadly
 1573 permitted. In cases like (c), the δ -ray will bias the measurement of the
 1574 particle's position in whichever direction it is emitted.

1575 6.1.2 Improving Measurement with Neural Networks

1576 To address these problems, a series of [NNs](#) were created [55]. The first esti-
 1577 mates the number of particles in a given cluster, the second estimates their

1578 positions within the cluster, and the third assesses the uncertainty of the
 1579 position measurement. They are referred to, respectively, as the “Number”,
 1580 “Position”, and “Error” NNs.

1581 These NNs are taken from the AGILEPack library [56], and trained using
 1582 simulated ATLAS MC. Each NN is given the following inputs:

- 1583 • a 7×7 grid of cluster ToT information¹
- 1584 • a 7-element vector containing the y -size of the pixels in the grid²
- 1585 • the layer of the pixel detector that the cluster was observed in
- 1586 • a variable indicating whether the cluster is located in the barrel or
 1587 endcap
- 1588 • θ and ϕ variables projecting the incident angles of the particle on the
 1589 sensor³
- 1590 • the pixel module’s η index, a label assigned to each module that
 1591 differentiates modules based on their η position

1592 After the Number NN predicts a number of particles associated with the
 1593 cluster, required to be between 1 and 3, the same inputs are fed to one of
 1594 three Position NNs based on the determined number of particles, which
 1595 then outputs the x and y positions of each of the particles. Then, the same
 1596 inputs combined with the output of the Position NN are fed into one of
 1597 three Error NNs (also distinguished by number of particles), which outputs
 1598 an uncertainty for each of the position predictions made. An example of
 1599 the output of this process can be seen in Figure 52, where the improved
 1600 position resolution from the ability to identify a multi-particle cluster is
 1601 evident.

1602 The particle location predictions from the NNs are then handed to the
 1603 tracking software, which now can use these multiple particle position es-
 1604 timations as independent hits to be fit. As a result, tracks in dense envi-
 1605 ronments have fewer clusters shared between multiple tracks, and their
 1606 trajectories are known to a greater degree of precision.

1607 6.2 IMPACT OF THE NEURAL NETWORK

1608 The NN was first applied to 7 TeV data, where it improved position res-
 1609 olution for particles in small and large clusters. Figure 53 shows the im-
 1610 provement from the addition of the NN in x resolution in different cluster

¹ Clusters spanning more than seven pixels in either direction are rare, but when they occur they are rejected, and the original charge interpolation estimate of a single particle’s position is kept.

² The pixel detector contains some long pixels at the edges of modules, and this is intended to help the NN identify these cases.

³ If the NN is applied before tracking is performed, these angles project to the nominal interaction point, and if tracking has already been performed, the angles are taken from the track fit to the cluster.

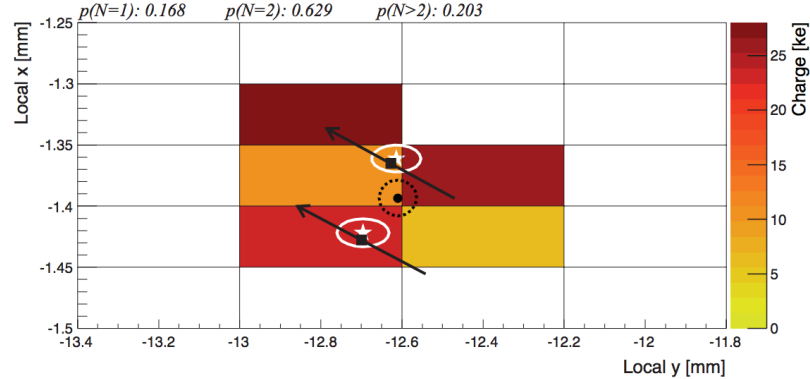


Figure 52: One example of a two-particle cluster and its truth information compared with the output of the NNs. The boxes represent pixels, with a color scale indicating ToT. At top, the $p(N = i)$ values give the output of the Number NN, the probabilities that the cluster contains 1, 2, and 3 particles. Given the highest probability is for $N = 2$, the other NNs predict the position and errors of the two particles (in white). The black arrows and squares represent the truth information from the cluster, and the black dot and dotted line show the position measurement for the un-split cluster [55].

1611 sizes. The improvement from charge interpolation clustering is particu-
 1612 larly evident in the 4-pixel case, where the double peaked structure of the
 1613 interpolation method has been completely removed with the NN.

1614 6.2.1 The Neural Network in 13 TeV Data

1615 In Run 2, the tracking algorithm is first run on the CCA clusters with posi-
 1616 tions determined via charge interpolation, where it constructs tracks with
 1617 loose quality requirements. In this step, the tracking algorithm allows
 1618 shared clusters, clusters used in multiple track fits [57]. The NN is then
 1619 used to identify which clusters are likely to have had multiple particles
 1620 pass through them, and to estimate the positions of those particles. In the
 1621 case that the cluster is determined to have resulted only from one particle,
 1622 tracks that share that cluster are penalized. In general, tracks with more
 1623 than two shared clusters are rejected.

1624 Because the NN is trained only with MC simulations, any mismodeling of
 1625 the way charge is deposited in the ATLAS detector could cause the NN to
 1626 perform in an unexpected way when applied to data. The potential impact
 1627 of this mismodeling was investigated with 13 TeV MC [58]. The goal of
 1628 these studies was to determine which variables the NN's predictions were
 1629 most sensitive to, and whether it was likely that these variables could be
 1630 mismodeled enough to produce unexpected results in data.

1631 One example of a variable capable of significantly altering the NN out-
 1632 puts was the overall charge scale. To study its impact, the ToT of all pixels
 1633 in a cluster were scaled up and down, and the resulting outputs of the
 1634 NN were compared, as shown in Figure 54. In this case, the likelihood to

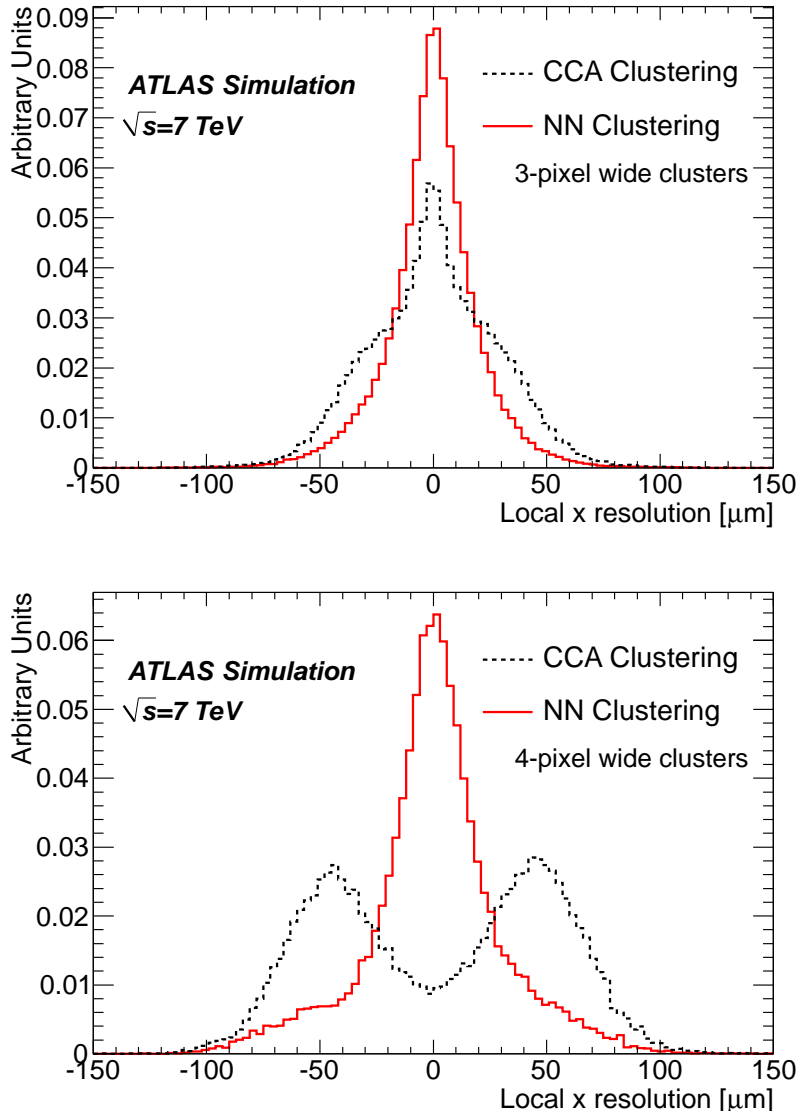


Figure 53: x resolutions for clusters with 3 (top) and 4 (bottom) pixels in the x direction in 7 TeV data for CCA (using only charge interpolation to determine position) and NN clustering taken from MC [55].

misidentify multi-particle clusters and single particle clusters depended significantly on this scaling. However, experts on the simulation of this scale agree that it's unlikely to be mismodeled by more than 10%, so very extreme effects from a difference between data and MC are unlikely. Overall, it was found that variations on the cluster charge produced a significant impact on predictions, while all other variations, such as incidence angle variation and spatial smearing of charge, had a minimal effect.

In addition to studies on the impact of alterations of individual simulation variables, studies directly comparing the NN output in data and MC were performed. Figure 55 shows a comparison of how often the NN identifies different types of clusters in data and MC. Each figure is made using by selecting pairs of collimated tracks that share a common cluster on a given

1647 layer, then calculating the fraction of those clusters that are determined by
1648 the **NN** to be single or multi-particle clusters. This fraction is plotted as a
1649 function of the distance between the two tracks in the cluster's layer. Very
1650 good agreement is seen between the two samples, demonstrating that the
1651 **MC**-trained **NN** performs similarly on both **MC** and data.

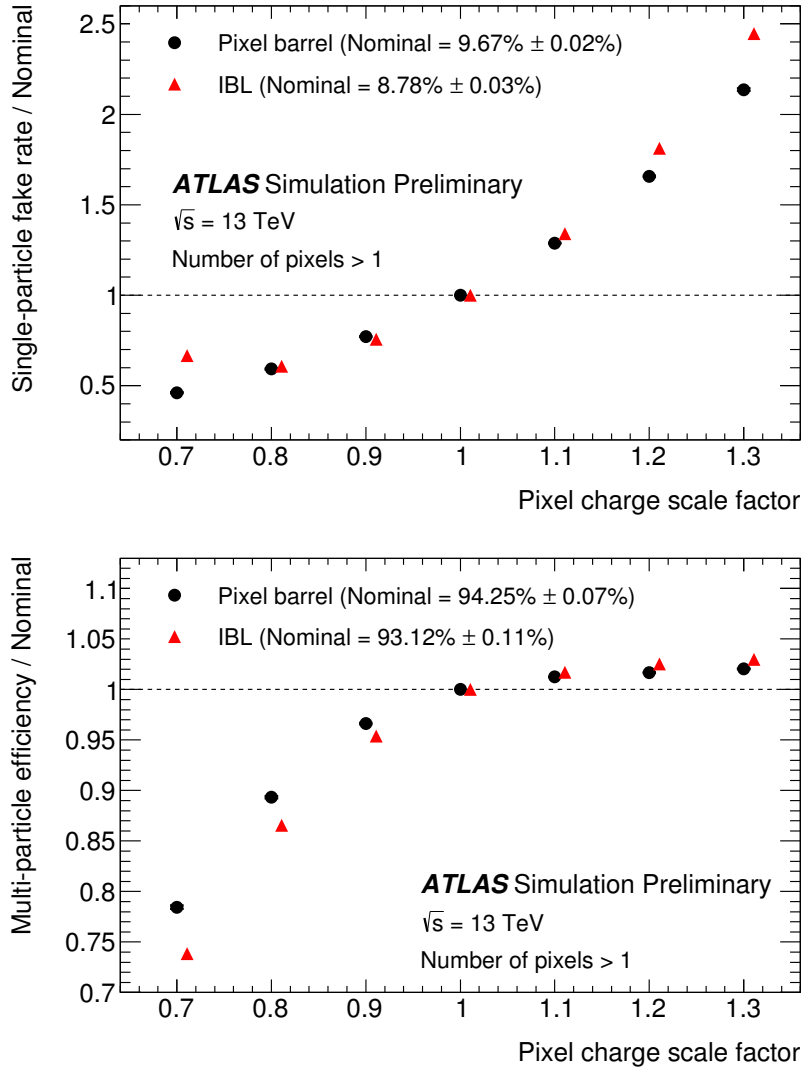


Figure 54: Performance of the pixel neural network used to identify clusters created by multiple charged particles, as a function of constant coherent scaling of the charge in each pixel in the cluster. The top figure shows the rate at which the neural network wrongly identifies clusters with one generated particle as clusters with multiple particles. The bottom figure shows the rate at which the neural network correctly identifies clusters generated by multiple particles as such.

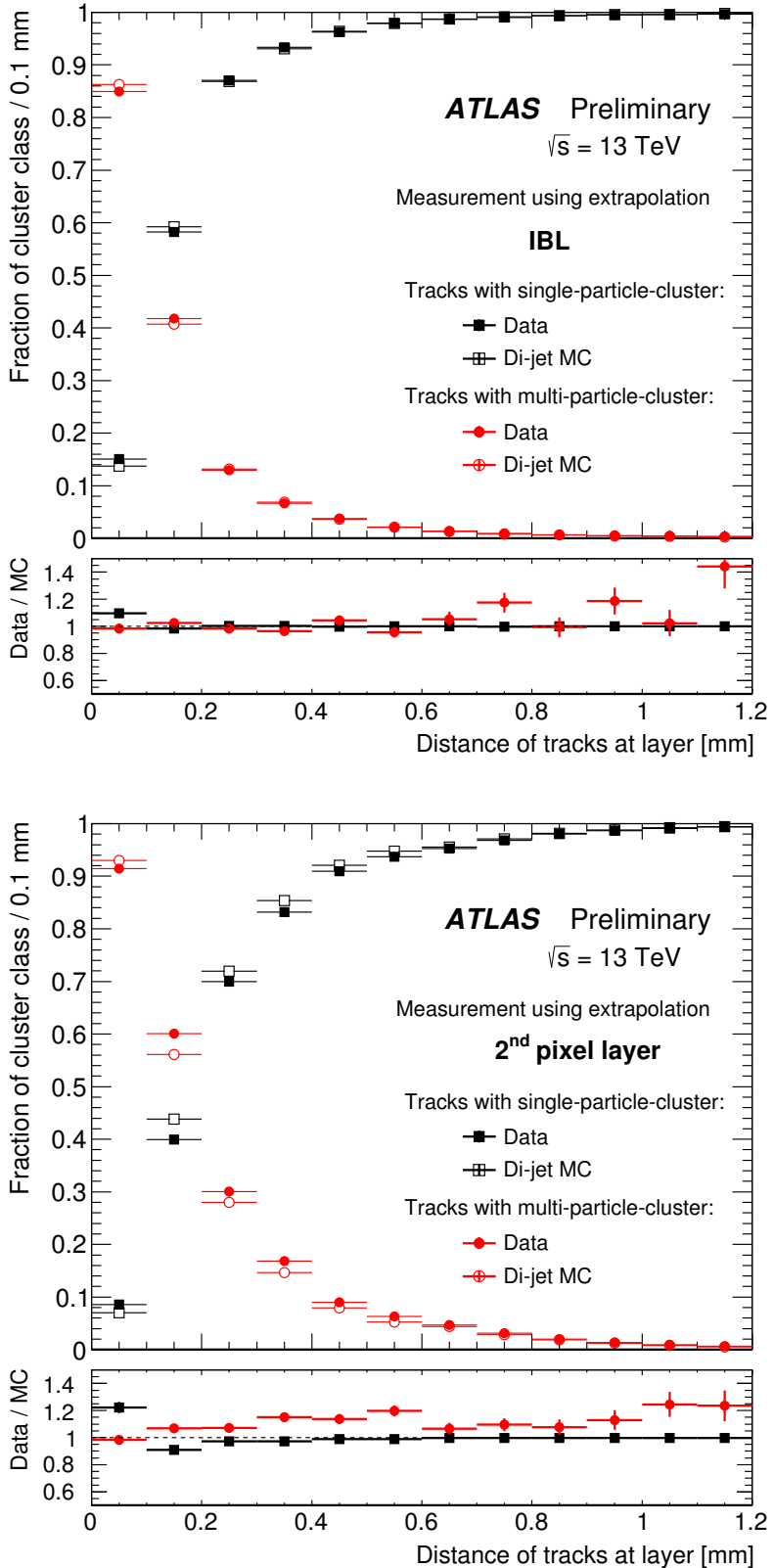


Figure 55: Fraction of cluster classes as a function of the distance between tracks for IBL (top) and 2nd pixel layer (bottom).

1652

Part IV

1653

SEARCHING FOR SUPERSYMMETRY

1654

This section describes an analysis of the ATLAS data carried out by the author and her analysis team. The analysis was performed on events from $p - p$ collisions provided by the LHC at $\sqrt{s}=13$ TeV. It searches for events like those described in [Section 2.2.3](#), which contain a Z boson decaying to leptons, jets, and missing transverse energy. The selection of a signal region in which to search for these events, background estimates, systematic uncertainty estimates, results, and interpretations are all discussed.

1655

1656

1657

1658

1659

1660

1661

1662

1663

1664 BACKGROUND PROCESSES

1665 This analysis is fundamentally a search for Supersymmetry ([SUSY](#)) in events
 1666 with two leptons whose invariant mass is consistent with a Z boson. Ad-
 1667 ditional event selections are made to reduce Standard Model ([SM](#)) pro-
 1668 cesses relative to potential [SUSY](#) processes, defined by simplified models
 1669 discussed in [Section 2.2.3](#). [SUSY](#) events typically have large amounts of
 1670 E_T^{miss} , H_T (the scalar sum of the p_T of all jets and the leading two leptons
 1671 in an event), and many jets. All of these features can help isolate these
 1672 events from backgrounds. To understand what cuts would optimize the
 1673 sensitivity of the search, it is essential to first understand what these [SM](#)
 1674 backgrounds are.

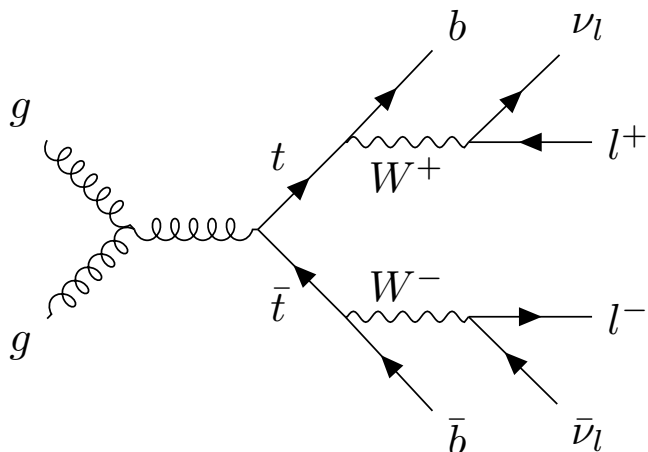


Figure 56: An example Feynman diagram of $t\bar{t}$ production and decay.

1675 TOP-ANTITOP ($t\bar{t}$) production is the largest background for this search.
 1676 [Figure 56](#) shows an example of this process, which results in many jets, lep-
 1677 tons, and neutrinos, which are seen in the detector as E_T^{miss} . Thus, $t\bar{t}$ events
 1678 naturally have high E_T^{miss} and H_T , jets, and leptons from two different W
 1679 boson decays, which may coincidentally form an invariant mass consistent
 1680 with a Z boson. These events are very difficult to separate from potential
 1681 signals, though keeping the mass window small and requiring E_T^{miss} and
 1682 H_T above the typical values for $t\bar{t}$ events helps reduce this background.

1683 DIBOSON (VV) production is the next leading background. These events
 1684 can contain real Z bosons and will peak on-Z like a signal. In addition, in
 1685 events like [Figure 57](#), an additional W boson can decay to another lepton
 1686 and a neutrino, providing E_T^{miss} . The pictured process can occur with asso-
 1687 ciated jets, but at reduced rates, so adding a jet requirement to the signal
 1688 region helps reduce these events. If the W boson in this diagram instead

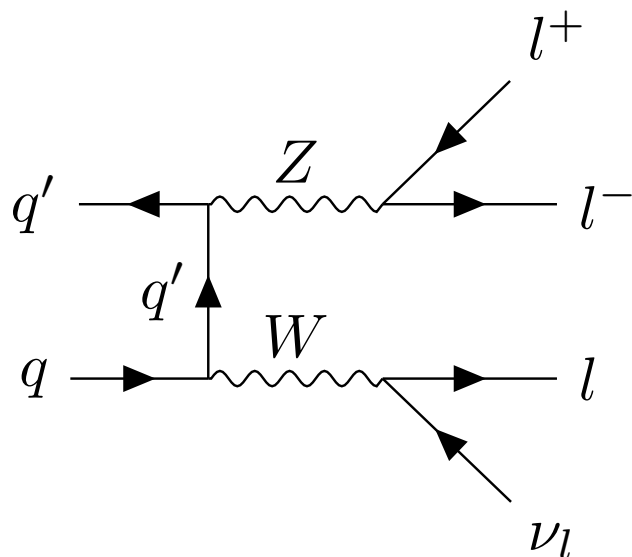


Figure 57: An example Feynman diagram of the production and decay of a WZ event.

1689 decayed to two jets, there would be no true E_T^{miss} from a neutrino, so a
 1690 E_T^{miss} cut in conjunction with a jet cut is very effective in reducing the total
 1691 diboson background. A veto on a third lepton could also be used to reduce
 1692 this background, but, depending on the signal model considered, this veto
 1693 can also decrease signal acceptance, so it is not used in this analysis.

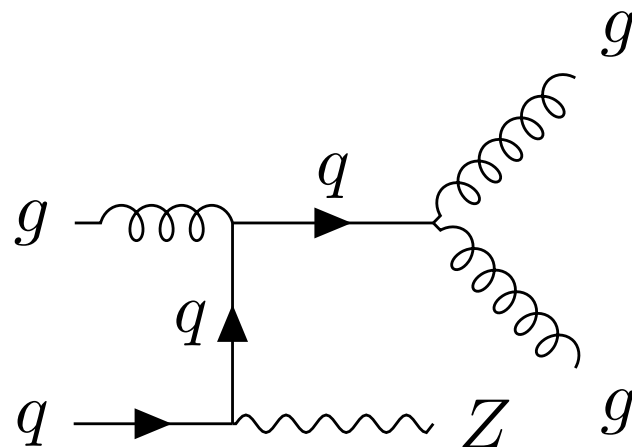


Figure 58: An example Feynman diagram of the production and decay of a $Z/\gamma^* + \text{jets}$ event.

1694 $Z/\gamma^* + \text{jets}$ processes are very common but, as shown in Figure 58,
 1695 don't produce any true E_T^{miss} . A high H_T cut helps reduce this background,
 1696 but this process often occurs with associated jets, producing many events
 1697 with large amounts of hadronic activity. E_T^{miss} is the most powerful variable
 1698 to reduce this background, because though events with mismeasured jets

1699 or leptons can fake E_T^{miss} , mismeasurements drastic enough to produce
 1700 hundreds of GeV of E_T^{miss} are rare.

1701 Other processes can contribute to the Standard Model background at
 1702 lower rates. Processes similar to $Z/\gamma^* + \text{jets}$ but with a W boson instead of
 1703 a Z have real E_T^{miss} from leptonic W decays, but only one lepton. However,
 1704 a fake or non-prompt lepton can cause these events to look very similar to
 1705 simulated signals. Additionally, there are rare processes such as $t\bar{t}$ produc-
 1706 tion in association with bosons that will also be difficult to separate from
 1707 signal processes.

1708 7.1 DATA AND MONTE CARLO SAMPLES

1709 This analysis uses data collected by the ATLAS detector from $p - p$ colli-
 1710 sions at a center-of-mass energy of 13 TeV in 2015 and 2016, corresponding
 1711 to a total luminosity of 14.7 fb^{-1} . The data collected using a combination
 1712 of unprescaled single and dilepton triggers, discussed in greater detail in
 1713 [Chapter 9](#). In addition, photon events are collected for use in a control
 1714 region using both prescaled and unprescaled triggers, with the lowest trig-
 1715 ger threshold at 20 GeV.

1716 MC samples are generated for each background process that appears
 1717 in the signal and validation regions. [Table 2](#) details the method used to
 1718 produce each sample, and more information can be found in [Section 2.3](#).
 1719 These simulated background events, in conjunction with the simulated
 1720 signal discussed in [Section 2.2.3](#), are used to determine approximate sensi-
 1721 tivities of the search and optimize signal regions and amount of data used.
 1722 The background MC also provides a valuable cross-check for many of the
 1723 data-driven background estimates discussed in [Chapter 10](#), and in some
 1724 cases, provides the primary estimate of the background.

Table 2: Simulated background event samples used in this analysis with the corresponding matrix element and parton shower generators, cross-section order in α_s used to normalise the event yield, underlying-event tune and PDF set.

Physics process	Generator	Parton Shower	Cross section	Tune	PDF set
$t\bar{t} + W$ and $t\bar{t} + Z$ [59, 60]	MG5_AMC@NLO	Pythia 8.186	NLO [61, 62]	A14	NNPDF23LO
$t\bar{t} + WW$ [59]	MG5_AMC@NLO	Pythia 8.186	LO [26]	A14	NNPDF23LO
$t\bar{t}$ [63]	POWHEG Box v2 r3026	Pythia 6.428	NNLO+NNLL [64, 65]	PERUGIA2012	NULO CT10
Single-top (Wt) [63]	POWHEG Box v2 r2856	Pythia 6.428	Approx. NNLO [66]	PERUGIA2012	NULO CT10
WW , WZ and ZZ [67]	SHERPA 2.1.1	SHERPA 2.1.1	NLO [68, 69]	SHERPA default	NULO CT10
$Z/\gamma^*(\rightarrow \ell\ell) + \text{jets}$ [70]	SHERPA 2.1.1	SHERPA 2.1.1	NNLO [71, 72]	SHERPA default	NULO CT10
$\gamma + \text{jets}$	SHERPA 2.1.1	SHERPA 2.1.1	LO [30]	SHERPA default	NULO CT10
$V(=W, Z)\gamma$ signal	SHERPA 2.1.1	SHERPA 2.1.1	LO [30]	SHERPA default	NULO CT10
	MG5_AMC@NLO	Pythia 8.186	NLO	A14	NNPDF23LO

1725

1726 OBJECT IDENTIFICATION AND SELECTION

1727 This section describes the identification and selection of objects in the
 1728 events of this analysis. Objects are first required to pass *baseline* selections,
 1729 which are used for Overlap Removal ([OR](#)) and the calculation of E_T^{miss} ,
 1730 then have tighter *signal* selections applied, which define the objects consid-
 1731 ered in the final analysis of events. Definitions are presented for electrons,
 1732 muons, and jets, which are all required in the Signal Region ([SR](#)) of the
 1733 analysis, as well as photons, which are used in background estimation.
 1734 This section refers to quality definitions described in [Chapter 5](#).

1735 8.1 ELECTRONS

1736 Electrons are reconstructed using the Egamma algorithm discussed in [Sec-](#)
 1737 [tion 5.1](#). All electrons are required to be within $|\eta| < 2.47$, to ensure that all
 1738 tracks are consistently within the tracking capability of the [ID](#). Baseline lep-
 1739 tons are required to have $p_T > 10 \text{ GeV}$ and pass the [LHLoose](#) quality stan-
 1740 dard. Signal leptons are further required to be of [LHMedium](#) quality with
 1741 [GradientLoose](#) isolation, and must have $p_T > 25 \text{ GeV}$. Additional cuts on
 1742 impact parameter are made for electrons with the goal of identifying only
 1743 electrons coming from the primary vertex of the event, the vertex with the
 1744 highest associated p_T . These requirements, and all the other requirements
 1745 made on the electrons can be seen in [Table 3](#).

Cut	Value/description
Baseline Electron	
Acceptance	$p_T > 10 \text{ GeV}, \eta^{\text{clust}} < 2.47$
Quality	Loose
Signal Electron	
Acceptance	$p_T > 25 \text{ GeV}, \eta^{\text{clust}} < 2.47$
Quality	Medium
Isolation	GradientLoose
Impact parameter	$ z_0 \sin \theta < 0.5 \text{ mm}$ $ d_0 / \sigma_{d_0} < 5$

Table 3: Summary of the electron selection criteria. The signal selection require-
 ments are applied on top of the baseline selection.

1746 With these requirements, the ATLAS detector is 95% efficient at identify-
 1747 ing electrons with $p_T > 25 \text{ GeV}$, which rises to 99% at $p_T > 60 \text{ GeV}$ [[73](#)]. Scale
 1748 factors are applied to correct [MC](#) to match data efficiencies. These efficien-

1749 cies are measured as a function of p_T and η , and include both electron
1750 identification efficiencies and trigger efficiencies.

1751 **8.2 MUONS**

1752 Muons are reconstructed according to the process discussed in [Section 5.3](#).
1753 Baseline muons are required to have $p_T > 10$ GeV and $|\eta| < 2.5$, including
1754 muons that can be tracked both by the [ID](#) and the [MS](#), and must pass a
1755 Medium quality cut. Signal muons are additionally required to have $p_T >$
1756 25 GeV, and to have [GradientLoose](#) isolation. As with the electrons, quality
1757 cuts are made to ensure that the muon is consistent with coming from
1758 a decay from the event’s primary vertex. Additionally, the muon must
1759 not be flagged [isBadMuon](#), which reduces the number of events with very
1760 inconsistent [ID](#) and [MS](#) tracks. The full set of requirements can be seen in
1761 [Table 4](#).

Cut	Value/description
Baseline Muon	
Acceptance	$p_T > 10$ GeV, $ \eta < 2.5$
Quality	Medium
Signal Muon	
Acceptance	$p_T > 25$ GeV, $ \eta < 2.5$
Quality	Medium
Isolation	GradientLoose
Impact parameter	$ z_0 \sin \theta < 0.5$ mm $ d_0/\sigma_{d_0} < 3$
isBadMuon	MCP isBadMuon Flag

Table 4: Summary of the muon selection criteria. The signal selection requirements are applied on top of the baseline selection.

1762 Muons with $p_T > 25$ GeV are identified with a 95% efficiency, which
1763 rises to 99% for muons with $p_T > 80$ GeV[[74](#)]. Including trigger and iso-
1764 lation requirements, these efficiencies drop to about 80% for muons with
1765 $p_T > 25$ GeV and 90% for muons with $p_T > 200$ GeV. This drop is largely
1766 the consequence of incomplete η coverage of the [RPCs](#), discussed in [Sec-](#)
1767 [tion 5.3](#). Scalefactors to correct the [MC](#) identification efficiencies according
1768 to data are used.

1769 **8.3 JETS**

1770 Jets are reconstructed according to [Section 5.4](#), with baseline jets using the
1771 [AntiKt4EMTopo](#) algorithm, with a minimum p_T of 20 GeV and $|\eta| < 2.8$.
1772 Signal jets increase this p_T requirement to 40 GeV and decrease their ac-

1773 ceptance to $|\eta| < 2.5$. [JVT](#) requirements are enforced to reduce the number
1774 of jets from pile-up. The full set of requirements can be seen in [Table 5](#).

Cut	Value/description
Baseline jet	
Collection	AntiKt4EMTopo
Acceptance	$p_T > 20 \text{ GeV}$, $ \eta < 2.8$
Signal jet	
Acceptance	$p_T > 30 \text{ GeV}$, $ \eta < 2.5$
JVT	$ \text{JVT} > 0.59$ for jets with $p_T < 60 \text{ GeV}$ and $ \eta < 2.4$
Signal b -jet	
b -tagger Algorithm	MV2c20
Efficiency	77 %
Acceptance	$p_T > 30 \text{ GeV}$, $ \eta < 2.5$
JVT	$ \text{JVT} > 0.59$ for jets with $p_T < 60 \text{ GeV}$ and $ \eta < 2.4$

Table 5: Summary of the jet and b -jet selection criteria. The signal selection requirements are applied on top of the baseline requirements.

1775 Though no b -jets are required in the [SR](#) of this analysis, some Control
1776 Regions ([CRs](#)) use b -enhanced and b -vetoed regions to determine the im-
1777 pact of heavy flavor. These b -jets are identified using the [MV2c20](#) algorithm
1778 at a 77% efficient working point, and are only identified for $|\eta| < 2.5$.

1779 8.4 PHOTONS

1780 Photons are used to estimate the $Z/\gamma^* + \text{jets}$ background in this analy-
1781 sis, and they are reconstructed according to [Section 5.2](#). Baseline and sig-
1782 nal photons are nearly identical. Each must pass a tight selection with
1783 [FixedCutTight](#) isolation and have $p_T > 25 \text{ GeV}$ as well as $|\eta| < 2.37$. Sig-
1784 nal photons with $1.37 < |\eta| < 1.6$ are rejected due to an discontinuity
1785 in the calorimeter which results in very large energy resolutions in this
1786 region. The full selection requirements can be seen in [Table 6](#).

Cut	Value/description
Baseline Photon	
Acceptance	$p_T > 25 \text{ GeV}, \eta < 2.37$
Quality	tight
Signal Photon	
Acceptance	$p_T > 25 \text{ GeV}, \eta < 2.37$ rejecting $1.37 < \eta < 1.6$
Quality	tight
Isolation	FixedCutTight

Table 6: Summary of the photon selection criteria.

1787

1788 EVENT SELECTION

1789 The goal of this analysis is to identify events resembling [Figure 13](#) in col-
 1790 lisions in the ATLAS detector. In order to do this, a Signal Region ([SR](#)) is
 1791 defined with the goal of maximizing the identification efficiency of signal-
 1792 like events while minimizing [SM](#) backgrounds. However, because this anal-
 1793 ysis reinvestigates an excess of events seen in Run 1 with the ATLAS de-
 1794 tector, the signal region was frozen and could not be reoptimized for the
 1795 new, higher energy data in Run 2. The [SR](#), called *SRZ*, was predetermined,
 1796 including events with two opposite-sign, same-flavor leptons that recon-
 1797 struct a mass, $m_{\ell\ell}$, close to that of the Z boson, with the additional require-
 1798 ment of two jets, $E_T^{\text{miss}} > 225 \text{ GeV}$, and H_T of at least 600 GeV. Additionally,
 1799 a cut on $\Delta\phi(\text{jet}_{12}, p_T^{\text{miss}})$ was made in order to reduce the number of events
 1800 with high E_T^{miss} due to mismeasurement of one of the leading two jets.

1801 Though this [SR](#) was fixed, the methods used to estimate its expected [SM](#)
 1802 backgrounds were not. A set of Control Regions ([CRs](#)) and Validation Re-
 1803 gions ([VRs](#)) were chosen to make these estimations possible. [CRs](#) are regions
 1804 in which the collected data can be used to make an estimate of an expected
 1805 background in the [SR](#), while [VRs](#) are used to confirm the efficacy of these
 1806 methods. Both [CRs](#) and [VRs](#) are designed to minimize contamination from
 1807 the [BSM](#) process being searched for. This is desirable because signal con-
 1808 tamination in a [CR](#) can lead to an overestimate of the [SM](#) background in
 1809 the [SR](#), disguising a genuine signal as background. Contamination in a [VR](#),
 1810 where background estimates are being validated, can make it appear that
 1811 the [SM](#) background is not well described by an estimate, causing analyzers
 1812 to adjust the method to account for the difference, and again, disguising
 1813 the effect of the same signal in the [SR](#).

1814 The strategy for estimating the [FS](#) backgrounds, for example, depends
 1815 on a series of [CRs](#) and [VRs](#) depicted in [Figure 59](#). One estimate, the fla-
 1816 vor symmetry method, takes data from CR-FS, a different-flavor region with
 1817 slightly wider $m_{\ell\ell}$ bounds than the [SR](#), and uses these events to predict
 1818 the contribution of flavor symmetric processes to SRZ. An independent
 1819 method called a sideband fit uses a control region CRT to measure the
 1820 flavor symmetric events outside of the Z mass window, and uses [MC](#) to
 1821 extrapolate inside the Z mass window to SRZ. Then, both methods are
 1822 validated at lower E_T^{miss} with an otherwise identical series of regions, with
 1823 VRS corresponding to SRZ, VRT corresponding to CRT, and VR-FS corre-
 1824 sponding to CR-FS.

1825 Each background estimation requires its own set of these regions, and
 1826 the full list of regions used in this analysis can be seen in [Table 7](#). In ad-
 1827 dition to the Flavor Symmetric ([FS](#)) regions described above, there is one
 1828 more [CR](#), CR- γ , which is a photon region used to predict the number of
 1829 $Z/\gamma^* + \text{jets}$ events, a process described in [Section 10.2](#). Additional [VRs](#),

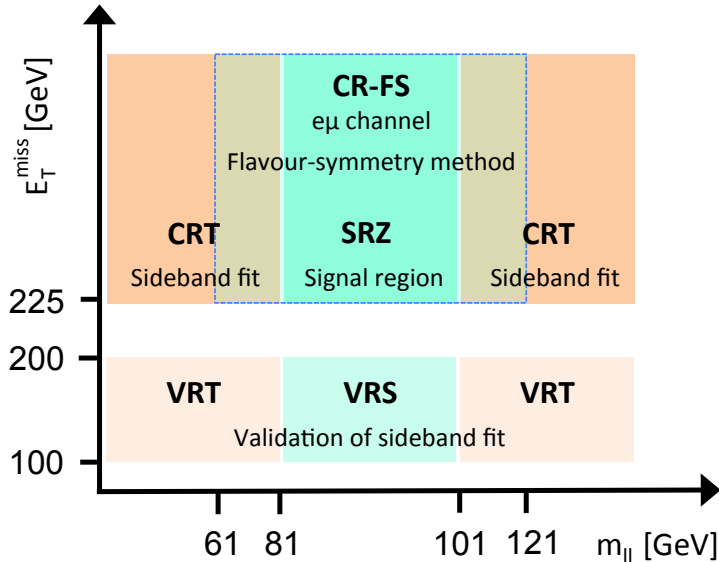


Figure 59: Schematic diagrams of the control, validation and signal regions for the on-shell Z (top) and edge (bottom) searches. For the on-shell Z search the various regions are shown in the $m_{\ell\ell} - E_T^{\text{miss}}$ plane, whereas in the case of the edge search the signal and validation regions are depicted in the $H_T - E_T^{\text{miss}}$ plane.

1830 VR-ZZ, VR-WZ, and VR-3L, are introduced in order to validate the back-
 1831 grounds taken directly from MC. There are several additional regions used,
 1832 for example, in the estimation of the fakes and $Z/\gamma^* + \text{jets}$ backgrounds,
 1833 that are defined in their respective sections.

1834 **9.1 TRIGGER STRATEGY**

1835 In order to collect data for the analysis, triggers must be chosen that pro-
 1836 vide good efficiency in each of the SR, VR, and CRs. This analysis primarily
 1837 depends on triggers on leptons, which are required in nearly every region.
 1838 To simplify the application of trigger scalefactors, which correct MC yields
 1839 for a given trigger to match the data efficiencies, events are broken down
 1840 into a series of kinematic ranges, each with a designated trigger. These
 1841 regions can be seen in Table 8.

1842 In kinematic regions where single lepton triggers are fully efficient, they
 1843 are preferentially used. In lower- p_T ranges, dilepton triggers are used, tar-
 1844 geting either ee , $\mu\mu$, or $e\mu$ events. Electron triggers are selected over muon
 1845 triggers when possible because they have higher efficiencies in most cases.

1846 In CR- γ , there are no leptons, so an alternate trigger strategy must be
 1847 used. Section 10.2.1 describes this triggering scheme, which includes a
 1848 combination of prescaled and unprescaled photon triggers to allow for the
 1849 collection of low- p_T $\gamma + \text{jets}$ events.

Table 7: Overview of all signal, control and validation regions used in the on-shell Z search. More details are given in the text. The flavour combination of the dilepton pair is denoted as either “SF” for same-flavour or “DF” for different flavour. All regions require at least two leptons, unless otherwise indicated. In the case of CR γ , VR-WZ, VR-ZZ, and VR-3L the number of leptons, rather than a specific flavour configuration, is indicated. The main requirements that distinguish the control and validation regions from the signal region are indicated in bold. Most of the kinematic quantities used to define these regions are discussed in the text. The quantity $m_T(\ell_3, E_T^{\text{miss}})$ indicates the transverse mass formed by the E_T^{miss} and the lepton which is not assigned to either of the Z-decay leptons.

On-shell Z regions	E_T^{miss} [GeV]	H_T [GeV]	n_{jets}	$m_{\ell\ell}$ [GeV]	SF/DF	$\Delta\phi(\text{jet}_{12}, p_T^{\text{miss}})$	$m_T(\ell_3, E_T^{\text{miss}})$ [GeV]	$n_{\text{b-jets}}$
Signal region								
SRZ	> 225	> 600	≥ 2	$81 < m_{\ell\ell} < 101$	SF	> 0.4	—	—
Control regions								
CRZ	< 60	> 600	≥ 2	$81 < m_{\ell\ell} < 101$	SF	> 0.4	—	—
CR-FS	> 225	> 600	≥ 2	61 < $m_{\ell\ell}$ < 121	DF	> 0.4	—	—
CRT	> 225	> 600	≥ 2	> 40 , $m_{\ell\ell} \notin [81, 101]$	SF	> 0.4	—	—
CR γ	—	> 600	≥ 2	—	$0\ell, 1\gamma$	—	—	—
Validation regions								
VRZ	< 225	> 600	≥ 2	$81 < m_{\ell\ell} < 101$	SF	> 0.4	—	—
VRT	100–200	> 600	≥ 2	> 40 , $m_{\ell\ell} \notin [81, 101]$	SF	> 0.4	—	—
VRS	100–200	> 600	≥ 2	$81 < m_{\ell\ell} < 101$	SF	> 0.4	—	—
VR-FS	100–200	> 600	≥ 2	61 < $m_{\ell\ell}$ < 121	DF	> 0.4	—	—
VR-WZ	100–200	—	—	—	3 ℓ	—	< 100	0
VR-ZZ	< 100	—	—	—	4 ℓ	—	—	0
VR-3L	60–100	> 200	≥ 2	$81 < m_{\ell\ell} < 101$	3 ℓ	> 0.4	—	—

Lepton p_T	Trigger in 2015	Trigger in 2016
Di-electron channel		
$p_T(e_1) > 65 \text{ GeV}$	HLT_e60_lhmedium	HLT_e60_lhmedium_nod0
$p_T(e_1) \leq 65 \text{ GeV}$	HLT_2e17_lhloose	HLT_2e17_lhvloose_nod0
Di-muon channel		
$p_T(\mu_1) > 52.5 \text{ GeV}$	HLT_mu50	HLT_mu50
$p_T(\mu_1) \leq 52.5 \text{ GeV}$	HLT_mu24_mu8noL1	HLT_2mu14_nomucomb
Electron-muon channel		
$p_T(e) > 65 \text{ GeV}$	HLT_e60_lhmedium	HLT_e60_lhmedium_nod0
$p_T(e) \leq 65 \text{ GeV}$ and $p_T(\mu) > 52.5 \text{ GeV}$	HLT_mu50	HLT_mu50
$p_T(e) \leq 65 \text{ GeV}$ and $p_T(\mu) \leq 52.5 \text{ GeV}$ and $p_T(e) < p_T(\mu)$	HLT_e7_lhmedium_mu24	HLT_e7_lhmedium_nod0_mu24
$p_T(e) \leq 65 \text{ GeV}$ and $p_T(\mu) \leq 52.5 \text{ GeV}$ and $p_T(\mu) < p_T(e)$	HLT_e17_lhloose_mu14	HLT_e17_lhloose_nod0_mu14

Table 8: Lepton trigger requirements used for the analysis in different regions of lepton- p_T phase space.

1850 9.2 SIGNAL EFFICIENCY AND CONTAMINATION

1851 Using the simplified models discussed in [Section 2.2.3](#), the contributions
 1852 of potential signals in these regions can be studied. In the [SR](#), the goal
 1853 is to include as much of the potential signal as possible, while excluding
 1854 as much [SM](#) background as possible. [Figure 60](#) shows the acceptance and
 1855 efficiency for the simplified models at different mass points. Acceptance
 1856 is defined as the fraction of signal events that produce signatures that
 1857 kinematically match the [SR](#), while the efficiency is the fraction of these
 1858 events expected to be correctly identified by the ATLAS detector.

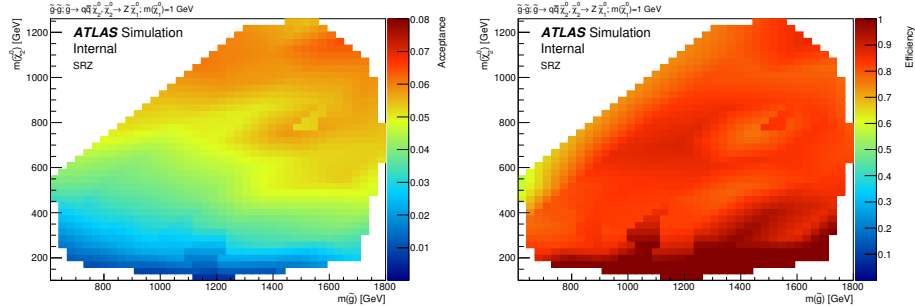


Figure 60: Signal region acceptance (left) and efficiency (right) in SRZ for the simplified model with gluino pair production with $\tilde{\chi}_2^0$ decays to $\tilde{\chi}_1^0$ and an on-shell Z boson with 1GeV neutralino LSP. Acceptance is calculated by applying the signal-region kinematic requirements to truth objects in [MC](#), which do not suffer from identification inefficiencies or measurement resolutions.

1859 A similar test is done for the main [CRs](#) and [VRs](#) which estimates their sus-
 1860 ceptibility to signal contamination. Figures [61](#) and [62](#) show the fraction of
 1861 events in these regions expected to come from signal for different points
 1862 on the simplified model's mass grid. Contamination is highest in VRS, at

1863 low $m_{\tilde{g}}$. However, past analyses have already excluded most models with
 1864 $m_{\tilde{g}} < 800$ GeV, so these regions are not important targets for this search
 1865 [1].

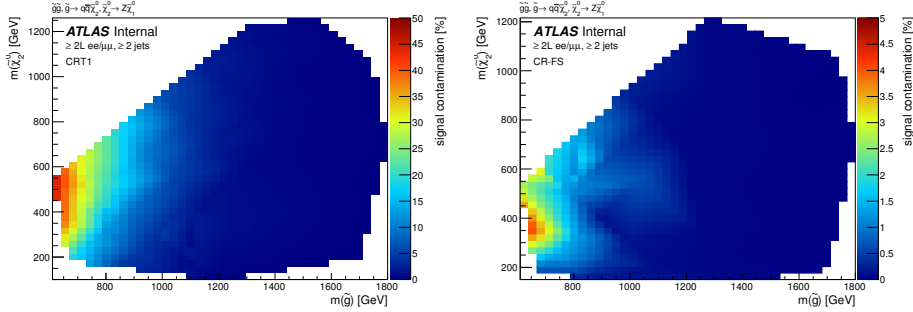


Figure 61: Expected signal contamination in CRT (left) and CR-FS (right) for the signal model with gluino pair production, where the gluinos decay to quarks and a neutralino, with the neutralino subsequently decaying to a Z boson and a 1GeV neutralino LSP.

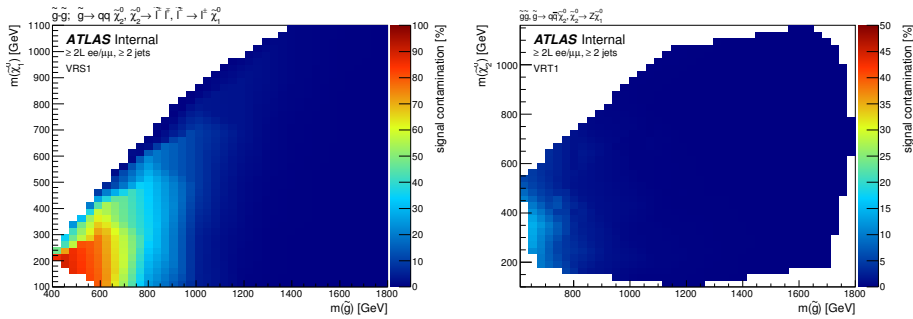


Figure 62: Expected signal contamination in VRS (left) and VRT (right) for the signal model with gluino pair production, where the gluinos decay to quarks and a neutralino, with the neutralino subsequently decaying to a Z boson and a 1GeV neutralino LSP.

1866
1867 BACKGROUND ESTIMATION

1868 This analysis requires two leptons that reconstruct to a Z mass, jets, E_T^{miss} ,
1869 and H_T . Any standard model processes that produce this signature will
1870 appear as a background to the search. The most important task of the
1871 analysis is to identify and estimate these backgrounds, so that any excess
1872 of events appearing on top of the standard model background can be iden-
1873 tified. The main backgrounds for this analysis are described in [Chapter 7](#).
1874 The largest background is from flavor symmetric processes, with smaller
1875 contributions coming from diboson processes, $Z/\gamma^* + \text{jets}$, rare top pro-
1876 cesses, and fake and non-prompt leptons.

1877 10.1 FLAVOR SYMMETRIC PROCESSES

1878 Flavor Symmetric ([FS](#)) backgrounds include any processes that produce
1879 pairs of leptons with uncorrelated flavor in the final state. In this analysis,
1880 the largest contribution comes from $t\bar{t}$, with additional events from pro-
1881 cesses like WW and $Z \rightarrow \tau\tau$. In these processes, each lepton comes from
1882 a different decay. Unlike a $Z \rightarrow \ell\ell$ decay then, these leptons' flavors are
1883 completely independent.

1884 10.1.1 *Flavor Symmetry Method*

1885 As a consequence of the independence of the lepton flavors, any [FS](#) process
1886 should produce ee , $\mu\mu$, and $e\mu$ events in a 1:1:2 ratio. This ratio is taken
1887 advantage of in the flavor symmetry method by measuring $e\mu$ events in
1888 data and using them to predict the contribution of these processes in the
1889 ee and $\mu\mu$ channels. [1]

1890 To estimate the number of events in SRZ, a control region called CR-FS is
1891 used. Both regions are defined in [Table 7](#). CR-FS is very similar to SRZ with
1892 two changes: it requires different-flavor leptons instead of the same-flavor
1893 leptons required by SRZ, and the $m_{\ell\ell}$ range it covers has been expanded
1894 by a factor of three, now ranging from 61 to 121 GeV. The expansion of the
1895 $m_{\ell\ell}$ window is done to increase the number of events in the control region,
1896 thus lowering the statistical uncertainty of the prediction¹.

1897 This control region is expected to be about 95% pure in [FS](#) processes,
1898 with most of the remaining events coming from fake or non-prompt lep-

¹ Though this statistical uncertainty is no longer dominant for the analysis, the method was developed for a smaller dataset for which this expansion dramatically decreased the total uncertainty on the background prediction. [75] Because of previous excesses seen, the signal region was not reoptimized for the larger dataset used in this search, but in future iterations of this analysis, the signal region will likely have tighter cuts, making this decreased statistical uncertainty significant once again.

tons. The **FS** portion is made up primarily of $t\bar{t}$ ($\sim 80\%$), with additional contributions from Wt ($\sim 10\%$), WW ($\sim 10\%$), and $< 1\% Z \rightarrow \tau\tau$.

After the number of data events are measured in CR-FS, correction factors are applied to account for trigger efficiencies, selection efficiencies, the $m_{\ell\ell}$ expansion, and the purity of the control region. Combining these factors, the estimate for number of events in the ee and $\mu\mu$ channels is as follows:

$$N_{ee}^{\text{est}} = \frac{1}{2} \cdot f_{\text{FS}} \cdot f_{Z\text{-mass}} \cdot \sum_{i=1}^{N_{e\mu}^{\text{data}}} k_e(p_T^\mu, \eta^\mu) \cdot \alpha(p_T^{\ell_1}, \eta^{\ell_1}), \quad (30)$$

$$N_{\mu\mu}^{\text{est}} = \frac{1}{2} \cdot f_{\text{FS}} \cdot f_{Z\text{-mass}} \cdot \sum_{i=1}^{N_{e\mu}^{\text{data}}} k_\mu(p_T^e, \eta^e) \cdot \alpha(p_T^{\ell_1}, \eta^{\ell_1}), \quad (31)$$

where $N_{e\mu}^{\text{data}}$ is the number of data events observed in CR-FS, f_{FS} is the **FS** purity in CR-FS, $f_{Z\text{-mass}}$ is the fraction of events in the widened $m_{\ell\ell}$ range expected to be in the on- Z range (taken from $t\bar{t}$ MC), $k_e(p_T, \eta)$ and $k_\mu(p_T, \eta)$ are relative selection efficiencies for electrons and muons, calculated in bins of p_T and η of the lepton to be replaced, and $\alpha(p_T, \eta)$ accounts for the different trigger efficiencies for events in each channel, binned based on the kinematics of the leading lepton. These k and α factors are calculated from data in an inclusive on- Z selection ($81 < m_{\ell\ell}/\text{GeV} < 101$, ≥ 2 jets), according to:

$$k_e(p_T, \eta) = \sqrt{\frac{N_{ee}^{\text{meas}}}{N_{\mu\mu}^{\text{meas}}}} \quad (32)$$

$$k_\mu(p_T, \eta) = \sqrt{\frac{N_{\mu\mu}^{\text{meas}}}{N_{ee}^{\text{meas}}}} \quad (33)$$

$$\alpha(p_T, \eta) = \frac{\sqrt{\epsilon_{ee}^{\text{trig}}(p_T, \eta) \times \epsilon_{\mu\mu}^{\text{trig}}(p_T, \eta)}}{\epsilon_{e\mu}^{\text{trig}}(p_T, \eta)} \quad (34)$$

where $\epsilon_{ee/\mu\mu}^{\text{trig}}$ is the trigger efficiency² and $N_{ee/\mu\mu}^{\text{meas}}$ is the number of $ee/\mu\mu$ events in the inclusive on- Z region described above. Here $k_e(p_T, \eta) = 1/k_\mu(p_T, \eta)$, and this k factor is calculated separately for leading and sub-leading leptons, and the appropriate k value is selected based on which of the leptons is to be replaced.

Electron, muon, and trigger efficiencies are all quite close to one, and as a consequence, these correction factors are typically within 10% of unity, except in the region $|\eta| < 0.1$ where, because of the lack of coverage of the muon spectrometer, they are up to 50% from unity.

² This efficiency is defined by taking all events in the inclusive on- Z selection mentioned above and determining the fraction that passes the relevant trigger requirement defined by [Table 8](#). Because the offline selection made on these events already has some trigger dependence, this calculation of efficiency could be slightly biased. This effect is considered in [Section 11.1.1](#), and the uncertainty applied to the estimate as a result is described.

Region	ee prediction	$\mu\mu$ prediction	combined prediction
SRZ	16.50 ± 2.11	16.67 ± 2.04	33.16 ± 3.94
VRS	49.70 ± 4.61	49.60 ± 4.56	99.31 ± 8.47

Table 9: Yields in signal and validation regions for the flavor symmetric background. Errors include statistical uncertainty, uncertainty from MC closure, uncertainty from the k and α factors, uncertainty due to deriving triggers efficiencies from a DAOD, and uncertainty on the MC shape used to correct for the $m_{\ell\ell}$ expansion.

1924 The estimate is corrected for contamination of non-**FS** backgrounds in
 1925 CR-**FS**. A scaling factor is determined by subtracting these backgrounds
 1926 from the number of $e\mu$ events measured in CR-**FS**, then determining the
 1927 fraction of the original data events that this pure-**FS** number represents.
 1928 The estimate for the non-**FS** backgrounds is taken from **MC** for all processes
 1929 except fakes, which are predicted from data using the matrix method de-
 1930 scribed in [Section 10.3](#).

1931 A prediction is made both for the signal region, SRZ, and the lower- E_T^{miss}
 1932 validation region, VRS. This process is performed separately for the two
 1933 data taking periods, 2015 and 2016, because of the changing triggers and
 1934 conditions. The results are then summed together, as shown in [Table 9](#).
 1935 The uncertainties in this table are discussed in [Section 11.1.1](#).

1936 10.1.2 Sideband Fit Method

1937 As a crosscheck to the flavor symmetry method, a **MC**-based method is
 1938 used. This method is called a *sideband fit*, and it begins with a **MC** estimate
 1939 of the signal region across an $m_{\ell\ell}$ range that includes all values above 40
 1940 GeV. This region, excluding the on-Z range that makes up the **SR**, is used
 1941 as a control region, defined as CRT in [Table 7](#).

1942 The total data yield is measured in CRT, and the **MC** is fit to match this
 1943 yield with one normalization factor which scales the overall $t\bar{t}$ background.
 1944 As mentioned in the previous section, $t\bar{t}$ is the dominant **FS** background,
 1945 making up about 80% of the total events. All other backgrounds contribut-
 1946 ing to this control region are constrained by their uncertainties, which are
 1947 used as nuisance parameters in the fit. The normalization factor from this
 1948 fit is then applied to the $t\bar{t}$ **MC** yield in the **SR**, and combined with the **MC**
 1949 predictions of the other **FS** processes in the **SR** to give a final estimate of
 1950 this background. The results of the fit can be seen in [Table 10](#).

1951 The method is repeated in VRS to validate the method. The normal-
 1952 ization factors, listed in [Table 11](#), are significantly different for the two
 1953 regions. This is expected because there is a known problem in which the
 1954 $t\bar{t}$ **MC** over-predicts the high- E_T^{miss} tail. This effect can be seen in a data-**MC**
 1955 comparison in [Figure 63](#). This is likely due to a mismodeling of the top
 1956 quark p_T distribution, which does not match the spectrum seen in data [76,

BACKGROUND ESTIMATION

channel	$ee/\mu\mu$ CRT	$ee/\mu\mu$ SRZ	ee SRZ	$ee/\mu\mu$ SRZ
Observed events	273	60	35	25
Fitted bkg events	272.76 ± 16.88	49.33 ± 8.04	27.09 ± 4.73	22.70 ± 3.80
Fitted flavour symmetry events	236.96 ± 21.66	28.96 ± 7.47	16.41 ± 4.33	12.55 ± 3.29
Fitted WZ/ZZ events	4.03 ± 1.13	14.27 ± 4.45	7.81 ± 2.45	6.46 ± 2.07
Fitted SHERPA Z/γ^* + jets events	1.95 ± 0.14	0.00 ± 0.00	0.00 ± 0.00	0.00 ± 0.00
Data-driven Z/γ^* + jets (γ + jets) events	0.00 ± 0.00	3.10 ± 2.25	$1.02^{+1.25}_{-1.02}$	2.08 ± 1.38
Fitted rare top events	4.04 ± 1.04	2.90 ± 0.76	1.39 ± 0.38	1.50 ± 0.40
Data-driven fake lepton events	25.78 ± 14.26	$0.10^{+0.18}_{-0.10}$	0.46 ± 0.45	0.10 ± 0.01
MC exp. SM events	366.71	61.01	33.73	27.74
MC exp. flavour symmetry events	331.32	40.72	23.09	17.63
MC exp. WZ/ZZ events	4.02	14.20	7.77	6.43
MC exp. SHERPA Z/γ^* + jets events	1.94	0.00	0.00	0.00
Data-driven exp. Z/γ^* + jets (γ + jets) events	0.00	3.10	1.02	2.08
MC exp. rare top events	4.04	2.89	1.39	1.50
Data-driven exp. fake lepton events	25.39	0.10	0.46	0.10

Table 10: Background fit results from the sideband fit method. The $t\bar{t}$ MC's normalization is taken as a free parameter in the fit to data in CRT, then that normalization factor is applied in SRZ. The results are shown here both divided between the ee and $\mu\mu$ channels and summed together. All other backgrounds are taken from MC in CRT, while in SRZ, the Z/γ^* + jets contribution is taken from the γ + jets method. The uncertainties quoted include both statistical and systematic components.

1957 77]. However, this method corrects for this mismodeling by performing fits
1958 in regions very kinematically similar to the signal region.

Fit region	$t\bar{t}$ normalization
CRT	0.64 ± 0.18
VRT	0.80 ± 0.09

Table 11: Summary of the $t\bar{t}$ normalization factors calculated by the sideband fit to CRT and VRT for the 2015+2016 data.

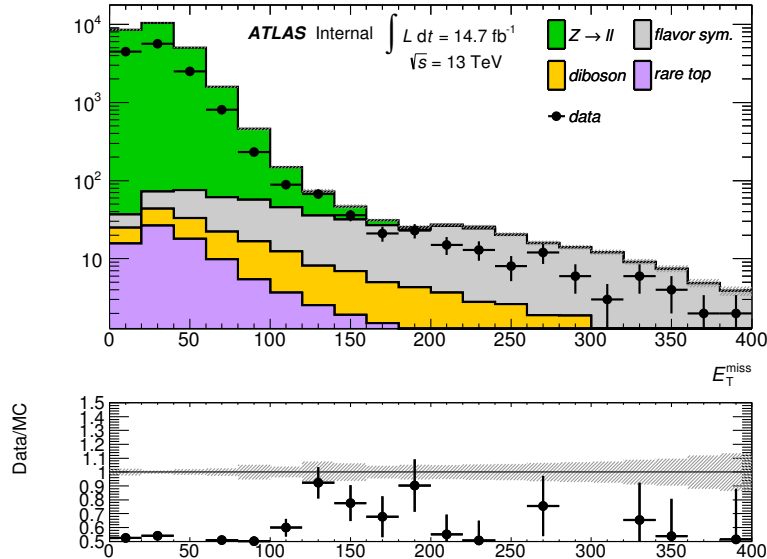


Figure 63: Comparison of data and MC in a selection like SRZ, without the E_T^{miss} cut.

1959 This method is extremely effective as a crosscheck because it uses a com-
1960 pletely independent dataset from the flavor symmetry method, and the
1961 two methods have very little overlap in dependence on MC. They produce
1962 consistent results in both SRZ and VRS, as shown in Table 12.

1963 10.2 Z/γ^* + JETS BACKGROUND

1964 The Z/γ^* + jets background is mainly produced by a process called Drell-
1965 Yan in which annihilating quark/anti-quark pairs produce a Z boson or
1966 a virtual photon. These bosons then decay to two leptons, which, in the
1967 case of the Z boson, naturally appear in the Z-mass window. The bo-
1968 son typically recoils off a hadronic system, which can satisfy the jet and
1969 H_T requirement in SRZ. However, this process rarely produces real E_T^{miss}
1970 (though occasionally neutrinos do appear in its hadronic decays), so most
1971 events with large amounts of E_T^{miss} are the result of extreme mismeasure-
1972 ment. Because SRZ cuts on the very high E_T^{miss} tails of a Z distribution, a
1973 small change in the assumptions about jet resolution or energy scale in MC

Region	Flavour-symmetry	Sideband fit
SRZ	33 ± 4	29 ± 7
VR-S	99 ± 8	92 ± 25

Table 12: Comparison of FS background predictions from the nominal method, the flavor symmetry method, and the cross-check, the sideband fit method. Uncertainties include statistical and systematic uncertainties in both cases.

1974 can drastically change the prediction, and a low $Z/\gamma^* + \text{jets}$ prediction
 1975 can result in a signal-like peak appearing in the final result.

1976 Because of this volatility in the MC prediction in these high E_T^{miss} tails, a
 1977 data-driven method is used to estimate this background. The method uses
 1978 $\gamma + \text{jets}$ events which, like the $Z/\gamma^* + \text{jets}$ events, contain one boson recoil-
 1979 ing against a hadronic system. These $\gamma + \text{jets}$ events are then corrected for
 1980 the kinematic differences between γ and Z s [20, 78]. The sample of $\gamma + \text{jets}$
 1981 events is taken from CR- γ , defined in Table 7. This region is similar to the
 1982 SRZ selection without the E_T^{miss} requirement, but it vetoes events with lep-
 1983 tons and requires at least one photon. Additionally, the $\Delta\phi(\text{jet}_{12}, p_T^{\text{miss}})$ cut
 1984 in SRZ, which is designed to reduce the background from mismeasured
 1985 jets, is removed for this region because of its unpredictability at very low
 1986 values of E_T^{miss} , when the angle of the E_T^{miss} is much less meaningful.

1987 Despite their similarities, there are many theoretical differences between
 1988 γ and Z events. The massive Z boson recoils differently against a jet system
 1989 than the massless photon. Another consequence of its masslessness is that
 1990 photons cannot appear in decays with no jets because such a decay would
 1991 always violate conservation of energy in some frame. As a consequence,
 1992 many kinematic variables have different shapes between the two samples.
 1993 Figure 64 shows a MC comparison of boson p_T between γ and Z events,
 1994 demonstrating the shape differences between the two processes.

1995 The most significant experimental difference between Z and γ events
 1996 is that Z bosons rapidly decay, in the case of this analysis, to two leptons,
 1997 which are then be observed by the ATLAS detector. In contrast, the photon
 1998 is stable, and can be directly detected by ATLAS. This means that the re-
 1999 constructed Z boson and the directly observed photon have very different
 2000 energy resolutions, which can result in different amounts of E_T^{miss} in the
 2001 two events.

2002 Ultimately, the goal of this method is to predict the E_T^{miss} distribution of
 2003 the $Z+\text{jets}$ background. These differences between $Z+\text{jet}$ and $\gamma+\text{jet}$ events
 2004 can be broken down into two categories: differences which affect the jet
 2005 energy and measurement, and differences which affect the boson energy
 2006 and measurement. The differences in the hadronic system are simpler, and
 2007 mostly consist of different numbers and energies of jets between the two
 2008 samples, which can be accounted for via reweighting in a variable that's
 2009 representative of the total energy scale of the event. The differences in the

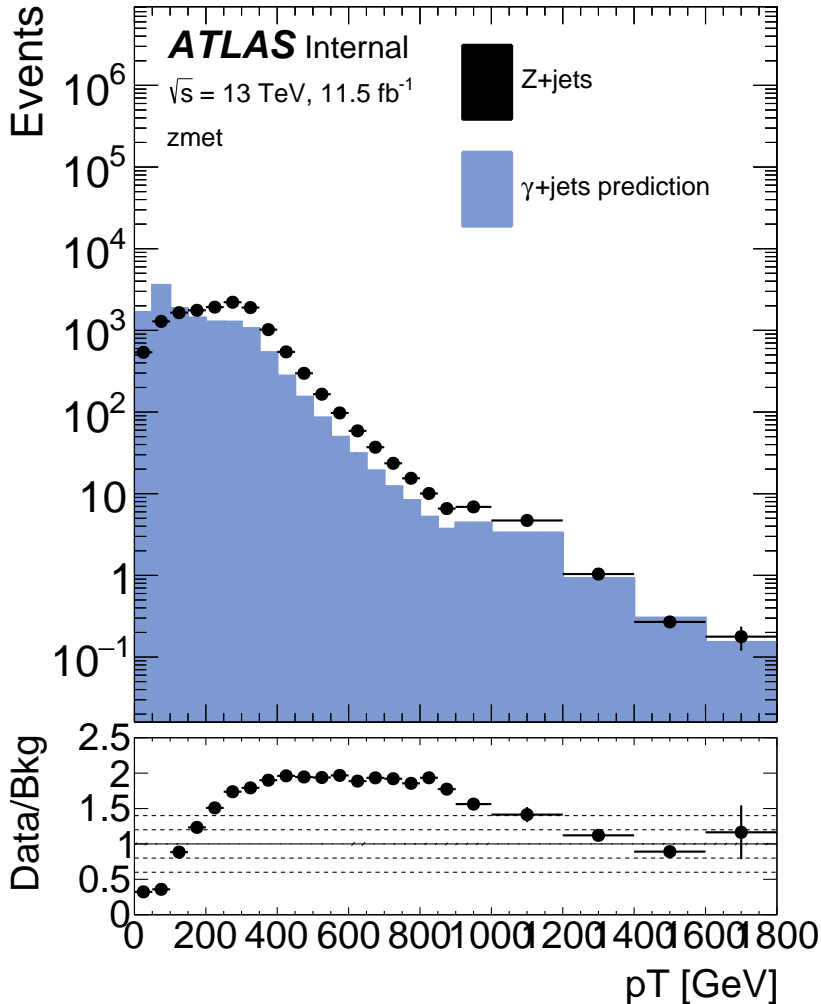


Figure 64: MC comparison of boson p_T in a selection of photon and $Z \rightarrow \ell\ell$ events with $H_T > 600$ GeV.

2010 bosons are more complex, and require the application of smearing func-
 2011 tions based on the different observed objects. Together these corrections
 2012 allow for complete modeling of the $Z/\gamma^* + \text{jets}$ E_T^{miss} spectrum with $\gamma+\text{jet}$
 2013 events.

2014 10.2.1 Photon and Z Event Selection

2015 The baseline photon events come from an inclusive CR with no E_T^{miss} cut,
 2016 a lepton veto, and the requirement of at least one photon, which is called
 2017 CR- γ and defined in Table 7³. This selection is very pure in $\gamma+\text{jet}$ events,
 2018 but some $V\gamma$ events are also included, which can include real E_T^{miss} . These
 2019 backgrounds are subtracted off at the end off the estimation procedure.

³ This region includes an H_T cut, which requires the translation of photon p_T into an equivalent di-lepton p_T scalar sum. This process is described in Section 10.2.4.

2020 The triggering scheme for these events is more complicated than in other
 2021 regions because the lowest unprescaled photon trigger requires a photon
 2022 p_T of at least 120 (140) GeV in 2015 (2016) datataking, but the method re-
 2023 quires events with much lower p_T to predict the full Z -boson p_T spectrum.
 2024 To accomplish this, the lower- p_T photons are broken down into small p_T
 2025 ranges with a different prescaled trigger required in each range, listed in
 2026 [Table 13](#). The events in each selection are then weighted by the prescale
 2027 value of the trigger used to reconstruct a smooth p_T spectrum.

p_T Range [GeV]	Trigger Name
2015 Data-Taking	
$37 < p_T < 45$	HLT_g35_loose_L1EM15
$45 < p_T < 50$	HLT_g40_loose_L1EM15
$50 < p_T < 55$	HLT_g45_loose_L1EM15
$55 < p_T < 125$	HLT_g50_loose_L1EM15
$p_T > 125$	HLT_g120_loose_L1EM15
2016 Data-Taking	
$25 < p_T < 30$	HLT_g20_loose_L1EM12
$30 < p_T < 40$	HLT_g25_loose_L1EM12
$40 < p_T < 45$	HLT_g35_loose_L1EM12
$45 < p_T < 50$	HLT_g40_loose_L1EM12
$50 < p_T < 55$	HLT_g45_loose_L1EM12
$55 < p_T < 65$	HLT_g50_loose_L1EM12
$65 < p_T < 75$	HLT_g60_loose_L1EM12
$75 < p_T < 85$	HLT_g70_loose_L1EM12
$85 < p_T < 105$	HLT_g80_loose_L1EM12
$105 < p_T < 145$	HLT_g100_loose_L1EM12
$p_T > 145$	HLT_g140_loose_L1EM12

Table 13: List of triggers used to collect photon events in 2015 and 2016 data-taking.

2028 These γ events can then be compared to baseline $Z \rightarrow \ell\ell$ events with
 2029 a similar selection. These events have the same dilepton requirements as
 2030 SRZ, without the $m_{\ell\ell}$ cut. They also have no E_T^{miss} cut, but like the photons,
 2031 are required to have $H_T > 600$ GeV as in SRZ.

2032 10.2.2 Smearing of Photon Events

2033 While Z +jet events are measured as a pair of leptons recoiling against
 2034 a hadronic system, γ +jet events are measured only as one object recoil-
 2035 ing against jets. In addition, detector resolution is different for electrons,

2036 muons, and photons. The impact of these differences must be corrected
 2037 for in γ +jet events in order for them to accurately predict the E_T^{miss} distribution
 2038 of the Zs. Luckily, in most cases, the resolution of the photon's p_T
 2039 is better the Z boson's, so the photon events can be smeared to emulate
 2040 the Zs.

2041 To isolate mismeasurement of boson p_T , this method uses $E_{T,\parallel}^{\text{miss}}$, the E_T^{miss}
 2042 projection on an axis defined by the momentum of the boson. Figure 65
 2043 shows the $E_{T,\parallel}^{\text{miss}}$ distribution in MC for the two samples, and demonstrates
 2044 the discrepancies between them. The core of the photon distribution some-
 2045 what similar to the $Z \rightarrow ee$ distribution because, in the high- p_T limit, mea-
 2046 surements of both photons and electrons are primarily taken from the elec-
 2047 tronagnetic calorimeter and should have similar resolutions. For muons,
 2048 which rely only on tracks to determine p_T , the resolution becomes very
 2049 large at high p_T values where the tracks are nearly straight. As a conse-
 2050 quence, the resolutions for photon and $Z \rightarrow \mu\mu$ events are very different.

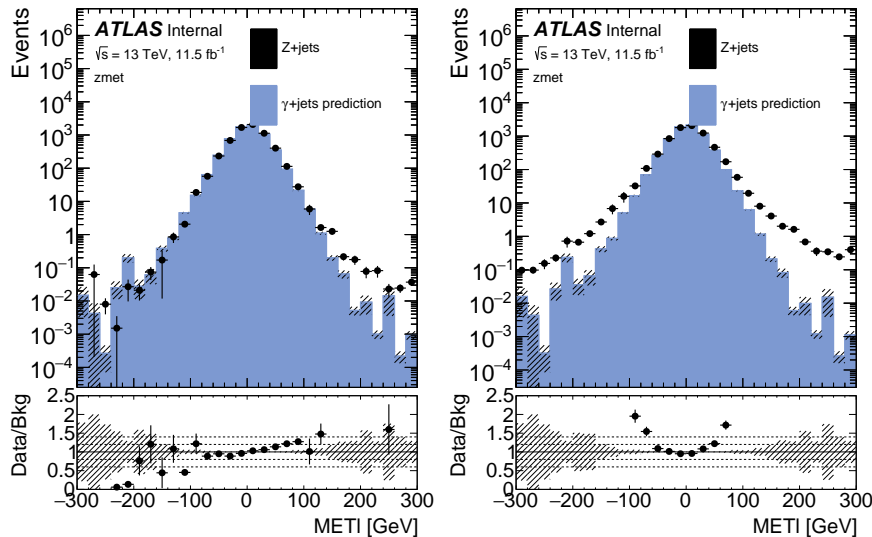


Figure 65: $E_{T,\parallel}^{\text{miss}}$ distributions in MC for $Z + \text{jets}$ ee (left) and $\mu\mu$ (right) channels compared to $\gamma + \text{jets}$ in an inclusive region with $H_T > 600$ GeV.

2051 A function to smear photon events is derived from the deconvolution of
 2052 the photon and lepton response functions, taken from 1-jet CRs with no H_T
 2053 cut, which are otherwise identical to the baseline Z and γ selections. This
 2054 region is chosen because it is orthogonal to the SR, so the resolution can
 2055 be obtained from data as well as MC. In these regions, events are binned
 2056 in boson p_T , and in each bin, a $E_{T,\parallel}^{\text{miss}}$ distribution is made. The smearing
 2057 function is derived for each bin via the deconvolution of the $Z/\gamma^* + \text{jets}$
 2058 and $\gamma + \text{jets}$ distributions.

2059 Next, for each photon event, the smearing function matching the event's
 2060 photon p_T is sampled, yielding a smearing factor Δp_T . The photon's p_T is
 2061 then adjusted according to

$$p_T^{\gamma'} = p_T^\gamma + \Delta p_T \quad (35)$$

2062 and the corresponding change in E_T^{miss} is made,

$$E_{T,\parallel}^{\text{miss}'} = E_{T,\parallel}^{\text{miss}} - \Delta p_T. \quad (36)$$

2063 The nominal smearing function is taken from MC in order to remove con-
 2064 tamination from other backgrounds, and the resulting $E_{T,\parallel}^{\text{miss}}$ distributions
 2065 can be seen in Figure 66. Though there is a small amount of oversmearing
 2066 in the negative tail, the improvement in agreement between the distribu-
 2067 tions is clear.

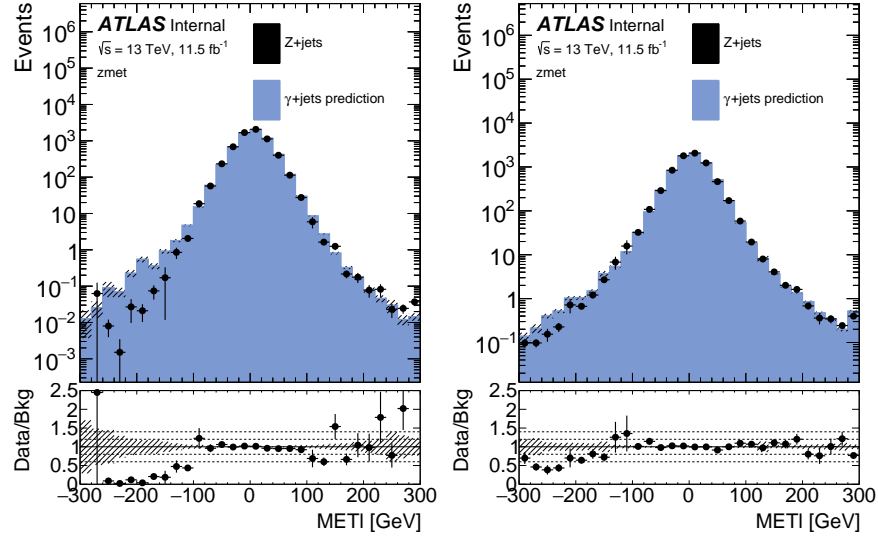


Figure 66: $E_{T,\parallel}^{\text{miss}}$ distributions in MC for Z+jets ee (left) and $\mu\mu$ (right) channels compared to $\gamma + \text{jets}$ in an inclusive region with $H_T > 600 \text{ GeV}$ after the smearing procedure has been performed. These distributions have also been p_T reweighted, as described in Section 10.2.3.

2068 10.2.3 p_T Reweighting of Photon Events

2069 Next, the photon events are reweighted to match the boson p_T of the Z
 2070 events. This is accomplished by making histograms of boson p_T for γ and
 2071 Z events, similar to that in Figure 64, and with binning identical to that
 2072 used in Section 10.2.2. Photons are binned based on their smeared p_T deter-
 2073 mined in the previous step. A reweighting factor $f(p_T)$ is then calculated
 2074 in each bin, according to

$$f(x) = \frac{N_{Z/\gamma^*+\text{jets}}(x)}{N_{\gamma+\text{jets}}(x)} \quad (37)$$

2075 in MC, and in data according to

$$f(x) = \frac{N_{\text{data}}(x) - N_{t\bar{t}}(x) - N_{VV}(x)}{N_{\gamma+\text{jets data}}(x)} \quad (38)$$

2076 where the contamination from other backgrounds is taken from MC and
 2077 subtracted from the Z selection. The resulting reweighting factors can be
 2078 seen in Figure 67 and are calculated independently for ee and $\mu\mu$ events.

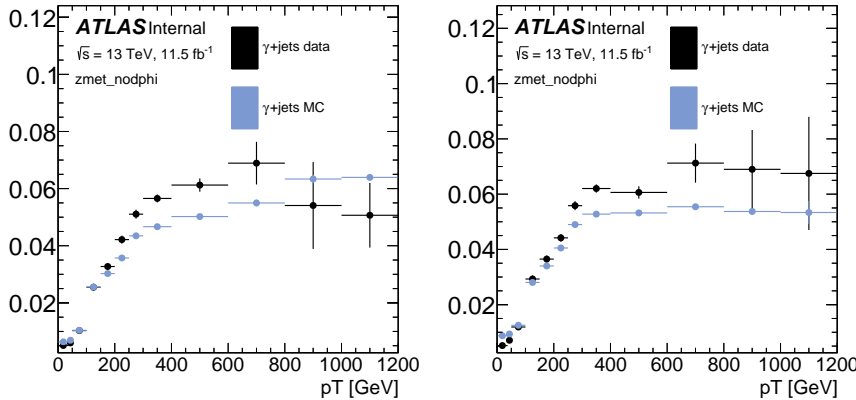


Figure 67: Photon reweighting factors for the ee (left) and $\mu\mu$ (right) channels derived from data and MC.

2079 This reweighting, though it is performed on the boson p_T , primarily
 2080 serves to produce more similar jet distributions between the γ and Z sam-
 2081 ples. Because, excluding E_T^{miss} contributions, the boson p_T must match the
 2082 energy of the jet system off which it recoils, these two variables are closely
 2083 tied. Once the two samples have similar amounts of hadronic energy, the
 2084 E_T^{miss} contribution from mismeasurement of jet energy should also be sim-
 2085 ilar.

2086 Together, the boson smearing and p_T reweighting produce a E_T^{miss} spec-
 2087 trum in the modified photon events that closely match that of the Z events.
 2088 Figures 68 and 69 show the comparison of the E_T^{miss} distributions be-
 2089 fore any alteration, with only p_T reweighting, and after the smearing and
 2090 reweighting, demonstrating the impact of each step. Once the E_T^{miss} distri-
 2091 bution is well described, the $\Delta\phi(\text{jet}_{12}, p_T^{\text{miss}})$ can be applied.

2092 10.2.4 Determining H_T and $m_{\ell\ell}$

2093 One complication thus far ignored is that CR- γ has no leptons, but some
 2094 quantities that define the SR require them, namely H_T (which includes
 2095 the p_T of the two leading leptons) and $m_{\ell\ell}$. Both of these variables are
 2096 determined by creating histograms binned in the boson p_T and sampling.

2097 In the case of H_T , distributions of the scalar sum of the p_T of the leading
 2098 leptons are made for each Z p_T bin. A sampled value from the distribu-
 2099 tion is then added to the H_T of the jets in a photon event to produce the
 2100 final estimate. This sampling is done before any reweighting is performed
 2101 because the H_T is needed to make the preselection for the reweighting
 2102 process. However, the smearing is performed inclusively in H_T , so this
 2103 procedure can be performed using the smeared photon p_T to choose the
 2104 distribution to sample.

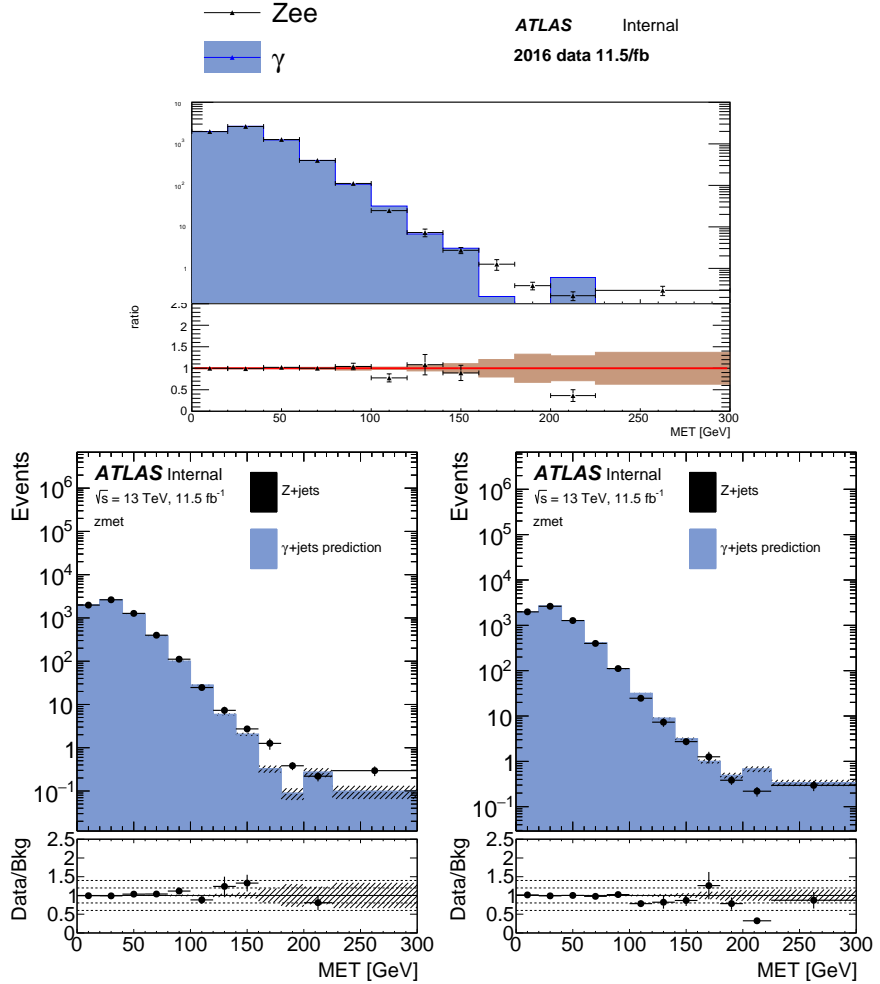


Figure 68: E_T^{miss} distribution comparing MC distributions of photon and Z events before any smearing is applied (top), with only p_T reweighting applied (bottom left), and after p_T reweighting and smearing have both been applied (bottom right) in the ee channel of 2016 data.

2105 The $m_{\ell\ell}$ determination is done after both the smearing and reweighting,
 2106 and is tied closely to the smearing step. Mismeasurements in lepton p_T
 2107 can create E_T^{miss} in a $Z/\gamma^* + \text{jets}$ event, but the same event is likely to mi-
 2108 grate off the Z $m_{\ell\ell}$ window due to the mismeasured lepton. Thus it is very
 2109 important that the two effects be carefully correlated in the manipulated
 2110 photon events. To achieve this, MC Z events from the 1-jet CR described in
 2111 Section 10.2.2 are used to make two-dimensional distributions of $m_{\ell\ell}$ as
 2112 a function of the difference between reconstructed and true Z p_T for the
 2113 ee and $\mu\mu$ channels. A photon event then uses the Δp_T assigned to it dur-
 2114 ing the smearing process to index the distribution, and an $m_{\ell\ell}$ value is
 2115 sampled from the corresponding bin ⁴

⁴ Ideally this Δp_T would also include the difference between the true and reconstructed p_T of the photon events, but this information is of course not accessible in data. Luckily, in the events in the final SR this value is typically negligible compared to the Δp_T from smearing, so the impact is small.

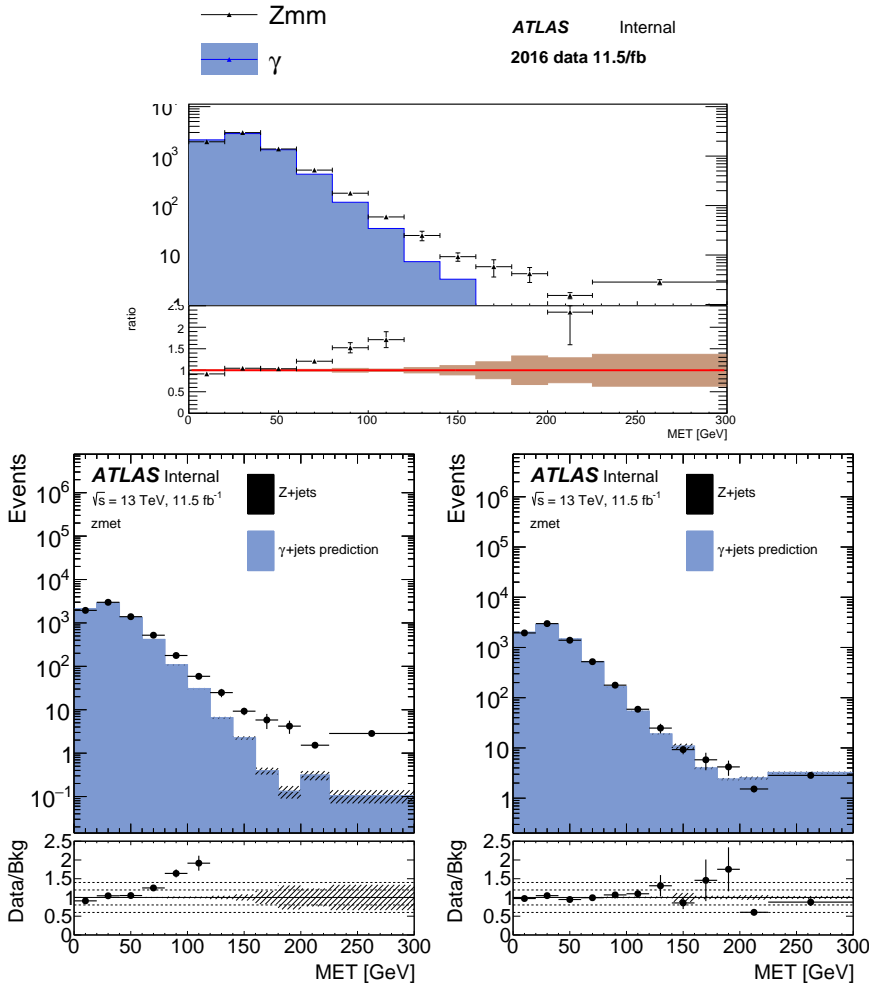


Figure 69: E_T^{miss} distribution comparing MC distributions of photon and Z events before any smearing is applied (top), with only p_T reweighting applied (bottom left), and after p_T reweighting and smearing have both been applied (bottom right) in the $\mu\mu$ channel of 2016 data.

To test the soundness of this procedure, it is repeated purely in MC, and the results of the MC prediction and the data prediction are compared to the $m_{\ell\ell}$ distribution in $Z/\gamma^* + \text{jets}$ MC in Figure 70. After the $m_{\ell\ell}$ distribution has been emulated, a cut requiring that the photon events be “on the Z mass peak” can be required.

10.2.5 Subtraction of $V\gamma$ Events

At high E_T^{miss} , where the signal region lies, contamination of CR- γ with $V\gamma$ events becomes significant, as shown in Figure 71. These events must be subtracted from the $\gamma + \text{jets}$ prediction because, once the photons are corrected to approximate Zs, they essentially provide a (not very accurate) prediction of diboson events, which are already accounted for in another background estimate.

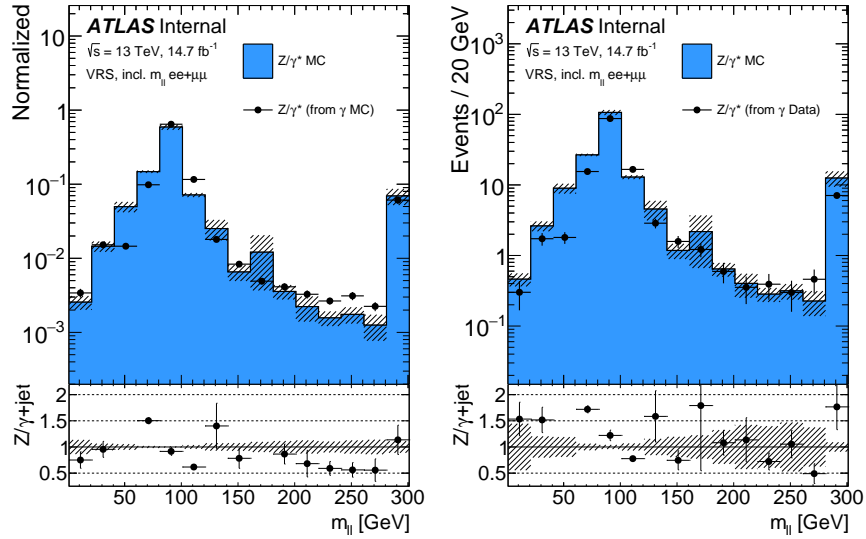


Figure 70: $Z/\gamma^* + \text{jets}$ MC $m_{\ell\ell}$ distribution compared to the prediction from $\gamma + \text{jets}$ method performed on MC (left) and the prediction from $\gamma + \text{jets}$ method performed on data (right).

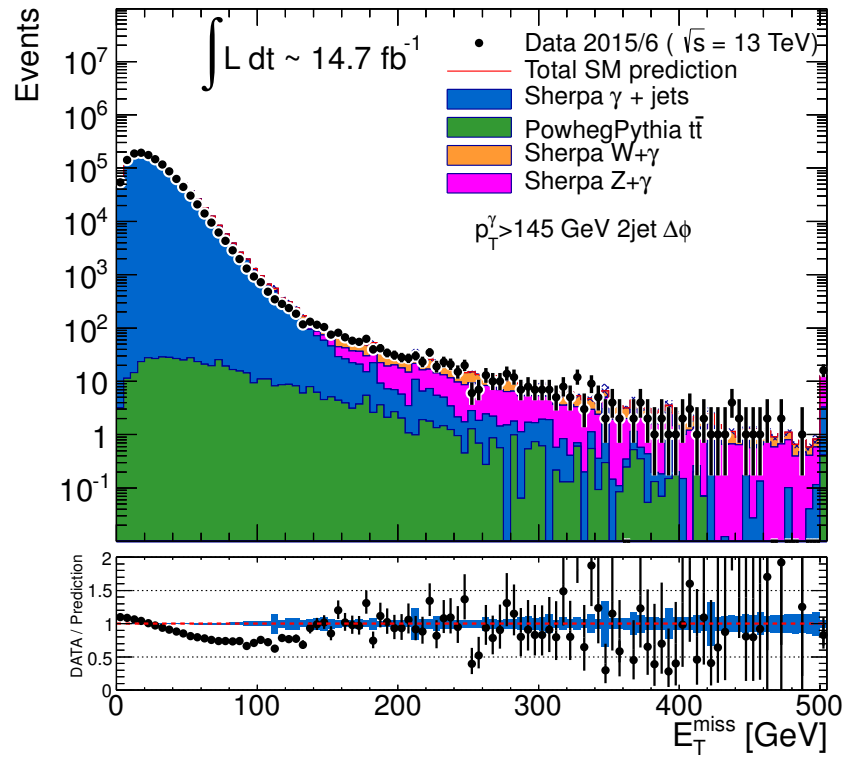


Figure 71: Comparison of data and MC in CR- γ without any H_T cut, including the contributions from various $V\gamma$ processes.

2128 This subtraction accomplished by performing the $\gamma + \text{jets}$ method on $V\gamma$
 2129 MC to approximate these backgrounds' contribution to the final E_T^{miss} dis-
 2130 tribution. This contribution is then subtracted from the $\gamma + \text{jets}$ prediction,

²¹³¹ the impact of which can be seen in [Figure 72](#). As expected, the impact is
²¹³² greatest at high E_T^{miss} where these backgrounds are most significant.

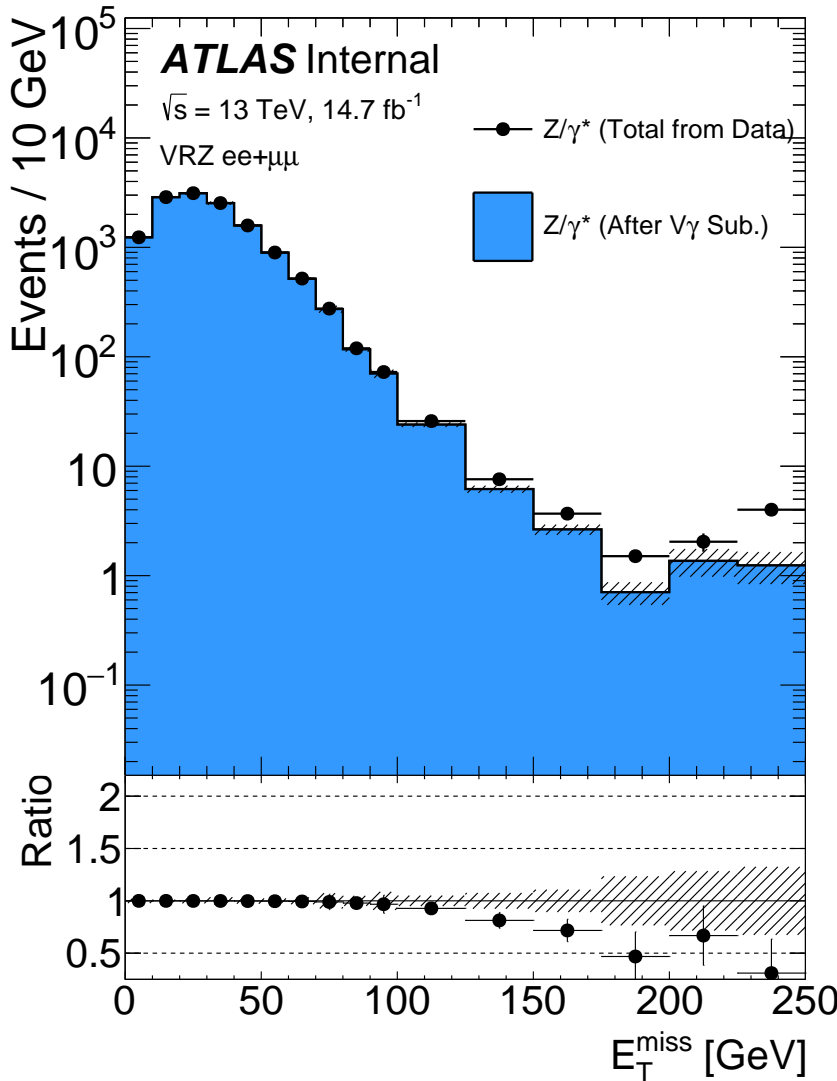


Figure 72: Total $\gamma + \text{jets}$ data prediction in SRZ (excluding the E_T^{miss} cut) and the prediction after the $V\gamma$ subtraction.

²¹³³ 10.2.6 Validation in Data

²¹³⁴ The $\gamma + \text{jets}$ jets method is validated in a region called VRZ, defined in
²¹³⁵ [Table 7](#), which is similar to SRZ, but with an inverted E_T^{miss} cut. [Figure 73](#)
²¹³⁶ shows the low- E_T^{miss} portion of this VR where the $Z/\gamma^* + \text{jets}$ background
²¹³⁷ is dominant. Here, the three data-driven background estimates, as well
²¹³⁸ as the remaining MC backgrounds are stacked and compared to the data
²¹³⁹ yield in this region, demonstrating excellent agreement across a wide E_T^{miss}
²¹⁴⁰ range.

²¹⁴¹ An additional check can be made in VRZ by removing the $\Delta\phi(\text{jet}_{12}, \mathbf{p}_T^{\text{miss}})$
²¹⁴² intended to suppress the $Z/\gamma^* + \text{jets}$ background from jet mismeasurement.

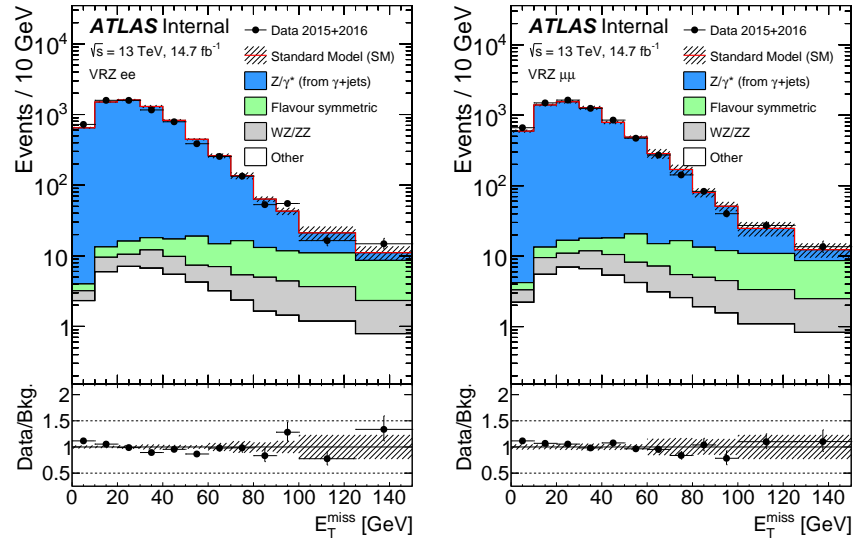


Figure 73: E_T^{miss} distribution in VRZ ee (left) and $\mu\mu$ (right) with total data yield compared to the sum of the prediction from the $\gamma + \text{jets}$ method, the prediction from the flavor symmetry method, the prediction from the fake background estimation (included under “other”), and the remaining backgrounds taken from MC.

2143 Figure 74 shows the distribution of this variable in VRZ, and demonstrates
 2144 that, even at low values where the $Z/\gamma^* + \text{jets}$ background is dominant,
 2145 the $\gamma + \text{jets}$ method models it accurately.

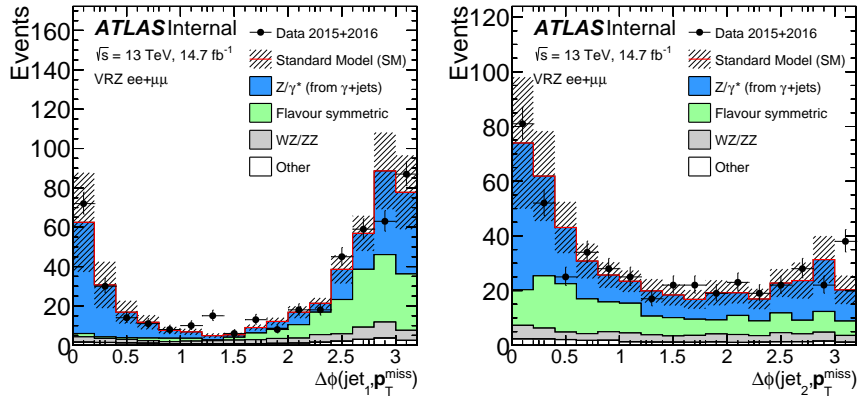


Figure 74: $\Delta\phi(\text{jet}, p_T^{\text{miss}})$ distribution for the leading jet (left) and the subleading jet (right). The comparison is performed in VRZ with the cut on $\Delta\phi(\text{jet}_{12}, p_T^{\text{miss}})$ removed. The total data yield is compared to the sum of the prediction from the $\gamma + \text{jets}$ method, the prediction from the flavor symmetry method, the prediction from the fake background estimation (included under “other”), and the remaining backgrounds taken from MC.

2146 10.3 FAKE AND NON-PROMPT LEPTONS

2147 The *fakes* background consists of processes that produce only one lepton,
 2148 but whose events are otherwise kinematically similar to the [SR](#). These pro-
 2149 cesses include semileptonic $t\bar{t}$, W -jets, and single top processes. Though
 2150 these processes typically only produce one lepton, they can be recon-
 2151 structed with two leptons due to a hadron being misidentified as a lepton
 2152 or due to a real non-prompt lepton resulting from photon conversions or
 2153 B -hadron decays. As with the $Z/\gamma^* + \text{jets}$ background, it is very difficult
 2154 to predict with [MC](#) because the flaws in reconstruction are typically less
 2155 well described by the models used in [MC](#) production than the successes.
 2156 Nonetheless, a rough estimate can be made of this background by using
 2157 [MC](#), which indicates that the number of fake events in SRZ is consistent
 2158 with zero.

2159 Despite the small predicted contribution in the [SR](#), a data-driven method
 2160 called the *matrix method* is employed to estimate these fake events [79]. This
 2161 method is also used to estimate the fakes contribution to other control and
 2162 validation regions where their impact is more significant.

2163 In the matrix method, the quality requirements for signal leptons are
 2164 loosened to give a selection of baseline leptons (see [Table 3](#) and [Table 4](#)),
 2165 which consist of a higher fraction of fake leptons. In each [CR](#), [VR](#), or [SR](#), the
 2166 remaining kinematic selections are made on the baseline leptons, and the
 2167 number of leptons in the region which pass the signal lepton requirements
 2168 (N_{pass}) and the number which fail (N_{fail}) are measured. For a 1-lepton
 2169 selection, these quantities can be used to predict the number of fake events
 2170 that pass the selection according to:

$$N_{\text{pass}}^{\text{fake}} = \frac{N_{\text{fail}} - (1/\epsilon^{\text{real}} - 1) \times N_{\text{pass}}}{1/\epsilon^{\text{fake}} - 1/\epsilon^{\text{real}}}. \quad (39)$$

2171 The efficiencies ϵ^{real} and ϵ^{fake} give the relative identification efficiency
 2172 from baseline to signal for genuine, prompt leptons and fake and non-
 2173 prompt leptons, respectively. For a 2-lepton selection, the principle is the
 2174 same, but the equation is more complicated, requiring a four-by-four ma-
 2175 trix to account for possible combinations of real and fake leptons.

2176 To calculate ϵ^{real} , the tag-and-probe method is performed a selection of
 2177 $Z \rightarrow \ell\ell$ data events, CR-real, described in [Table 14](#). In this method, one *tag*
 2178 lepton passing a signal selection is required, as is another *probe* lepton pass-
 2179 ing a baseline requirement. Distributions in $m_{\ell\ell}$ for events with a tag and
 2180 a passing probe and events with a tag and a failing probe are produced
 2181 and fit, and the efficiency is computed using the ratio acquired from the
 2182 fit. A comparison of data and [MC](#) in CR-real can be seen in [Figure 75](#).

2183 The fake efficiency, ϵ^{fake} , is determined using the tag-and-probe method
 2184 in CR-fake, also described in [Table 14](#). This region is different from all
 2185 other regions considered in this analysis because it requires same-sign lep-
 2186 tons. Very few processes genuinely produce two same-sign leptons, so this
 2187 region is enhanced in fake leptons. An upper limit on $E_{\text{T}}^{\text{miss}}$ is placed on

Fakes regions	E_T^{miss} [GeV]	H_T [GeV]	n_{jets}	$m_{\ell\ell}$ [GeV]	SF/DF	OS/SS	n_{ℓ}
CR-real	–	> 200	≥ 2	81–101	2ℓ SF	OS	2
CR-fake	< 125	–	–	> 12	2ℓ SF/DF	SS	≥ 2

Table 14: Control regions used to measure efficiencies of real and fake leptons. The flavour combination of the dilepton pair is denoted as either “SF” for same-flavour or “DF” for different flavour. The charge combination of the leading lepton pairs are given as “SS” for same-sign or “OS” for opposite-sign.

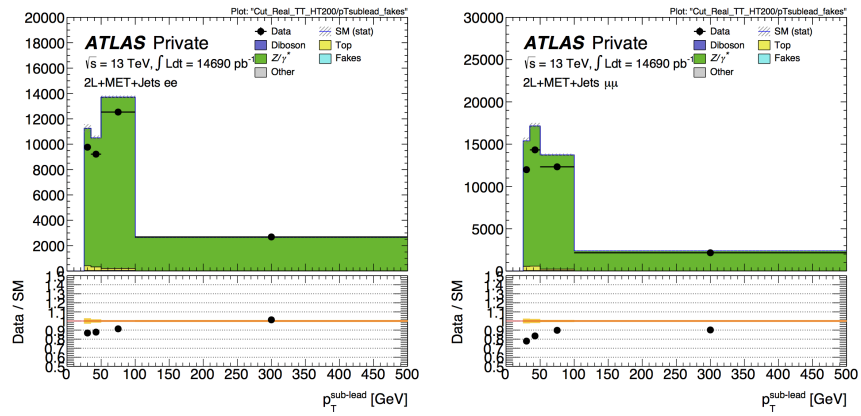


Figure 75: Sub-leading lepton p_T for ee (left) and $\mu\mu$ (right) events in the tight-tight region used to measure the real-lepton efficiency for 2016.

2188 CR-fake to limit the possible contamination from BSM processes. According-
 2189 ing to MC, real, prompt leptons make up about 7% (11%) of the baseline
 2190 electron (muon) sample and about 10% (61%) of the signal electron (muon)
 2191 sample in this region. These real lepton backgrounds are subtracted from
 2192 the CR-fake yields when calculating the efficiencies. Figure 76 shows a
 2193 comparison of data and MC in this region.

2194 This method is validated in a fakes-rich validation region with a same-
 2195 sign lepton requirement, $E_T^{\text{miss}} \geq 50\text{GeV}$, ≥ 2 jets, and a veto on $m_{\ell\ell}$ on
 2196 the Z-mass peak for same flavor channels. The results of this validation
 2197 can be seen in Figure 77. With the systematic uncertainties, discussed in
 2198 Section 11.1.3, the prediction agrees well with the data across a wide range
 2199 of $m_{\ell\ell}$ values.

2200 10.4 DIBOSON AND RARE TOP PROCESSES

2201 The remaining backgrounds are diboson processes (excluding WW, which
 2202 is included in the FS background) and rare top processes. Dibosons events

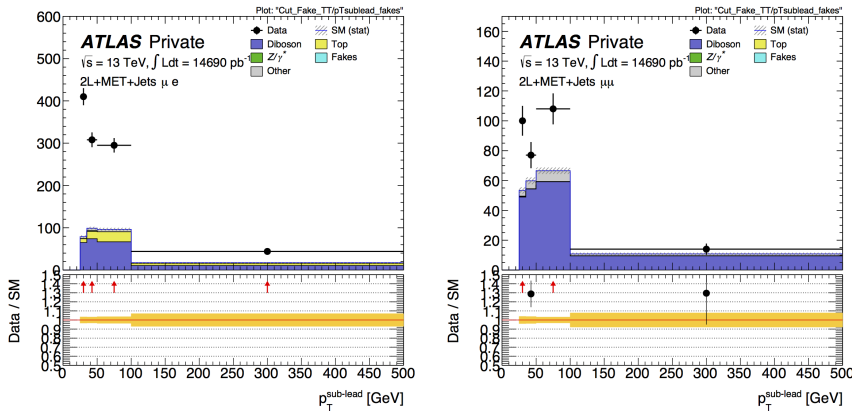


Figure 76: Sub-leading lepton p_T for μe (left) and $\mu \mu$ (right) events in the tight-tight region used to measure the fake-lepton efficiency for 2016.

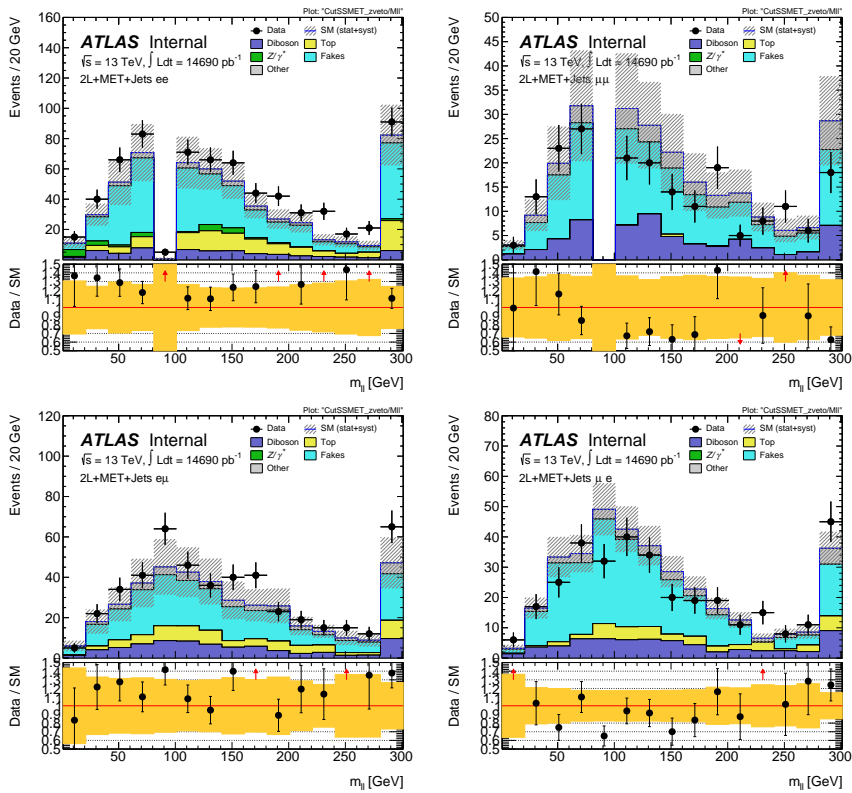


Figure 77: Same sign validation regions in the ee (top left), $\mu\mu$ (top right), $e\mu$ (bottom left) and μe (bottom right) channels combining 2015+2016 data. Uncertainty bands include both statistical and systematic uncertainties.

make up about 30% of the events in SRZ, while rare top process contributions are much smaller. Both are taken directly from MC, with validation regions to confirm the accuracy of the prediction. These regions are described in Table 7, and target different parts of these backgrounds. VR-ZZ is a four-lepton selection designed to select a very pure sample of ZZ events. VR-WZ requires three leptons and makes specific cuts on m_T , the

transverse mass, and E_T^{miss} in order to select mostly $WZ \rightarrow ll\nu\nu$ events. VR-3L is similar to VR-S, but loosens the H_T and E_T^{miss} cuts and requires at least three leptons. This region is designed to target any ≥ 3 -lepton process in a region as kinematically close to SRZ as possible while still maintaining enough events to validate. The makeups of these multilepton validation regions, as well as VRS, are shown in [Table 15](#).

	VR-S	VR-WZ	VR-ZZ	VR-3L
Observed events	236	698	132	32
Total expected background	224 ± 41	613 ± 66	139 ± 25	35 ± 10
Flavour-symmetric	99 ± 8	-	-	-
WZ/ZZ events	27 ± 13	573 ± 66	139 ± 25	25 ± 10
Rare top events	11 ± 3	14 ± 3	0.44 ± 0.11	9.1 ± 2.3
$Z/\gamma^* + \text{jets}$ events	84 ± 37	-	-	-
Fake lepton events	4 ± 4	26 ± 6	-	0.6 ± 0.3

[Table 15](#): Yields in validation regions. In VRS, data-driven background estimates are used for $Z/\gamma^* + \text{jets}$, fakes, and [FS](#) processes. All other backgrounds are taken from [MC](#), including all backgrounds in the multi-lepton [VRS](#). Uncertainties include statistical and systematic components.

To confirm that the kinematics are well modeled in the diboson validation regions, distributions of boson mass and p_T are shown in [MC](#) and data. Figures [78](#) and [79](#) show these distributions for VR-WZ, and [Figure 80](#) shows these distributions for VR-ZZ.

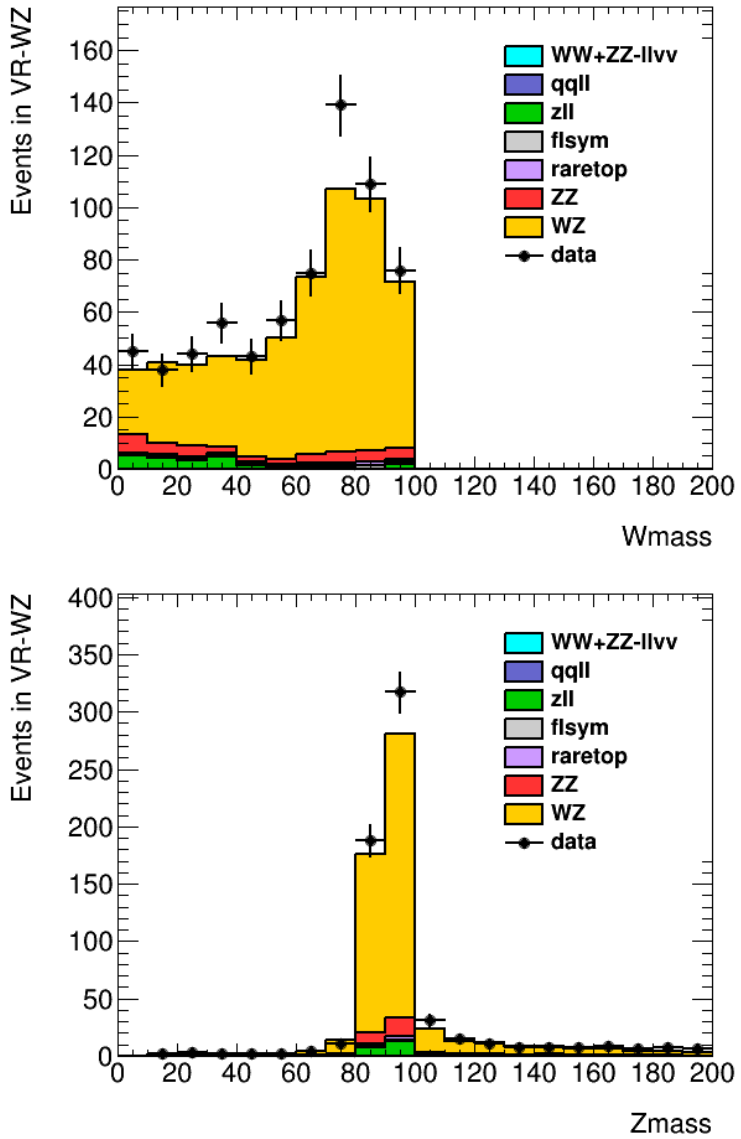


Figure 78: Distribtuions of data and MC in VR-WZ. Reconstructed transverse mass of the W (top) and mass of the Z (bottom).

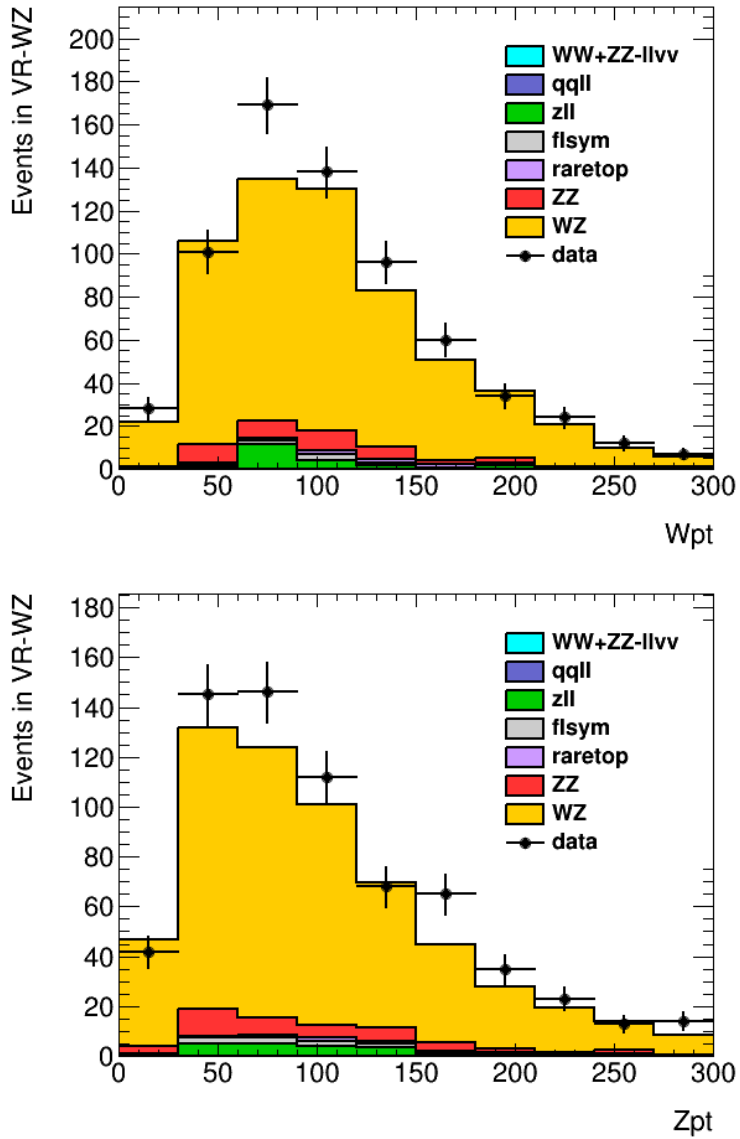


Figure 79: Distributions of data and MC in VR-WZ. p_T of the W (top) and Z (bottom).

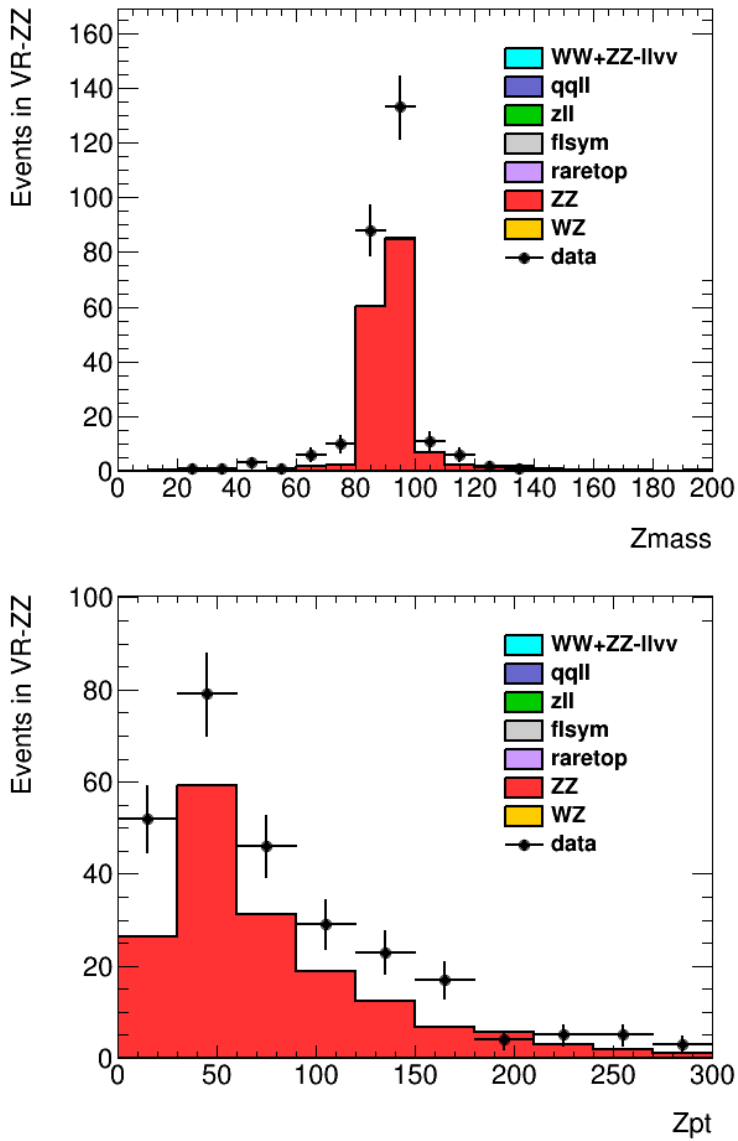


Figure 8o: Distributions in VR-WZ. On the top, mass of the Z bosons in the event, and on the bottom, p_T of the Z bosons.

2219

2220 SYSTEMATIC UNCERTAINTIES

2221 11.1 UNCERTAINTIES ON DATA-DRIVEN BACKGROUNDS

2222 11.1.1 *Uncertainties on the Flavor Symmetry Method*

2223 The flavor symmetry method is a data driven method that makes its esti-
 2224 mate primarily on based events populating an [SR-like CR](#) in the different-
 2225 flavor channel. The statistical uncertainty on these events makes up the
 2226 dominant uncertainty on the method. To reduce this uncertainty, the $m_{\ell\ell}$ range
 2227 on the [CR](#) is expanded, approximately tripling the number of events in [CR-FS](#). The statistical uncertainty is reduced by this expansion, though it is
 2228 still significantly higher than any of the other systematic uncertainties on
 2229 this method, as seen in [Table 16](#). Also included in the statistical uncertainty
 2230 column is the uncertainty on the number of non-[FS](#) events in [CR-FS](#), which
 2231 is used to scale the prediction to account for contamination in the [CR](#).
 2232

Reg.	Ch.	Pred.	Uncertainties					
			stat. clos.	MC and α	k and α	dAOD usage	$m_{\ell\ell}$ shape	total
SRZ	ee	16.50	1.82	0.88	0.53	0.12	0.22	2.11
	$\mu\mu$	16.67	1.83	0.79	0.33	0.11	0.23	2.04
	$ee+\mu\mu$	33.16	3.66	1.07	0.86	0.23	0.45	3.94
VRS	ee	49.70	3.21	2.34	2.20	0.34	0.75	4.61
	$\mu\mu$	49.60	3.14	2.88	1.40	0.31	0.75	4.56
	$ee+\mu\mu$	99.31	6.34	4.00	3.60	0.65	1.49	8.47

Table 16: Uncertainties in the on-Z signal and validation regions. Nominal predictions are given with statistical uncertainty (including uncertainty from subtracted backgrounds), MC Closure uncertainty, uncertainty on the prediction from varying k and α by their statistical uncertainties, comparing the efficiencies from AODs to that of DAOs, and on the $m_{\ell\ell}$ widening, which includes MC statistics and a data/MC comparison in a loosened region.

2233 The next largest contribution to the uncertainty comes from [MC](#) closure
 2234 tests, which are used to determine how effective the method is in its predic-
 2235 tion. If, for example, using weights derived from an inclusive selection at
 2236 high E_T^{miss} lead to a bias, the closure test would indicate that and an appro-
 2237 priate uncertainty could be placed on the estimate based on the difference
 2238 between the [MC](#) prediction and the prediction from the flavor symmetry
 2239 method.

2240 In this test, the entire **FS** procedure is performed on $t\bar{t}$ **MC**, including a
 2241 recalculation of weighting factors α and k . The prediction from $e\mu$ events
 2242 in **MC** is compared to the **MC** ee and $\mu\mu$ events, as seen in [Figure 81](#). The dif-
 2243 ference between the two predictions is then summed in quadrature with
 2244 the statistical uncertainty on each prediction to give the total closure un-
 2245 certainty seen in [Table 16](#). In these closure tests, all predictions agree within
 2246 the statistical uncertainty, so the largest contributor to the resulting error
 2247 is **MC** statistics.

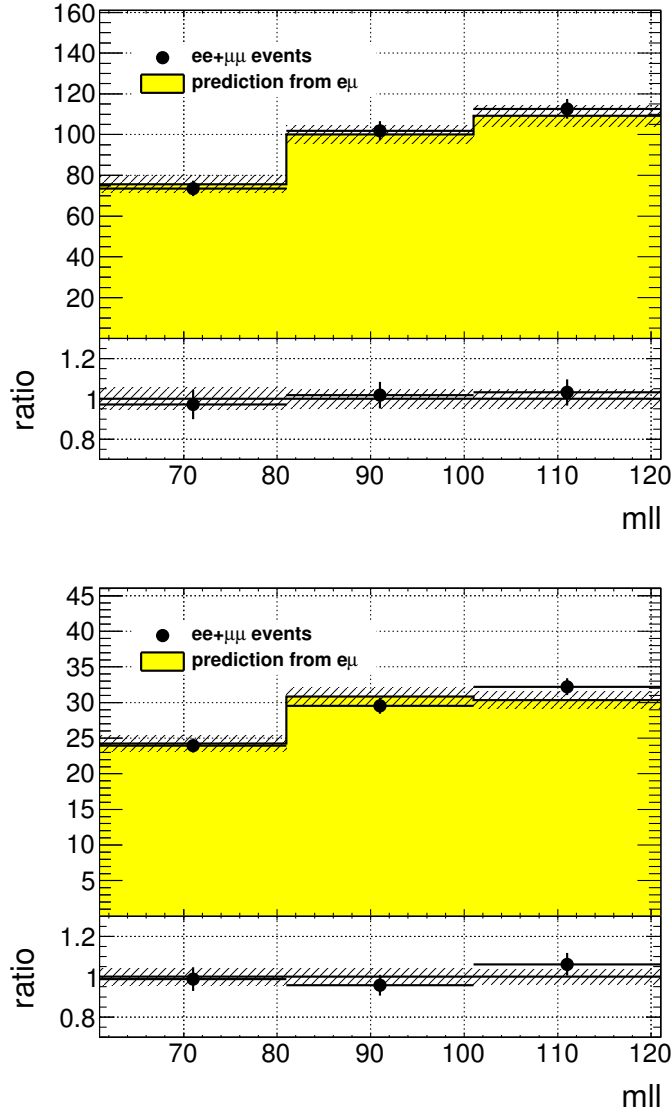


Figure 81: **MC** closure plots of VRS (top) and SRZ (bottom). The number of events from **MC** (black points) is compared to the number of events predicted from the flavor symmetry method (yellow histogram). The comparison is performed before the expanded m_{ll} window is used to predict the on-Z bin, but because the shape is taken from the same **MC**, the result is identical.

2248 A small uncertainty is added based on the statistical uncertainty on the
 2249 k and α factors derived from data. These factors are measured in many dif-
 2250 ferent bins (see, for example, the different measurements of k in Figure 82),
 2251 and as a consequence, some bins can have very large statistical uncertain-
 2252 ties. To assess the uncertainty on the total estimate, each measurement
 2253 of these factors is varied by its uncertainty in order to produce the max-
 2254 imum and minimum possible prediction. The differences with respect to
 2255 the nominal prediction are used to create a symmetrized error, which is
 2256 included in Table 16.

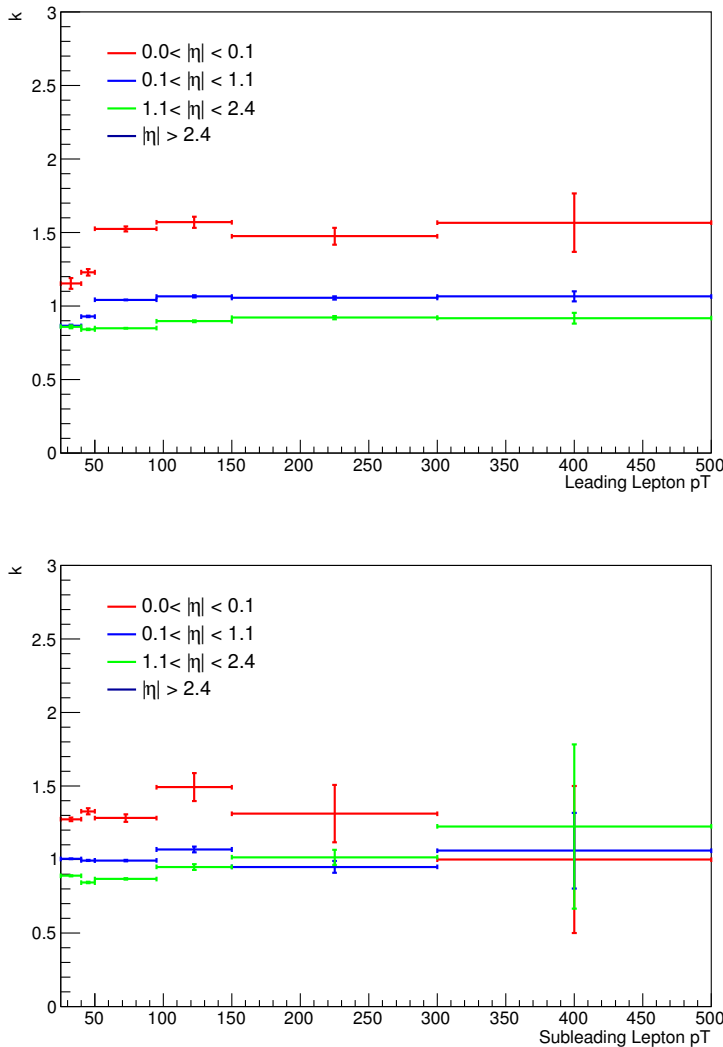


Figure 82: Measurements of k , the ratio of electron to muon events, in bins of p_T and η . On the top is the measurements indexed by the leading lepton, while the measurements indexed by the subleading lepton are on the bottom. These efficiencies are for the 2016 dataset.

2257 The next uncertainty considers a potential bias in the way the α factors
 2258 are calculated. Because they are derived from data, there is already trig-
 2259 ger dependence in data collection; only events passing a trigger are stored.

Additional trigger dependence is created by the data format used for analysis. ATLAS data and MC are stored in a format called Analysis Object Data (AOD), but smaller, slimmer versions of these datasets, called derived AODs (dAODs) are used for analysis. These dAODs are designed with specific analyses in mind, filtering on the triggers and objects required by the analyses. As a consequence, in the dAOD used in this analysis, there are explicit requirements that lepton or E_T^{miss} triggers are passed in order for events to be included.

As a consequence, the trigger efficiencies ϵ^{trig} used in Equation 34 to define α do not consider all possible data events. The ϵ^{trig} factor is calculated for each trigger using events passing the kinematic selection for that trigger, outlined in Section 9.1. The efficiency factor is then measured according to the equation

$$\epsilon^{\text{trig}} = \frac{N_{\text{trig}}}{N_{\text{all}}} \quad (40)$$

where N_{trig} is the number of events passing the trigger in the kinematic selection and N_{all} is all events in the selection. The latter measurement is the one subject to this bias, as it contains only the events that pass at least one trigger required for inclusion in the dAOD. As a consequence of these missing events, the ϵ^{trig} values will be artificially high. However, because the ratio of trigger efficiencies for the different channels is the only quantity needed for this analysis, the missing events will only bias the prediction if the different channels are differently impacted by the trigger preselection.

Calculating the flavor symmetry method's dependence on these biases requires the use of MC. With a generated MC sample, there is no trigger dependence, so an unskimmed sample can be compared to a typical skimmed MC dAOD to identify the effect of the skimming. Figure 83 shows a comparison of the α factors calculated for different bins in E_T^{miss} from the nominal source, data, as well as these two MC sources. A E_T^{miss} dependence would be the most likely bias between the two MC-derived α factors because E_T^{miss} triggers are the only triggers besides lepton triggers that will allow an event to be accepted into the dAOD used by this analysis. Though there is some difference between the data-derived α and those taken from MC, it is clear from this plot that there is very little dependence on the choice of an unskimmed or skimmed sample. The calculation of the uncertainty is performed by repeating the flavor symmetric method in MC with each of the two α factors and using the difference between the estimates as a symmetric error.

The last uncertainty relates to the main MC dependence of the method - the $m_{\ell\ell}$ shape of the FS background. A correction factor is taken from MC in order to account for the $m_{\ell\ell}$ widening, and the accuracy of that factor must be checked. Its shape is compared to that of data in region similar to VR-FS, but with an H_T cut lowered to 300 GeV to increase statistics. The difference between the fraction of events on the Z-mass peak in data and MC in this region is taken as a systematic uncertainty. To confirm that using

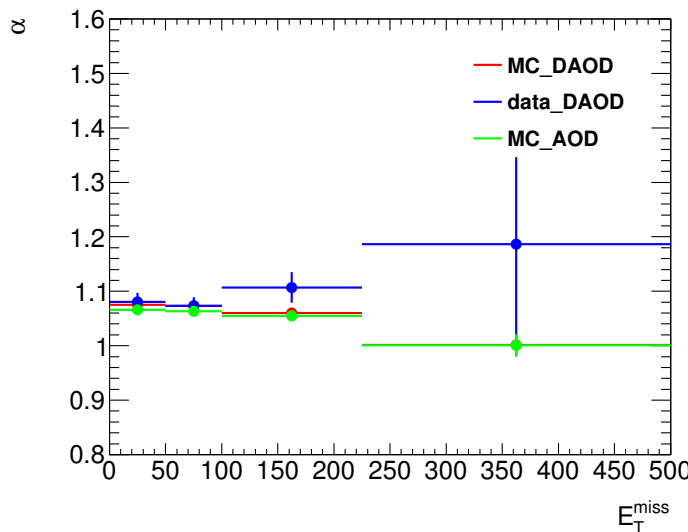


Figure 83: α , the trigger efficiency ratio, calculated as a function of E_T^{miss} from three different sources: data (blue), the usual skimmed $t\bar{t}$ MC (red), and an unskimmed $t\bar{t}$ MC (green).

2304 this lowered H_T cut still gives a valid answer, the fractions are compared
 2305 as a function of H_T in Figure 84. In these plots, especially in the higher-
 2306 statistics 2016 plot, it is clear both that the data and MC agree very well
 2307 and that there is no strong H_T dependence.

2308 All the uncertainties are calculated independently for the two datasets,
 2309 then added together. Statistical uncertainties, including the MC closure sta-
 2310 tistical uncertainties and the k and α uncertainties, are added in quadrature
 2311 between the two years. Uncertainties that are more likely to be correlated,
 2312 such as the difference between the two estimates in MC closure and the
 2313 dependence on using a dAOD to calculate trigger efficiencies, are added
 2314 linearly. The total uncertainty is about 12% of the nominal prediction in
 2315 SRZ and about 9% in VRS.

2316 11.1.2 *Uncertainties on the $\gamma + \text{jets}$ Method*

2317 One of the largest sources of uncertainty on the $\gamma + \text{jets}$ method is derived
 2318 by comparing the results from reweighting in different variables. Though
 2319 boson p_T is used as the nominal reweighting variable, the differences in
 2320 the kinematics of γ and Z events also impact number of jets, H_T , and E_T
 2321 (which includes the mass of the boson). The $\gamma + \text{jets}$ method is repeated
 2322 using each of these variables to reweight, and their E_T^{miss} distributions are
 2323 shown in Figure 85. The maximum difference from the nominal prediction
 2324 is symmetrized and used as an uncertainty on the method.

2325 Another uncertainty is applied to estimate the validity of using MC in a
 2326 1-jet CR to determine the smearing functions. Smearing functions are made
 2327 using data from the same 1-jet region and using MC in a ≥ 2 -jet region
 2328 otherwise identical to the 1-jet CR. These distributions are also shown in
 2329 Figure 85, and like the alternate reweighting distributions, are used to find

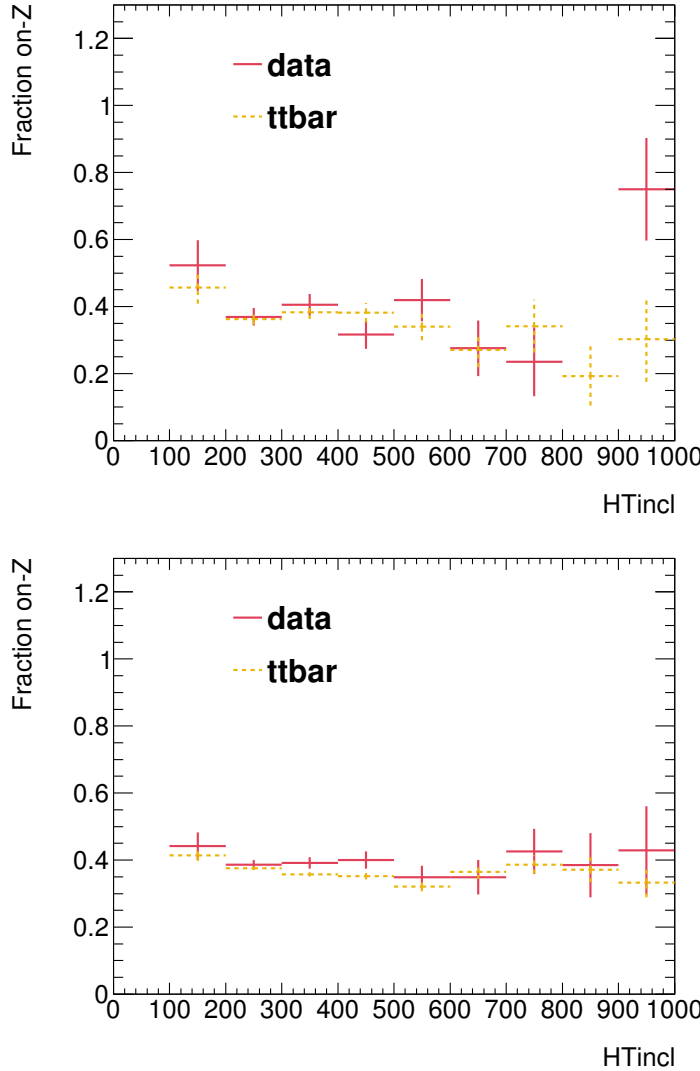


Figure 84: Plots of the fraction of on-Z events with a VR-FS-like selection as a function of H_T . The top figure shows 2015 data and MC while the bottom figure shows the same for 2016.

2330 a maximum difference from the nominal prediction which is translated
 2331 into a symmetric error.

2332 As in the flavor symmetric method, the full procedure is carried out on
 2333 MC in order to test MC closure, including a recalculation of any weights
 2334 that are typically derived from data. The resulting comparison between
 2335 $Z/\gamma^* + \text{jets}$ MC and the $\gamma + \text{jets}$ method performed on MC can be seen
 2336 in Figure 86. The final non-closure uncertainty is taken from VRS, where
 2337 larger numbers of events give a clearer picture of the success of the method
 2338 than in SRZ. In this region, the statistical uncertainty on the prediction is
 2339 compared to the non-closure, and the larger of the two is used as the final
 2340 uncertainty.

2341 The uncertainty on the $V\gamma$ contamination in CR- γ is also considered.
 2342 An uncertainty on the MC prediction is made based on comparison of data

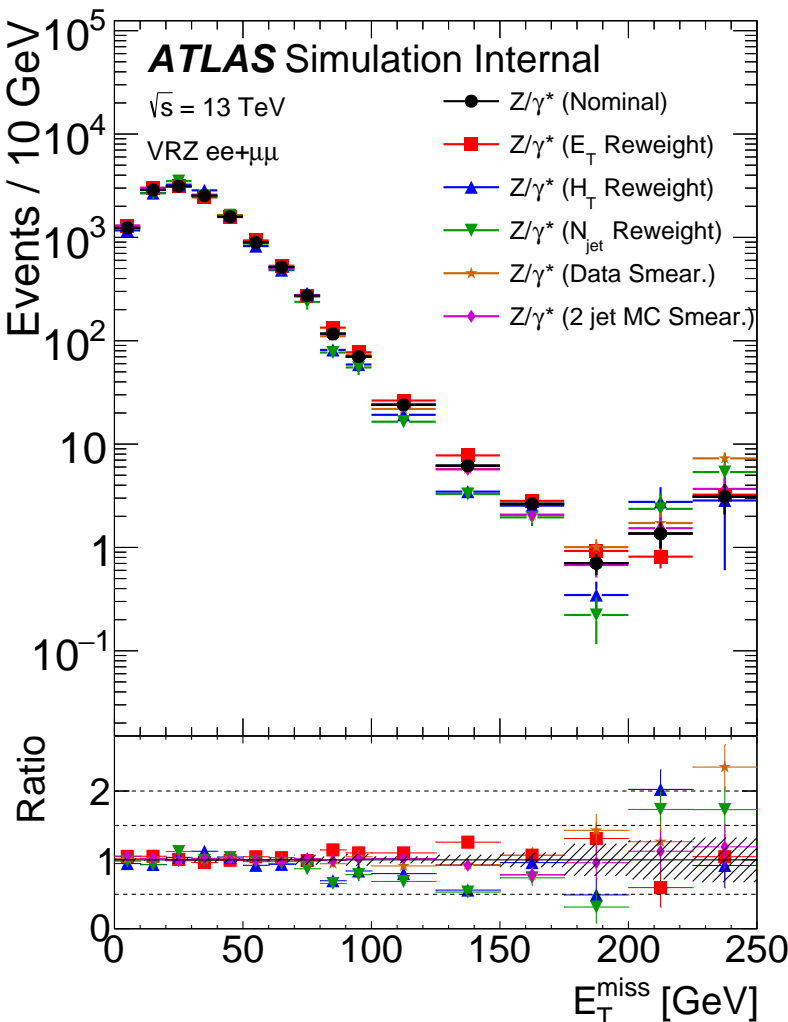


Figure 85: E_T^{miss} distributions for $\gamma + \text{jets}$ predictions using different reweighting variables, as well as distributions with the nominal reweighting but with smearing functions taken from data and from MC in a ≥ 2 -jet region.

and MC in a $W + \text{jets}$ VR, shown in Figure 87. This VR is similar to CR- γ , but instead of vetoing events with leptons, requires at least one well-isolated lepton with a p_T over 25 GeV. At E_T^{miss} values over 100 GeV, region is about 90% pure in $W\gamma$ processes. The MC agrees well with data in this region, even at very high E_T^{miss} , so an uncertainty of 16% based primarily on statistical uncertainty in this VR is placed on the $V\gamma$ MC. This uncertainty is propagated to the final result through the subtraction procedure.

An uncertainty on the $m_{\ell\ell}$ shape is determined using MC closure as well. The comparison of $m_{\ell\ell}$ shapes in $Z/\gamma^* + \text{jets}$ MC and the $\gamma + \text{jets}$ method applied to MC is shown in Figure 70. As with the main MC closure test, the maximum of the statistical uncertainty and the non-closure is taken as the final uncertainty on this background.

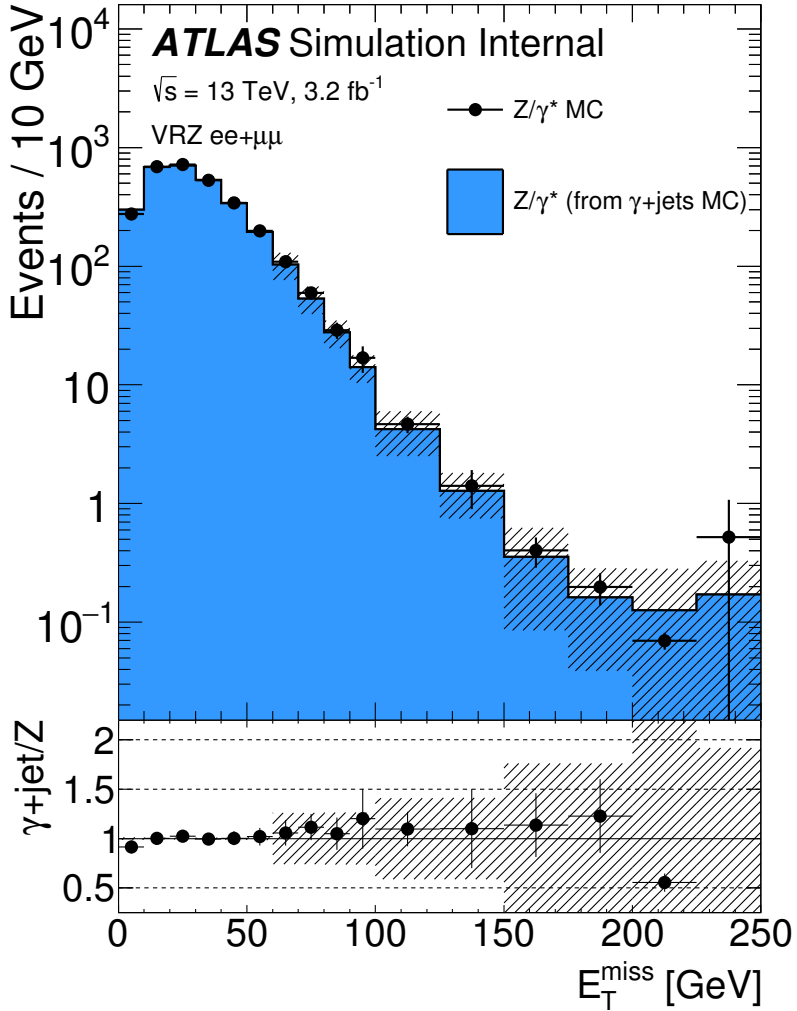


Figure 86: MC closure of the γ + jets method as a function of E_T^{miss} comparing the MC prediction of the Z background with the γ + jets method performed on γ + jets MC. The uncertainty band includes both statistical and reweighting uncertainties.

2355 One last uncertainty based on the statistical uncertainty on the number
2356 of γ + jets data events used for this method is also included. The full
2357 breakdown of uncertainty in SRZ can be seen in Table 17.

2358 11.1.3 Uncertainties on the Fakes Background

2359 Systematic uncertainties on the fakes background are derived from a se-
2360 ries of variations on the nominal method. Variations include scaling the
2361 real and fake efficiencies up and down by their statistical uncertainties,
2362 scaling the prompt lepton contamination in CR-fake up and down by 20%,
2363 and by requiring and vetoing b -tagged jets in CR-fake to determine the
2364 dependence on heavy flavor. Statistical uncertainties can also be large in
2365 regions with small numbers of events in the baseline selection, such
2366 as SRZ. In other regions, the b -tagging dependence provides the largest

Ch.	Pred.	Uncertainties (%)						
		$V\gamma$ sub.	MC clos.	$m_{\ell\ell}$ shape	re- weight	smear	stat.	total
ee	1.02	53.0	21.0	19.0	100.0	65.0	56.0	145.0
$\mu\mu$	2.08	27.0	14.0	23.0	30.0	59.0	40.0	86.0
$ee+\mu\mu$	3.1	36.0	16.0	22.0	43.0	60.0	33.0	92.0

Table 17: Uncertainty breakdown for the $\gamma + \text{jets}$ method in SRZ. Uncertainties considered are the impact of MC uncertainty on $V\gamma$ backgrounds, MC closure, uncertainty on $m_{\ell\ell}$ shape (also determined via MC closure), reweighting uncertainties, smearing uncertainties, and statistical uncertainty on the $\gamma + \text{jets}$ events used in the method.

uncertainty. The full breakdown of uncertainties for the most important regions are listed in Table 18.

Variation	SRZ	CRT	CRFS	VRFS	VRS	VRT
Nominal	0.10 ± 1.61	25.39 ± 5.35	3.73 ± 2.19	10.53 ± 3.56	3.64 ± 3.20	80.06 ± 9.80
EL F Up	0.15	30.23	3.96	10.93	3.56	92.46
EL F Down	0.06	21.80	3.52	10.18	3.54	70.07
EL R Up	0.25	26.17	3.92	11.10	4.13	82.57
EL R Down	-0.07	24.51	3.52	9.92	3.10	77.24
MU F Up	-0.20	32.48	4.77	16.41	5.25	86.48
MU F Down	0.29	20.17	2.91	7.04	2.87	70.12
MU R Up	0.13	25.67	3.78	10.66	3.81	81.18
MU R Down	0.05	25.04	3.67	10.38	3.44	78.72
Total Sys	+0.26 -0.35	+8.64 -6.39	+1.08 -0.87	+5.92 -3.56	+1.70 -0.97	+14.24 -14.42
Total Sys (%)	+261.05 -354.72	+34.01 -25.19	+29.05 -23.23	+56.22 -33.85	+46.57 -26.60	+17.78 -18.02
Real Cont. Up	0.23	20.97	3.06	8.08	3.15	68.79
Real Cont. Down	-0.01	29.67	4.38	12.95	4.16	90.23
b-jet	0.31	40.44	5.28	8.98	5.63	120.50
no b-jet	0.16	23.44	3.08	11.38	3.97	70.55
Total Sys	+0.25 -0.11	+15.65 -4.83	+1.69 -0.93	+2.56 -2.90	+2.09 -0.49	+41.71 -14.74
Total Sys (%)	+260.46 -109.06	+61.66 -19.02	+45.30 -24.85	+24.32 -27.58	+57.31 -13.35	+52.10 -18.42

Table 18: Systematic uncertainties on the fake-lepton background for on-Z regions for 2015+2016 yields. The nominal yield includes statistical uncertainty from the baseline selection in a given region. The following rows indicate the results of varying the real and fake lepton efficiencies up and down by their statistical uncertainty. Real cont. gives an uncertainty on the contamination of real leptons in the fake lepton efficiency. b-jet and no b-jet indicate the impact of requiring or vetoing b-tagged jets in the regions used to measure the fake efficiency.

11.2 THEORETICAL AND EXPERIMENTAL UNCERTAINTIES

Experimental uncertainties cover any detector effect or LHC condition that may not be modeled precisely correctly in MC. For each uncertainty, a standard prescription from the ATLAS experiment is followed. Uncertainties are included on the following parameters:

- 2374 • Luminosity (2.9%) [80, 81]
- 2375 • Jet energy scale [50]
- 2376 • Jet energy resolution [50]
- 2377 • Jet vertex tagging
- 2378 • Heavy flavor tagging
- 2379 • E_T^{miss} soft term [53]
- 2380 • e/μ momentum scale
- 2381 • e/μ trigger, reconstruction, and identification efficiencies
- 2382 • Pile-up

2383 These uncertainties are applied to all MC samples used in the analysis.
 2384 This includes signal models, diboson and rare top samples for the nominal
 2385 estimate, and all backgrounds taken from MC in the sideband fit.

2386 Theoretical uncertainties include cross-section uncertainties, scale uncer-
 2387 tainties, and PDF uncertainties. For the diboson samples, the scale uncer-
 2388 tainties, given in Table 19 are calculated by varying each scale up and
 2389 down by a factor of two. These are combined with a 6% cross-section un-
 2390 certainty and a generator uncertainty obtained by comparing PowHEG and
 2391 SHERPA MC yields in a given region. This generator uncertainty, shown in
 2392 Table 20, is dominant in most regions. Rare top processes are given a 13%
 2393 PDF and scale variation uncertainty [26] and a 22% cross section uncer-
 2394 tainty [60–62].

2395 Signal models have both the central value and uncertainty on cross-
 2396 sections taken from an envelope of predictions using different scales and
 2397 PDF sets [82]. The signal processes are calculated at Next-to-Leading-Logarithmic
 2398 Accuracy (NLO+NLL); they are initially calculated at NLO in the strong
 2399 coupling constant, with additional terms from next-to-leading-logarithmic
 2400 resummation of soft gluon emission [83–87].

2401 11.3 IMPACT OF UNCERTAINTIES ON THE SIGNAL REGION

2402 The breakdown of each major uncertainty’s contribution to the total un-
 2403 certainty in SRZ is shown in Table 21. The dominant uncertainty is the
 2404 diboson generator uncertainty, followed by the statistical uncertainty from
 2405 the FS background. Uncertainties smaller than 1% are not shown in the
 2406 table.

$VV \rightarrow ll\nu\nu$ Samples							
	SRZ	VRS	CRT	VRT	VRWZ	VRZZ	VR ₃ L
resummation	0.07	0.03	0.01	0.02	0.00	0.00	0.00
renormalization	0.13	0.17	0.16	0.22	0.00	0.00	0.00
factorization	0.01	0.01	0.01	0.03	0.00	0.00	0.00
total	0.15	0.17	0.16	0.22	0.00	0.00	0.00
$WZ \rightarrow lll\nu$ Samples							
	SRZ	VRS	CRT	VRT	VRWZ	VRZZ	VR ₃ L
resummation	0.07	0.05	0.13	0.08	0.02	0.00	0.01
renormalization	0.26	0.20	0.28	0.21	0.07	0.00	0.18
factorization	0.04	0.04	0.02	0.06	0.01	0.00	0.02
total	0.28	0.21	0.31	0.23	0.07	0.00	0.18
$ZZ \rightarrow llll$ Samples							
	SRZ	VRS	CRT	VRT	VRWZ	VRZZ	VR ₃ L
resummation	0.27	1.07	0.01	0.01	0.06	0.01	0.53
renormalization	0.28	0.26	0.30	0.60	0.07	0.04	0.14
factorization	0.27	0.25	0.30	0.58	0.13	0.02	0.16
total	0.48	1.13	0.43	0.84	0.16	0.05	0.57

Table 19: Fractional uncertainties of dibosons in signal and validation regions from Sherpa scale variations.

Region	Sherpa Events/fb ⁻¹	Sherpa Events	Powheg Events/fb ⁻¹	Powheg Events	% Difference
WZ Samples					
SRZ+VRZ	5.219	76.722	3.286	48.300	37.046
CRT+VRT	1.060	15.583	0.742	10.913	29.970
WW/ZZ Samples					
SRZ+VRZ	1.921	28.244	0.685	10.070	71.424
CRT+VRT	6.281	92.332	3.142	46.188	55.474

Table 20: Comparison of yields in on-Z and off-Z regions in Sherpa and Powheg diboson MC at 14.7 fb⁻¹.

Source	Relative systematic uncertainty [%]
SRZ	
Total systematic uncertainty	17
WZ/ZZ generator uncertainty	13
Flavour symmetry (statistical)	7
WZ/ZZ scale uncertainty	6
$Z/\gamma^* + \text{jets}$ (systematic)	4
Flavour symmetry (systematic)	3
$Z/\gamma^* + \text{jets}$ (statistical)	2
Fake-leptons	1

Table 21: Overview of the dominant sources of systematic uncertainty on the total background estimate in the signal regions. The values shown are relative to the total background estimate, shown in %.

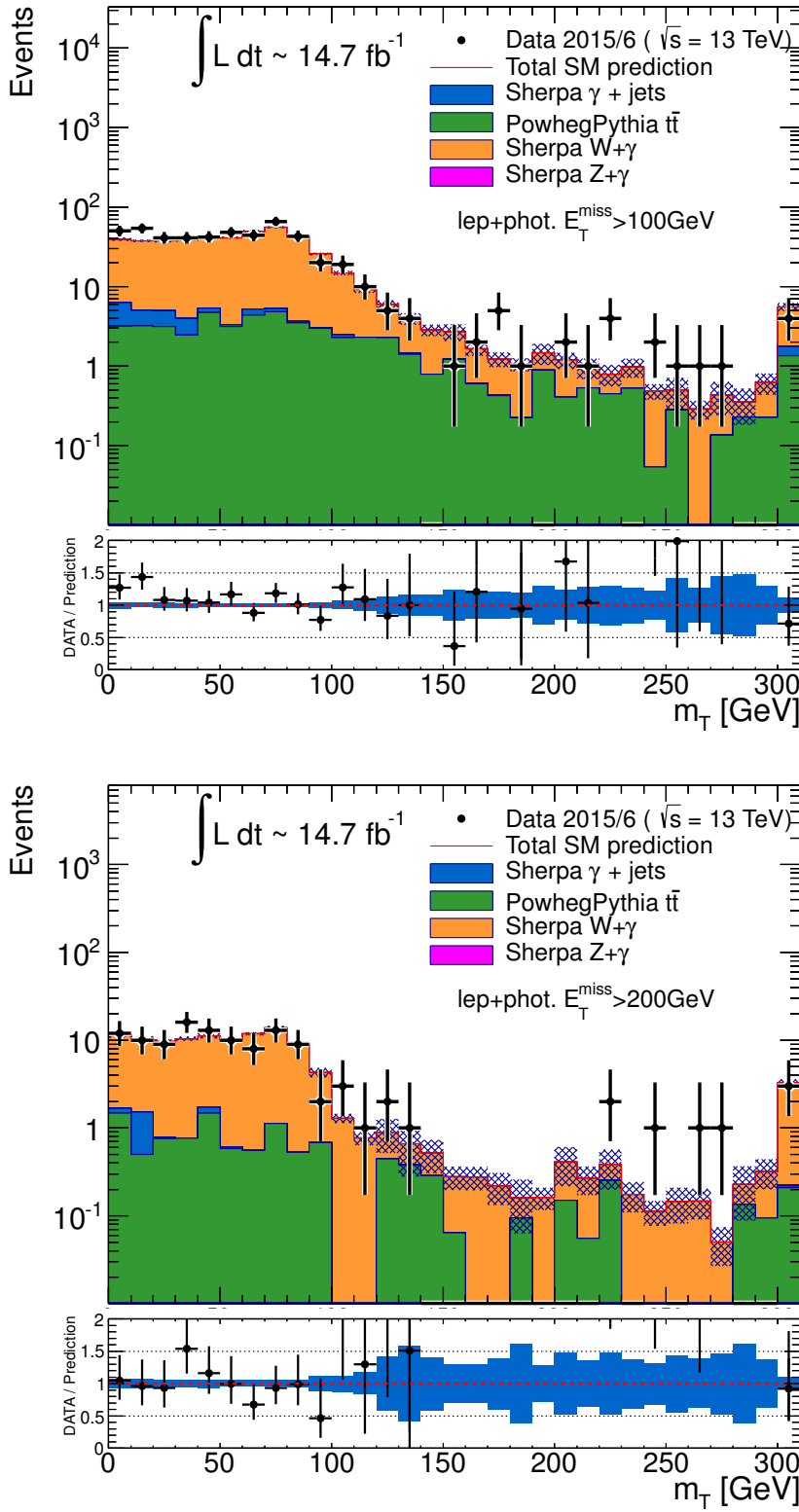


Figure 87: Distributions of $m_T(\ell, E_T^{\text{miss}})$, the transverse mass of the lepton and the E_T^{miss} in a VR designed to target $W\gamma$ processes. Top is the distribution with a E_T^{miss} cut at 100 GeV, and bottom is the same distribution with a E_T^{miss} cut of 200 GeV.

2407

2408 RESULTS

2409 The results of the search can be seen in [Table 22](#), which displays the ex-
 2410 pected and observed numbers of events in SRZ, both divided by channel
 2411 and inclusively. The predictions and uncertainties for each background are
 2412 shown, though many of these uncertainties are correlated between back-
 2413 grounds, so the final uncertainty does not correspond to a simple addition
 2414 in quadrature of each error. A total of sixty events are observed, with 53.5 ± 9.3
 2415 events expected. [Figure 88](#) shows the expected and observed results
 2416 visually for the **SR** as well as three **VRs**, all designed to verify the accuracy
 2417 of the backgrounds taken from **MC**. Excellent agreement is seen in all cases,
 2418 with the largest deviation at about 1σ .

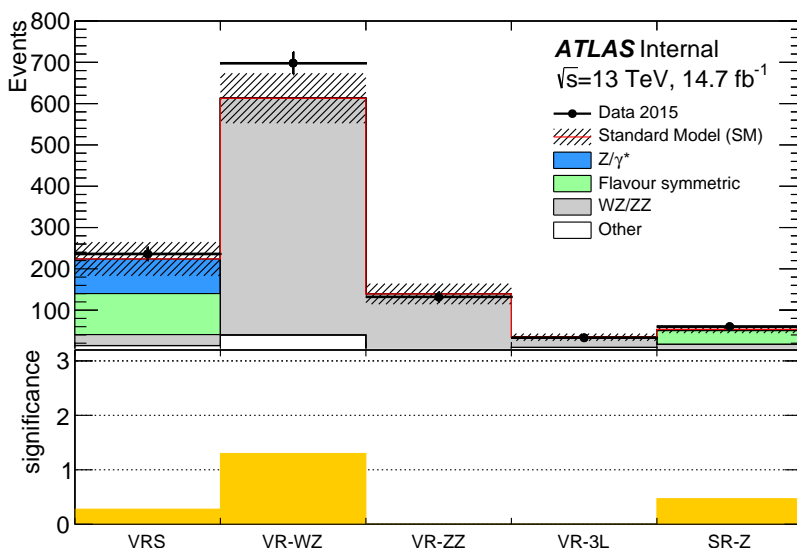


Figure 88: Comparison of background predictions and data yields in four validation regions, as well as the signal region. Definitions of all regions can be found in [Table 7](#), with both rare top and fake backgrounds grouped together under the “other” label. The uncertainty band includes all statistical and systematic uncertainties. Below is a panel of the one-sided statistical significances of the deviations between the predicted and observed quantities for each region.

2419 [Table 22](#) also shows several statistical interpretations of the results. The
 2420 discovery p -value for zero signal strength, which gives the probability that
 2421 the observed events are compatible with a **SM**-only hypothesis, is given as
 2422 0.32. The significance is listed as 0.47σ , which is a reinterpretation of the p -
 2423 value into a gaussian significance. This p -value is one-sided; when the data
 2424 yield is less than expected the p -value is set to 0.5, and the significance is
 2425 set to 0. S^{95} , the upper limit on the number of signal events that could be

Table 22: Number of events expected and observed in the ee , $\mu\mu$, and combined channels. Expected predictions include all systematic and statistical uncertainties discussed in Chapter 11. Also shown is the discovery p -value for zero signal strength ($p(s = 0)$) [88], Gaussian significance, 95% CL observed and expected upper limits on the number of signal events (S^{95}), and the corresponding observed upper limit on the visible cross section ($\langle\epsilon\sigma\rangle_{\text{obs}}^{95}$).

	SRZ	SRZ ee	SRZ $\mu\mu$
Observed events			
	60	35	25
Total expected background events	53.5 ± 9.3	27.1 ± 5.1	26.8 ± 4.4
Flavour-symmetric ($t\bar{t}$, Wt , WW and $Z \rightarrow \tau\tau$) events	33.2 ± 3.9	16.5 ± 2.1	16.7 ± 2.0
Z/γ^* + jets events	3.1 ± 2.8	$1.0^{+1.3}_{-1.0}$	2.1 ± 1.4
WZ/ZZ events	14.2 ± 7.7	7.8 ± 4.3	6.4 ± 3.5
Rare top events	2.9 ± 0.8	1.4 ± 0.4	1.5 ± 0.4
Fake-lepton events	$0.1^{+0.8}_{-0.1}$	$0.5^{+0.7}_{-0.5}$	$0^{+0.2}_{-0.2}$
$p(s = 0)$	0.32	0.15	0.5
Significance (σ)	0.47	1.00	0
Observed (Expected) S^{95}	$28.2 (24.5^{+8.9}_{-6.7})$	$22.0 (15.8^{+6.5}_{-4.5})$	$12.9 (14.0^{+5.7}_{-3.9})$
$\langle\epsilon\sigma\rangle_{\text{obs}}^{95}$ [fb]	1.9	1.5	0.88

in the SR at a 95% CL, is determined both for the expected and observed number of events. This limit is also reinterpreted based on the integrated luminosity used in the search to produce an upper limit on the visible cross-section of signal events, $\langle\epsilon\sigma\rangle_{\text{obs}}^{95}$.

The predictions in SRZ, combined with the MC shapes, are used to produce plots in a broader $m_{\ell\ell}$ range, seen in Figure 89. These plots are useful demonstrations of efficacy of the background estimation methods, showing the well-modeled $Z/\gamma^* + \text{jets}$ shape in the same-flavor region, and in the different-flavor region, demonstrating that there are no extreme fluctuations within the region used to predict the flavor symmetric background.

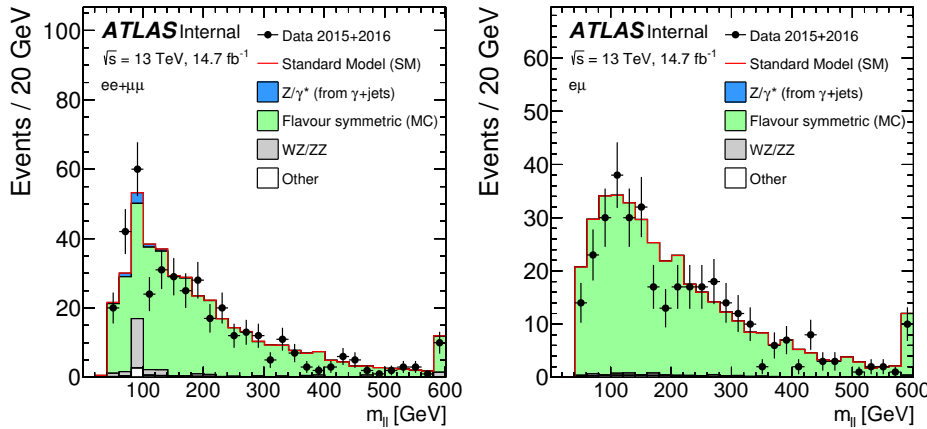


Figure 89: Comparisons as a function of $m_{\ell\ell}$ of background predictions with observed data in an SRZ-like region, with the $m_{\ell\ell}$ cut removed. Left is the same-flavor channel, where all background shapes are taken from MC and scaled to their SRZ predictions, except for the $Z/\gamma^* + \text{jets}$ background, which is taken entirely from the data-driven background. Right is the different-flavor channel, in which the backgrounds are taken directly from MC, except for $t\bar{t}$, which is scaled to match the total data yield.

Focusing in on the SR itself, comparisons of background predictions, observed events, and signal models can be made as a function of key variables for the analysis. Figure 90 shows several of these. The first two figures focus on the features of the SR events' leading leptons; they give the mass and p_T of a hypothetical parent particle reconstructed from the leptons. In the case of events with a real Z boson, these variables simply give that boson's mass at p_T . The next two figures show distributions in the two most important variables used to differentiate signal from background, E_T^{miss} and H_T . In this analysis, where the frozen SR resulted in cuts on these quantities that are lower than those that would be chosen based on a new optimization, these plots show that, even in more sensitive regions, no large excess above the SM background is seen. The last pair of figures relates to the jets in the event, showing the total number of jets and the total number of b -jets in the SR events. The b -jet quantity is not explicitly cut on in the analysis because the fraction of b -jets produced is extremely model dependent. However, an excess at high b -jet

2452 multiplicity would suggest a BSM process. In each of these distributions,
 2453 the observed distributions match the background predictions very well,
 2454 and no evidence for any of the superimposed signal models is seen.

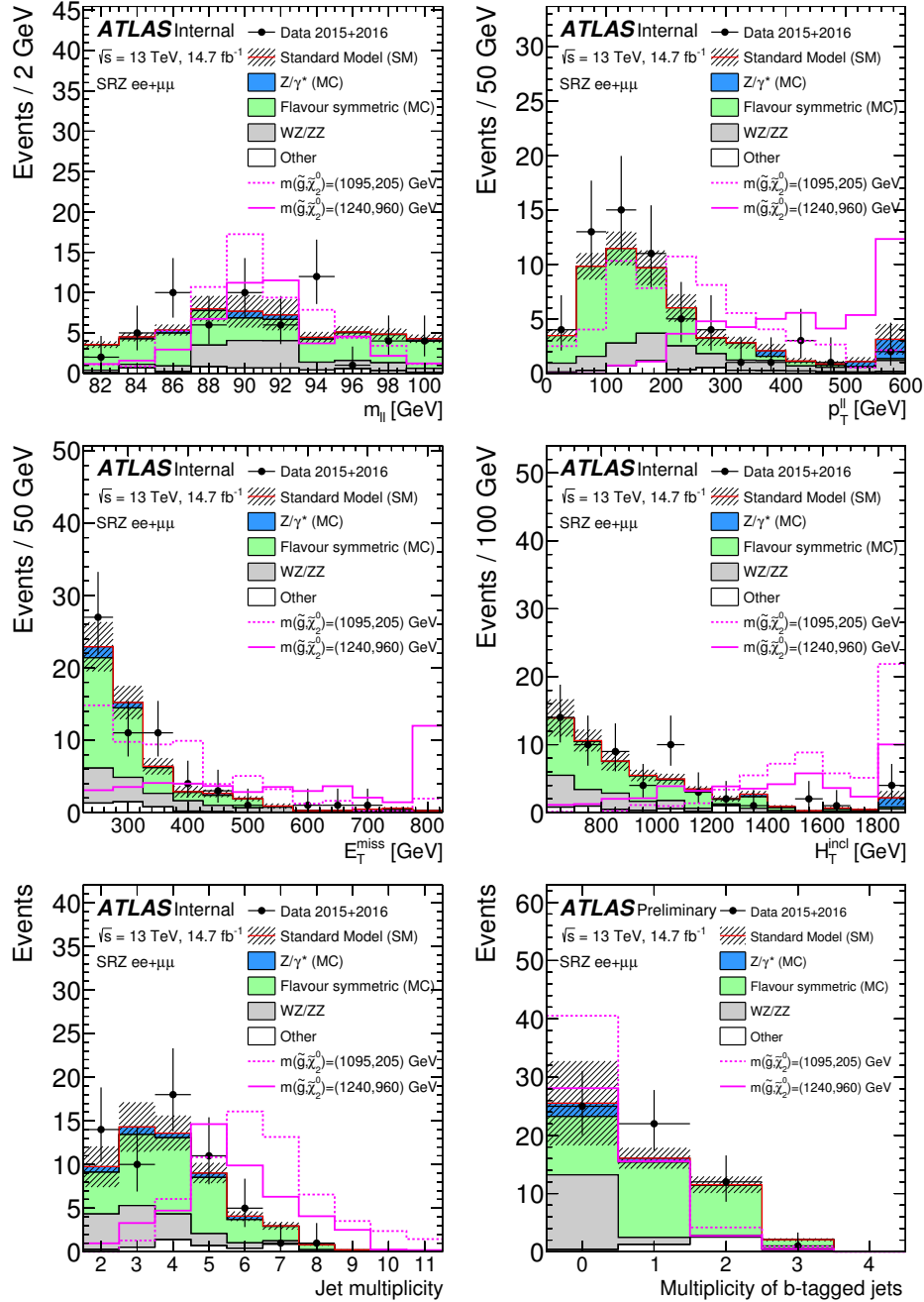


Figure 90: Distributions of observed data, background predictions, and simulated signals are shown in SRZ as a function of $m_{\ell\ell}$, $p_T^{\ell\ell}$, E_T^{miss} , H_T , number of jets, and number of b -jets. The two example signals have $(m(\tilde{g}), m(\tilde{\chi}_2^0)) = (1095, 205) \text{ GeV}$. All background shapes are taken from MC, and in the case of flavor symmetric and $Z/\gamma^* + \text{jets}$ backgrounds, their yields are scaled to match the data-driven predictions. Uncertainties include statistical and systematic components.

2455 Comparisons of the observed and expected yield are also made as a
2456 function of $\Delta\phi(\text{jet}_{12}, p_T^{\text{miss}})$, shown in Figure 91. Here, results are shown
2457 in a region similar to SRZ with the cut on this variable removed, showing
2458 the efficacy of the background prediction in a region enhanced in $Z/\gamma^* +$
2459 jets events. Again, excellent agreement is seen between the background
2460 prediction and observed data.

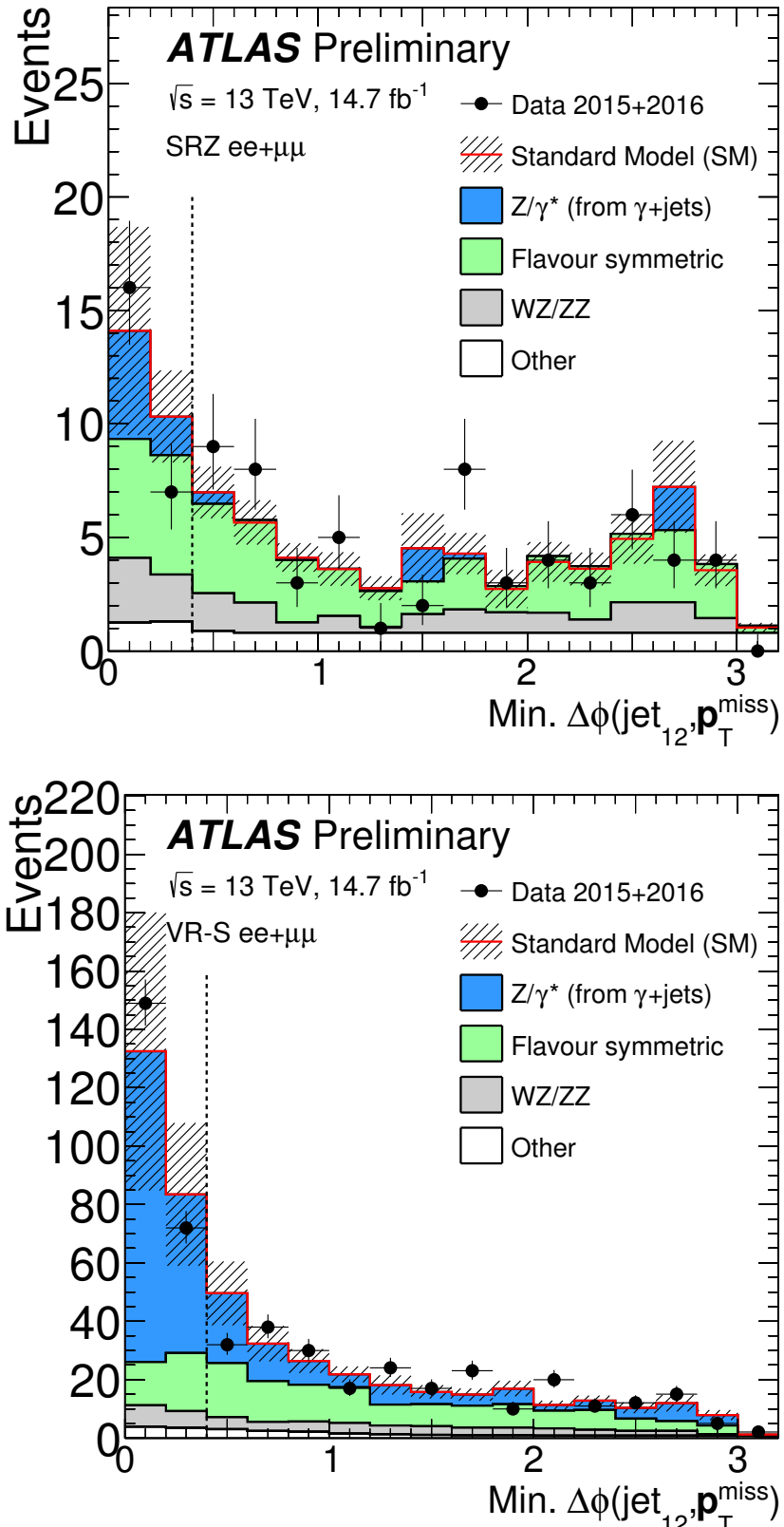


Figure 91: Comparisons as a function of $\Delta\phi(\text{jet}_{12}, \mathbf{p}_T^{\text{miss}})$ of background predictions with observed data in an SRZ-like (left) and VRS-like (right) region, with the $\Delta\phi(\text{jet}_{12}, \mathbf{p}_T^{\text{miss}})$ cut removed. All background shapes are taken from MC and scaled to their SRZ predictions, except for the Z/ γ^* + jets background, which is taken entirely from the data-driven background.

2461
2462 INTERPRETATIONS

2463 Using the simplified models discussed in [Section 2.2.3](#), these results can be
 2464 interpreted into exclusions of theories based on the masses of the particles
 2465 involved. Of course, these exclusions include all the assumptions of the
 2466 models used, so they shouldn't be interpreted to mean that no theory
 2467 with a given set of particle masses can possibly exist, but they do provide
 2468 a helpful guideline for targeting future searches and comparing results
 2469 from different analyses.

2470 Limits are determined using a program called HistFitter [88], designed
 2471 within the ATLAS experiment, which builds upon the capabilities of ROOT
 2472 [89], RooStats [90], and HistFactory [91] to combine the uncertainties of
 2473 the various background predictions, including their correlations, and pro-
 2474 duce cross-section limits at 95% CL using the CL_S prescription [92, 93]. In
 2475 this prescription, a likelihood is constructed based on the expected signal
 2476 and background contributions to the SR. Nuisance parameters are created
 2477 based on the statistical and systematic uncertainties for each data-driven
 2478 background, as well as for each systematic applied to the MC-driven back-
 2479 ground estimates. The fit uses Gaussian models for nuisance parameters
 2480 for all signal and background uncertainties, except for the statistical un-
 2481 certainty on data- and MC-driven background estimates, which are inter-
 2482 preted as Poissonian. Experimental uncertainties are considered fully cor-
 2483 related across the signal and background MC-based estimates.

2484 A fit is performed, leaving a signal strength parameter (μ) free, to max-
 2485 imize the likelihood, and subsequent fits are preformed to at discrete μ
 2486 values to determine the relative likelihood of each value. Using this rela-
 2487 tive likelihood, the probability of a background-only hypothesis, p_b , can be
 2488 determined by setting $\mu = 0$, as well as the probability of a signal + back-
 2489 ground hypothesis p_{s+b} with any non-zero signal strength, but nominally
 2490 with $\mu = 1$. The confidence limit is constructed as a ratio

$$CL_S = \frac{p_{s+b}}{1 - p_b}. \quad (41)$$

2491 Then, if CL_S falls below 5%, the signal + background hypothesis can be
 2492 excluded at 95%. Expected exclusion limits are constructed by assuming
 2493 the observed data precisely matches the prediction, and 1σ uncertainty
 2494 bands are formed by varying the nuisance parameters away from their fit-
 2495 ted values to produce a change in the likelihood. The observed limit uses
 2496 the actual observation of data in the SR to set exclusion limits, so any excess
 2497 above the expected background will result in worse limits than expected,
 2498 and any deficit will result in better limits. This exclusion is typically dis-
 2499 played with error bands that represent a 1σ variation in the cross-section
 2500 of the signal models.

2501 The simplified model discussed in [Section 2.2.3](#), in which pair-produced
 2502 gluinos decay via a $\tilde{\chi}_2^0$ to jets, a Z boson, and a $\tilde{\chi}_1^0$ LSP, is produced in two
 2503 grids, which differ by their choice of the LSP mass. The first grid assumes
 2504 a light LSP, fixing its mass to 1 GeV for all mass points, and is shown
 2505 as a function of \tilde{g} and $\tilde{\chi}_2^0$. The second grid is defined as a function of \tilde{g}
 2506 and $\tilde{\chi}_1^0$, and its varying LSP mass is defined relative to the $\tilde{\chi}_2^0$ mass by
 2507 $m(\tilde{\chi}_1^0) = m(\tilde{\chi}_2^0) - 100$ GeV. [Figure 92](#) shows the first of these grids, along
 2508 with exclusions on a similar simplified model, which replaces the gluinos
 2509 with squarks and uses the same mass scheme. The exclusion contours on
 2510 the second grid is shown in [Figure 93](#), as a function of $m(\tilde{g})$ and $m(\tilde{\chi}_1^0)$.

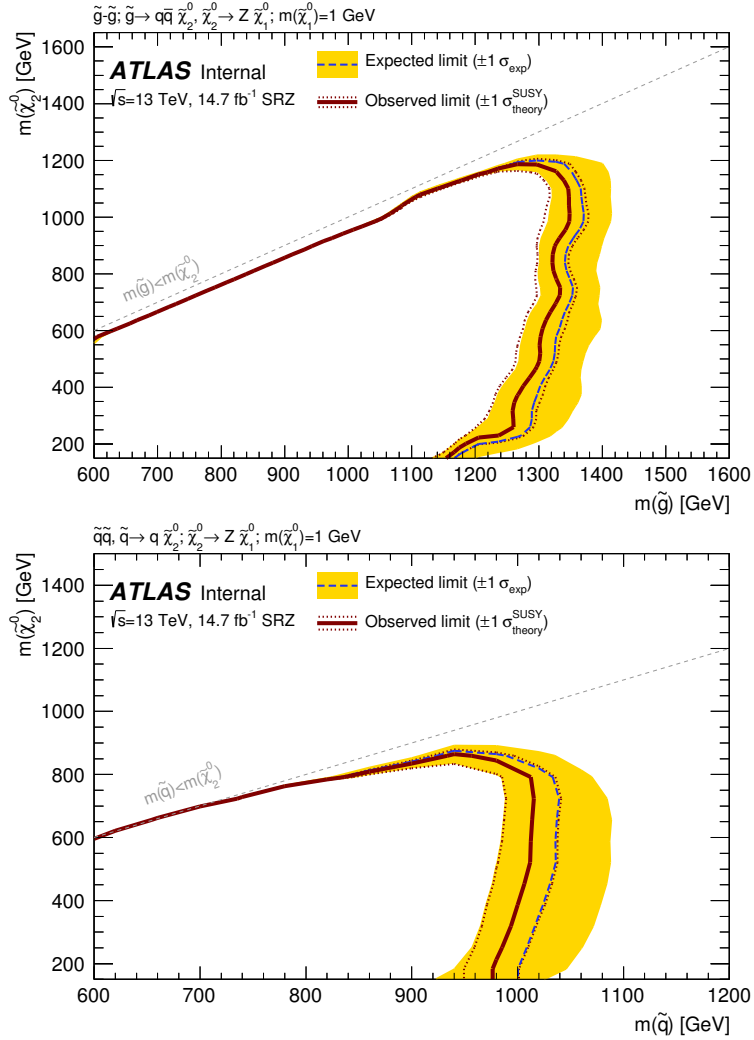


Figure 92: Expected and observed exclusion contours derived from the results in SRZ for the (top) $\tilde{g}-\tilde{\chi}_2^0$ on-shell grid and (bottom) $\tilde{q}-\tilde{\chi}_2^0$ on-shell grid. The dashed blue line indicates the expected limits at 95% CL and the yellow band shows the 1σ variation of the expected limit as a consequence of the uncertainties in the background prediction and the experimental uncertainties in the signal ($\pm 1\sigma_{\text{exp}}$). The observed limits are shown by the solid red line, with the dotted red lines indicating the variation resulting from changing the signal cross section within its uncertainty ($\pm 1\sigma_{\text{theory}}^{\text{SUSY}}$).

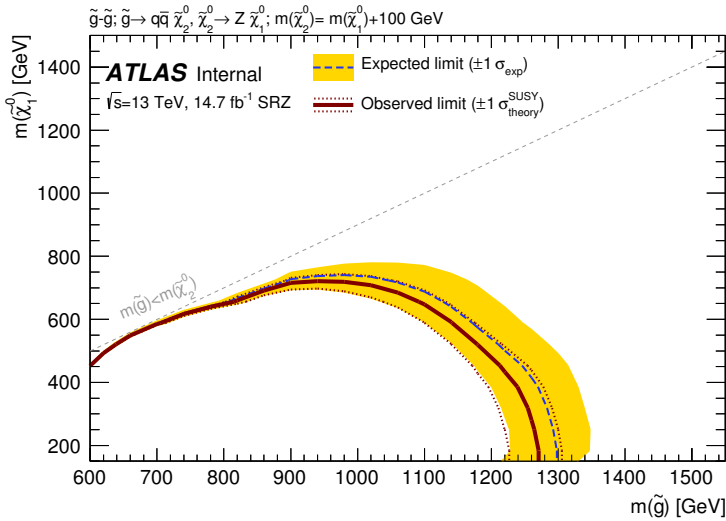


Figure 93: Expected and observed exclusion contours derived from the results in SRZ for the $\tilde{g}-\tilde{\chi}_1^0$ on-shell grid. The dashed blue line indicates the expected limits at 95% CL and the yellow band shows the 1σ variation of the expected limit as a consequence of the uncertainties in the background prediction and the experimental uncertainties in the signal ($\pm 1\sigma_{\text{exp}}$). The observed limits are shown by the solid red line, with the dotted red lines indicating the variation resulting from changing the signal cross section within its uncertainty ($\pm 1\sigma_{\text{theory}}^{\text{SUSY}}$).

2511 In general, the observed exclusions are slightly weaker than the expected
 2512 exclusions, due to a very small excess of events observed in SRZ. The
 2513 observed lower limit on $m(\tilde{g})$ is about 1.3 TeV for models with $m(\tilde{\chi}_2^0) = 500$
 2514 GeV for the $\tilde{g}-\tilde{\chi}_2^0$ grid. These improve significantly on the previous ATLAS
 2515 exclusion, which used different models for interpretation, but placed a
 2516 lower limit on $m(\tilde{g})$ at around 900 GeV for similar $m(\tilde{\chi}_2^0)$.

2517

Part V

2518

CONCLUSIONS

2519

2520

2521 CONCLUSIONS AND OUTLOOK

2522 After a series of moderate excesses observed by the ATLAS experiment
 2523 in events with a Z boson, jets, and E_T^{miss} , this analysis performed on 14.7
 2524 fb^{-1} of 13 TeV data sees excellent agreement between observations and
 2525 the background expectation. The resulting exclusion pushes the gluino
 2526 mass lower limit beyond 1 TeV, putting further constraints on possible
 2527 SUSY models. Along with the many other searches for SUSY, this exclusion
 2528 limits the phase space available for natural SUSY models. However, SUSY is
 2529 adaptable; new theories stretching those bounds are continually proposed
 2530 as tighter experimental constraints are set, and there are always small gaps
 2531 in the exclusions where sparticles could hide.

2532 ATLAS's dataset for 2016 includes 36 fb^{-1} , more than twice the lumi-
 2533 nosity included in this search. Because no excess was seen in this analysis,
 2534 the next search in this channel will be able to re-optimize its signal re-
 2535 gions for this larger dataset. In fact, because the signal region has been
 2536 frozen since the 8 TeV search, this analysis's signal region hasn't ever been
 2537 re-optimized for the increased energy of the LHC's collisions. A new sig-
 2538 nal region that increases E_T^{miss} and H_T requirements will allow for better
 2539 sensitivity to SUSY processes.

2540 In addition, the current signal region, in which 60 events were observed
 2541 with 14.7 fb^{-1} , will be populated enough to be subdivided based on event
 2542 features. The current search is agnostic to the number of b -jets in the event,
 2543 for example, but there are now enough events to separate this signal region
 2544 into complementary b -tagged and b -vetoed regions, allowing analyzers to
 2545 independently target models which produce b -jets and those that don't,
 2546 and in the latter case, to dramatically reduce the $t\bar{t}$ background. Signal
 2547 regions can also be binned in other model-dependent features, like number
 2548 of jets, and the E_T^{miss} and H_T requirements can be increased independently,
 2549 targeting different event topologies.

2550 The LHC will continue to run through 2018 with a possible increase to
 2551 $\sqrt{s} = 14 \text{ TeV}$, and will shut down for upgrades until 2021. Three more
 2552 years of data-taking at 14 TeV will follow, with approximately twice the
 2553 current luminosity, referred to as Run 3. After that, the LHC will shut down
 2554 again to prepare for the High Luminosity Large Hadron Collider (HL-LHC),
 2555 which will begin data-taking in 2026 at a luminosity approximately five
 2556 times the current rate. This run will result in roughly 3000 fb^{-1} , which
 2557 will allow for dramatically better sensitivity in SUSY searches. An example
 2558 can be seen in Figure 94, which shows the potential exclusions on a simple
 2559 gluino pair-production model with decays via squarks to a LSP, for the
 2560 approximate luminosities of Run 3 and the HL-LHC.

2561 Searches like this one will surely be repeated with higher and higher
 2562 luminosities, the analyses increasing both in sensitivity and in complexity.

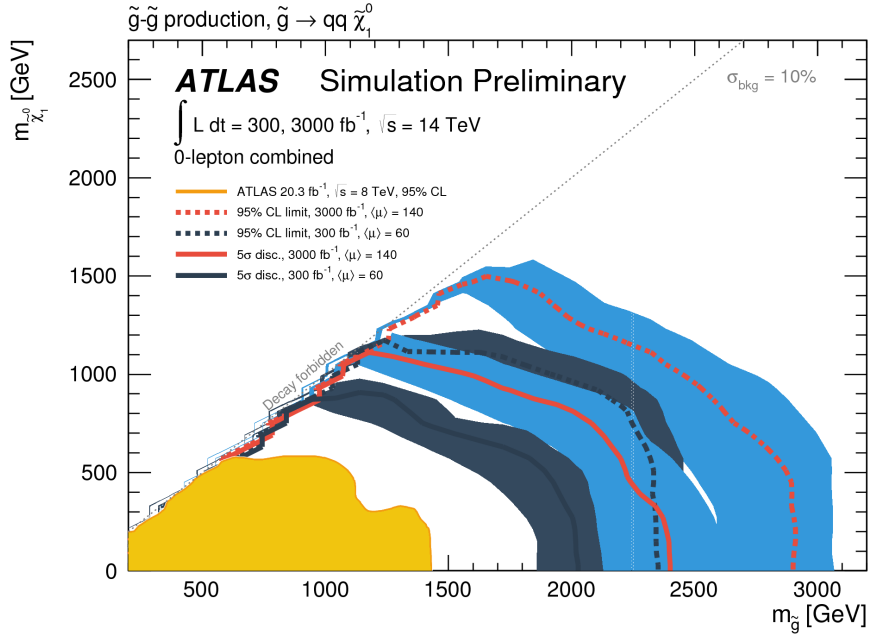


Figure 94: Expected 95% CL exclusion contours (dashed) and 5 σ discovery contours (solid) for $L_{int} = 300^{-1}$ (black) and 3000^{-1} (red) for gluino pair-production, with 1σ bands representing the uncertainty on the production cross-section. Superimposed is the observed 8 TeV exclusion for similar models. [94]

2563 Whether or not they uncover any hints of physics beyond the Standard
 2564 Model remains to be seen.

BIBLIOGRAPHY

- [1] ATLAS Collaboration. "Search for supersymmetry in events containing a same-flavour opposite-sign dilepton pair, jets, and large missing transverse momentum in $\sqrt{s} = 8$ TeV pp collisions with the ATLAS detector." In: *Eur. Phys. J. C* 75 (2015), p. 318. doi: [10.1140/epjc/s10052-015-3518-2](https://doi.org/10.1140/epjc/s10052-015-3518-2). arXiv: [1503.03290 \[hep-ex\]](https://arxiv.org/abs/1503.03290).
- [2] ATLAS Collaboration. *A search for supersymmetry in events containing a leptonically decaying Z boson, jets and missing transverse momentum in $\sqrt{s} = 13$ TeV pp collisions with the ATLAS detector.* ATLAS-CONF-2015-082. 2015. URL: <http://cdsweb.cern.ch/record/2114854>.
- [3] C. P. Burgess and G. D. Moore. *The standard model: A primer.* Cambridge University Press, 2006. ISBN: 9780511254857, 9781107404267, 9780521860369.
- [4] S. L. Glashow. "Partial Symmetries of Weak Interactions." In: *Nucl. Phys.* 22 (1961), pp. 579–588. doi: [10.1016/0029-5582\(61\)90469-2](https://doi.org/10.1016/0029-5582(61)90469-2).
- [5] Abdus Salam. "Renormalizability of Gauge Theories." In: *Phys. Rev.* 127 (1 1962), pp. 331–334. doi: [10.1103/PhysRev.127.331](https://doi.org/10.1103/PhysRev.127.331). URL: <http://link.aps.org/doi/10.1103/PhysRev.127.331>.
- [6] Steven Weinberg. "A Model of Leptons." In: *Phys. Rev. Lett.* 19 (21 1967), pp. 1264–1266. doi: [10.1103/PhysRevLett.19.1264](https://doi.org/10.1103/PhysRevLett.19.1264). URL: <http://link.aps.org/doi/10.1103/PhysRevLett.19.1264>.
- [7] D. Galbraith. *The Standard Model of the Standard Model.* 1997. URL: <http://davidgalbraith.org/portfolio/ux-standard-model-of-the-standard-model/>.
- [8] P. Hut and K. A. Olive. "A cosmological upper limit on the mass of heavy neutrinos." In: *Physics Letters B* 87 (Oct. 1979), pp. 144–146. doi: [10.1016/0370-2693\(79\)90039-X](https://doi.org/10.1016/0370-2693(79)90039-X).
- [9] Huang, Qing-Guo, Wang, Ke, and Wang, Sai. "Constraints on the neutrino mass and mass hierarchy from cosmological observations." In: *Eur. Phys. J. C* 76.9 (2016), p. 489. doi: [10.1140/epjc/s10052-016-4334-z](https://doi.org/10.1140/epjc/s10052-016-4334-z). URL: <http://dx.doi.org/10.1140/epjc/s10052-016-4334-z>.
- [10] The MEG Collaboration. "Search for the Lepton Flavour Violating Decay $\mu^+ \rightarrow e^+ \gamma$ with the Full Dataset of the MEG Experiment." In: (2016). eprint: [arXiv:1605.05081](https://arxiv.org/abs/1605.05081).
- [11] LHCb collaboration. "Observation of $J/\Psi p$ resonances consistent with pentaquark states in $\Lambda_b^0 \rightarrow J/\Psi K^- p$ decays." In: (2015). doi: [10.1103/PhysRevLett.115.072001](https://doi.org/10.1103/PhysRevLett.115.072001). eprint: [arXiv:1507.03414](https://arxiv.org/abs/1507.03414).
- [12] David J Griffiths. *Introduction to elementary particles; 2nd rev. version.* Physics textbook. New York, NY: Wiley, 2008. URL: <https://cds.cern.ch/record/111880>.

- [13] Johan Messchendorp. "Physics with Charmonium – A few recent highlights of BESIII." In: *PoS Bormio2013* (2013), p. 043. arXiv: [1306.6611 \[hep-ex\]](#).
- [14] A. D. Martin, W. J. Stirling, R. S. Thorne, and G. Watt. "Parton distributions for the LHC." In: (2009). DOI: [10.1140/epjc/s10052-009-1072-5](#). eprint: [arXiv:0901.0002](#).
- [15] F. Zwicky. "Die Rotverschiebung von extragalaktischen Nebeln." In: *Helvetica Physica Acta* 6 (1933), 110–127.
- [16] T. S. van Albada, J. N. Bahcall, K. Begeman, and R. Sancisi. "Distribution of dark matter in the spiral galaxy NGC 3198." In: *The Astrophysical Journal* 295 (Aug. 1985), pp. 305–313. DOI: [10.1086/163375](#).
- [17] Stephen P. Martin. "A Supersymmetry primer." In: (1997). [Adv. Ser. Direct. High Energy Phys. 18, 1 (1998)]. DOI: [10.1142/9789812839657_0001](#), [10.1142/9789814307505_0001](#). arXiv: [hep-ph/9709356 \[hep-ph\]](#).
- [18] Craig J Copi, David N. Schramm, and Michael S. Turner. "Big-Bang Nucleosynthesis and the Baryon Density of the Universe." In: (1994). DOI: [10.1126/science.7809624](#). eprint: [arXiv:astro-ph/9407006](#).
- [19] NobelPrize.org. *The Nobel Prize in Physics 2004 - Popular Information*. 2016. URL: https://www.nobelprize.org/nobel_prizes/physics/laureates/2004/popular.html.
- [20] CMS Collaboration. "Search for physics beyond the standard model in events with a Z boson, jets, and missing transverse energy in pp collisions at $\sqrt{s} = 7$ TeV." In: *Phys. Lett. B* 716 (2012), pp. 260–284. DOI: [10.1016/j.physletb.2012.08.026](#). arXiv: [1204.3774 \[hep-ex\]](#).
- [21] CMS Collaboration. "Search for physics beyond the standard model in events with two leptons, jets, and missing transverse momentum in pp collisions at $\sqrt{s} = 8$ TeV." In: *JHEP* 04 (2015), p. 124. DOI: [10.1007/JHEP04\(2015\)124](#). arXiv: [1502.06031 \[hep-ex\]](#).
- [22] *Search for new physics in final states with two opposite-sign same-flavor leptons, jets and missing transverse momentum in pp collisions at sqrt(s)=13 TeV*. Tech. rep. CMS-PAS-SUS-15-011. Geneva: CERN, 2015. URL: <https://cds.cern.ch/record/2114811>.
- [23] Wim Beenakker, Christoph Borschensky, Michael Krämer, Anna Kulesza, and Eric Laenen. *NNLL-fast: predictions for coloured supersymmetric particle production at the LHC with threshold and Coulomb resummation*. 2016. eprint: [arXiv:1607.07741](#).
- [24] Richard D. Ball et al. "Parton distributions with LHC data." In: *Nucl. Phys.* B867 (2013), pp. 244–289. DOI: [10.1016/j.nuclphysb.2012.10.003](#). arXiv: [1207.1303 \[hep-ph\]](#).
- [25] Hung-Liang Lai et al. "New parton distributions for collider physics." In: *Phys. Rev. D* 82 (2010), p. 074024. DOI: [10.1103/PhysRevD.82.074024](#). arXiv: [1007.2241 \[hep-ph\]](#).

- [26] J. Alwall, R. Frederix, S. Frixione, V. Hirschi, F. Maltoni, O. Matte-laer, H. S. Shao, T. Stelzer, P. Torrielli, and M. Zaro. “The automated computation of tree-level and next-to-leading order differential cross sections, and their matching to parton shower simulations.” In: *JHEP* 07 (2014), p. 079. DOI: [10.1007/JHEP07\(2014\)079](https://doi.org/10.1007/JHEP07(2014)079). arXiv: [1405.0301 \[hep-ph\]](https://arxiv.org/abs/1405.0301).
- [27] P. Nason. “A new method for combining NLO QCD with shower Monte Carlo algorithms.” In: *JHEP* 0411 (2004), p. 040. arXiv: [hep-ph/0409146 \[hep-ph\]](https://arxiv.org/abs/hep-ph/0409146).
- [28] S. Frixione, P. Nason, and C. Oleari. “Matching NLO QCD computations with parton shower simulations: the POWHEG method.” In: *JHEP* 0711 (2007), p. 070. arXiv: [0709.2092 \[hep-ph\]](https://arxiv.org/abs/0709.2092).
- [29] S. Alioli, P. Nason, C. Oleari, and E. Re. “A general framework for implementing NLO calculations in shower Monte Carlo programs: the POWHEG BOX.” In: *JHEP* 1006 (2010), p. 043. arXiv: [1002.2581 \[hep-ph\]](https://arxiv.org/abs/1002.2581).
- [30] T. Gleisberg et al. “Event generation with Sherpa 1.1.” In: *JHEP* 0902 (2009), p. 007. arXiv: [0811.4622 \[hep-ph\]](https://arxiv.org/abs/0811.4622).
- [31] T. Sjöstrand, S. Mrenna, and P. Skands. “PYTHIA 6.4 Physics and Manual.” In: *JHEP* 0605 (2006), p. 026. DOI: [10.1088/1126-6708/2006/05/026](https://doi.org/10.1088/1126-6708/2006/05/026). arXiv: [hep-ph/0603175 \[hep-ph\]](https://arxiv.org/abs/hep-ph/0603175).
- [32] S. Agostinelli et al. “GEANT4: A simulation toolkit.” In: *Nucl. Instrum. Meth. A* 506 (2003), pp. 250–303. DOI: [10.1016/S0168-9002\(03\)01368-8](https://doi.org/10.1016/S0168-9002(03)01368-8).
- [33] Morad Aaboud et al. “A measurement of material in the ATLAS tracker using secondary hadronic interactions in 7 TeV pp collisions.” In: (2016). arXiv: [1609.04305 \[hep-ex\]](https://arxiv.org/abs/1609.04305).
- [34] Lyndon Evans and Philip Bryant. “LHC Machine.” In: *Journal of Instrumentation* 3.08 (2008), S08001. URL: <http://stacks.iop.org/1748-0221/3/i=08/a=S08001>.
- [35] *LEP design report*. Copies shelved as reports in LEP, PS and SPS libraries. Geneva: CERN, 1984. URL: <https://cds.cern.ch/record/102083>.
- [36] ATLAS Collaboration. “The ATLAS Experiment at the CERN Large Hadron Collider.” In: *JINST* 3 (2008), S08003. DOI: [10.1088/1748-0221/3/08/S08003](https://doi.org/10.1088/1748-0221/3/08/S08003).
- [37] The CMS Collaboration. “The CMS experiment at the CERN LHC.” In: *Journal of Instrumentation* 3.08 (2008), S08004. URL: <http://stacks.iop.org/1748-0221/3/i=08/a=S08004>.
- [38] The LHCb Collaboration. “The LHCb Detector at the LHC.” In: *Journal of Instrumentation* 3.08 (2008), S08005. URL: <http://stacks.iop.org/1748-0221/3/i=08/a=S08005>.

- [39] The ALICE Collaboration. “The ALICE experiment at the CERN LHC.” In: *Journal of Instrumentation* 3.08 (2008), So8002. URL: <http://stacks.iop.org/1748-0221/3/i=08/a=S08002>.
- [40] W.J. Stirling. *proton-(anti)proton cross sections*. 2013. URL: <http://www.hep.ph.ic.ac.uk/~wstirlin/plots/plots.html>.
- [41] ATLAS Collaboration. *2015 start-up trigger menu and initial performance assessment of the ATLAS trigger using Run-2 data*. ATL-DAQ-PUB-2016-001. 2016. URL: <http://cds.cern.ch/record/2136007>.
- [42] “Electron performance measurements with the ATLAS detector using the 2010 LHC proton-proton collision data.” In: *Eur. Phys. J. C* 72 (2012), p. 1909. DOI: [10.1140/epjc/s10052-012-1909-1](https://doi.org/10.1140/epjc/s10052-012-1909-1). arXiv: [1110.3174 \[hep-ex\]](https://arxiv.org/abs/1110.3174).
- [43] *Electron efficiency measurements with the ATLAS detector using the 2015 LHC proton-proton collision data*. Tech. rep. ATLAS-CONF-2016-024. Geneva: CERN, 2016. URL: <http://cds.cern.ch/record/2157687>.
- [44] ATLAS Collaboration. *Measurement of the photon identification efficiencies with the ATLAS detector using LHC Run-1 data*. 2016. eprint: [arXiv: 1606.01813](https://arxiv.org/abs/1606.01813).
- [45] *Photon identification in 2015 ATLAS data*. Tech. rep. ATL-PHYS-PUB-2016-014. Geneva: CERN, 2016. URL: <https://cds.cern.ch/record/2203125>.
- [46] *Photon Identification Efficiencies using 2016 Data with radiative Z boson decays*. Tech. rep. EGAM-2016-003. Geneva: CERN, 2016. URL: <https://atlas.web.cern.ch/Atlas/GROUPS/PHYSICS/PLOTS/EGAM-2016-003/index.html>.
- [47] *Official Isolation Working Points*. Geneva, 2016. URL: <https://twiki.cern.ch/twiki/bin/view/AtlasProtected/IsolationSelectionTool#Photons>.
- [48] ATLAS Collaboration. “Muon reconstruction performance of the ATLAS detector in proton–proton collision data at $\sqrt{s}=13$ TeV.” In: (2016). DOI: [10.1140/epjc/s10052-016-4120-y](https://doi.org/10.1140/epjc/s10052-016-4120-y). eprint: [arXiv: 1603.05598](https://arxiv.org/abs/1603.05598).
- [49] Matteo Cacciari, Gavin P. Salam, and Gregory Soyez. “The Anti-k(t) jet clustering algorithm.” In: *JHEP* 0804 (2008), p. 063. DOI: [10.1088/1126-6708/2008/04/063](https://doi.org/10.1088/1126-6708/2008/04/063). arXiv: [0802.1189 \[hep-ph\]](https://arxiv.org/abs/0802.1189).
- [50] ATLAS Collaboration. *Jet Calibration and Systematic Uncertainties for Jets Reconstructed in the ATLAS Detector at $\sqrt{s} = 13$ TeV*. ATL-PHYS-PUB-2015-015. 2015. URL: <http://cds.cern.ch/record/2037613>.
- [51] ATLAS Collaboration. *Tagging and suppression of pileup jets with the ATLAS detector*. ATLAS-CONF-2014-018. 2014. URL: <http://cdsweb.cern.ch/record/1700870>.
- [52] ATLAS Collaboration. *Expected performance of the ATLAS b-tagging in Run-2*. ATL-PHYS-PUB-2015-022. 2015. URL: <http://cdsweb.cern.ch/record/2037697>.

- [53] ATLAS Collaboration. *Expected performance of missing transverse momentum reconstruction for the ATLAS detector at $\sqrt{s} = 13$ TeV*. ATL-PHYS-PUB-2015-023. 2015. URL: <http://cds.cern.ch/record/2037700>.
- [54] ATLAS Collaboration. *Performance of missing transverse momentum reconstruction for the ATLAS detector in the first proton-proton collisions at $\sqrt{s}=13$ TeV*. ATL-PHYS-PUB-2015-027. 2015. URL: <http://cds.cern.ch/record/2037904>.
- [55] ATLAS Collaboration. “A neural network clustering algorithm for the ATLAS silicon pixel detector.” In: *JINST* 9 (2014), P09009. DOI: [10.1088/1748-0221/9/09/P09009](https://doi.org/10.1088/1748-0221/9/09/P09009). arXiv: [1406.7690 \[hep-ex\]](https://arxiv.org/abs/1406.7690).
- [56] Luke de Oliveira. *AGILEPack: Algorithms for Generalized Inference, Learning, and Extraction*. 2016. URL: <http://lukedeo.github.io/AGILEPack/>.
- [57] ATLAS Collaboration. *Measurement of performance of the pixel neural network clustering algorithm of the ATLAS experiment at $\sqrt{s} = 13$ TeV*. ATL-PHYS-PUB-2015-044. 2015. URL: <http://cdsweb.cern.ch/record/2054921>.
- [58] ATLAS Collaboration. *Robustness of the Artificial Neural Network Clustering Algorithm of the ATLAS experiment*. ATL-PHYS-PUB-2015-052. 2015. URL: <http://cdsweb.cern.ch/record/2116350>.
- [59] ATLAS Collaboration. *Modelling of the $t\bar{t}H$ and $t\bar{t}V$ ($V = W, Z$) processes for $\sqrt{s} = 13$ TeV ATLAS analyses*. ATL-PHYS-PUB-2016-005. 2016. URL: <http://cds.cern.ch/record/2120826>.
- [60] M. V. Garzelli, A. Kardos, C. G. Papadopoulos, and Z. Trocsanyi. “ $t\bar{t}W^{+-}$ and $t\bar{t}Z$ Hadroproduction at NLO accuracy in QCD with Parton Shower and Hadronization effects.” In: *JHEP* 11 (2012), p. 056. DOI: [10.1007/JHEP11\(2012\)056](https://doi.org/10.1007/JHEP11(2012)056). arXiv: [1208.2665 \[hep-ph\]](https://arxiv.org/abs/1208.2665).
- [61] J. M. Campbell and R. K. Ellis. “ $t\bar{t}W$ production and decay at NLO.” In: *JHEP* 1207 (2012), p. 052. arXiv: [1204.5678 \[hep-ph\]](https://arxiv.org/abs/1204.5678).
- [62] A. Lazopoulos, T. McElmurry, K. Melnikov, and F. Petriello. “Next-to-leading order QCD corrections to $t\bar{t}Z$ production at the LHC.” In: *Phys. Lett. B* 666 (2008), p. 62. arXiv: [0804.2220 \[hep-ph\]](https://arxiv.org/abs/0804.2220).
- [63] ATLAS Collaboration. *Simulation of top quark production for the ATLAS experiment at $\sqrt{s} = 13$ TeV*. ATL-PHYS-PUB-2016-004. 2016. URL: <http://cds.cern.ch/record/2120417>.
- [64] M. Czakon, P. Fiedler, and A. Mitov. “Total Top-Quark Pair-Production Cross Section at Hadron Colliders Through $O(\alpha_s^4)$.” In: *Phys. Rev. Lett.* 110 (2013), p. 252004. arXiv: [1303.6254 \[hep-ph\]](https://arxiv.org/abs/1303.6254).
- [65] M. Czakon and A. Mitov. “Top++: A Program for the Calculation of the Top-Pair Cross-Section at Hadron Colliders.” In: *Comput. Phys. Commun.* 185 (2014), p. 2930. DOI: [10.1016/j.cpc.2014.06.021](https://doi.org/10.1016/j.cpc.2014.06.021). arXiv: [1112.5675 \[hep-ph\]](https://arxiv.org/abs/1112.5675).

- [66] N. Kidonakis. "Two-loop soft anomalous dimensions for single top quark associated production with a W^- or H^- ." In: *Phys. Rev. D* 82 (2010), p. 054018. doi: [10.1103/PhysRevD.82.054018](https://doi.org/10.1103/PhysRevD.82.054018). arXiv: [1005.4451 \[hep-ph\]](https://arxiv.org/abs/1005.4451).
- [67] ATLAS Collaboration. *Multi-Boson Simulation for 13 TeV ATLAS Analyses*. ATL-PHYS-PUB-2016-002. 2016. URL: <http://cds.cern.ch/record/2119986>.
- [68] J. M. Campbell and R. K. Ellis. "An update on vector boson pair production at hadron colliders." In: *Phys. Rev. D* 60 (1999), p. 113006. arXiv: [hep-ph/9905386 \[hep-ph\]](https://arxiv.org/abs/hep-ph/9905386).
- [69] J. M. Campbell, R. K. Ellis, and C. Williams. "Vector boson pair production at the LHC." In: *JHEP* 1107 (2011), p. 018. arXiv: [1105.0020 \[hep-ph\]](https://arxiv.org/abs/1105.0020).
- [70] ATLAS Collaboration. *Monte Carlo Generators for the Production of a W or Z/ γ^* Boson in Association with Jets at ATLAS in Run 2*. ATL-PHYS-PUB-2016-003. 2016. URL: <http://cds.cern.ch/record/2120133>.
- [71] S. Catani, L. Cieri, G. Ferrera, D. de Florian, and M. Grazzini. "Vector boson production at hadron colliders: a fully exclusive QCD calculation at NNLO." In: *Phys. Rev. Lett.* 103 (2009), p. 082001. arXiv: [0903.2120 \[hep-ph\]](https://arxiv.org/abs/0903.2120).
- [72] S. Catani and M. Grazzini. "An NNLO subtraction formalism in hadron collisions and its application to Higgs boson production at the LHC." In: *Phys. Rev. Lett.* 98 (2007), p. 222002. arXiv: [hep-ph/0703012 \[hep-ph\]](https://arxiv.org/abs/hep-ph/0703012).
- [73] ATLAS Collaboration. *Electron efficiency measurements with the ATLAS detector using the 2012 LHC proton–proton collision data*. ATLAS-CONF-2014-032. 2014. URL: <http://cdsweb.cern.ch/record/1706245>.
- [74] ATLAS Collaboration. "Muon reconstruction performance of the ATLAS detector in proton–proton collision data at $\sqrt{s} = 13$ TeV." In: *Eur. Phys. J. C* 76 (2016), p. 292. doi: [10.1140/epjc/s10052-016-4120-y](https://doi.org/10.1140/epjc/s10052-016-4120-y). arXiv: [1603.05598 \[hep-ex\]](https://arxiv.org/abs/1603.05598).
- [75] ATLAS Collaboration. *Search for supersymmetry in final states with jets, missing transverse momentum and a Z boson at $\sqrt{s} = 8$ TeV with the ATLAS detector*. ATLAS-CONF-2012-152. 2012. URL: <http://cds.cern.ch/record/1493491>.
- [76] ATLAS Collaboration. "Measurement of the differential cross-section of highly boosted top quarks as a function of their transverse momentum in $\sqrt{s} = 8$ TeV proton-proton collisions using the ATLAS detector." In: *Phys. Rev. D* 93.3 (2016), p. 032009. doi: [10.1103/PhysRevD.93.032009](https://doi.org/10.1103/PhysRevD.93.032009). arXiv: [1510.03818 \[hep-ex\]](https://arxiv.org/abs/1510.03818).
- [77] CMS Collaboration. "Measurement of the integrated and differential t-tbar production cross sections for high-pt top quarks in pp collisions at $\sqrt{s} = 8$ TeV." In: *Phys. Rev. D* (2016). Submitted. arXiv: [1605.00116 \[hep-ex\]](https://arxiv.org/abs/1605.00116).

- [78] ATLAS Collaboration. *Search for physics beyond the Standard Model in events with a Z boson and large missing transverse momentum using $\sqrt{s} = 7$ TeV pp collisions from the LHC with the ATLAS detector.* ATLAS-CONF-2012-046. 2012. URL: <http://cdsweb.cern.ch/record/1448222>.
- [79] ATLAS Collaboration. “Search for squarks and gluinos in events with isolated leptons, jets and missing transverse momentum at $\sqrt{s} = 8$ TeV with the ATLAS detector.” In: *JHEP* 1504 (2015), p. 116. DOI: [10.1007/JHEP04\(2015\)116](https://doi.org/10.1007/JHEP04(2015)116). arXiv: [1501.03555 \[hep-ex\]](https://arxiv.org/abs/1501.03555).
- [80] ATLAS Collaboration. “Improved luminosity determination in pp collisions at $\sqrt{s} = 7$ TeV using the ATLAS detector at the LHC.” In: *Eur. Phys. J. C* 73 (2013), p. 2518. DOI: [10.1140/epjc/s10052-013-2518-3](https://doi.org/10.1140/epjc/s10052-013-2518-3). arXiv: [1302.4393 \[hep-ex\]](https://arxiv.org/abs/1302.4393).
- [81] ATLAS Collaboration. “Luminosity determination in pp collisions at $\sqrt{s} = 8$ TeV using the ATLAS detector at the LHC.” In: *to be submitted to Eur. Phys. J. C* ().
- [82] Michael Kramer et al. *Supersymmetry production cross sections in pp collisions at $\sqrt{s} = 7$ TeV.* 2012. arXiv: [1206.2892 \[hep-ph\]](https://arxiv.org/abs/1206.2892).
- [83] W. Beenakker, R. Höpker, M. Spira, and P.M. Zerwas. “Squark and gluino production at hadron colliders.” In: *Nucl. Phys. B* 492 (1997), pp. 51–103. DOI: [10.1016/S0550-3213\(97\)00084-9](https://doi.org/10.1016/S0550-3213(97)00084-9). arXiv: [hep-ph/9610490 \[hep-ph\]](https://arxiv.org/abs/hep-ph/9610490).
- [84] A. Kulesza and L. Motyka. “Threshold resummation for squark-antisquark and gluino-pair production at the LHC.” In: *Phys. Rev. Lett.* 102 (2009), p. 111802. DOI: [10.1103/PhysRevLett.102.111802](https://doi.org/10.1103/PhysRevLett.102.111802). arXiv: [0807.2405 \[hep-ph\]](https://arxiv.org/abs/0807.2405).
- [85] A. Kulesza and L. Motyka. “Soft gluon resummation for the production of gluino-gluino and squark-antisquark pairs at the LHC.” In: *Phys. Rev. D* 80 (2009), p. 095004. DOI: [10.1103/PhysRevD.80.095004](https://doi.org/10.1103/PhysRevD.80.095004). arXiv: [0905.4749 \[hep-ph\]](https://arxiv.org/abs/0905.4749).
- [86] W. Beenakker et al. “Soft-gluon resummation for squark and gluino hadroproduction.” In: *JHEP* 0912 (2009), p. 041. DOI: [10.1088/1126-6708/2009/12/041](https://doi.org/10.1088/1126-6708/2009/12/041). arXiv: [0909.4418 \[hep-ph\]](https://arxiv.org/abs/0909.4418).
- [87] W. Beenakker et al. “Squark and gluino hadroproduction.” In: *Int. J. Mod. Phys. A* 26 (2011), pp. 2637–2664. DOI: [10.1142/S0217751X11053560](https://doi.org/10.1142/S0217751X11053560). arXiv: [1105.1110 \[hep-ph\]](https://arxiv.org/abs/1105.1110).
- [88] M. Baak et al. “HistFitter software framework for statistical data analysis.” In: *Eur. Phys. J. C* 75 (2014), p. 153. DOI: [10.1140/epjc/s10052-015-3327-7](https://doi.org/10.1140/epjc/s10052-015-3327-7). arXiv: [1410.1280 \[hep-ex\]](https://arxiv.org/abs/1410.1280).
- [89] Rene Brun and Fons Rademakers. “ROOT — An object oriented data analysis framework.” In: *Nuclear Instruments and Methods in Physics Research Section A: Accelerators, Spectrometers, Detectors and Associated Equipment* 389.1 (1997), pp. 81 –86. ISSN: 0168-9002. DOI: <http://cdsweb.cern.ch/record/1448222>.

- [dx.doi.org/10.1016/S0168-9002\(97\)00048-X](https://doi.org/10.1016/S0168-9002(97)00048-X). URL: <http://www.sciencedirect.com/science/article/pii/S016890029700048X>.
- [90] Lorenzo Moneta, Kevin Belasco, Kyle Cranmer, Sven Kreiss, Alfio Lazzaro, Danilo Piparo, Gregory Schott, Wouter Verkerke, and Matthias Wolf. *The RooStats Project*. 2010. eprint: [arXiv:1009.1003](https://arxiv.org/abs/1009.1003).
- [91] Kyle Cranmer, George Lewis, Lorenzo Moneta, Akira Shibata, and Wouter Verkerke. “HistFactory: A tool for creating statistical models for use with RooFit and RooStats.” In: (2012).
- [92] Glen Cowan, Kyle Cranmer, Eilam Gross, and Ofer Vitells. “Asymptotic formulae for likelihood-based tests of new physics.” In: *Eur. Phys. J. C* 71 (2011), p. 1554. DOI: [10.1140/epjc/s10052-011-1554-0](https://doi.org/10.1140/epjc/s10052-011-1554-0). arXiv: [1007.1727 \[physics.data-an\]](https://arxiv.org/abs/1007.1727).
- [93] A. Read. “Presentation of search results: the CLs technique.” In: *Journal of Physics G: Nucl. Part. Phys.* 28 (2002), pp. 2693–2704. DOI: [10.1088/0954-3899/28/10/313](https://doi.org/10.1088/0954-3899/28/10/313).
- [94] *Prospects for a search for direct pair production of top squarks in scenarios with compressed mass spectra at the high luminosity LHC with the ATLAS Detector*. Tech. rep. ATL-PHYS-PUB-2016-022. Geneva: CERN, 2016. URL: <https://cds.cern.ch/record/2220904>.